COMMISSION OF THE EUROPEAN COMMUNITIES

Joint Research Centre - Karlsruhe Establishment

EUROPEAN INSTITUTE

FOR TRANSURANIUM ELEMENTS

Annual Report 1987

TUAR-87

1988

EUR 11783 EN

COMMISSION OF THE EUROPEAN COMMUNITIES

Joint Research Centre - Karlsruhe Establishment

EUROPEAN INSTITUTE

FOR TRANSURANIUM ELEMENTS

Annual Report 1987

TUAR-87

1988

Published by the
COMMISSION OF THE EUROPEAN COMMUNITIES
Directorate-General
Telecommunications, Information Industries and Innovation
Bâtiment Jean Monnet
LUXEMBOURG

Luxembourg: Office for Official Publications of the European Communities, 1988

Catalogue number: CD-NA-11783-EN-C

Printed in the Federal Republic of Germany

Commision of the European Communities
Joint Research Centre
Nuclear Fuels and Actinide Research Programme
Programme Progress Report 1987
TUAR 87
EUR-Report Nr. 11783 EN

Abstract

Within the frame of the European Fast Reactor Consortium the sub-project **OPDEF** is participating since 1985 in the development of a "pure" nitride fuel for an optimised He-bonding pin concept.

In 1987 five He-bonded mixed nitride pins were fabricated according to specifications for the 19 pin bundle of the irradiation NIMPHE 1. The fuel specifications were established in collaboration with LECA and SEFCA, CEN Cadarache, who fabricated the other 15 pins for this bundle. The irradiation in the PHENIX reactor started in October 1987. The fuel structures were analysed for porosity, grain size, plutonium distribution and oxygen and carbon impurities. Subsequently preparation began for the fabrication of 2 nitride and 2 carbide pins for the 7 pin capsule of NIMPHE 2.

First results of the post irradiation analysis of the six pins of NILOC 1 and 2 after 0.5 atom% burn-up revealed some clad ovalisations and different degrees of fuel restructuring depending on linear rating and initial gap size.

Simulation experiments on the gas release from UN and UO_2 pellets after annealing at 1500° C under 1 kbar Argon showed characteristic differences in burst-release between the two fuels on cooling.

Point defects introduced into UN (sinters and simple crystals) by quenching and by bombardment with Xe and Kr ions were studied by electric resistivity measurements and by Rutherford backscattering. In the ion-bombarded specimens a complex defect structure was observed extending to a depth much larger than the range of the implanted ions.

In the sub-project **Properties of Reactor Materials at High Temperatures** the laser-heated autoclave has been tested and the experimental heating/cooling conditions have been thoroughly investigated up to 4500 K, under high pressure and acoustic levitation conditions. With these results a computer program has been constructed to evaluate the specific heat from the obtained experimental curves.

Measurements of C_p in uranium dioxide was delayed by unexpected levitation instability under pulse heating. Improved solutions are being implemented.

Emissivity X-point phenomena have been measured in other nine refractory metals: The important property was found that at the melting point the sample behaves like a grey-body. Extrapolations of other published data showed that this is true for most of the metals.

The apparatus for the measurement of the thermal conductivity of liquid UO_2 has been further improved by implementing a powerful software for the final evaluation and by increasing the velocity of the thermal data acquisitions and the precision of the temperature measurements.

The **OFT** project was continued in 1987 along the lines defined previously:

i) analysis of technical LWR oxide fuel irradiated up to high burn-up (53 GWd/t) after both steady state base irradiation and after transient testing, and in close cooperation with international projects and industry;

ii) analysis of basic experiments on radiation damage and diffusion and release of volatile fission products; and

iii) a broad modelling approach using the computer codes TRANSURANUS, FUTURE and MITRA.

Post-irradiation analysis of high burn-up and transient-tested LWR fuel was extended from UO_2 to MOX fuel, i.e. LWR fuel containing about 3 % Pu. Detailed microstructural data and radial profiles of Xe and Cs were obtained up to burn-ups of 53 GWd/t. Pu-distribution in MOX fuel was studied, and high burn-up UO_2 was additionally tested in hot cell anneals to measure release of fission products. Temperatures near the melting point (2700° C) were reached. In UO_2 fuels irradiated to above ~ 45 GWd/to, a porous outer ring was observed associated with a pronounced local increase in burn-up due to increased Pu formation. The influence of burn-up on Cs- and Xe-retention was measured.

Basic laboratory experiments showed that significant amounts of Te and Cs (up to 1 at.%) can be located in substitutional sites or on lattice strings. High resolution transmission electron microscopy was used to study precipitation of Te into bubbles. The temperature range for venting of pressurized, rare-gas filled pores on heating and cooling of UO_2 was determined to be rather narrow (800 - 1300° C). The emf-cell developed previously to measure oxygen potentials of irradiated fuel was successfully used to obtain results for (U, Pu)O_2 irradiated to the very high burn-up of 11 at.%. The oxygen potential increased continuously up to this burn-up. Finally, in addition to channeling experiments to study the radiation damage in UO_2 experimentally, Monte Carlo calculations were used to deepen the theoretical insights in fission damage in UO_2.

The modelling activity was successfully continued. The TRANSURANUS code was improved, tested with about 50 very different test data cases and was released to different users. The incorporated models for stress-corrosion cracking and axial friction were improved and models for Pu-redistribution and pore mobility were integrated. The mechanistic fission product behaviour code FUTURE was applied to interpret the hot cell annealing tests, and the third code MITRA which includes short-lived fission products and decay chains was finalized and successfully tested to model available in-pile release experiments.

Finally, a new activity was started to investigate the potential of UO_2 for direct storage. A method to measure very small leach rates was developed and a significant increase in leach rates of highly damaged UO_2 was found.

In the context of sub-project **FACT**, the irradiation experiment SUPERFACT was continued during the reporting period, in the Phenix reactor. Two 'homogeneous' fuel pins, containing 2% americium in the one case and 2% neptunium in the other; one fuel pin containing 20% Np, 20% Am, and one containing 45% Np make up this experiment.

The post-irradiation analyses of KNK II MTE-L pellets continued and their radiochemical analysis was begun.

The interaction of uranium-americium mixed oxides with liquid sodium was studied. Americium III and higher valencies of uranium were identified in the mixed oxides (U, Am)O_{2-x} in contrast to corresponding uranium-plutonium oxides where the uranium is always found in a valence state of IV or less.

In Sub-project **SHAPE** efforts were concentrated on an attempt to compare release rates of particulate contaminant matter dispersed from burning plexiglass in small scale experiments involving (U,Pu)O_2-powder with those measured under real-size laboratory conditions with Eu-Ce-oxide as a stand-in for plutonium oxide. Good agreement was found as to the amount of contaminant (1.5%) released into the ventilation systems, thus underlining the validity of fire experiments with Pu-simulants for the interpretation of "realistic" fire situations, involving heavy radioactive elements. A new series of fire experiments with polycarbonate, polythene and neoprene as burning material was launched. - In our alpha-recoil studies, the much-disputed phenomenon of increased filter penetration in the presence of alpha emitters could be demonstrated to be linked to the presence of radon in the decay chain of the nuclide(s) present in the aerosol.

In the frame of Subproject **REPRO**, the studies of the parameters governing the dissolution of advanced fuels were continued; the composition of the dissolution off-gas and the formation of ammonium ions in the dissolver solution were measured. The behaviour of the advanced fuels was compared to that of UO_2 fuels; activation energies were calculated. Dissolution of UN in nitric acid highly enriched in ^{15}N were carried out with the aim to investigate the secondary exchange reactions taking place between the various reaction products. The calibration of the gas analysis system, by GC-MS, revealed the strong influences of memory effects in the column.

For the separation of the individual actinides the combined extraction chromatographic columns (TBP /ion exchange) were finally tested; the Ln/An separation was improved. The data acquisition program for spectroscopy was extended to the higher wavelengths in the absorption spectrum and to include Np in the calculation matrix. The spectroscopic studies on U, Pu, Np and Am were concluded; the molar extinction coefficients were re-measured as a function of the strength of the nitric acid. The formation of colloids of plutonium was measured as a function of acidity and time.

The goal of the **Actinide Project** is the understanding of the properties of the actinide containing solids in terms of the electronic structure of their constituents and of the contribution of the 5f electrons to the chemical bond. These studies are also relevant to selected aspects of the actinide behaviour in nuclear wastes.
During the reporting period the mineralization technique has been miniaturized and applied to the preparation of transplutonium element compounds.

Search for new materials with interesting magnetic properties was directed toward ternary compounds containing Rh, Ru or Tc together with Np and Si.

The in-house high pressure capabilities have been extended to the measurement of optical reflectivity.

Photoelectron spectroscopic techniques have been used to understand the early stages of reaction between actinide metals or intermetallics with single gases.

Continued access to major European neutron and synchrotron facilities has been essential for the physics experiments carried out during the reporting time.

Collaborative studies extended over the entire project enhance its effectiveness through exchange of ideas and by making the best use of our sample producing capability; in 1987 more than 20 Laboratories in Europe and in the US carried out studies with our samples

Analytical work for the **EURATOM Safeguards Directorate** was continued. The direct measurement of U and Pu by mass-spectrometric isotope dilution has been achieved. ^{243}Am spike must be added to allow the isobaric interference of ^{241}Am with ^{241}Pu to be corrected.

A K-edge densitometer has been field-tested and is in routine use in our laboratory for ECSAM output samples. Excellent agreement was found between results from K-edge and titration for Pu and U.

The isotopic composition of Pu can be determined by γ-spectroscopy and the K-edge detector has been used for this purpose. ^{242}Pu is difficult to measure, however, and a general correlation involving the other Pu isotopes has been previously invoked. Better results are obtained if a batch- or reactor-specific correlation is used and this is also advantageous for the Safeguards inspector.

A laboratory robot is routinely in use for the chemical conditioning of ECSAM samples: No reliability problems have been observed up to now. Three input samples are processed by the robot in one batch, yielding 12 loaded mass-spectrometry filaments.

The aim of **Prospective Studies** on aerosol scavenging is to investigate the feasibility of the use of high intensity acoustic waves to combat a release of radioactive or toxic material into the atmosphere. The potential areas of application range from small scale laboratory "spills" to major releases of hazardous aerosol and gas into the atmosphere. To date, the studies have concentrated on

a) Acoustic aerosol agglomeration
b) Acoustically enhanced toxic gas absorption
c) Acoustically induced particle drift.

In the agglomeration studies it is important to investigate the cohesive nature of different aerosols and to quantify the agglomeration rate and the flocculation index (ratio of final to initial diameter) as a function of time and sound pressure level. It is also necessary to establish the aerosol mass loading required for effective agglomeration. During the reporting period agglomeration studies on a variety of aerosol including Latex spheres and polydisperse alumina and Uranium-Plutonium oxide nuclear fuel have been made.

Activated carbon, in aerosol form, is not a good absorber of gas. This is due to the fact that the viscous boundary layer around the particles acts to shield the gas to be absorbed from the carbon surface. In the present studies a high intensity sound field is used to disturb this viscous boundary layer in an attempt to modify the absorption kinetics of the gas to be absorbed. Results will be presented on the absorption of NO_2 (concentration 500 ppm) on micron size activated carbon aerosol in the presence of a sound field.

Once the aerosol has been agglomerated, or the toxic gas has been absorbed onto the carbon aerosol, it is desirable to remove the aerosol from the system. In principle this can be achieved through an acoustically induced particle drift mechanism in which only the particles and not the gas is moved. One such mechanism is provided by the averaged Oseen force in which as a result of the non-linear interaction of the sound wave, drift velocities in excess of 1 ms^{-1} have been predicted theoretically. Results of a preliminary experimental investigation of these drift forces will be described.

In the frame of the subproject **Radioactive Waste Management and the Fuel Cycle** we have completed the verification of the OXAL-MAW process. The capabilities of this process, previously developed at JRC Ispra with simulated highly active solutions to produce an "alpha free" waste, were verified with medium active process solutions using samples of a few liters. The characterization of the resulting solidified product is also underway. In addition, we have examined the suitability of leaching vessels to be used in active waste experiments. Furthermore certain quality control aspects of the leaching procedure for glass specimens were evaluated.

In the subproject **Safety of waste disposal in continental geological formations** we have continued our intense research activity on physical processes occurring in the near field in a salt formation and in the glass itself, with emphasis on radiation damage effects and fracture behaviour. These studies have involved curium doped glasses where correlations between hardness, crack length, critical load and leach rates have been established. A study by ion implantation has revealed that the temperature at which the damage is produced is an important parameter on the properties of nuclear waste glasses. The radiation stability of the tailor made waste ceramic Synroc B has been studied via ion implantation, leaching experiments and curium doping. A study on alkali diffusion in waste glass has been completed and has shown that cesium thermodiffusion will be a minor effect during long term storage. We also have shown the influence of metal inclusions on the results of Vickers identation on fission product containing waste glasses.

In the reporting period, an activity was initiated to characterize highly active glasses in the hot cells (collaboration ENEA/COMSVITE/JRC Ispra). The first efforts were centered on morphology studies, as well as distribution and composition of the matrix and precipitated phases.

As a contribution to the JRC Programme on **Fissile Materials Management**, computer programs have been written for the SAL (Software Analytical Laboratory) of IAEA to check the consistency of reprocessing input analysis performed there. The programs were written in FORTRAN and include extensive plotting routines for graphical output.

A prototype K-edge/XRF densitometer, constructed at KfK is being field-tested in the Institute. A single X-ray tube is used for both measurements which normally last 3×1000 seconds. The uranium concentration is determined by K-edge absorption and the Pu/U ratio from the X-ray fluorescence spectrum. The results for 22 batches, measured by this technique and by IDMS (isotope dilution mass-spectrometry) have been compared. A slight, significant, positive bias for the hybrid measurements was found which could have been caused by the presence of undissolved matter in the solutions.

A new mass-spectrometry technique, the so-called 'flash evaporation technique', has been developed and applied to sub-nanocurie samples of U and Pu. Comparisons made with the standard technique on NBS standards demonstrated the reliability of the method.

A laboratory robot is being programmed to condition, separate and mount sub-nanocurie amounts directly on mass-spectrometer filaments. Amounts as small as these can be transported relatively freely and can then be measured using the 'flash' technique in an ECSAM laboratory. Instructions for the robot are expected to be given from an 'expert system' at present under development on a PC.

Commission of the European Communities
Joint Research Centre
Karlsruhe Establishment
Federal Republic of Germany

TUAR 87

European Institute for Transuranium Elements Annual Report

January - December 1987

Table of Contents

Foreword
to the Annual Progress Report 1987 of the European Institute for Transuranium Elements (TUAR 87)

As a consequence of the recent re-orientation of JRC research policy, the Joint Research Centre is being restructured. The traditional organisation by sites and directorates will be replaced by "Institutes". The JRC will run less by "Programmes", but more by "Institutes". Although this reorganisation leaves the European Institute for Transuranium Elements what it always used to be, it implies a strengthening of its responsabilities.

As from 1987 our Institute will publish annually its proper Progress Report.

The staff of JRC Karlsruhe has so far reported semiannually (and since 1986 annually) only the projects of their work in the frame of the Plutonium Programme or, later, the Nuclear Fuels and Actinide Research Programme. These periodic programme reports dealt therefore only with part of the work executed at the Institute, their distribution was restricted to a small group of authorized persons, and only after two years they were considered freely accessible.

TUAR 87 is the first Institute's Report not only with a new cover, but also with other features which clearly distinguish it from its predecessors:

- It covers not only work done in the field of Nuclear Fuels and Actinide Research, but concerns all fields of research treated at the Institute within the reporting period; such as Safeguards, Reactor Safety and Waste Management.

- It is an open publication.

We hope that this will further promote the exchange of information with laboratories which are active in related areas within the Community and abroad and attract new interest in our work.

TUAR 87 may contain helpful information for those colleagues and friends who plan to come to Karlsruhe in October 1988, when the Institute celebrates its 25th anniversary with a Symposium "Transuranium Elements Today and Tomorrow - Properties, Problems, Prospects". Proceedings of this Symposium will be published in a special report which can be obtained from the address given on the next page.

Karlsruhe, September 1988 J. van Geel

Inquiries concerning the Symposium "Transuranium Elements Today and Tomorrow" should be addressed to

Dr Ulrich Benedict
Scientific Secretary of the Symposium
"Transuranium Elements Today and Tomorrow"
Postfach 2340
D-7500 Karlsruhe 1

Executive Summary

Making use of advanced nuclear fuel production techniques developed at JRC Karlsruhe, five helium-bonded mixed uranium-plutonium nitride fuel pins for a fast flux irradiation experiment were characterized and fabricated, and the experiment was started on October 30, 1987, in the PHENIX reactor at Marcoule. Considerable improvements in safety and reliability for the fast reactor fuel cycle are expected from this new line of research, which is closely coordinated with similar efforts in France and carried out in accordance with recommendations of the European Fast Breeder Consortium ("The Club of Five"). Fuel fabrication for a second irradiation test is under way. An examination of newly developed mixed nitride fuels after irradiation to 0.5 a/o burn-up in the Petten High Flux Reactor, carried out in the same context, revealed marked differences to findings obtained on carbide fuel which was previously irradiated under similar conditions, thus increasing our understanding of and confirming expectations into the technological potential of mixed nitrides as a safe and reliable fast breeder fuel.

A laser autoclave developed for measurements of thermophysical properties of nuclear materials at extremely high temperatures of interest to nuclear safety studies became operational. It was first used for a systematic investigation of the optical emissivity of refractory metals below and above their melting temperatures. In all cases studied it was observed that spectral emissivities at different wavelengths converge and cross-over at the melting point ("X-point"), which means that at their melting temperatures all materials behaved optically like "grey bodies". If this could be shown to be generally true, it would be an effect of considerable technical importance since it would furnish a means of calibrating optical temperature measuring devices which have to operate under difficult experimental conditions (for example under high pressures which affect the absorptive properties of the gas surrounding the specimen to be investigated).

An experiment to convert long-lived actinides extracted from the waste of nuclear power stations into short-lived fission products was started by irradiating "minor actinide" (i.e. americium and neptunium-containing) fuel pins in the PHENIX reactor at Marcoule, France. Two of the pins of this experiment contain 2% Np or 2% Am ("homogeneous fuel"). Of the other two pins, one has 45% Np and the other one 20% Np and 20% Am. The experiment was designed to test the behaviour of minor-actinide containing oxide fuel under fast flux conditions. The method under investigation offers the possibility to reduce the potential risk associated with the disposal and storage of high-active nuclear waste by several orders of magnitude. Parallel studies with metallic fuel containing minor actinides are under preparation on a contractual basis for third parties.

Actinide research performed at JRC Karlsruhe aimes at an understanding of how electrons from the (unfilled) 5f shell characteristic for this group of elements in the Periodic Table contribute to the chemical and physical properties of these metals and their compounds. For this purpose it is necessary to perform structural, electrical, magnetic and physico-chemical investigations with well-characterised specimens, mostly in single crystal form. The mineralisation technique developed in previous years for single crystal growth of uranium and plutonium compounds has been extended in 1987 to neptunium compounds, and in a new effort to miniaturize this procedure, small crystals of AmBi and AmTe were produced. Single crystals of $PuFe_2$ and UFe_2 were prepared and used for neutron diffraction and magnetization studies. These systems are particularly interesting because they exhibit a strong hybridisation between 5f and 3d electrons. This phenomenon is also the subject of considerable theoretical efforts involving band structure calculations. In the same context, high-pressure experiments have been performed by subjecting actinides and actinide compounds to pressures up to 500 kbar and measuring their interatomic distances. Experiments of this kind have revealed a hitherto unknown phase transition at about 450 kbar in plutonium. Observations of this kind lead to a better understanding of electronic interactions in solids in general and are widely recognized as valuable contributions to solid state physics.

The Institute provided three ultrasonic thermometers and their data acquisition systems for the PAHR-Celia 1 simulated debris test bed rig which was irradiated in the MELUSINE reactor at Grenoble. One of the instruments monitored a drastic dry-out effect with a temperature rise of up to 1K/s and thus contributed essentially to the success of the experiment To instrument a SCARABEE in-pile experiment (BF3), the Institute develops an ultrasonic liquid level detector cabable to operate up to 3000°C in the presence of sodium vapour.

In R&D work on the destructive analysis of fissile materials, a new concept was developed for the on-site verification of reprocessing plant input sample analysis using a robot which conditions and separates uranium and plutonium and deposits them in sub-nanocurie amounts on mass spectrometer filaments. The analysis is then performed with the novel "flash evaporation technique" which avoids most of the disadvantages of conventional mass spectrometical techniques and which has been successfully employed to analyse extremely small amounts of U and Pu.

In the context of studies related to the management of radioactive waste, equipment and methods for for leaching tests with active waste glass samples were investigated. The effect of radiation on the mechanical strength and on the leaching properties of (curium-doped) glasses was studied in detail. Highly active glasses were characterised in our hot cells by determining, in a first effort, the composition of the matrix and the distribution of precipitated phases.

U and Pu concentrations have been directly measured for the first time by the mass spectrometric isotope dilution technique on reprocessing plant input samples using ^{243}Am spikes to correct for isobaric interferences. A K-edge densitometer has been brought into use for the routine analysis of U and Pu solutions after reprocessing and good results were obtained in comparison with those from the standard titration method.

Information technology is gaining in importance also in the domaine of radiation protection. Recent progress in the field at JRC Karlsruhe concerned the extended use of data processing equipment for monitoring the presence of alpha emitters in laboratory air. This helped to bring down the detection limits and to identify significantly high results among the large amount of measured data thus reducing the need for frequent individual incorporation checks.

Air cleaning under chemico-toxicological and radiological aspects is a subject of imminent public concern. Prospective studies are being undertaken at JRC Karlsruhe in order to demonstrate that micron-sized aerosol particles can be agglomerated and trapped in an acoustic field of high intensity. During the reporting period rapid acoustic agglomeration has been demonstrated in standing sound waves for a number of different dusts composed of latex spheres, polydisperse alumina and uranium-plutonium oxide fuel particles on a laboratory scale. Medium-size pilot experiments to test the technological viability of this technique are under preparation.

40 plutonium dioxide standard samples weighing from 10 g to 2.9 kg were prepared on a contract basis and in collaboration with ALKEM for non-destructive testing at the PERLA facility in Ispra.- Other major contract work performed at JRC Karlsruhe in 1987 concerned the development of methods for the purification of (enriched) UO_2 samples and the measurement of the oxygen potential of irradiated LWR fuel specimens. - A number of isotope analyses were performed on spent fuel specimens upon request from various utilities in the Federal Republic.

Planned Activities

Review of Activities Planned for the Reporting Period

	1987											
	1	2	3	4	5	6	7	8	9	10	11	12
1 Operation Limits of Nuclear Fuels												
Optimization of Dense Fuel						(2)[1]	(3)			(5)[9]	[4][8]	[7]
Properties of Reactor Materials at High Temperatures		(2)	(3)(4) (7)[7]			(1)			[2](9)	[3][4]	[1]	(5)[5] (6)[6] (8)[9]
2 Transient Behaviour of Oxide Fuels and Fission Product Release (under Severe Fuel Damage Conditions)	(1)[1]	(2)[2]				(3)(4) [3][4]	[5]	(5)			(6)	(7)
3 Actinide Cycle Safety												
Formation of Actinides												[1][2] [3]
Safe Handling of Nuclear Fuels				(1)				(2)	[2]	(3)	[3](4)	[4]
Reprocessing of Nuclear Fuels		(1)[3]		(2)[2]	(3)	(4)[4]	[8]	[1][9]	[6]	(5)	(6)[5]	(7)
4 Actinide Research												
Actinide Chemistry			(1)		[1]	(2)	(3)[2]		(4)(6)	[3]	(5)[4]	
Actinide Physics			(1)[1]		(2)	(3)[2] [3](7)	(4)(8)	[4][7]	(5)[5]	(10)	(6)[6] [10] [8]	(9) [9]
5. Work for the Euratom Safeguards Controls Directorate	[3]				[2]							[1]
6. Prospective Studies				(1)		[1][2]	(5)	[3]	[5]	[4]		(6)[6]
7. Reactor Safety				[1]			[2]		[3]			
8. Radioactive Waste Management			[1]	[6]			[2]	[3]	[4]	[5]		
9. Safeguards and Fissile Materials Management			[2]							[1]		(3)(4)

( ) Planned [ ] Achieved

1.1 Advanced Fuel Optimisation

1 NIMPHE 1 shipment to Cadarache
2 POMPEI + SWELLAC + NILOC 3 shipment to HFR
3 NIMPHE 2 shipment to Cadarache
4 Characterisation of fuels for irradiation (structure, thermal stability)
5 Comparison of thermal stability between MN with low and high oxygen content
6 Thermal diffusivity measurements
7 Start of post-irradiation analysis of NILOC 1 + 2
8 Start of modelling of NIMPHE 1 + 2 and SWELLAC
9 First diffusivity data for modelling available

1.2 Properties of Reactor Materials at High Temperatures

1 Testing and improvement of laser autoclave
Complete system operational
2 Systematic measurement of emissivity on metals
3 Reevaluation of methods for UO_2 density measurements
4 Decision point about method for density measurements
5 First results about temperature distribution and pressure on levitated sphere available
6 First results on X-point in metals
7 Existence of UO_3-molecules
8 Evaporation mechanism of MO_{2-x} tentatively established
9 Software and hardware problems solved, start of experiments on solid and liquid IO_2

2.0 Oxide Fuel Transients

1 Development of simplified versions of FUTURE code started
2 Installation of OFT Data Bank System
3 Second hot cell transients evaluated
4 PIE data collected at 35 and 45 GWd/t
5 Results on thermal gas solubility available
6 Start of PIE for Risø III (fuel transport not possible due to known difficulties)
7 Release of FUTURE for general use (see point 8 for 1988)

3.1 Formation of Actinides

1 Post irradiation analysis of KNK II b fuel samples
2 Na - Am - U compatibility study
3 Comparison of prediction and experiment in spent LWR fuel

3.2 Safe Handling of Nuclear Fuels

1 3-D glove-box models installed and running at TU
2 Comparison of results for large and small-scale fire experiments
3 Completion of work on alpha recoil experiment
4 Experimental results on acoustic scavenging and decision on continuation of this work

3.3 Reprocessing of Nuclear Fuels

1 Chemical tests for Multipurpose Unit
2 Peroxy complexes of Pu studied
3 Np reduction on irradiated solutions studied
4 Analysis of off-gas from nitride dissolution completed
5 Dissolution test of UN in HNO_3 enriched in ^{15}N
6 Studies on NH_4-ions in nitride dissolver solution
7 OMA installation in hot cell operational

4.1 Actinide Chemistry

1 Preparation of $(U_{1-x}Np_x)Pd_3$ intermetallics with An = Np and Pu
2 Preparation of AmX (X = Te and Bi) single crystals
3 Single crystal neutron experiments on UCp_3Cl
4 Surface reaction studies of O_2 and CO on clean metal
5 Preparation of ^{242}Pu from oxide form
6 Assembling low temperature X-ray equipment

4.2 Actinide Physics

1 High pressure X-ray diffraction on Cm-Am alloys and on Pu metal completed
2 High pressure X-ray absorption at LURE synchrotron
3 Polarized-neutron experiments on single crystal $PuFe_2$
4 High resolution photoemission experiments on Np metal
5 Band structure calculations of $AnFe_2$ series
6 Start of investigations on Np chalcogenide single crystals
7 High pressure reflectivity studies started
8 Low temperature photoemission capability constructed
9 Neutron investigation on CmO_2 initiated
10 Neutron investigation on $NpCo_2$ initiated

5.0 Work for the Safety Euratom Controls Directorate

1 Direct IDMS of fuel samples
2 Installation of K-edge densitometer for routine analysis
3 Installation of analytical robot

6.0 Prospective Studies

1 Acoustic agglomeration demonstrated on laboratory scale and quantified for various pressure levels
2 Preliminary absorption capacity measurements
3 Construction of test chamber for aerosol absorption studies
4 First measurements of toxic gas $*NO_2$ absorption by micron size activated carbon aerosol in a sound field
5 Experimental programme started
6 Start of Oseen drift experiments
7 Decision on continuation of the work

7.0 Reactor Safety

1 Modification of TRANSURANUS for coupling with the EAC
2 Improvement of structure and speed of the MITRA code
3 Fabrication, calibration and utilisation of 2 ultrasonic thermometers

8.0 Waste Management

1 Verification of oxal process
2 Suitability tests of leaching vessels
3 Radiatioin damage studies with Cm-doped glasses and ceramics
4 Study of alkali diffusion in waste glasses
5 Study of fracture toughness of waste glasses
6 Characterisation of highly active waste glasses

9.0 Safeguards and Fissile Materials Management

1 MS technique for sub/nanocurie amounts of U & Pu
2 Testing of hybrid K-edge device
3 Development of robot for on-site installation
4 Development of an expert system

Activities Planned for 1988

		1988						
		1	2	3	4	5	6	II
1	**Operation Limits of Nuclear Fuels**							
	Optimization of Dense Fuel		1			2 3	4	5 6 7
	Properties of Reactor Materials at High Temperatures		9	1 6 12	3 10 15 20	4 11 16 24	5 7 17 21	2 23 8 18 22 13 19 14
2	**Transient Behaviour of Oxide Fuels and Fission Product Release (under Severe Fuel Damage Conditions)**	1	2		3	4,5	6,7	8 9 10
3	**Actinide Cycle Safety**							
	Formation of Actnides	5		1		4	6	2 3
	Safe Handling of Nuclear Fuels			1	2		3	4 5 6 7
	Reprocessing of Nuclear Fuels			1			2	3 4 5,6
4	**Actinide Research**							
	Preparation, Characterisation, Application		3			2	1	4
	Electronic structure studies					3		1 4 2 6 5
	High pressure studies		1				2	5 3 4
5	**Work for the Euratom Safeguards Controls Directorate**			1				
6	**Prospective Studies**							1
7	**Reactor Safety**		1,2			3		4,5
8	**Radioactive Waste Management**	1			2		3,4	5,6
9	**Safeguards and Fissile Materials Management**			2			1	3 4

1.1 Advanced Fuel Optimisation

1 Nimphe 2 shipment to Cadarache
2 POMPEI + SWELLAC shipment to HFR
3 Start or irradiation of NIMPHE 2
4 PIE of NILOC 1 + 2 terminated
5 Characterization of NIMPHE 2 and SWELLAC fuels
6 Measurement of thermal expansion and thermal stability of MN
7 Model for begin of life of nitride and carbide fuel performance ready

1.2 Properties of Reactor Materials at High Temperatures

1 Amelioration of the leviation performance at high temperature
2 Decision point: Implementation of splat-cooling techniques for production of amorphous ceramics
3 First controlled pulse heatings
4 Data collection and error estimation of the effective heat losses
5 Evaluation of the heat-up and cool-down curves
6 Calibration of the x-ray-shadow apparature
7 Assessment of the achievable precision
8 Preliminary measurements
9 Substitution of defective parts
10 Start measurements
11 Evaluation of thermal conductivity
12 Machine planning starts
13 Construction of furnace and implementation of the laser-flash and high-speed pyrometers
14 Testing and calibration work starts
15 Design for gamma-shielding of the furnace starts
16 Decision point final location of the machine
17 Starts calibration of TOF and Quadrupole
18 Modification of the present setup to improve sensitivity
19 Starts shielding construction
20 Iterating procedure to deduce C_p
21 Evaluation of the x-ray-shadow imaging
22 Study of the physical background of the emissivity properties of UO_2 and assessment of the new interpolating functions
23 Definition of the procedure for the calculation of thermal conductivity in the laser-flash experiments
24 Starts collection of the database for the relevant compounds

2.0 Oxide Fuel Transients

1 RISØ III, Analysis with TRANSURANUS
2 SIMFUEL, 6 % b.u., TEM, implantations, start
3 FUTURE, Application to RISØ results
4 Hot cell anneals of high b.u. UO_2, start
5 Channeling study, damage in UO_2, report
6 EMF measurements, start with UO_2
7 REM, TEM, EMPA of RISØ III, start
8 Decision point on simplified FUTURE version
9 BUMMEL, end of irradiation
10 Evaluation and report on SIMFUEL results

3.1 Formation of Actinides

1 Complettion of KNK II b analyses
2 Comparision of KNK II b analyses with calculations
3 End of KNK II a irradiation
4 Start of comparative study on partitioning MA's
5 Start of "Fingerprint analysis" of spent fuels
6 Start of analysis of MA's in high burn-up MA fuel

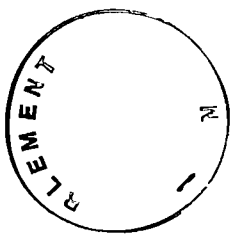

3.2 Safe Handling of Nuclear Fuels

1 Particle size measurements during fire experiments started
2 Aerosol re-suspension from suspension and solutions started
3 Detector design for low-level activity measurements started
4 Decision: Participation in Phébus. Remote particle monitoring equipment designed, and modification started
5 3 D aerosol dispersion model installed + running
6 First results of fire model calculations available
7 Start of acoustic cyclone pre-treatment work

3.3 Reprocessing of Nuclear Fuels

1 Purification of Np and Am, (HPLC), started
2 Colloids of Pu, studied
3 Dossolution of UN in HNO_3 enriched in 15N, completed
4 OMA at glovebox, operational
5 Destruction of NH_4^+- ions in nitride dissolver solutions, done
6 Irradiatiated MN dissolved

4.0 Actinide Research

Preparation, Characterization, Application

1 Setting up of equipment for the preparation of ^{242}Pu metal from the oxide (begin)
2 Surface reaction studies of gases on actinide metals and actinide - transition metal intermetallics (begin)
3 Preparation of new compounds of Np and Tc (begin)
4 Mössbauer spectroscopy of Np-Ru, Np-Tc, Am Bi... compounds (begin)

Electronic structure studies

1 Photoemission studies on δ-Pu and Pu-Am alloys (completed)
2 Photoemission studies on Pu chalcogenides (begin)
3 Neutron experiments on NpSb single crystals
4 Band structure studies extended to random alloy systems (begin)
5 Low temperature photoemission capability improved
6 Neutron investigation of CmO_2 (continued)

High pressure studies

1 X-ray diffraction study of Pu metal and PuSb (completed)
2 Optical reflectivity of U and Th (completed)
3 Optical reflectivity of Np and Pu chalcogenides (completed)
4 Low T resistivity equipment operational for U and Th samples
5 X-ray diffraction study of Pu-Am alloys (completed)

5.0 Work for the Safeguards Controls Directorate (Lux)

1 Installation of second analytical robot

6.0 Prospective Studies

1 Decision on continuation of the work

7.0 Reactor Safety

1 Coupling of TRANSURANUS code to EAC with regard to thermohydraulics and in-pile motion
2 Extension of TRANSURANUS to fuel-coolant interaction
3 MITRA ready for testing and comparison with experiments
4 Fabrication. calibration and utilisation of two ultrasonic thermometers
5 Design of equipment for source term studies

8.0 Waste Management

1 Radiation damage and diffusion studies in waste forms continued
2 soxhlet leach tests on active waste glasses
3 Microanalysis of structure and composition of waste glasses by SEM and EDAX
4 Round robin test
5 Definition of promising alternative waste matrices
6 Characterisation of cement matrix

9.0 Safeguards and Fissile Materials Management

1 Refinement of "flash evaporation" technique
2 Field testing of hybrid K-edge device
3 Field test of robot for on-site use
4 Development of expert system

1 Operation Limits of Nuclear Fuels

1.1 Optimisation of Dense Fuels

Introduction

The mixed nitride (U, Pu)N has several properties which makes it an attractive future LMFBR fuel for the optimised fast-reactor fuel-cycle provided its in-pile performance is as good as that of the presently used oxide fuel [1].

Only limited experience has been gained with irradiating nitride fuels up to the present and this pertains to fuel specifications, pin designs and operation conditions which are of little interest for future fuel cycle conditions. The mixed nitride has to be optimised with regard to fuel and pin specifications and fabrication in order to meet the future requirements for its in-pile operation and reprocessing. These requirements have been explained already [1] and need not be repeated (TUAR 86, 17-18).

During 1987 a large part of the work of the project "Optimization of Dense Fuels" consisted of the fabrication and characterisation of five fuel pins for the irradiation experiment NIMPHE 1, and the start of the fuel (carbide and nitride) fabrication for the irradiation experiment NIMPHE 2. Furthermore, the post-irradiation examination of the short term irradiations NILOC 1 and NILOC 2 could finally be started.

The basic studies on uranium nitride were continued.

At the end of 1987 the fuel fabrication of NIMPHE 2 and the post-irradiation examination of NILOC were still continuing; they will both be finished early in 1988.

Fuel Fabrication and Characterization

Fabrication of Mixed Nitride Pins for the Irradiation NIMPHE 1

The irradiation experiment NIMPHE 1 was prepared in collaboration with CEA, DECPu (Plutonium Fuel Research Department), Cadarache [2]. The Institute fabricated mixed nitride fuel pellets for five pins by carbothermic reduction of a $UO_{2+x}+PuO_2+C$ blend. The fuel was specified with an oxygen and carbon content of less than 1000 ppm and a pellet density of 82 % TD. The cladding material was delivered by CEA, Cadarache.

The fuel pellets for two pins were fabricated by the conventional carbothermic reduction - ballmilling - pressing - sintering technique (type C) and those for the other three pins by the direct pressing of the reacted porous material after the carbothermic reaction (type DP).

As starting material, the previously investigated carbon powder "UF2" (TUAR 86, 22) was chosen. Both the PuO_2 and UO_2 powders were used "as available". The UO_2 powder, a granulate having a grain size between 0.1 and 0.8 mm, was sieved < 125 µm in order to diminish diffusion distances and improve both the kinetics of the carbothermic reduction and ensure good microhomogeneity of the reaction product. The PuO_2 powder, containing 0.7 % agglomerates > 63 µm (up to 1 mm), was used as delivered. These powders were mechanically blended and pressed. For the synthesis of the desired low oxygen and carbon (< 1000 ppm) nitride fuel, an excess of carbon in the masterblend was used.

The carbothermic reduction temperature was 1875 K for 17 h under flowing nitrogen, followed by treating with a gas mixture of nitrogen / hydrogen. One part of the reaction product was comminuted by a fast turning hammermill to particle sizes < 60 µm (pin no. 5), another part by additional ballmilling (pin no. 2) and then pelletised. The third part was directly recompacted into pellets and sintered at 2000 K for 17 h under a nitrogen / hydrogen mixture.

Both the oxygen and carbon content of the nitride was below 1000 ppm after the carbothermic reduction and sintering steps. The pellet diameters of pins no. 3 and 5 were adjusted with a tolerance of ± 5 µm by centerless grinding.

The pellets were loaded into stainless-steel tubes, filled with helium and T.I.G. welded. After the final check pins numbered 1, 2, 3, 5 were sent to Cadarache for assembling together with the fuel pins fabricated by DECPu - SEFCA / CEN.Ca.

Fuel and fuel pin data are reported in Tab. 1.1.

Table 1.1 Data For Fuel Pins NIMPHE 1

Fuel data (U, Pu)N		NIMPHE 1				
		1	2	3	4	5
Fabrication method		DP*	C*	DP*	DP*	C*
Pu / (U + Pu)		20.99	20.93	20.88	20.93	21,.3
Fissile material						
Pu-239	w/o	84.73	84.73	84.73	84.73	84.73
Pu-241	w/o	1.41	1.41	1.41	1.41	1.41
Pu-235	w/o	0.77	0.77	0.77	0.77	0.77
Fuel density (% TD)		83.1	81.4	82.4	81.8	81.9
Stand. deviation		0.65	0.63	0.41	0.97	0.38
XRD Param.	Å	4.8910	4.8912	4.8914	4.8907	4.8910
C	w/o	0.034	0.015	0.010	0.033	0.035
O	w/o	0.053	0.047	0.038	0.037	0.034
N	w/o	5.37	5.44	5.45	5.43	5.41
Mean pellet diam.	(mm)	5.387	5.458	5.418	5.426	5.419
Stand. deviation		0.017	0.008	0.004	0.019	0.005
Bonding		He	He	He	He	He
Gap (µm)		124	94	112	110	111

*DP: Direct Pressing C: Conventional

Fuel Characterisation by Ceramography, SEM and EMPA

Fuel pellets of the NIMPHE 1 production were analysed by quantitative ceramography, SEM, mercury porosimetry for open porosity and autoradiography and electron probe microanalysis for plutonium distribution.

Typical microstructures of the fuels are shown in Fig. 1.1. The pore shapes of the five materials are rather similar. The porosity of the material of pin 2 was found to be distributed homogenously. In the other fuels the local porosity showed a certain inhomogeneity with the pores mostly

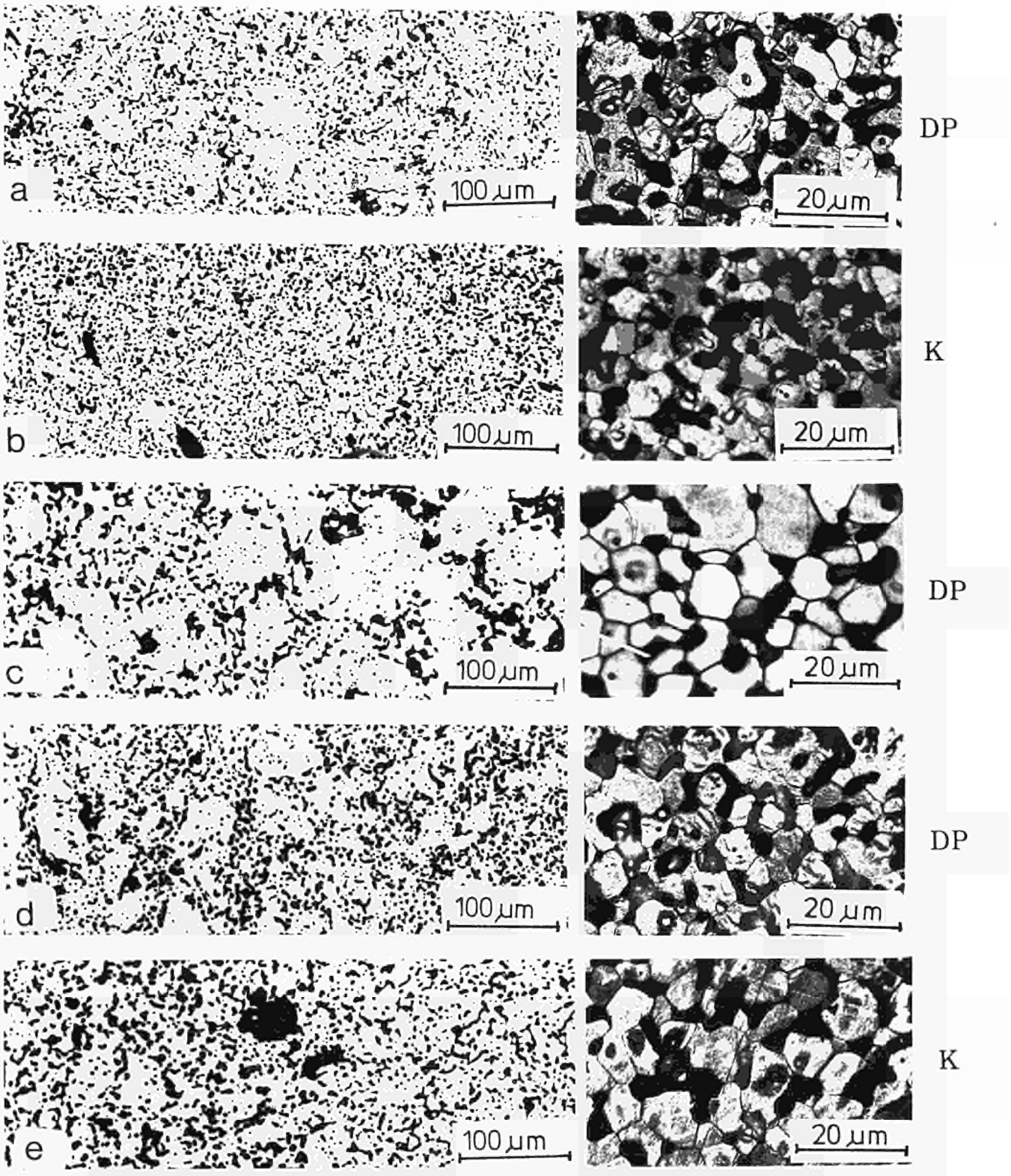

Fig. 1.1 *Microstructure of as-sintered MN pellets (NIMPHE 1 irradiation experiment). a) to e) represent the material in fuel pins 1 to 5.*

located around zones (of 60 to 100 µm diameter) with somewhat higher density. In Fig. 1.2, mean porosity values measured at 3 radial positions in pellet cross-sections of each type of fuel have been collected. The material of pin 1 is about 2 % more dense than that of the others. All pellets analysed are slightly less dense at the periphery than in the centre.

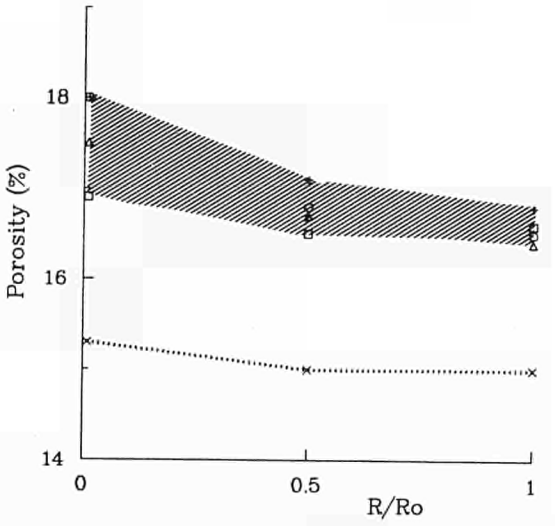

Fig. 1.2 *Radial porosity distribution observed, in as-sintered MN pellets. Material in pin: x 1, O 2, Δ 3, □ 4, + 5*

Fig. 1.3 shows SEM-micrographs of fracture surfaces from fuels of pins 1, 2, 3 and 5. Comparison of these structures with the polished and etched microstructures of Fig. 1.1 shows that practically all pores are located on grain boundaries. Mercury porosimetry indicates furthermore that they should be all interconnected (open porosity). Mean grain sizes for the various fuels were determined by the

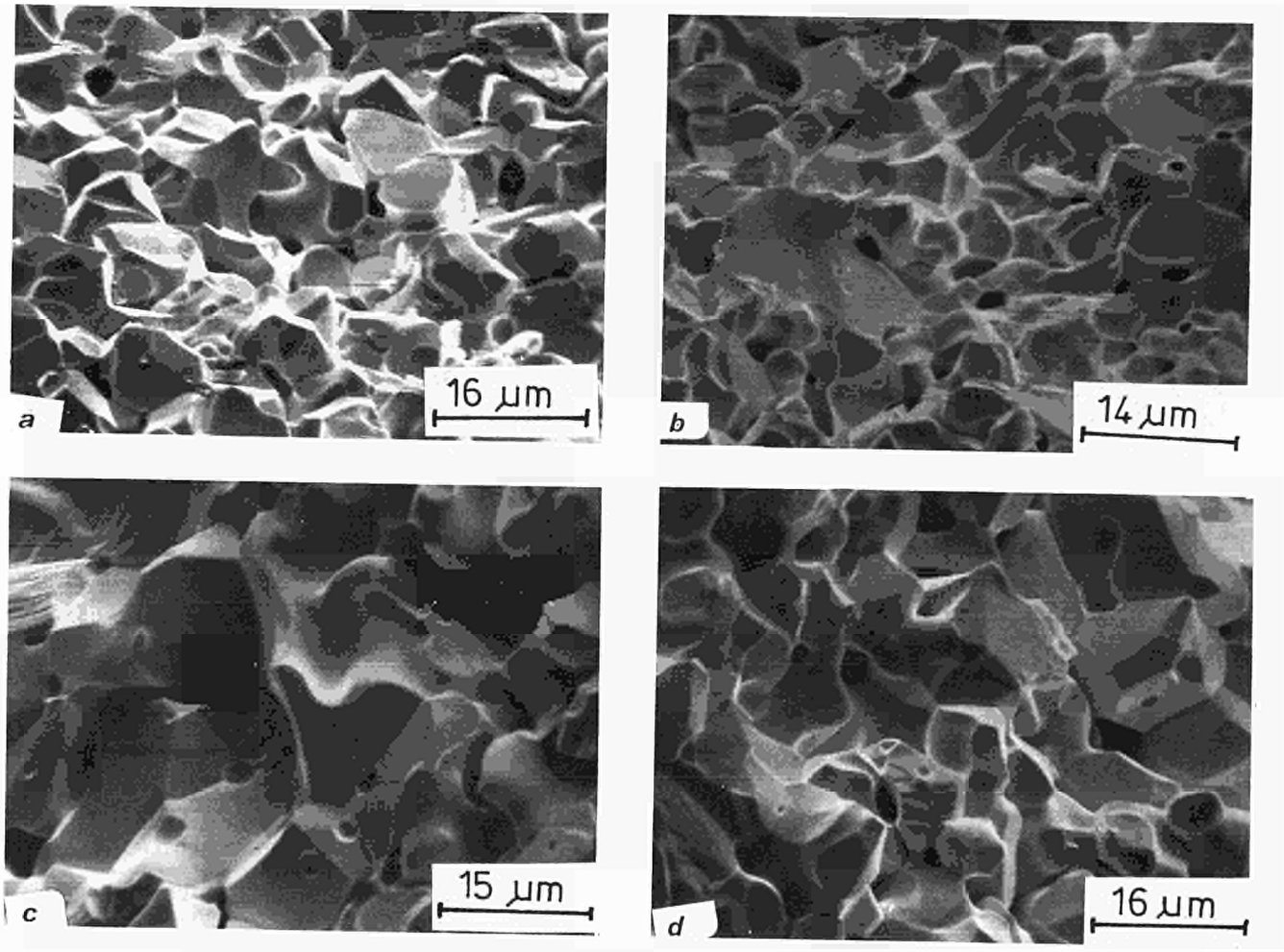

Fig. 1.3 *SEM micrographs showing typical microstructures of as-sintered MN type fuel (NIMPHE). a) to d): MN in pins 1, 2, 3 and 5 respectively*

intercept method on the polished and etched samples; the values range between 6.5 and 9 µm.

The main results for each fuel type have been collected in Tab. 1.2. A slightly lower (~ 1 %) density is always obtained by pellet geometry and weighing as compared with quantimet measurements. This may be due to small cracks or density variations in the pellets which are not observed in pellet cross sections.

Autoradiography and electron probe micro-analysis (EMPA) of pellet cross sections show a certain inhomogeneity in the plutonium distribution of the three fuels prepared by direct pressing.

EMPA point analysis of the specimens from the fuels of pins 1, 3 and 4 gave Pu concentrations that varied between 10 and 38 %. The homogeneity of the plutonium distribution, however, is better than these figures would imply. For example, X-ray line scanning on a specimen from pin 4 showed that the bulk of the fuel contained between 18 and 22 wt% Pu which is close to the specified value of 19.8 wt%. Along a diametrical line scan about 100 domains with more than 25 wt% Pu were counted. Most of these were smaller than 5 µm; the largest was about 20 µm in size. Likewise, fuel domains with less than 15 wt% Pu rarely exceeded 20 µm in size. One domain measuring 100 µm was found on the diametrical line scan made on the specimen from pin 4. Similar observations were made on specimens from the fuels for pins 1 and 3.

The alpha autoradiographs of specimens of the three directly pressed fuels showed several spots rich in Pu which were about 0.5 mm in size but these could not be located with the microprobe.

Table 1.2 Grain size and porosity of MN type fuel pellets

Pin No.	Fabrication route	Density*) (% Th.D)	Mean grain size (µm)	Total porosity (Quantimet) (V %)	Open porosity (Hg-porosimetry) (V %)
1	DP	83.0	8.0	15.0	18
2	K	81.5	7.5	17.5	17
3	DP	82.5	9.5	16.5	-
4	DP	81.5	6.5	16.6	-
5	K	82.0	9.0	17.2	18

DP = direct pressing and K = conventional fabrication route

*) Geometrical density

The Irradiations NILOC 1 and 2

Purpose and Preparation of the Irradiations NILOC (Nitride fuel, low in oxygen and carbon)

The aim of this irradiation was to test the initial fuel restructuring of three types of pellet fuels: type K fabricated by the conventional pellet production method, type P by direct pressing and type G by direct pressing of a granulate. The irradiation NILOC 1 consisted of 3 pins with PHENIX pin geometry in a TRIO-capsule and NILOC 2 had 3 pins of the geometry used in Super PHENIX 1.

The specifications of the fuel and for the irradiation conditions as well as a short description of fabrication and fuel characterisation have been given in the previously (TUAR 86 19 - 28). Since the post-irradiation examination is not yet finished, only some general remarks will be made here.

Irradiation Conditions

As previously reported (TUAR 86, 19) the start of the irradiations was originally planned for September 1986. Irradiation of NILOC 1 started on December 18th 1986 and was completed on January 12th 1987. Irradiation of NILOC 2 started on February 12th and was completed on March 10th 1987. Both experiments performed correctly; however the expected irradiation conditions of both experiments were in not met. Pins P and G were in each case irradiated at a higher linear power than specified. The main irradiation results of the experiments NILOC 1 and 2 are condensed in Tab. 1.3.

Table 1.3 Experiments NILOC 1 and NILOC 2, irradiation conditions

	NILOC 1			NILOC 2		
	P	G	K	P	G	K
burn-up a/o	0.58	0.58	0.48	0.66	0.62	0.53
mean heat load kW/m	55.4	55.2	45.2	101.03	90.6	78.9

Radial Temperature profiles at the beginning of irradiation (B.O.L.) were estimated for the positions of the fuel sections analysed. The surface and center temperatures are collected in Tab. 1.4. As usual in advanced fuels at B.O.L., the size of the clad-fuel gap determines to a large extent the fuel centre temperature. Axial power and clad temperature profiles at B.O.L. are given in Fig. 1.4a and b for pins K and P.

The pin positions designated 2.1 and 2.2 in the first column of Tab. 1.4 were chosen for destructive examination. Their locations along the pin axis are indicated in Fig.'s 1.4a and 1.4b, i.e. they were chosen close to the flux maximum at different initial clad gaps. In this way the restructuring of the fuel can be studied over a relatively large temperature range at a burn-up of roughly 0.5%. It can be seen from Tab.'s 1.3 and 1.4 that only pins K1 and K2 had linear ratings χ close to the specified values (45 and 73 kW/m respectively) whereas pins P and G produced considerable "overpower", with pin P2 reaching 38%. Therefore a third section, 2.3, was investigated in pin P2 at a location off the flux maximum closer to the specified power.

Table 1.4 NILOC, at B.O.L. Calculated surface and center temperatures at selected cross-sections

PIN	Pin position cut	Outer clad temperature °C	χ kW/m	fuel-clad gap mm	fuel surface temperature °C	fuel centre temperature °C
2 K	2.1	584	76.0	0.070	1010	1370
	2.2	582	75.8	0.130	1320	1660
2 G	2.1	615	86.0	0.100	1220	1610
	2.2	620	86.0	0.130	1410	1780
2 P	2.1	660	96.5	0.070	1140	1580
	2.2	653	97.2	0.130	1480	1880
	2.3	628	70.5	0.130	1340	1650
1 K	2.1	449	46.0	0.070	840	1080
	2.2	452	46.0	0.115	1090	1310
1 G	2.1	484	56.4	0.070	940	1230
	2.2	488	56.4	0.115	1230	1490
1 P	2.1	510	56.8	0.070	970	1250
	2.2	509	56.6	0.115	1230	1500

Post-Irradiation Examinations

The analysis of the clad diameters did not reveal any strong clad deformation for the three pins of NILOC 1 and for pin K of the experiment NILOC 2, i.e. the pin with the average value of 76 kW/m for the maximum rating. In contrast the other two pins of NILOC 2 with the highest maximum ratings of 90 and 101 kW/m showed strong fuel/clad mechanical interaction. This consisted mainly of considerable clad ovalisation and correlated with the local linear rating along the pin axis.

The axial migration of ^{137}Cs correlated similarly with the linear rod power. Pins with $\chi < 80$ kW/m did not show caesium migration, whereas in the two pins with $\chi \geq 90$ kW/m caesium had migrated to both ends of the fuel column, i.e. away from the region with the highest rating.

Sectioning of the pin positions 2.1 and 2.2 showed that all the pellets had fractured at least once completely across. It appears that the pellets of type G had a somewhat higher tendency to fracture than those of types P and K.

Optical and scanning electron microscopy revealed that a large part of the pellets had restructured to different degrees. Restricted to different ranges of temperature and linear rating the following in-pile mechanisms could be identified which had operated for certain periods over the initial 0,5% burn-up:

- fission gas precipitation in intragranular bubbles,
- fission gas precipitation in grain boundary bubbles,
- fuel swelling and fuel densification.

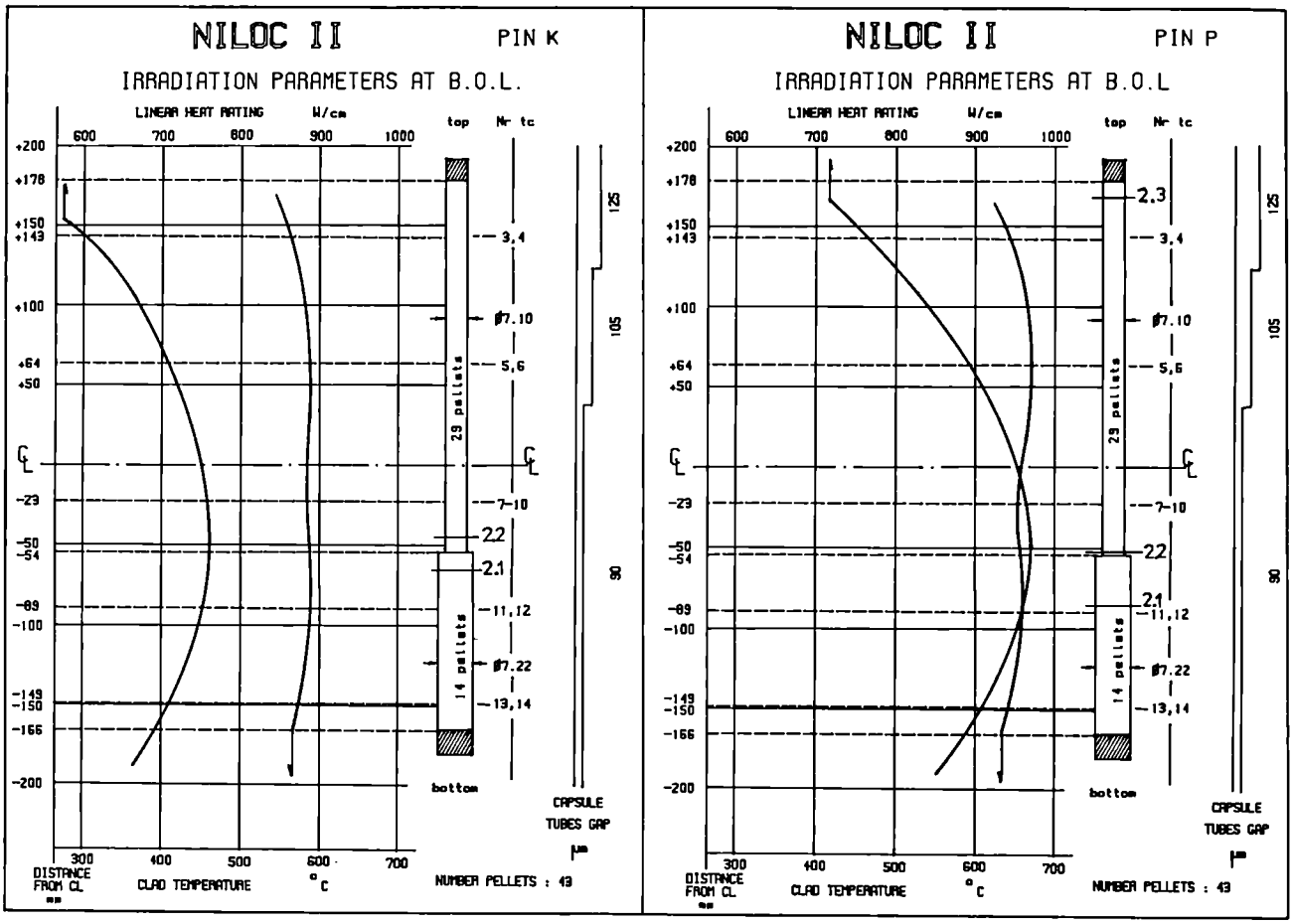

Fig. 1.4 Linear Rating and Clad temperature of Pins NILOC II K and NILOC II P at the beginning of Irradiations (B.O.L.)

The quantitative analysis of the various phenomena has been started. It will finally provide the basis for a realistic description of the various mechanisms as they have operated during the first 25 days of irradiation.

References

[1] H. Blank, "Specification and characterization of dense fuels for LMFBR's", paper presented at Int. Conf. on Characterization and Quality Control of Nuclear Fuels, Karlsruhe 25-27/5/87, J. Nucl. Mat. 153 (1988) 171

[2] H. Bernard, P. Bardelle, D. Warin, Technical Committee Meeting on Advanced Fuel for F.B.R., IAEA, Vienna, 3-5 Nov. 1987.

Basic Studies on Nitrides

Simulation Study of Grain Boundary Venting. Cooling Bursts

Sintered UN was annealed at high pressure (1500°C, 1000 bar) in an argon atmosphere. This hot pressing procedure leads to closure of open pores which are filled with Ar at the experimental pressure. The UN was subsequently annealed in a UHV mass spectrometer with various heating rates and terminal temperatures of up to 2500 K. No measurable gas release was observed during heating, whereas many gas bursts were measured during cooling. The quantity of gas released per burst was a few

10^{11} Ar-atoms. The corresponding volume of gas is in the range of 10 μm^3. It appears therefore that individual pores are vented in each burst. These cooling bursts were observed at all temperatures between 2500 K and ambient, and a few individual bursts occurred even 35 min after reaching a temperature within 20 K of the ambient temperature. Fig. 1.5 shows the release rate (not to scale) for one cooling rate, indicating how the bursts could be resolved as individual events.

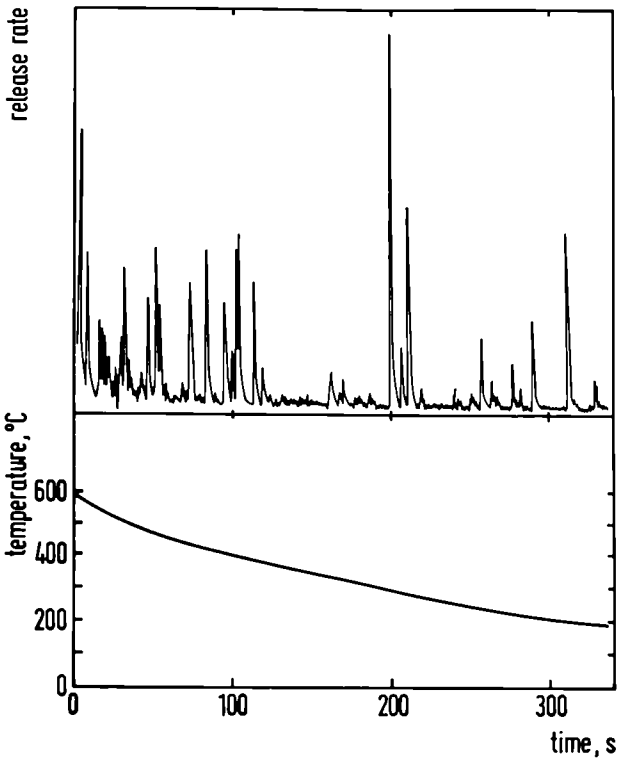

Fig. 1.5 *Argon release from UN upon cooling illustrating the narrow release peaks, and the fact that cooling bursts are observed at very low temperatures*

Cooling bursts are known to occur in operating oxide fuel and are explained as cracks venting grain boundary bubbles. The present results indicate, for the first time, that cooling bursts occur in UN as well, and they show that individual venting events occur even at very low temperatures, in contrast to UO_2, where these bursts are only observed in a rather narrow temperature range of about 1000 to 1500 K.

Point Defects in Uranium Nitride

Quenching of UN

By quenching uranium mononitride from high temperatures and measuring the increase in electrical resistivity as well as its recovery to the original value upon annealing, one can measure the formation and migration energies of quenched-in vacancies and interstitials. The knowledge of these basic physical parameters is necessary to interpret more complicated processes (grain growth, sintering, radiation damage or fission gas transport in nuclear fuels). The quenching apparatus described in TUAR 86, 28 and two different batches of UN were used: One batch of sintered UN (1700 °C, 24 h, vacuum, 85 % of theoretical density, and a content of ~ 1000 ppm each of oxygen and carbon) and highly dense arc-melted UN. Both types of UN were stoichiometric. The sinters were cut into small pieces (1x1x6 mm) and the arc melted material into bigger samples (1x1x12 mm). For quenching, these specimens were heated in a radio-frequency induction furnace under high-vacuum for 30 min at temperatures ranging from 1400 to 1700° C, and then dropped into copper powder cooled with liquid nitrogen.

The electrical resistivity of the samples was measured by the classical four probe potential drop method before and after the quench. All measurements were performed at room temperature. Basically, the quenched-in resistivity is a function of the annealing

temperature and of the type of defects thermally created. Usually, one assumes that at the most a very small fraction of the point defects recombines or forms clusters during the quenching process.

Results

Rather variable results were obtained. In the first experiments with sintered UN, the resistivity increased drastically by up to a factor of 2, and continued to increase (rather than to decrease as would be expected) during recovery anneals. Metallographic analysis showed microcrack formation perpendicular to the axis of the samples. These microcracks propagated during recovery anneals. Since these cracks form upon rapid heating, a reduction of the heat rate from 300 K/min to 50 K/min overcame this difficulty.

However, in a large series of successful quenchings with neither surface oxidation nor microcrack formation, the changes in resistivity were almost random. Relative increases ranging from 1 to 4 % were found, but sometimes $\Delta\rho$ stayed constant upon annealing without recovery, or it even increased slightly and linearly with temperature (10^{-3} $\mu\Omega$ cmK^{-1}).

For the best arc-melted specimen, two steps could be detected: a recovery step of 43 % around 100 °C and a second one of 57 % recovery around 500° C (Fig. 1.6). This total $\Delta\rho$ was only 3.85 $\mu\Omega$ cm and such precise measurements were only possible with this large size specimen.

All other recoveries were detected on very small changes in resistivity near to the limit of detection and were therefore not reproducible.

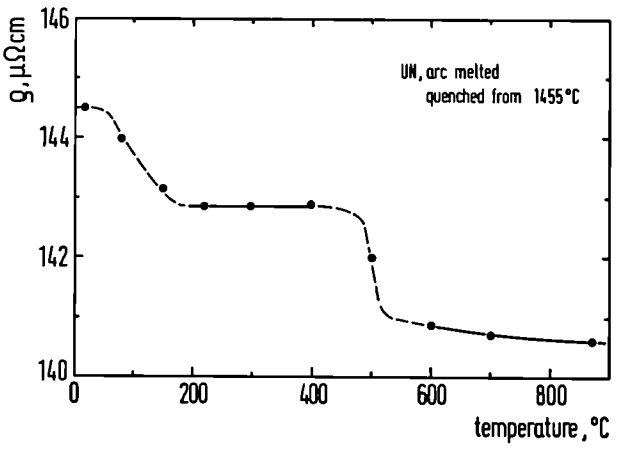

Fig. 1.6 Recovery of electrical resistivity of UN quenched from 1455° C

Probably, in the low density sinters, only a small fraction of the point defects are actually quenched-in and therefore very small or no changes in resistivity are measured, because of the high sink density (pores, grain boundaries) in these specimens. Also, the channeling work (see below) showed that radiation-induced point defects tend to migrate at room temperature and form extended defects even in UN single crystals. The point defects migrated out of the damage zone where they were produced. If this happens in quenched crystals as well, this would explain the small $\Delta\rho$-values found and the lack of significant recovery stages as they were found previously in uranium carbide [1].

Channeling measurements

Rutherford backscattering, RBS, in combination with the channeling effect (TUSR **86**, 29) was further used to study surface properties of UN. The technique was also applied to investigate radiation damage produced by ion implantation of Kr and Xe ions. As before, the experiments were performed at the van de Graaff accelerator and the ion implanter of the Institut für

Nukleare Festkörperphysik, KfK, in cooperation with O.Meyer and A.Turos

Little is known about channeling properties of UN single crystals. Only one short report on proton channeling in UN has been published up to now [2]. There is no information available in the literature concerning He-ion channeling and its applications to radiation damage investigations. It was therefore necessary to begin with the investigation of different surface preparation techniques in order to develop the best method to obtain UN single crystals with essentially defect-free surfaces. Care had also be taken to avoid any surface contamination during preparation, e.g. deposition of impurities and/or oxide layer formation (see TUAR 86, 29).

Surface preparation

Mononitride single crystals were oriented using X-ray diffraction with the {100} plane as the crystal surface. The crystals were then cut with a diamond saw into slices of about 1 mm thickness. After many trials the appropriate method of surface preparation was found: It consists of three steps:

- the samples should first be polished by hand using different grades of SiC paper down to 1.25 µm diamond paste;

- then, to release the mechanical stress produced by polishing, the samples should be annealed in vacuum (1-5x10^{-5} torr) at 1300° C for 30 min;

- finally, the samples should be electropolished in a Lenoir electrolyte (typically used for sample preparation in electron microscopy) with a current density of 1.5 A/cm^2 for relatively short times of about 10 sec.

Fig. 1.7 shows the random and aligned spectra obtained for 2 MeV ^{4}He-ions incident on a <100> UN single crystal prepared using the method described above. The very low χ_{min}-value of about 3 % indicates that the crystal surface is essentially defect-free. The low dechanneling rate confirms that there are no intrinsic defects in the bulk of the crystal either. One notes a quite pronounced surface peak which may produce an important part of dechanneling thus

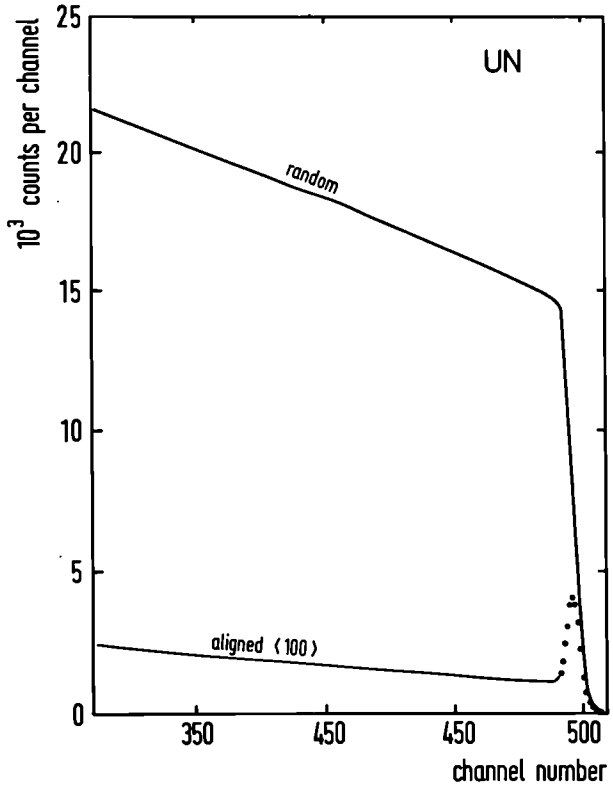

Fig. 1.7 Rutherford backscattering, RBS, energy spectra of 2 MeV He-ions from a UN single crystal in random direction or oriented with the beam parallel to the <100> direction (aligned case)

contributing to the χ_{min} value. It is thought that this peak is due to the spontaneous formation of a thin oxide layer on top of the crystal after electropolishing when the crystal becomes exposed to air. However, the presence of a small mosaic spread cannot be ruled out.

Radiation damage behavior of as-implanted UN single crystals

The UN single crystals were implanted with different doses of Xe-ions or Kr-ions at energies of 500 keV and 400 keV, respectively. Prior to implantation, the crystals were oriented by means of channeling. Only those crystals having $\chi_{min} \leq 4$ % were used for further experiments.

Fig. 1.8 shows the aligned and random backscattering spectra for 2 MeV ^{4}He-ions incident on UN single crystals implanted with Kr ions to the fluences of 1.5 x 10^{15} and 8 x 10^{15} ions/cm^2. The aligned spectra show a "surface peak" around channel 500. This peak is due to the surface atoms not being shielded by atomic rows, and possibly to a thin surface oxide layer on the UN. Similar peaks are always found as well on unimplanted crystals. No "damage peak" due to scattering on displaced U-atoms is seen within the range of the Kr ions. Such damage peaks are always found in ion-bombarded largely ionic or covalent materials such as UO_2 [3] or Si [4]. Rather, two characteristic portions of the spectra can be distinguished. The first begins just behind the surface peak and exhibits a large dechanneling rate. It extends down to a dose-dependent depth where the dechanneling rate abruptly decreases. Such a region is usually called a "dechanneling knee".

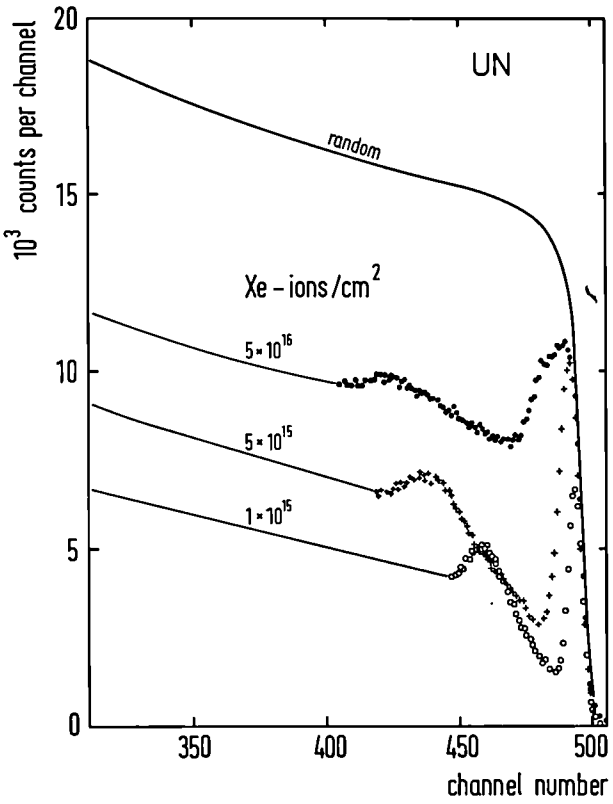

Fig. 1.8 Aligned and random RBS spectra for 2 MeV He-ions of UN single crystals implanted with Kr-ions

This dechanneling behavior is typical for ion implanted metals and is due to defect migration beyond the range of the ion beam during or after bombardment at room temperature leading to the formation of extended defects (dislocations, dislocation loops, stacking faults etc.) by agglomeration of displaced atoms and vacancies during ion bombardment. However, the formation of a fairly large surface peak and its increase with increasing implantation fluence indicates that regions containing simple defects or their clusters can form in the vicinity of the surface. It may also be speculated that this could be due to the disordering of the outermost layer as a result of the preferential sputtering of nitrogen. However, since the corresponding portion of the random spectra did not reveal a significant increase of the scattering yield, this

effect seems to be less probable. The crystals are defect-free at the depths below those corresponding to the "knee", as indicated by the low dechanneling rate at larger depths (smaller channel number in Fig. 1.8). At the higher doses, the knee is located at a depth corresponding to about 5 times the range of the Kr ions. Such a defect migration has never been observed with UO_2.

In conclusion, these experiments clearly indicate a largely metallic bonding in UN.

Similar results were obtained for Xe-ion implanted UN as shown in Fig. 1.9. The dechanneling rate is significantly higher in the near surface region than in the bulk crystal. The most important difference with respect to the spectra shown in Fig. 1.8 is the appearance of a peak in the "knee" region. The position of the peak changes with the implantation fluence as it is always located at the interface between distorted and undistorted regions of the crystal. The nature of this peak is not yet known. One possible explanation is that a large number of stacking faults was formed in this region due to the higher deposited energy density. This parameter has a larger value in the case of Xe-ion implantation than in that for Kr-ion implantation. Also the growth of the surface peak with increasing implantation fluence is more pronounced than in the case of Kr-ion implantation.

The very high defect density produced by the implantation with the highest dose ($5x10^{16}$ Xe/cm^2) has significantly changed the shape of both aligned and random spectra (not shown in Fig. 1.9). One notes a decrease of the scattering

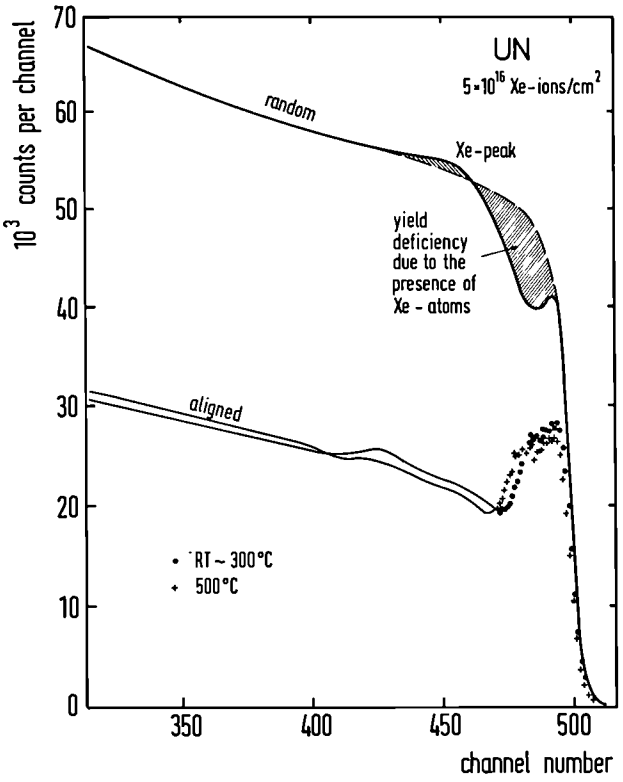

Fig. 1.9 As Fig. 1.8 UN implanted with different doses of Xe-ions

yield in the random spectrum in the region corresponding to the surface peak in the aligned spectrum. This is due to massive incorporation of Kr-atoms.

The nature of defects produced by ion implantation in UN can be investigated by performing a channeling analysis at different energies of incident ions. Such an approach is based on the fact that the dechanneling cross section for different defects depends in a characteristic manner on the ion energy.

For metals the following relations have been proposed:

a) $\sigma(\text{stacking faults}) \sim E^{0}$

b) $\sigma(\text{dislocation loops}) \sim E^{+1/2}$

c) $\sigma(\text{displaced atoms}) \sim E^{-1/2}$

d) $\sigma(\text{amorphous surface layer}) \sim E^{-1}$.

Thus the χ_{min}-value determined at different depths is a measure of the defect concentration whereas its energy dependence can be used for identification of the defect type.

Fig. 1.10 a-d show the channeling backscattering spectra for the UN sample implanted with $1x10^{15}$ Xe/cm^2 measured at incident ion energies of 2 MeV, 1.4 MeV, 1 MeV and 0.7 MeV. In order to be able to compare the χ_{min}-values for each incident energy, the energy-to-depth conversion function has to be calculated. Such a comparison has to be performed at energies corresponding to the same depth. The energy-depth relationship was calculated using the THICKC computer code and stopping power data of Ziegler [5].

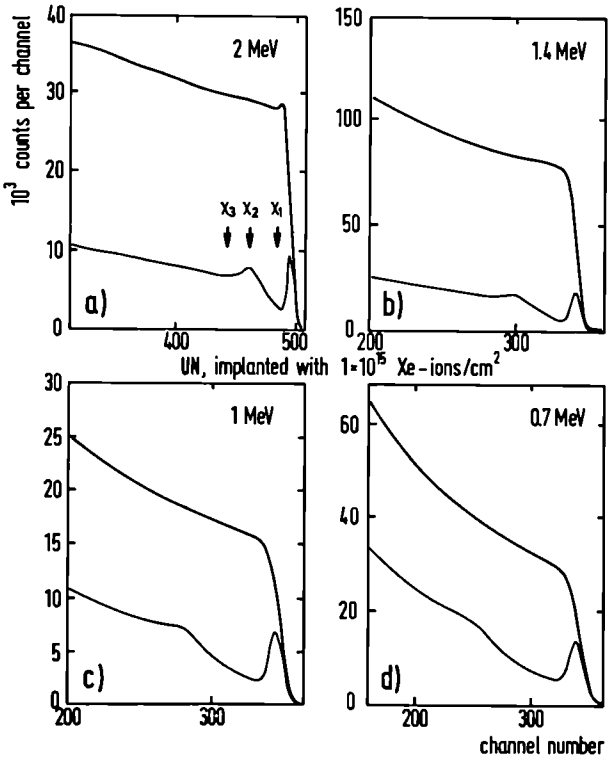

Fig. 1.10 RBS spectra of UN single crystals in random and aligned mode implanted with 1 x 10^{15} Xe-ions/cm^2; energy dependence of channeling

A peak can be seen in the aligned spectrum in Fig. 1.10a which appears in the vicinity of the channel 470. This peak decreases with decreasing incident He-ion energy and disappears completely at 0.7 MeV. This behavior can only be attributed to the formation of a dislocation network or of loops which agglomerated at the interface between damaged and damage-free regions of the crystal.

The presence of a small peak can also be seen in the random spectrum in the vicinity of the high energy edge. It is thought that this peak is due to the local enrichment in U atoms produced by preferential sputtering of N atoms. Such an effect was not observed for implantation with the lighter Kr ion.

The χ_{min} was measured at 3 characteristic points of the spectrum shown in Fig. 1.10a, i.e. just behind the surface peak χ_1, before the dechanneling knee χ_2 and behind the interface peak χ_3 (channel 440). The corresponding channels for the remaining spectra (Figs. 1.10b-d) and those measured for Kr implantation were evaluated with the aid of the above energy - depth relationships. The results of this spectra analysis are listed in Tab. 1.5 which includes also results for two specimens (H and K) where the energy dependence was not measured.

Sample B ($1x10^{15}$Xe/cm^2): The slow increase of χ_1 with decreasing energy indicates that the surface peak is composed of displaced U atoms. This conclusion is supported by the fairly constant number of displaced atoms as measured at different energies. Surprisingly, both χ_2 and χ_3 increase at lower energies which is untypical for extended defects. It may be speculated that such

Table 1.5 Evaluation of Rutherford-backscattering channeling spectre of ion-implanted UN single crystals

Sample	Implantation	Analyzing Beam Energy [MeV]	X_1	X_2	X_3	No of Displ. Atoms [x10^{15} cm^{-2}]	Displacement Efficiency [at. displ./ at. incident]
1	2	3	4	5	6	7	8
B	1x10^{15}Xe/cm^2	2.0 1.4 1.0 0.7	0.09 0.07 0.14 0.18	0.20 0.20 0.36 0.40	0.20 0.19 0.37 0.46	22 15 25 25	22 15 25 25
H	5x10^{16}Xe/cm^2	2.0	0.38	0.45	0.47	103	2
K	1x10^{15}Kr/cm^2	2.0	0.19	0.36	0.36	32	32
J	8x10^{15}Kr/cm^2	2.0 1.4 0.7	0.12 0.12 0.15	0.42 0.42	0.42 0.42	28 25 17	3.5 3.1 2.1
A	5x10^{16}Kr/cm^2	2.0 1.4 0.7	0.27 0.29 0.37	0.40 0.40 0.41	0.43 0.46 0.46	104 99 73	2 2 1.5

a behavior could be due to the displacement of U atoms by the large stress field produced by Xe-ion implantation though without formation of regular extended defects.

Samples J and A (8x10^{15} and 5x10^{16} Kr/cm^2): Both samples implanted with Kr ions revealed somewhat different defect structures than sample B. The value of χ_1 increases with decreasing energy in the same manner as for the sample B. For the sample J where the surface peak is much smaller, this effect is also less pronounced. On the other hand, both χ_2 and χ_3 remain constant as a function of energy, thus indicating the preferencial formation of stacking faults.

It should be noted that the number of displaced atoms in the surface peaks per incident ion (displacement efficiency) is about the same for both implants.

Summary

The defect structure of implanted UN crystals is very complicated. Besides the surface damage peaks which consist mostly of displaced atoms and their clusters, damaged regions extending to a depth much larger than the ranges of the implants were formed. Analysis of the energy dependence of channeling shows that this damage consists of extended defects. Stacking faults were indicated as well as interfacial dislocations. Since UN single crystals oxidise easily, thermal annealing has to be performed in an ultra-high vacuum furnace. These experiments will be described in the next report.

References:

[1] H. Matsui and Hj. Matzke, J. Nucl. Mater. 89 (1980) 41

[2] S. Nasu et al., J. Nucl. Mater. 54 (1974) 143

[3] Hj. Matzke and A. Turos, J. Nucl. Mater. 114 (1983) 349

[4] Hj. Matzke, Rad. Effects, 3 (1970) 93

[5] J.F. Ziegler, Helium Stopping Powers and the Ranges in All Elements, Pergamon, Oxford (1977)

Irradiation Experiments

NIMPHE 1 (TUAR 86, 20): Fabrication of the 5 mixed nitride fuel pins was completed and 4 pins were sent to CEN Cadarache in July 1987. Irradiation in the Phenix reactor was started in October 1987.

NIMPHE 2 (TUAR 86, 20): The first draft of specifications was sent to CEN Cadarache for approval in November. Fuel fabrication was begun in December 1987.

The state of experiments under preparation is summarised in Tab. 1.6. Although this table is placed in this chapter, it includes all irradiation experiments of the Institute's programme.

Collaborations with External Organisations

Projekt Schneller Brüter, KfK, Karlsruhe
Département d'Etudes des Combustibles à Base de Pu, CEA - CEN Cadarache
University of Salford, U.K.

Table 1.6 Irradiation experiments of the Institute

Experiment	Reactor	Scheduled beginning of irradiation	Aim of Experiment
Nitrides			
POMPEI	HFR	May 88	Fuel behaviour at high burn-up
SWELLAC	HFR	mid 88	Swelling accomodation
NIMPHE 2	Phenix	May 88	Fuel performance at high linear performance
Oxides			
VOLEX	HFR	December 87	In-pile volume expansion
BUMMEL	HFR	April 88	Measurement of bubble migration

1.2 Properties of Reactor Materials at High Temperatures

Introduction

The laboratory measurement of high-temperature thermophysical properties of oxide fuels is the main intent of this subproject.

In the context of the recent developments of the reactor safety analysis the data on the thermodynamic and transport properties of the fuel at temperatures above the melting point still represent a major source of uncertainty in the evaluation of hypothetical disruptive core accidents.

- The recently analysed EEOS in-pile tests, carried out at SANDIA, with the aim of determining the equation of state of UO_2 up to the critical point, have indeed shown an encouraging agreement with the theoretical predictions of the enthalpy and equilibrium partial pressure. However, the determination of the specific heat still presents essential difficulties since this quantity has to be evaluated as the differential of other experimental variables which are in turn affected by relatively large errors. A laboratory measurement of Cp remains therefore the only sufficiently accurate method to obtain a reliable value of this important quantity.

- New precise measurements of the thermal conductivity λ of molten UO_2 are urgently required since the uncertainty of the existing data proved to be unacceptable for current HCDA analysis.
In an attempt to approach the problem from an engineering point of view, experiments are being planned at CEA Cadarache in the CABRI facility, especially aimed at measuring the average thermal conductivity of the molten fuel mass. The concept of the experiment is based on the possibility of relating the melt displacement to the temperature profile in the pin and from this the thermal conductivity. This measurement is possible, at least in principle, but is rather intricate.
In this perspective, the laboratory measurements of λ at the Institute will not only serve as a consolidation of measures obtained with a very different method, but will also provide the data for a very useful validation test of the analysis of a large scale test like the CABRI λ experiment.

A third point has been investigated concerning the vaporisation mechanisms of solid UO_2.
Despite the great amount of experimental and theoretical work devoted worldwide to this subject a significant disagreement still exists in the interpretation of the data. Since these are normally used for high temperature extrapolations, it is important that they constitute a sound and coherent thermodynamic database.
A new aspect was considered here concerning the ionic contribution to the UO_2 total partial pressure. The formation of negative UO_3 ions was demonstrated to produce a marked shift of the calculated congruent vaporisation composition towards lower O/U values

reducing the existing discrepancies.

The work during the reporting period was mainly devoted to the development or improvement of analytical and experimental techniques. Satisfactory progress was achieved in the measurement of very high temperatures in a timescale of the order of 1 ms. The six-wavelength pyrometer was used to systematically study the spectral emissivity of several materials in the solid and liquid state.

An important result was the confirmation of the existence in metals of an X-point (crossing of the spectral emissivities) and that the temperature at which they behave like grey-bodies corresponds to the melting point. This property, which has been now found in a large number of metals having very different chemical and physical properties, represents a useful reference state for high temperature measurements.

High precision standard curves were obtained for the one-wavelength pyrometer used in the apparature for the measurement of the thermal conductivity of liquid UO_2. The errors originally faced were drastically reduced by improving the optics of the instrument. Errors of less than 5 K are at present found in the calibration range up to 2920 K. This enables reliable extrapolations to be carried out in the experimental range up to 4000 K. Furthermore, the data acquisition system, based on a mechanically operated 2D-scanning of the specimen surface temperature distribution, was also improved by ensuring an adequate measurement speed.

Problems were encountered in the use of the laser-heated autoclave when levitating samples. First, it has been realized that the cooling effects of the sonic field are much higher than expected. A thorough study was therefore performed in order to quantify and control the heat losses during pulse heating experiments. The results obtained make it possible to carry out the planned experiments in the originally foreseen temperature range.

Acoustic levitation proved to be a powerful technique, open to wide application perspectives. The technology of the ultrasonic-wave interference was further developed by producing high performance generators and transducers. However, substantial difficulties were faced during laser heating of levitated samples, as the induced changes in the speed of sound in the gas do often cause severe perturbations of the standing waves with more or less large displacements of the sample. At present, levitation devices presenting higher stability against thermal excursions are being developed.

Finally, the increasing experience which has been gained in the acoustic levitation technique is being applied in different fields such as aerosol agglomeration and scavenging and toxic gas absorption. A topical report on this subject is presented in chapter 6, "Prospective Studies".

Analysis of the Heating Conditions in the Laser-Heated Autoclave

The measurement of thermodynamical properties of nuclear fuels by means of pulse-heating experiments in a laser-heated autoclave, where the sample is levitated in an acoustic field, is based on the correct interpretation of the heating/cooling curve as a function of time.

To obtain the specific heat $C_p(T)$ the initial hypothesis was based on a simple model by which the energy-rate balance was written as

$$\frac{4}{3}\pi R^3 C_p \rho \frac{dT}{dt} = -4\pi R^2(\varepsilon\sigma T^4 + hT) + W \qquad (1)$$

where
- T = sample temperature
- t = time
- R = spherical sample radius
- ε = total emissivity
- σ = Stefan-Boltzmann constant
- ρ = density
- h = energy loss coefficient through convection
- W = laser energy power input per unit area

Equation (1) obviously applies to homogeneously heated samples. Furthermore, it was assumed that the contribution of the convection losses could be neglected at sufficiently high temperatures, so that (1) was reduced to a very simple equation from which C_p can be straightforwardly calculated from the experimental function $T = T(t)$ [1].

Meanwhile, the experience gained in a number of experiments has shown that both these hypotheses are in most cases not applicable. First, the effect of the sonic wind in the acoustic levitation field is very large and represents the major loss in eq. (1) up to temperatures as high as 4000-5000 K, depending on the type of gas used in the autoclave and on its pressure. Secondly, ceramic materials, like UO_2, under the optimum experimental conditions (sample radius ~0.25 mm, energy input 50-100 J in 100 ms) present a marked radial temperature gradient during both the laser energy deposition and the following cooling stage, down to temperatures of the order of 2000 K.

Finally, eq. (1) is not suitable to analyse the experiments and a more precise equation has to be considered having the form:

$$\frac{\delta}{\delta t}\int_{T_s(t)}^{T_c(t)} 4\pi r^2(T, t)\, C_p(T)\, \rho(T)/\text{grad}\,(T, r)\, dT = -4\pi R^2\left(\varepsilon\sigma T_s^4 + h(T_s)T_s\right) + W \qquad (1a)$$

where
- r = spherical radial coordinate
- T_s = (measured) surface temperature
- T_c = (calculated) central temperature
- grad T = (calculated) radial temperature gradient

It is clear that in eq. (1a) the knowledge of the function $T_s = T_s(t)$ is no longer sufficient to determine $C_p(T)$, because, in addition, the radial temperature profile $T = T(r, t)$ is required to solve

the integral equation. This has to be calculated by solving the heat transport equation in the sphere:

$$\frac{\delta T}{\delta t} = \nabla \kappa(T)\, \mathrm{grad}\,(T) \qquad (2)$$

where κ = thermal conductivity

with the boundary condition

$$\kappa(T)\ \frac{\delta T}{\delta x} = -\left(\varepsilon\sigma T_s^4(t) + hT_s(t)\right) + W \qquad (2a)$$

at $r = R$ and $t > 0$.

The solution of eqs. (1a) and (2) represents a complex mathematical problem all the more so because in eq. (2) liquid-solid phase transitions have to be taken into account with the proper enthalpy variations.

Finally, the evaluation of $C_p(T)$ has to be carried out by means of a computer program which solves the mentioned equations starting from the tabulated input functions $T_s(t)$, $\kappa(T)$ and $h(T_s)$.

The function $C_p(T)$ is calculated by an iterating procedure:

$C_p(T)$ is normally known up to a certain temperature T_M, so that the integral in (1a) can be evaluated up to this temperature. $C_p(T)$ is extended for $T > T_M$ by a suitable experiment sequence by which the maximum achieved temperature is increased in reasonably small steps ΔT and C_p is determined in the interval $T_M < T < T_M + \Delta T$.

It can be seen that the determination of C_p is virtually deduced from the thermal behavior of a spherical shell the thickness of which decreases when the effective temperature gradient is large. As a consequence, a limit has to be set to the gradients achieved, depending on the precision of the experimental measurements and of the input parameters.

Figs. 1.11 and 1.12 provide an insight in the thermal behaviour of an UO_2 spherical sample of 250 µm radius heated up to between 4000 and 5000 K. Fig. 1.11 shows the evolution of the temperature radial profile with time during the heat-up and the cool-down phases.Fig. 1.12 shows the ratio between the correct C_p calculated from eq. (1a) and that directly obtained from eq. (1). This curve shows very clearly in which regions of the curve $T_s = T_s(t)$ the evaluation of C_p becomes impossible or very uncertain. These are, in order of importance:

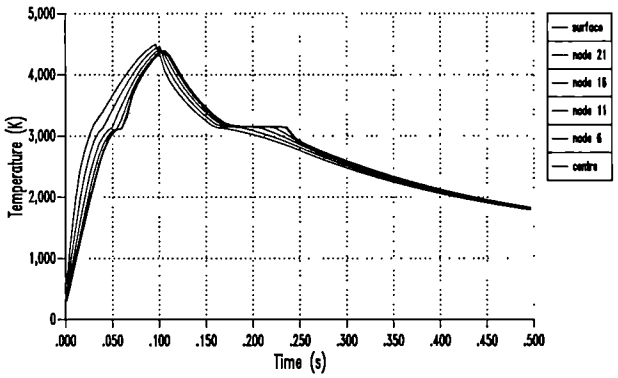

Fig. 1.11 *Calculated temperature evolution in an UO_2 sphere heated with a laser for 100 ms. The curves correspond to equidistant nodes*

1) "Plateau zones", i.e. flat branches of the curve corresponding to situations where a significant fraction of the specimen mass undergoes solid/liquid transitions. The sudden change in enthalpy results in a nominally infinite Cp.

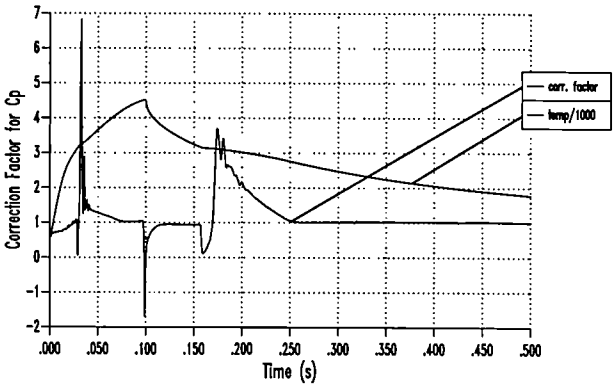

Fig. 1.12 *Error in the evaluation of the specific heat C_p in the different heating/cooling stages. The dashed curve is the surface temperature of Fig. 1.11 in 1000 K.*

2) Zones of stationary temperature, where dT/dt becomes very small (e.g. around the maximum of the temperature peak).

3) Near the inflection points of the cooling curve (e.g. around the knees of the "plateaux").

4) Whenever the internal temperature gradient is too large.

Normally, the errors encountered in situations 3) and 4) are limited and the apparent C_p is amenable to the correct value by means of the algorithms developed based on the solution of eq. 1a.

The problem consists now of evaluating the various error sources figuring in the terms of the equations and implied in their numerical solution. This analysis will finally lead to an assessment of the experimental error of Cp. Salient points of this work are reported in the following sections.

References

[1] TUSR 40, p. 23 (1986)

Effective Heat Losses during Laser Heating Experiments

As discussed in the preceding section, a precise determination of the heat loss coefficients is needed in order to deduce the specific heat from the sample cooling curves in the laser-heated autoclave. The experiments have shown that up to temperatures of the order of 4000 K the losses are not merely radiative, but important contributions due to gas convection phenomena are present.

Experimental Results

The samples are heated by four laser beams for 100 ms. The laser optics have been improved by using additional lenses and dielectric mirrors so that the heating efficiency is increased by a factor of 3.

A small camera has been mounted in the pyrometer in order to facilitate the alignment of the samples and to provide continuous monitoring of the sample image by means of a video recorder. The homogeneity of the surface temperature can thus be controlled as well as the absorption or refraction effects produced in the surrounding gas atmosphere.

The aim of the experiments was to identify and measure the various heat losses. Tungsten was chosen as reference material since its thermophysical properties are well established

up to the melting point. The specimen was a 1 mm large sphere held on a Tungsten needle. The experiments were performed with and without ultrasonic waves, with different gases (He, Ne, Ar, Kr, Xe) in the pressure range between 1 and 300 bar.

Three heat losses were therefore considered: Radiation, conduction through the needle and convection, whereby the first two are fixed and the third was investigated by changing the environmental conditions.

Loss by radiation

This loss is well known and could be determined on the basis of previous measurements of the total emissivity ε.

The radiative cooling rate of the sample was of the order of 3200 K/s at 3000 K and 1700 K/s at 2000 K, in agreement with the theoretical values.

Loss by conduction

The heat loss by conduction depends on the nature and the geometry of the holder. A sequence of experiments has been carried out with differently supported spheres with the intent of effectively suppressing heat conduction through the support. The results are summarised in Fig. 1.13. It can be seen that the lowest

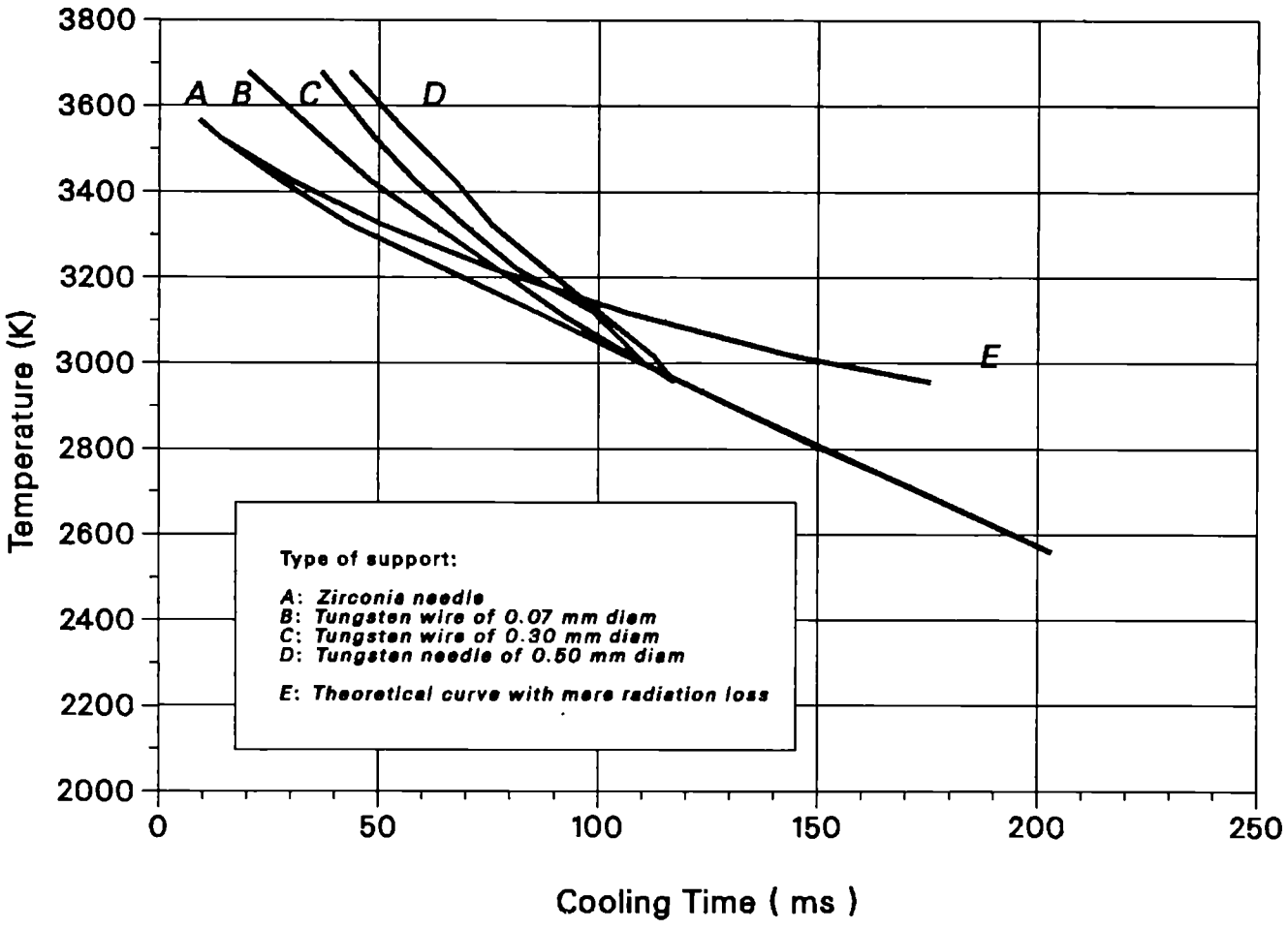

Fig. 1.13 *Cooling curves of a laser-heated tungsten sphere in vacuo with various types of mechanical supports*

conduction loss was obtained for ZrO_2- supported spheres, but it still represents a non-negligible contribution. The following test in gas atmosphere had therefore to be analysed by taking into account this loss.

Convective cooling

Free convection is very rapidly established (within a few milleseconds) and can be visualized by optical refraction even at low pressures. However, for low conducting gases its role is only relevant at high pressures so that a measurement of the loss coefficient over a wide pressure range is only possible for He, whose thermal conductivity is very high.

Figs. 1.14 and 1.15 show the cooling curves at various pressures and the rates in helium and

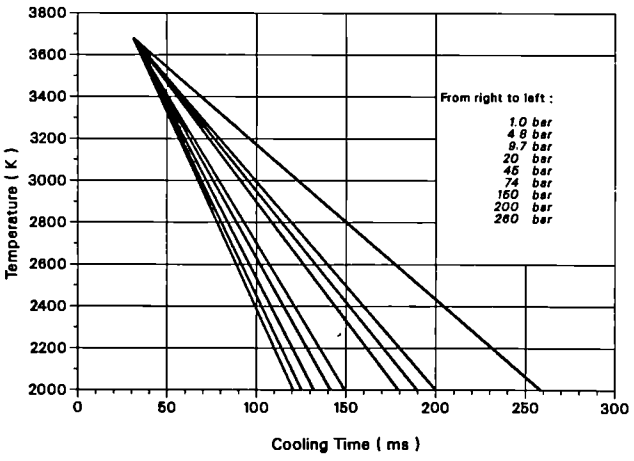

Fig. 1.14 *Measured cooling curves in Helium at various pressures of a W-sphere (Ø = 1 mm)*

argon. It can be seen that "h", which is proportional to

$$\frac{\Delta T}{\Delta t}$$

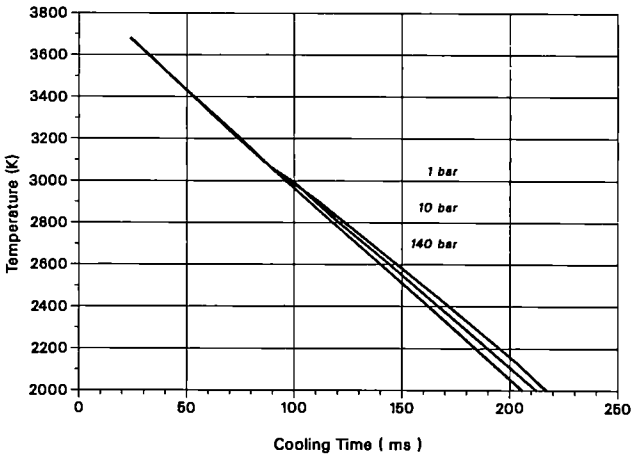

Fig. 1.15 *Idem as in Fig. 1.14, but in Argon*

increases with pressure. This is in agreement with the theoretical predictions which are discussed below.

Forced convection in the ultrasonic field increases dramatically overtaking all other heat loss mechanisms. This applies for low conducting gases like argon and, a fortiori, for helium, with which the cooling rates at 3000 K attain the order of magnitude of 10^4-10^5 K/s. Fig. 1.16 and

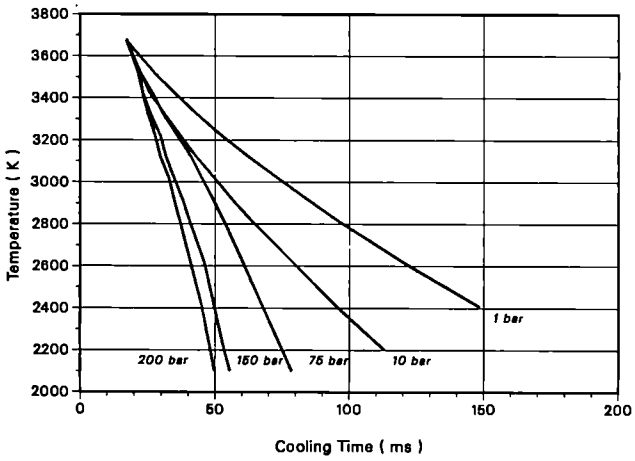

Fig. 1.16 *Cooling curves of a W-sample as in Fig. 1.14 in an ultrasonic standing wave field at 80 kHz in Helium*

1.17 show the cooling curves in Ar and He at various pressures. Forced convection cooling produced by acoustic waves depends on their amplitude and, in the use of standing waves, on the position of the sample between nodes and antinodes. The reference position was taken as that corresponding to the levitation condition of the sample.

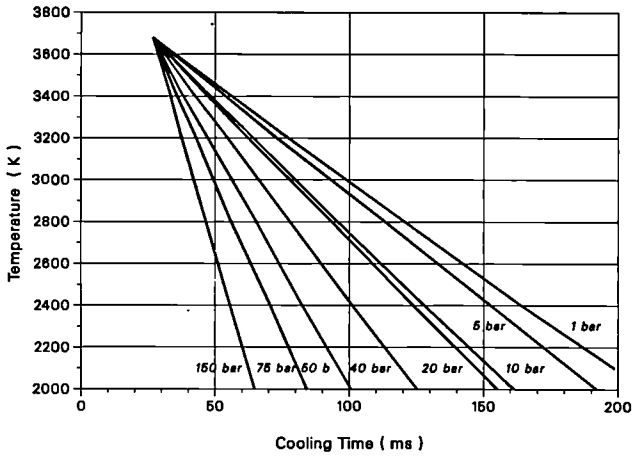

Fig. 1.17 Idem as in Fig. 1.16, but in Argon

Heat convection coefficient analysis

The heat transfer between the gas and the pulsing-heated sphere is briefly discussed in this section.

a) In the absence of a sonic field, the heat may be removed by free convection, i.e. by a flux which is generated by internal temperature differences in the gas.This complex problem of coupled heat- and mass-transfer has been widely investigated and phenomenological solutions exist and are applicable under steady-state conditions.In the case examined the heat capacity of the conducting layers is so small that no lagging effects are observed and the steady-state behaviour is immediately achieved.

Experiments were carried out where the conducting layer was visualized by refracting a light beam placed behind the heated samples (Fig. 1.18). The thickness of this layer is well described by the relationship [2].

$$\delta = [\, 3.93\, P_r^{-1/2}\, (0.952 + P_r)^{1/4}\, Gr_x^{-1/4}\,]\, x$$

where δ = conducting-layer thickness
Pr = Prandtl Number
Gr_x = Grashof Number
x = sample diameter

Figs. 1.19a and 1.19b show the calculated δ's and the heat transfer coefficients:

$$h = \frac{2k}{\delta}$$

(where k = gas thermal conductivity)

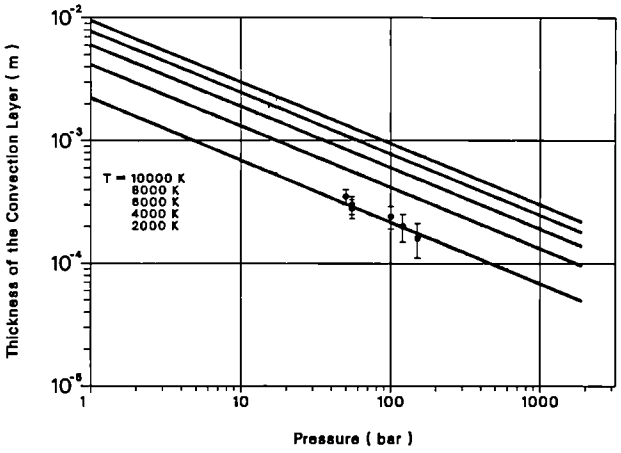

Fig. 1.19a Calculated thickness of the heat conduction layer in argon as a function of pressure at different temperatures. The dots are experimental points.

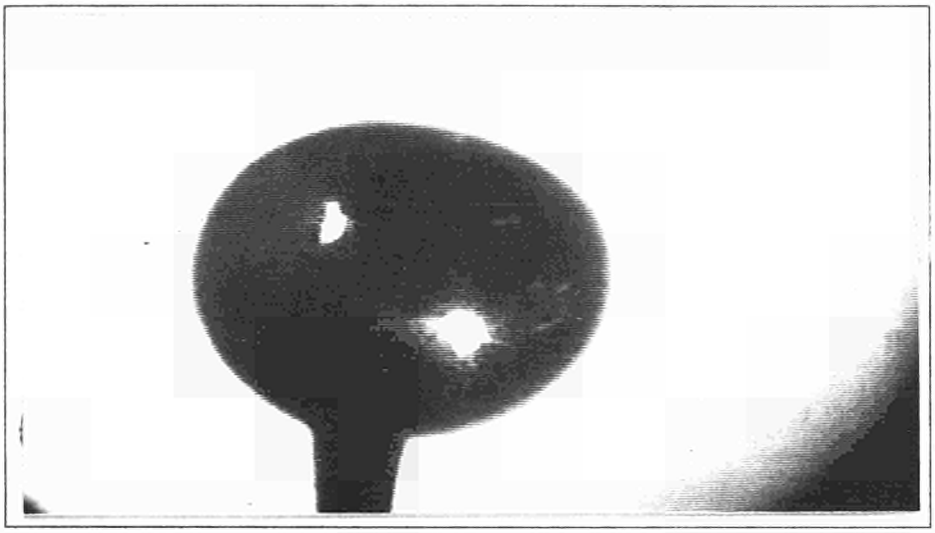

time = 0.

T = 300 K

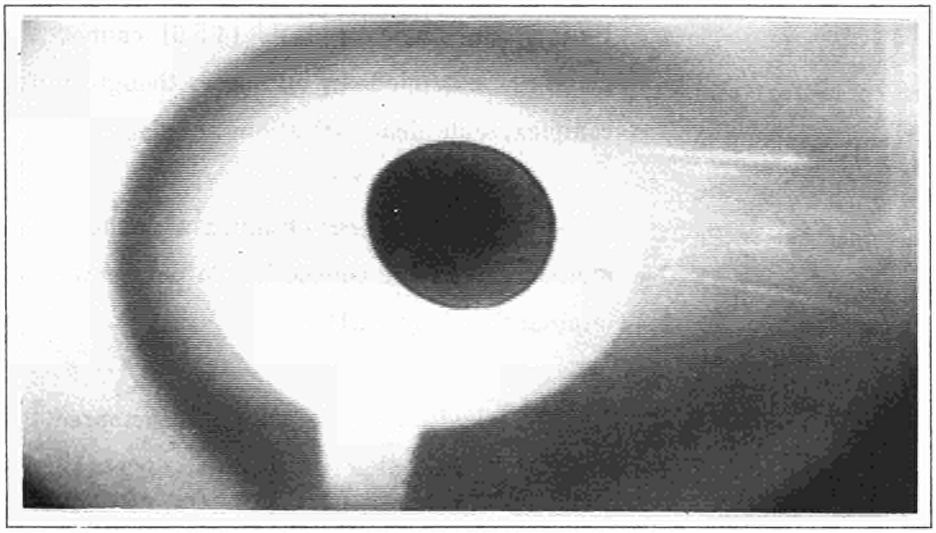

time = 100 ms

T = 3690 K

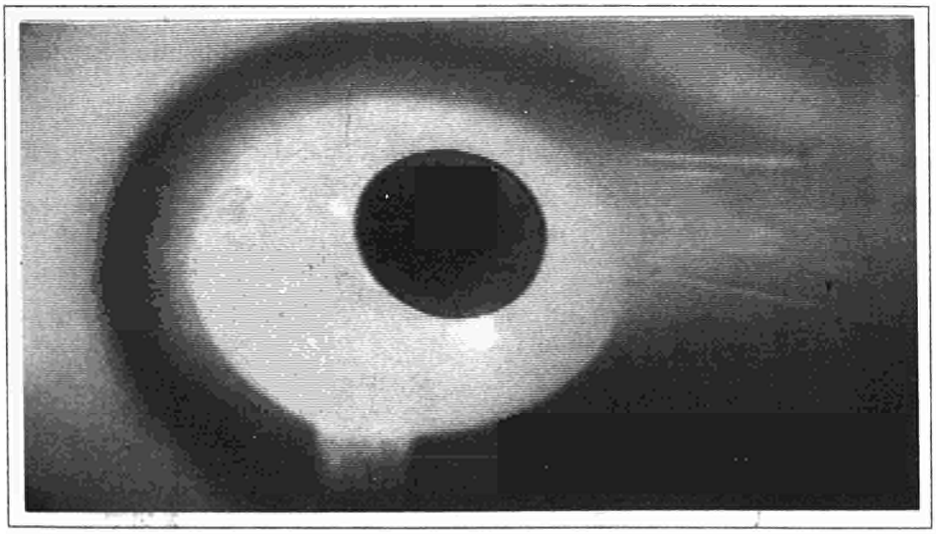

time = 150 ms

T = 3200 K

Fig. 1.18 *Visualized heat conduction layer during heating/cooling of a pin-supported W-sphere in argon at 140 bars. The top is turned by 90° counterclockwise*

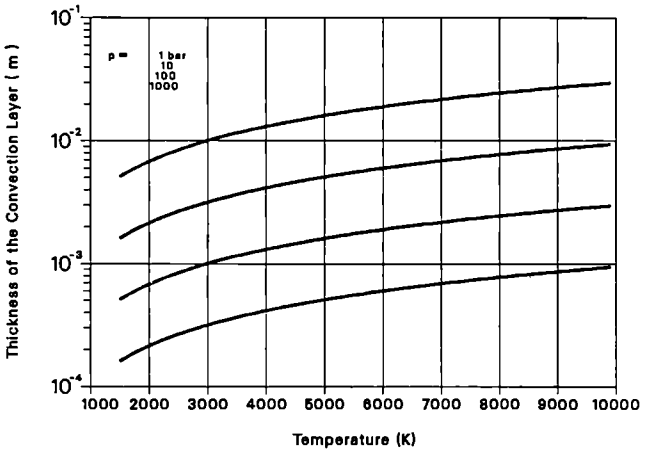

Fig. 1.19b Calculated thickness of the heat conduction as a function of temperature at different pressures

as a function of the gas pressure and temperature. The experimental points at 2000 K are indicated in Fig. 1.19a with dots. For the calculation of the dimensionless parameters Pr and Gr_x the thermal conductivity was obtained by extrapolating the available data [3] while the viscosities were deduced from the equation of state of monoatomic gases. Fig. 1.20 shows the convection coefficient as a function of gas pressure at five different temperatures. It can be seen that h increases with pressure and becomes

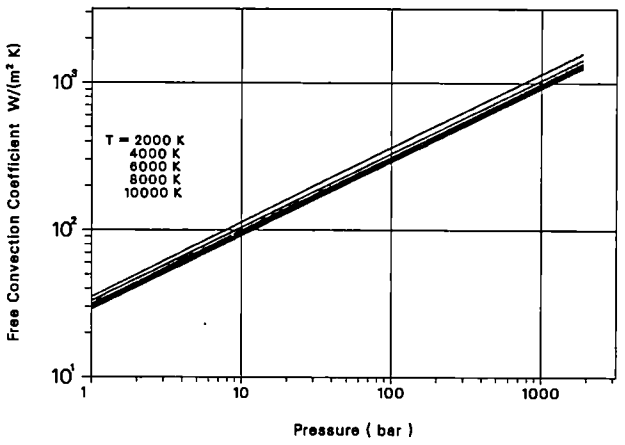

Fig. 1.20 Heat loss coefficient due to free convection as a function of pressure at different temperatures

effective in practice at pressures greater than 10 bars if one considers that at 10^3 w/m^{2}K the convection heat loss is equal to the radiation losses of tungsten at 3000 K. Since the Prandl number is nearly constant for all the rare gases, h is roughly proportional to the gas thermal conductivity so that for Xe, the least conducting inert gas, the convection losses are approximately a factor of 3 lower than in Ar.

b) The presence of the ultrasonic waves drastically changes the heat convection regime. Here the published experimental results are limited and their analysis [4,5,6] cannot be generally extended. In our case, though quite complex, some clear indications are given:

- First, the pictures obtained with the same method as for free convection do not show any laminar flow (Fig. 1.21).

- The levitation effect can be compared to that of a "wind" whose effective stream velocity supports the particle. This velocity can be evaluated by the equilibrium conditions between gravity and supporting force. By using this velocity to calculate the Reynolds number Re, a relationship found by Denton [7] for the heat transfer in sphere packed beds was used, providing the Nusselt number

$$Nu = 0.8\,[\,Re\,(v)\,]^{0.7}\,P_r^{1/3} \qquad (2)$$

The forced convection coefficient obtained from (2) is plotted in Fig. 1.22 as a function of gas pressure for He, Ar, Kr and Xe.

The results show that the heat losses by

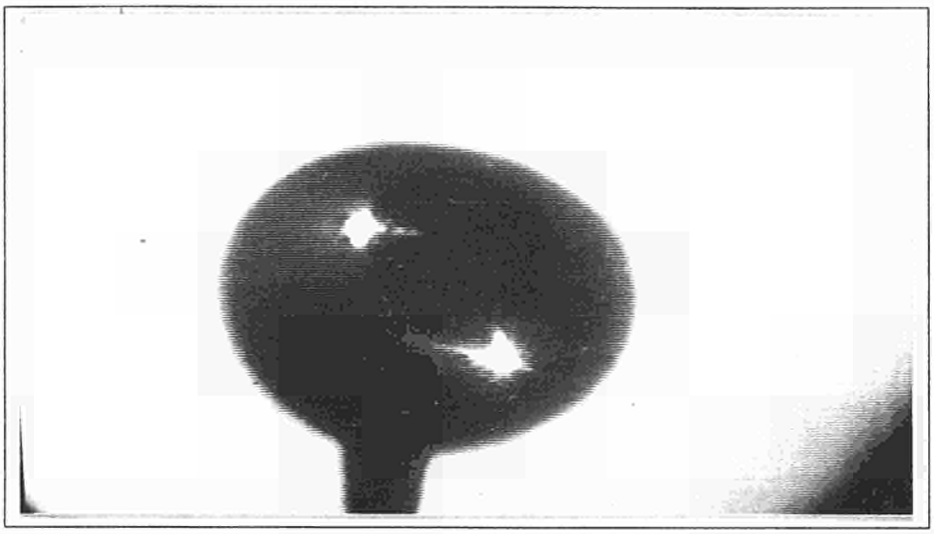

time = 0.

T = 300 K

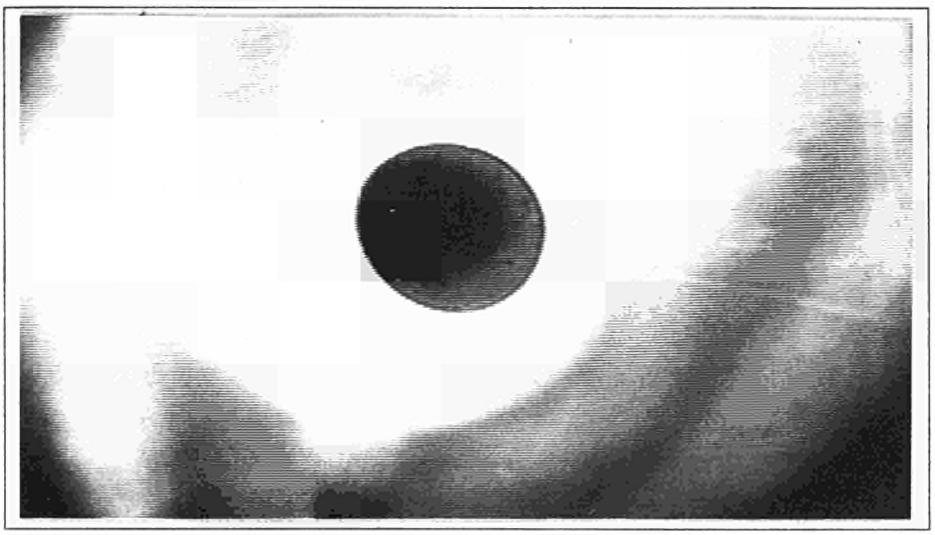

time = 100 ms

T = 3690 K

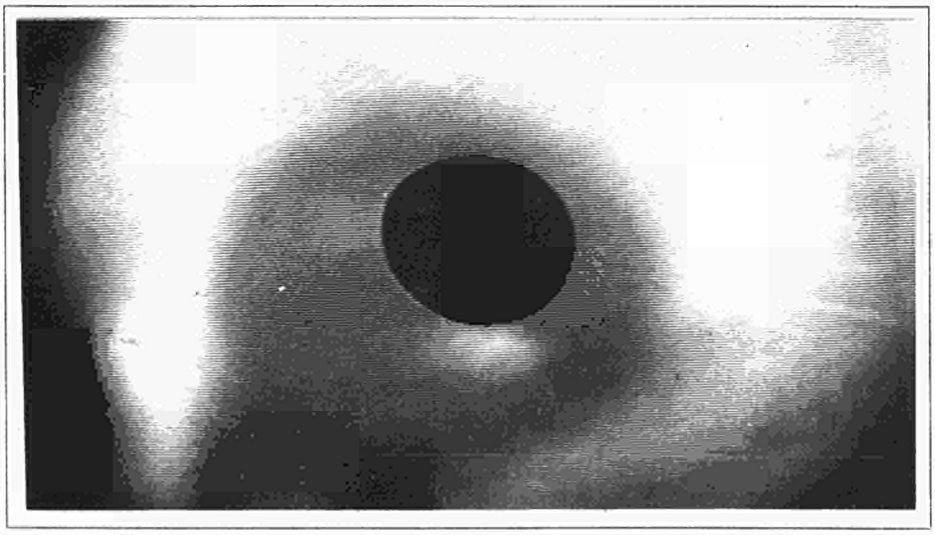

time = 150 ms

T = 2000 K

Fig. 1.21 *Pin-supported W-sphere heated in argon at 140 bars in an 80 kHz ultrasonic field. Compared to the case in Fig. 1.18 the conducting layer is absent.*

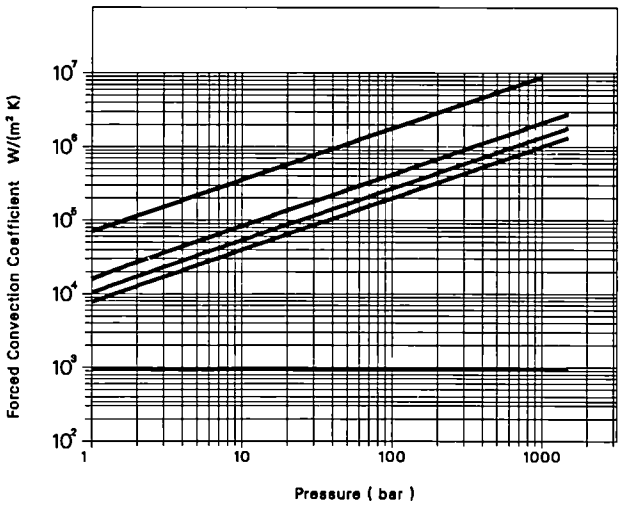

Fig.1.22 *Calculated heat loss coefficient in a 80 kHz sonic field with Helium (top), Argon, Krypton, Xenon (bottom). The horizontal line is the radiation loss in tungsten at 3600 K.*

ultrasonic forced convection may be larger by far than the radiation losses of tungsten at 3600 K even at atmospheric pressure.

Finally, an important property of both free and forced heat convection coefficients is that they decrease with increasing temperature. As a consequence, the cooling curves display a low curvature, compared with the cases of radiation cooling. This is clearly observed in the experimental curves presented above.

Conclusion

The results provide a database sufficient to evaluate all the heat losses involved in laser-heating experiments. These coefficients can be reasonally interpreted in terms of phenomenological descriptions based on classical fluid dynamics theory. Suitable formulae for the expression of the various convection losses can be written and evaluated in the experimental parameter range.

The present work is aimed at defining the reproducibility of the observed phenomena and, eventually, at predicting the experimental errors expected in the evaluation (or extrapolation) of the total heat loss coefficients for the various cases.

References

[2] E.R.G. Eckert "Heat and Mass Transfer", Chapt. 3, Mc Graw-Hill, New York (1963)

[3] D.L. Hagrman, US-Report EG 86 - CDAP 1029 (1979)

[4] R.M. Faud and J. Raye, US-Report WADC 59-18 ASTIA-AD 209532 (1959)

[5] T.W. Jackson, W.B. Harrison, W.C. Bateler, J. Heat Transfer, Trans ASME 81 Ser C (1959) 68

[6] H.N. McManus, Jr., E.E. Soehngen, J. Heat-Transfer, Trans. ASME 82 Ser C (1960) 166

[7] W.H. Denton, "General Discussion on Heat Transfer", J. Inst. Mech. Eng. London (1951) 370

Thermal Conductivity of Liquid UO_2

Thermal conductivity of liquid UO2 has been measured on isthermally heated UO2 encapsuled in tungsten containers [1,2] and on liquid UO2 contained in a (non-isothermal) solid UO2 crucible [3]. These two types of measurements gave vastly differing results.

The experiment reported here consists of heating a disk-shaped UO_2 sample first with a defocused laser beam from below, and then creating a molten droplet at the upper surface by additional heating with a second, more concentrated laser beam directed at the top. Thermal conductivity and diffusivity are deduced from the (temporal evolution of the) temperature profile at the sample surfaces, and from the penetration depth of the melting front. The sample surfaces are imaged onto two fiber-optical image guides, the other end of which are scanned mechanically with a small hole followed by a filter and a silicon photodiode. Scanning is performed in two dimensions with stepping motors with a resolution of 0.144 mm referred to the sample. In the original concept, the triggering of the scanning motors and of the voltmeters was under direct computer control.

Data Acquisition and Processing

HP-9000/310 as successor for HP-9845 computer

After terminal breakdown of the HP-9845 computer previously used, a HP-9000/310 was purchased. The new machine was selected essentially because of available software. This machine is intended both for control and data collection of the laser heated furnace and data evaluation. Real-time requirements imposed by the high vapour pressure of UO_2 at its melting point requires compiled code at least for the critical part of control and data collection. The manufacturer offered the 310 with a BASIC interpreter plus a Pascal or a C compiler operating in a single-user UNIX environment. Unfortunately, the configuration recommended and supplied by the manufacturer proved to be insufficient for both BASIC and UNIX. Except for the portability offered by a standarised operating system such as UNIX, no advantage could be found in the relatively complicated single-user UNIX that would have justified the appreciable investment in an appropriate upgrade.

A subsequently released BASIC-5 compiler will now provide the required speed instead. This allows the use of one operating system (BASIC), and is more flexible than the original concept. Unfortunately, it lacks portability to non-HP environments.

2D-Temperature Profile Scanning

Data collection speed is of crucial importance. The high vapour pressure of UO_2 at its melting point results in prohibitive sublimation/vaporisation and recondensation of UO_2 crystals around the molten zone, in spite of 6 bar argon furnace atmosphere, if exposure to the highest temperature exceeds about 5 seconds. On the other hand, these 5 seconds are just about required to establish stationary conditions which are needed for the deduction of the thermal

conductivity. Within this short time, as many data as possible, of optimum quality, must be recorded. The stepping motors used [4] can be operated at 800 to 1000 steps per second, provided that acceleration and deceleration is done more gradually. This speed is just about sufficient. Presentation and evaluation can then be done off-line.

In the original concept, the photo-currents were to be amplified by logarithmic converters [5], and measured by two fast digital voltmeters [6].

The resolution, including noise, of this arrangement was investigated. The noise of the voltmeters was found to be $\pm\frac{1}{2}$ least significant digit (1σ), or better than the resolution of the instrument. The noise from the logarithmic converter was found to be about 10 times higher than that of a linear setup; below 1800 K the reponse time of the logarithmic arrangement becomes the limiting factor. Therefore, the logarithmic concept was abandoned, the photo-currents were amplified by linear amplifiers [7], and recorded with programmed range switched 3437A voltmeters. The typical attainable resolution, converted to a temperature uncertainty from the instrumentation only, is shown in Fig.1.23 for filters of 60 nm bandwidth at 650 nm and 900 nm.

This does not solve the recording speed problem, however. Data-dependent range switching requires the read-out of every individual data point and a decision on the range for the next reading before the latter is triggered. Data conversion takes only 200 μs, the resulting 8 ASCII characters can be transfered in 100 μs, but even in the fastest version of compiled BASIC

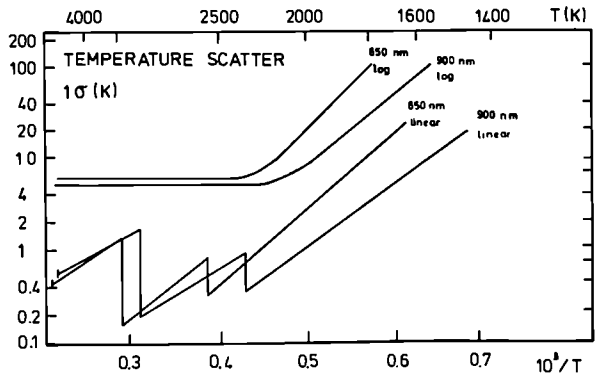

Fig. 1.23 *Temperature resolution (1σ) for top pyrometer resulting from the instrumentation noise and resolution only. Pre-amplifier set at 10^{-7}A/V. 60 nm bandwidth filters centered at 650 nm and at 900 nm. Voltmeter, either set at 10 V f.s. after logarithmic converter (curves labeled 'log') or operated in linear mode with programmed range switching at 0.19 V and at 1.90 V (curves labeled 'linear').*

each adressing of the voltmeter inserts an overhead for the configuration of the IEEE-488 bus of about 4.5 ms, or 9 ms for top + bottom. This overhead seems to come from the operating system of the 310 computer. No way has been found to circumvent it. At best, this system is about 10 times slower than required.

Therefore, an alternative control and data collection device was designed, employing an independent presettable clock, two fast 16-bit analog-to-digital converters (50 μs conversion time) with sample-and-hold and data buffer (one for each side of the sample), and a separate buffer for the scanning pattern that controls the stepping motors. 16-bit resolution eliminates the need for range switching. After setup of the clock

interval and of the scanning pattern and triggering the data collection device, it will take care of the complete data collection without further computer intervention, with more than adequate margins in speed.

Pyrometer calibration

The temperature sensors, consisting of transfer optics (image guide and lenses), limiting aperture, filter, and photodiode, represent monochromatic pyrometers.

Originally, these devices were equipped with Balzers Type K-65 interference filters, specified to pass a 60 nm-wide band centered at 650 nm. The transmission was not specified at longer wavelengths.

The pyrometers must be calibrated against some temperature transfer standard, such as a standard lamp. In the actual experiment, they must be operated at temperatures between 1600 K and 4000 K. No transfer standards are available that cover this temperature range. The available gas-filled tungsten ribbon band lamp was calibrated up to 2600 K (spectral temperature at 650 nm); data on a tubular 'black body' lamp (Quinn type) extend up to 2923 K. The calibration must thus be extrapolated over more than 1000°.

Wien's radiation law:

$$I = \int K(\lambda)(C_1/\lambda^5).\exp(-C_2/(\lambda T))\delta\lambda$$

served as a basis for this extrapolation. Here I is the photo-current, $K(\lambda)$ is the over-all instrument sensitivity, C_1 and C_2 are the Planck radiation constants, λ is the wavelength, and T is the absolute temperature. Within Wien's approximation, the logarithm of the photo-current against 1/T should be a straight line with slope $-C_2/\lambda$.

The result of a calibration with K-65 filters (Fig.1.24a) corresponded approximately to the

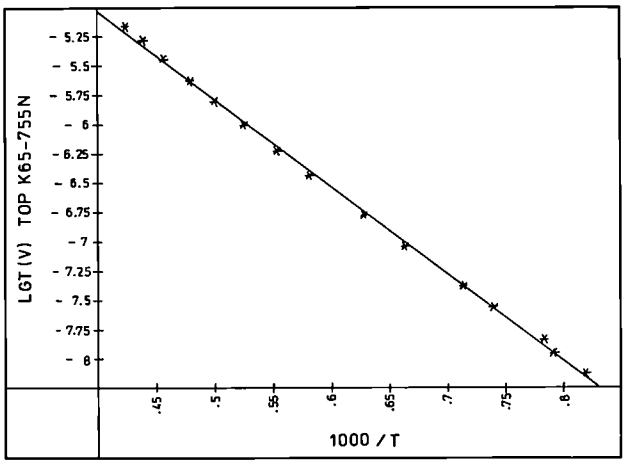

Fig. 1.24a Calibration of top pyrometer equipped with Balzers K-65 650 nm filter, using a logarithmic amplifier set at 2 V/decade. The slope of the linear fit corresponds to an effective wavelength of 880 nm.

expected relation. The best fit to log(I) vs. 1/T seems to be a parabola rather than a straight line. This is more clearly seen in Fig.1.24b,

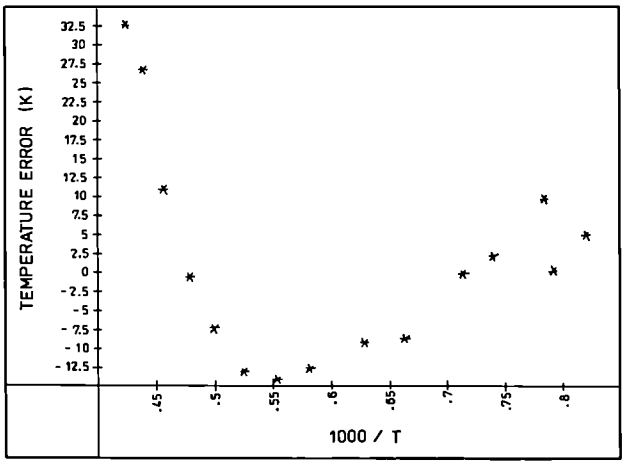

Fig. 1.24b Deviation from the linear fit of Fig.3a, expressed as temperature error.

which shows the deviations from the least squares fitted straight line in Fig.1.24a against 1/T, converted to temperature differences through a differentiated Wien's equation:

$$\delta T = (\lambda / C_2).T^2.(\delta I/I)$$

Extrapolation of a linear and of a parabolic fit to the data of Fig.1.24a to 4000 K leads to a difference (i.e. uncertainty) of 800 K. This is not acceptable. From Fig.1.24a an effective wavelength of 880 nm rather than the specified 650 nm, is obtained.

The discrepancy was explained through a measurement of the K-65 filter transmission in the infra-red (Fig. 1.25), for which no data were specified by the manufacturer. Fig. 1.25 also shows the typical sensitivity of silicon photodiodes. The transmitted bands at 950 nm and at 1047 nm contribute to the measured intensity with the 950 nm band lying close to the maximum of the diode sensitivity.

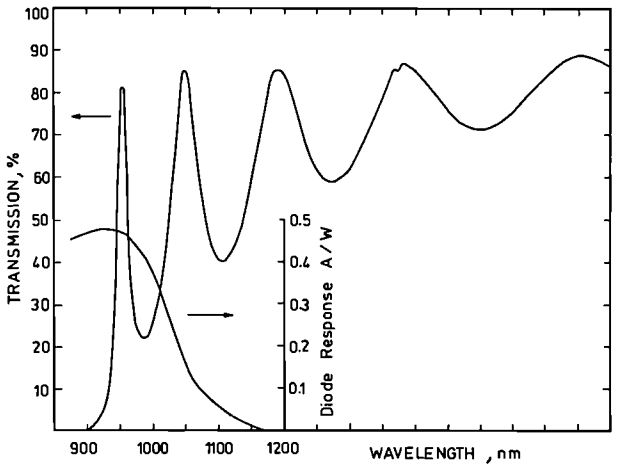

Fig. 1.25 *Transmission of Balzers K-65 filter (scale at left) and typical sensitivity of silicon photo-diode (scale at right).*

The situation improved drastically by using better filters [8], with guaranteed blocking at longer wavelengths. Calibration against tungsten ribbon lamps is possible at 650 nm but 900 nm appears to be the better choice as it produces a stronger signal at lower temperatures (see Fig. 1.23). The actual photo-current should follow Planck's equation:

$$I = \int K(\lambda)(C_1/\lambda^5).[\exp(C_2/(\lambda T))-1]^{-1}\,\delta\lambda$$

rather than Wien's equation. Above 3000 K the differences start to become appreciable. Therefore, the product of Planck's equation times the filter transmission coefficient times the diode sensitivity was integrated numerically over the wavelength and compared with a hypothetical pure-Wien radiator (Fig.1.26). The actual data

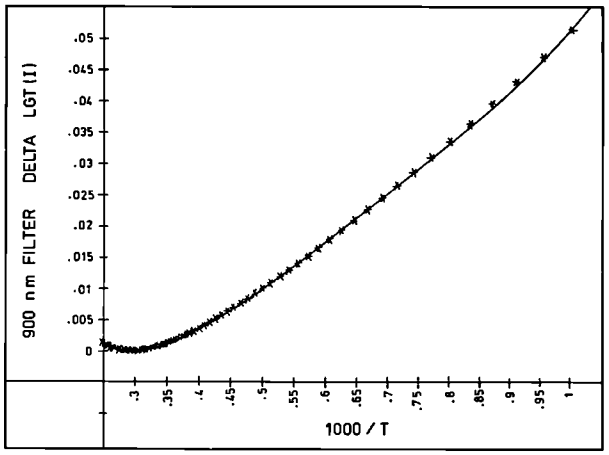

Fig. 1.26 *Difference in the ^{10}Log of the photo-current from a real Planck black body radiator measured with a CORION P70-900-A filter on one hand, and a hypothetical 900 nm narrow band Wien radiator on the other hand, calculated by numerical integration of Planck's equation multiplied by the filter transmission and the diode sensitivity, and of Wien's equation at 900 nm. The data points were calculated from 1000 K to 4000 K in 50 K steps. The drawn line is a least squares fitted 4th degree polynomial that was used in subsequent calculations.*

were correspondingly adjusted, resulting into a perfect linear fit (Fig.1.27a) with only a few

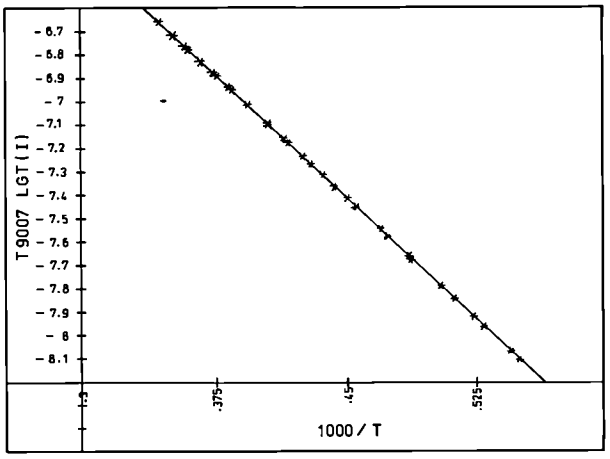

Fig. 1.27a Calibration of top pyrometer equipped with CORION P70-900-A filter, centered at 900 nm, against a Quinn-type 'black-body'-lamp. The slope of the linear fit corresponds to an effective wavelength of 890 nm.

degrees scatter (Fig.1.27b). The slope of the linear fit Fig.1.27a agrees with the filter centre wavelength to within 10 nm. The correction of Fig.1.26 is to be applied to all measured photocurrents.

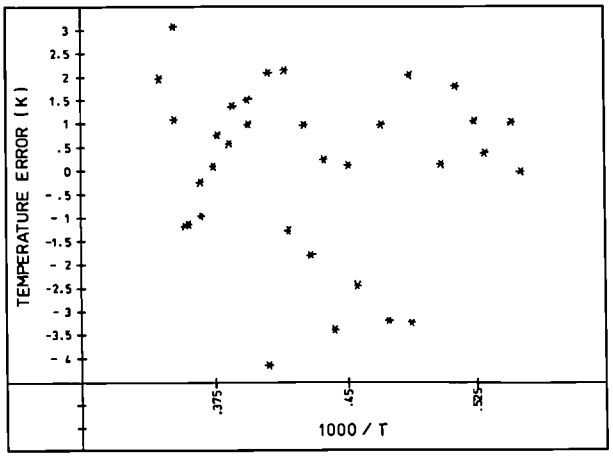

Fig. 1.27b Deviations from the linear fit of Fig.1.27a, expressed as temperature error.

Adjustment of the laser power

UO_2 is sensitive to thermal shock at temperatures below about 1300 K. The sample is first heated through the bottom surface by a defocused beam. This heating must at first be done very gradually until UO_2 shows sufficient plasticity at about 1300 K. The laser power must be continuously adjustable between $\approx 1\%$ and $>95\%$ of full power, without perturbing the location of the beam.

The CO_2 gas lasers used are prototypes, pumped by a DC discharge through the gas. They can be varied between 50% and full power by adjusting the conditions of the discharge; below 50% the discharge is unstable and tends to stall. An additional means for power adjustment is thus required. The beam is nearly 100% linearly polarised by the gas discharge tube exit window inclined at the Brewster angle. Power can be adjusted by a polariser/analyzer, rotatable around the beam axis, that should transmit power proportional to $\sin^2\alpha$, where α is the angular setting of the analyser.

The analysers must deflect the beam by less than 0.2 mrad, with a transmission adjustable from $<0.1\%$ to $>97\%$. Commercial units were found that meet these criteria [9]. They contain six ZnSe Brewster plates, three of which deflect part of the beam to one side, the other three to the other side, thereby compensating the offset. The analysers must absorb up to 200 W, with a power density up to 1 kW/cm^2. A small water leak developed in both units at the spot where the highest power density must be absorbed; the thin-walled aluminium had corroded away and a drop of water destroyed two of the six Brewster plates.

In order to continue operations whilst waiting for a suitable replacement an emergency solution had to be found. Welding the corroded housing was impossible, as was also a repair with an epoxy sealed aluminium strip. The thermal conductivity of epoxy is so low, that even a 0.1 mm thick layer should result in temperatures exceeding 500°C. The leaks were repaired succesfully, however, by ZnSe plates, sealed with epoxy along the edges. These plates are transparent at the laser wavelength; the power is absorbed behind the plates. One of the analysers now operates with 4 plates instead of 6, which increases the minimum transmission to 2%. This is admissible for the upper beam. In order to restrict the thermal load on the provisionally repaired housings, the laser power was reduced by deliberately misaligning the cavity mirrors whilst maintaining optimum discharge conditions. Surprisingly enough, this misalignment hardly affects the beam orientation. It does affect the mode structure and thereby the beam profile seriously.

First results on Al_2O_3 and UO_2

The evaluation of the thermal data is to be done by the method of finite elements. A 3-dimensional non- stationary non-linear computation is possible in principle, but the computation time exceeds that for a 2-dimensional model by orders of magnitude. Accurate axial alignment is thus looked for which justifies the use of a 2-dimensional model of cylindrical symmetry.

Operation of the system was checked with Al_2O_3 samples, because of its better thermal shock resistance and its lower vapour pressure that permits operation under vacuum. A TV camera constantly monitors the top surface. Visual inspection of top and bottom surfaces is possible with a telescope. After visual alignment of both laser beams, temperature profiles were recorded and plotted as isotherms. In particular on Al_2O_3, the isotherms plot turned out to be a far more sensitive indicator of beam misalignment than a TV monitor or the human eye with a telescope. On UO_2, with its lower conductivity and transparence, direct visual alignment is more successfull. Beam alignment is insufficiently preserved from one sample to the next, because of uncertainties in the sample position and of the effect of vibrations involved in opening and closing the furnace on the beam centering mirrors.

When the laser cavity mirrors are adjusted such as to obtain the maximum power output, the beam profiles exhibit strong deviations from axial symmetry (Fig.1.28a). Better symmetry is achievable with about 90% of the maximum power (Fig. 1.28b). This effect is presently under investigation. 90% of full power does however suffice to melt UO_2.

When only the upper beam was shut off after recording the molten UO_2 temperature profile, and the lower beam slowly decreased in power, a number of samples could be recovered unfractured. This was never attained in earlier measurements. The plasticity of UO_2 at 1400-1800°C appears sufficient to accomodate the large volume change on solidification.

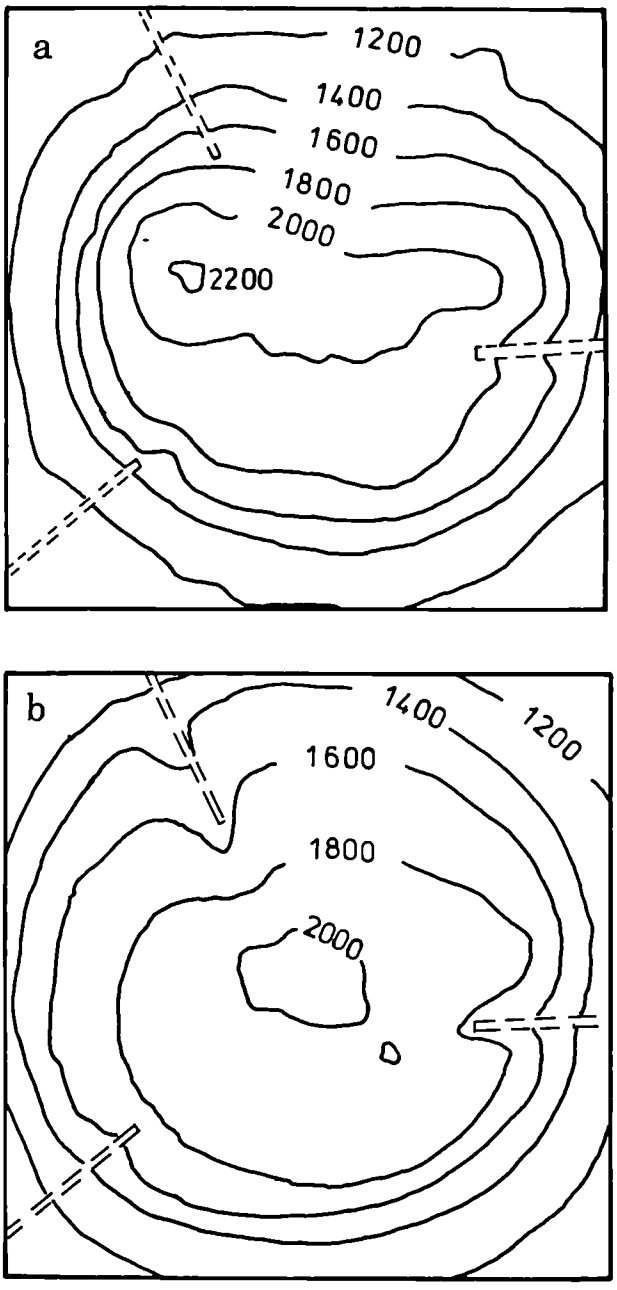

Fig. 1.28 *Isotherms plot of the lower surface of an Al_2O_3 sample (a) and of a UO_2 sample (b), heated only from below. The sample is placed on three thin tungsten supports, the shadows of which are clearly distinguishable in Fig.1.28b. In Fig. 1.28a, the laser was adjusted for maximum power, resulting in a beam profile with a pronounced deviation from axial symmetry*

References

[1] C.S. Kim, A. Blomquist, J. Haley, R.Land, J. Fischer, M.G. Chasanov, L.Leibowitz: in "Proc. 8th Symposium on Thermophysical Properties", Gaithersburg MD, (New York: ASME) pp 338-345 (1977)

[2] C. Otter, D. Damien: High Temp.-High Pressures **16** (1984) 1

[3] H.A. Tasman, D. Pel, J. Richter, H.-E. Schmidt: High Temp.-High Pressures 15 (1983) 419

[4] AIRPAX linear actuators Type K92221-P2

[5] Analog Devices Type 755N

[6] Hewlett-Packard 3437A, a 3½ digit instrument with a conversion time of 200 µs, and programmable range switching through IEEE-488 bus.

[7] EG&G 5005 set at 10^{-7}A/V

[8] CORION Type S40-650-A at 650 nm or Type P70-900-A at 900 nm

[9] II-VI Type PAZ-20 WC-6 - Based on six ZnSe Brewster reflectors

New Ionic Contributions to the Vapour Pressure of Urania

The approximate equality between recently published [1] values of the electron affinity, A, of the UO_3 molecule and the first ionisation energy, I, of UO_2 (5.2 and 5.5eV respectively) entails, via the gas phase equilibrium reaction

$$UO_2 + UO_3 \leftrightarrows UO_2^+ + UO_3^- \qquad (1)$$

significant ion contributions to the vapour pressure of urania, which have not previously been considered in the two phase equilibria, or in the interpretation of laser evaporation experiments [2, 3] to determine the vapour pressure of this nuclear fuel. In this report we investigate, through the above gas phase reaction, the implications of the high electron affinity of the UO_3 molecule on the total equilibrium vapour pressure and on the congruently vaporizing composition (CVC) of urania.

Application of the law of mass action to equation (1) (equilibrium constant $K_\pm$), together with the condition for charge neutrality, yields the following expressions for $p(UO_2^+)$ and $p(UO_3^-)$

$$p(UO_2^+) = p(UO_3^-) = \left[p(UO_2)\, p(UO_3)\, K_\pm \right]^{\frac{1}{2}} \qquad (2)$$

where

$$K_\pm \equiv \exp(-\Delta G_\pm / RT) \qquad (3)$$

and

$$\Delta G_\pm = I(UO_2) - A(UO_3) - T\left[\Phi(UO_2^+) - \Phi(UO_2) + \Phi(UO_3^-) - \Phi(UO_3)\right] \qquad (4)$$

The only known values of the functions Φ ($\equiv -[G°-H°(0)]/T$) appertaining to UO_2^+ and UO_3^- are those given by Glushko et al. [4] which are somewhat dependent on their values for the corresponding neutral species. Thus, for consistency, Glushko's Φ values must be used for both neutral and charged species [5]; this is done in the calculations reported below. It should be noted that despite the proximity of I(UO) and $A(UO_3)$, the UO^+ and UO_3^- pressures entailed by the analogy of equation (1) (with UO_2 replaced by UO) are by comparison negligible, as a consequence both of the negative value taken by the Φ term in the corresponding expression to equation (4), and the inequality $p(UO) \ll p(UO_2)$ near $O/U = 2.00$.

Results of the calculation for the ion enhancement factor of the total pressure over stoichometric $UO_{2.00}$ are given in Tab. 1.7 for the temperature range 2000-6000 K. Oxygen

Table 1.7 Results of the ion enhancement factor E in the urania vapour phase for two different oxygen potentials

T/K	E = Total ion pressure/Total neutral pressure	
	ΔG_{O_2} (GL)	ΔG_{O_2} (BOH)
2000	0.39	0.14
3000	0.68	0.54
4000	0.62	0.57
5000	0.32	0.43
6000	0.10	0.19

potentials from Green and Leibowitz [6] (denoted GL) and Babelot et al. [7] (denoted BOH) have been used in the calculation and represent most likely upper and lower bounds on ΔG_{O_2}. The results indicate that molecular ions can contribute significantly to the total vapour pressure even at 2000K. It should also be noted that although the total ion pressure increases monotonically with T, the ion enhancement factor E does not, in consequence of the rapid increase in the neutral oxygen pressure at higher T. In Fig.1.29 calculated values of the CVC (with and without ions) are compared to the experimental data [8-13] The CVC is more sensitive to the ion contribution when the GL oxygen potential is used and indeed brings the calculated CVC nearer to the main body of experimental data - a consequence of the much higher $p(UO_3)$ entailed by the GL oxygen potential.

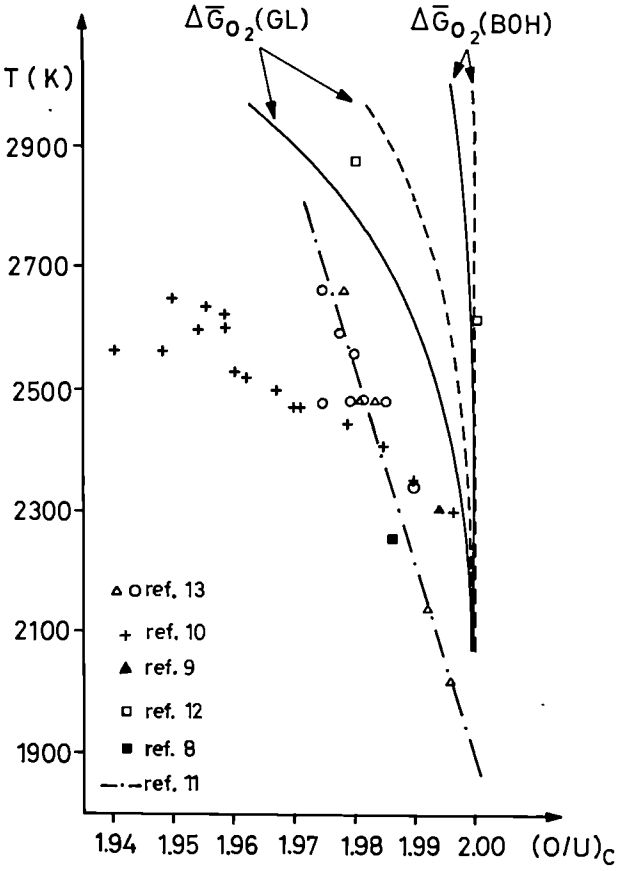

Fig. 1.29 *Temperature vs. the congruently vaporising composition of urania. Experimental data as shown. Calculated values - neutrals only - including ions*

It should be noted that existing considerations [14] of ionic contributions to the vapour pressure of urania are based only on the ionisation reaction $UO_n = UO_n^+ + e^-$ (n=1,2). Within the context of equation (1) however, the complementary electron capture reaction, $e^- + UO_3 = UO_3^-$, must also be admitted, the effect of which is to reduce the free electron density in the vapour by a factor 100. This renders the associated electron pressure negligible in comparison to the UO_2^+ and UO_3^- partial pressures, and could well account for the much lower absorption of laser radiation by inverse Bremsstrahlung found experimentally than would otherwise be expected.

In view of the large ion enhancement of the total vapour pressure found above, on the basis of the value of A reported in refs. [1] and [4], independent experimental verification of this value is urgently required.

References

[1] D.L. Hildenbrand, L.V. Gurvich, V.S. Yungman "The Chemical Thermodynamics of Actinide Elements and Compounds" Part 13 - The Gaseous Actinide Ions, IAEA Vienna 1985

[2] R.W. Ohse, J-F Babelot, C. Cercignani, J-P Hiernaut, M. Hoch, G.J. Hyland, J. Magill, J. Nucl. Mat. 130, (1985) 165

[3] M. Bober, J. Singer and M. Trapp, Proc. BNES Conf. on Science and Technology of Fast Reactor Safety, Guernsey, May 1986

[4] V.P. Glushko, L.V. Gurvich, G.A. Bergman, U.V. Veitz, V.A. Medvedev, G.A. Khachkuruzov, V.S. Yungman "Thermodynamic Properties of Individual Substances", Vol. 4., Academy of Sciences, Moscow 1982

[5] These differ somewhat from those made by D.W. Green in Int. J. of Thermodynamics 1, (1980) 61

[6] D.W. Green and L. Leibowitz, J. Nucl. Mat. 105, (1982) 184.

[7] J.-F. Babelot, R.W. Ohse, M. Hoch, J. Nucl. Mat. 137, (1986) 144

[8] J. Drowart, A. Pattoret, S. Smoes, Proc. Brit. Ceram. Soc. 8, (1967) 67

[9] R.J. Ackermann, E.G. Rauh, M.S. Chandrasekharaiah, Argonne National Laboratory Report: ANL 7048 (1969)

[10] R.K. Edwards, M.S. Chandrasekharaiah, P.M. Danielson, High Temp. Science 1, (1969) 98

[11] M. Tetenbaum, P.D. Hunt, J. Nucl. Mat. 34, (1970) 86

[12] G.T. Reedy, M.G. Chasanov, J. Nucl. Mat. 42, (1972) 341

[13] R.J. Ackermann, E.G. Rauh, M.H. Rand, Extended Synopsis for IAEA International Symposium on Thermodynamics of Nuclear Materials, Jülich 1979

[14] H.U. Karow, KfK Report 2390 (1977)

Study of the High Temperature Emissivity of Refractory Metals

The development of new pyrometers able to measure with a good precision temperatures of materials of unknown emissivity in a submillisecond time scale, up to 5000 K is urgently required for modern research in the domain of new materials (advanced ceramics, amorphous metals and new high temperature alloys).

One of the most important steps in setting up such an instrument is the calibration which must be performed with a black-body or with a grey body of known emissivity.

From experience it is very difficult to construct a fixed point black-body furnace for use above 1100 K. For higher temperatures, the radiance temperature of refractory metals at the melting point might be a good source for the calibration of one wave-length pyrometers working at 653 nm. Unfortunately, the temperature of materials of unknown emissivity can only be measured by multicolour pyrometers. It is thus of primary interest to calibrate such instruments with reliable procedures by using previous data [1].

It is in this context that a six-colour-pyrometer was used to measure the melting point of nine refractory metals and to evaluate the spectral emissivities (at the six wavelengths) and the total emissivity at temperatures up to the melting points.

This study has confirmed that metals at the melting point behave like grey bodies, i.e. their

emissivity is independent of the wavelength of the emitted light.

Experimental

The samples to be measured were small metallic spheres, 1 mm diameter, supported on a needle in a pure argon atmosphere and heated by 4 pulsed laser beams arranged in a tetrahedral configuration [2]. The samples were obtained from the manufacturer, Wagner (Stuttgart) and have a purity higher than 99.9 %. The measurements were made with a six-wavelength pyrometer as described elsewhere [3].

Typical temperature signals recorded during the cooling of samples are given in Fig. 1.30 for niobium, tungsten, tantalum, zirconium, vanadium, molybdenum, rhodium and hafnium. The temperature scatter increases for metals of low melting point because the temperature ranges evaluated for these metals is quite close to the sensitivity limit of the pyrometer. However the large number of measurements done over the melting plateau make it possible to obtain a good determination of the melting temperatures.

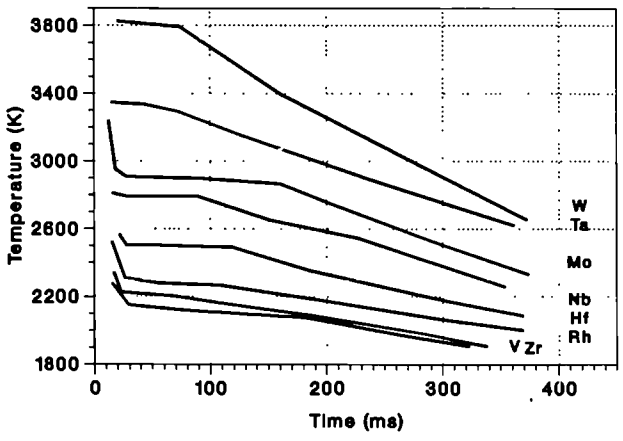

Fig. 1.30 Cooling curves of various metals in the laser-heated autoclave

Fig. 1.31 shows the spectral and total emissivities versus temperature for zirconium, vanadium, hafnium, rhenium and niobium. In

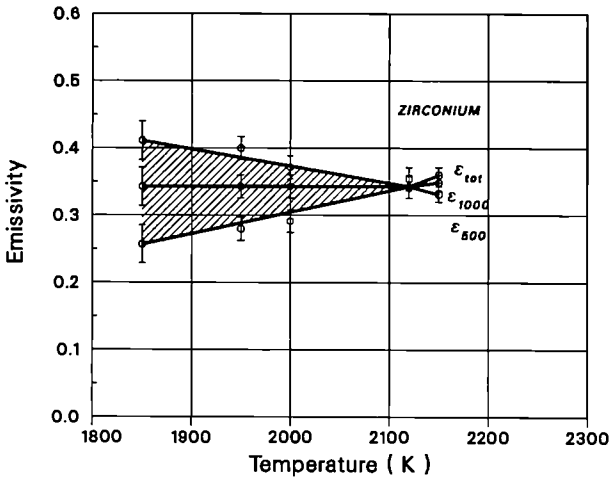

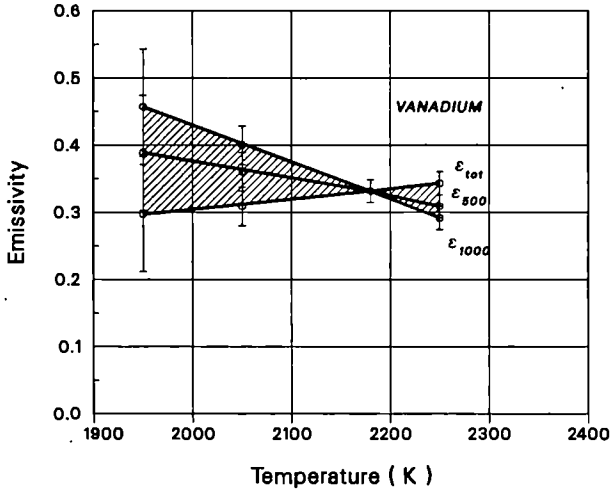

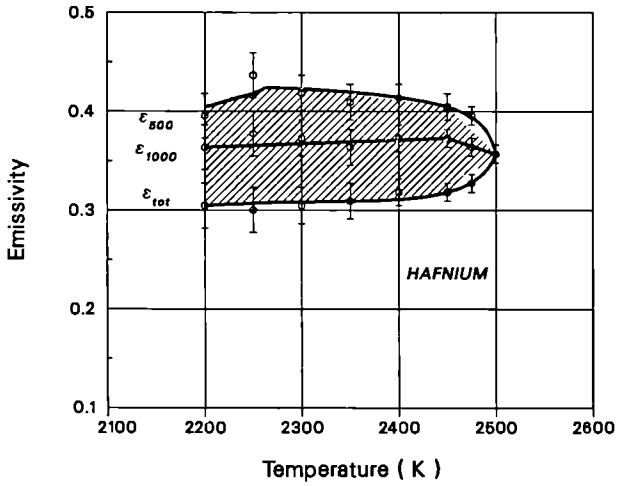

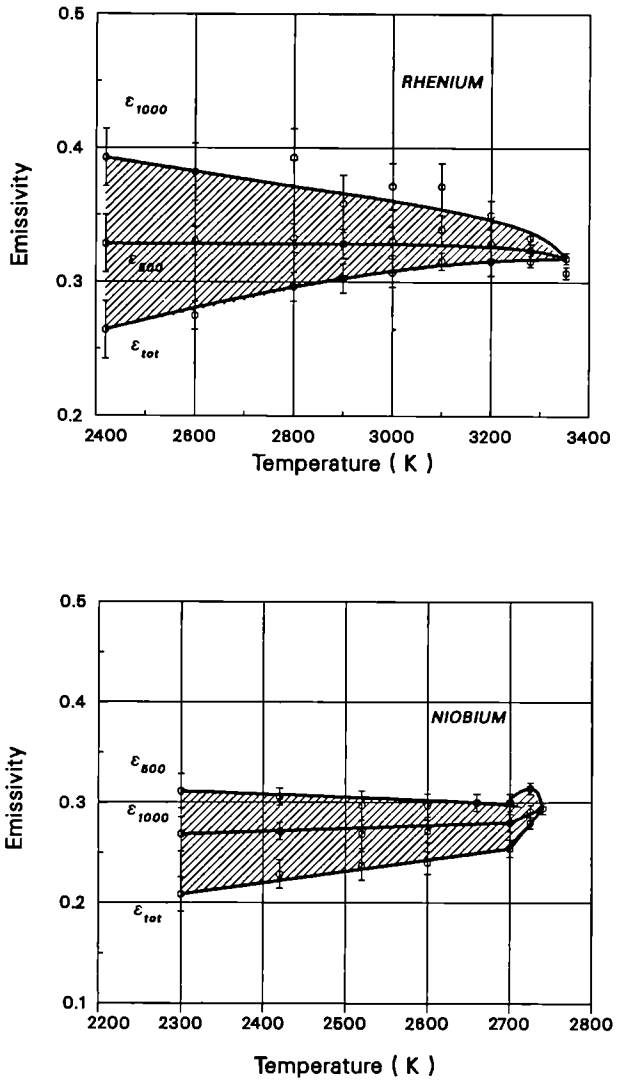

Fig. 1.31 *Measured emisivities as functions of temperature. The T_x - point corresponds in all cases to the melting point.*

this figure the values of the spectral emissivities for the shortest and the longest wavelengths measured are plotted, the 4 other values (600, 700, 800, 920 nm) are in the shaded region. As with temperature, the scatter in emissivity increases when the temperature decreases, especially for metals having low melting point (V, Zr, Rh) (for these cases the smoothed curves are presented with error bars).The wavelength dependence of the spectral emissivity of tungsten for different temperatures up to the melting point are shown in Fig. 1.32.

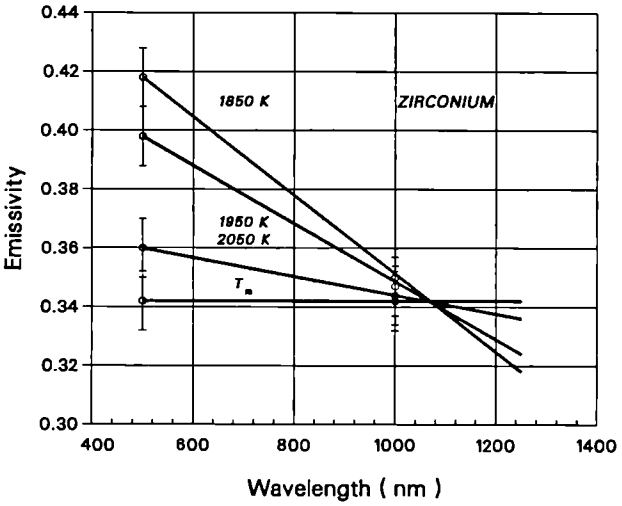

Fig. 1.32 *Spectral emissivity measured as a function of the wavelength for zirconium at different temperatures*

These results are summarised and compared with the existing data available in the literature, in Tab.1.8.

The grey-body-like nature of metals at their melting points is of primary importance when measurements are made under difficult experimental conditions such as those at ultra high temperatures and very high pressures (where the optical properties of surrounding gas change), since it represents a very useful reference state.

It is well known that for all metals and also for moderately conductive ceramics the isotherms of ε_λ are found to cross each other at a point λ_x or over a small $\delta\lambda$ interval. These results were extended up to and above the melting point T_m indicating that ε_λ (T_m) is independent of λ and equal to ε_T at λ_x.

Table 1.8 Emissivities Measurements in this work (tw) compared to literature data (lit)

Element	m.p.		$\varepsilon_{650,mp}$		$\varepsilon_{tot,mp}$		ε_x		λ_x	
	lit*	tw**	lit*	tw**	lit*	tw**	lit*	tw**	lit*	tw**
Mo	2890	2880	.31	.31	.30	.31	.30	.31	1300	1100
Ta	3280	3290	.33	.32	.32	.32	.30	.32	900	840
Nb	2741	2750	.33	.30	.30	.30	.32	.30	900	550
Zr	2125	2130	.32	.33	.32	.33	.33	.34	2500	1170
Rh***	2239	2250	.19	.22	.19	.22	-	.22	-	1300
Hf	2495	2480	.39	.35	-	.35	-	.35	-	1350
V	2193	2200	.31	.32	-	.32	-	.32	-	1400
Re	3450	3320	.36	.35	.36	.35	.35	.35	1000	1250
W	3685	3700	.36	.36	.35	.36	.36	.36	1280	1280

* literature value [31]

** this work

*** low purity: 0.4 % Ni, 0.1 % Si

The isochromate crossing-point is therefore a point T_x which corresponds or is very near to the melting temperature.

The slope and the shape of the function $\varepsilon_\lambda = \varepsilon_\lambda(T)$ varies for the different metals and, in particular, the value of λ_x ranges from 500 nm to 1040 nm. It would be interesting if a relationship between λ_x or ε_x with other known material properties were to be found. The brief survey on the emissivity models which follows below does not permit any conclusion to be drawn on the physical significance of λ_x and ε_x. However, it is worth remarking that as early as 1926 [4] a possible proportionality between λ_x or T^m was speculated .(At that time only the emissivity of liquid Au and W were known).

Later measurements however, have not brought to light any systematic relationship between λ_x and other material properties (Tab. 1.9). The only monotonic and approximately regular relationship was found between ε_x and the melting temperature (or the enthalpy of fusion which is in most cases nearly proportional to T_m). This indicates an increase of the emissivity (or absorptivity) with the strength of the interatomic bonding (Fig. 1.33).

Remarks on the X-point experimental results

The emissivity X-point phenomenon, discovered first by Weniger and Pfund in 1919 [5] has still not been fully interpreted in terms of reflection/absorption of electromagnetic waves.

Table 1.9 *Emissivities and thermodynamic data at the melting point*
T_m = *melting temperature*
ΔH_m = *heat of fusion*
γ = *electronic heat capacity coefficient*

	T_m (K)	ΔH_m (cal/mole)	$\gamma \cdot 10^4$ (cal/K mole)	$\varepsilon_{M.P.} = \varepsilon_x$	λ_x(nm)
Ag	1234	2855	1.47	~ 0.05	≈ 650
An	1336	2955	1.80	0.09	≈ 700
Cu	1357	3120	1.64	0.06	≈ 700
Co	1768	4120	12.00	0.22	-
Fe	1809	3630	12.00	0.35	900
Hf	2500	(1482)	6.30	0.35	1470
Ir	2727	6300	5.00	0.26	800
Mo	2890	6650	5.26	0.31	1100
Mn	1517	3500	28.00	0.50	-
Nb	2740	6300	18.00	0.30	550
Ni	1725	4210	16.80	~ 0.25	~ 1000
Os	3300	7590	6.00	~ 0.38	-
Pd	1823	4200	22.60	~ 0.20	~ 850
Pt	2093	4700	16.00	~ 0.25	~1200-1300
Re	3453	7900	5.60	0.36	~ 1200
Rh	2239	5150	13.00	0.22	~ 1300
Ta	3269	8108	5.00	0.32	840
W	3690	8400	2.50	0.36	1280
V	2190	5050	21.70	0.32	~ 1400
Y	1803	2732	20.00	0.35	-
Zr	2125	4900	~ 5.00	0.34	~ 1070

Even the existence of an emissivity X-point is still matter of debate both from the theoretical and experimental point of view. For instance, though the X-point of tantalum has been determined in this work, other high precision measurements [6] have shown that in this material the emissivity isochromates cross each other in a small, but distinguished wavelength interval between 780 and 820 nm for temperatures varying from 1200 to 2400 K. As shown in the preceding section the measurements of ε_λ indicate the existence of a single X-point at λ = 840 nm.

A word of caution should however be said concerning our experimental results. As reported [3], both temperatures and emissivities are deduced from the photodiode signals of the six-wavelength pyrometer, based on a postulated dependence of ε on λ and a suitable pre-

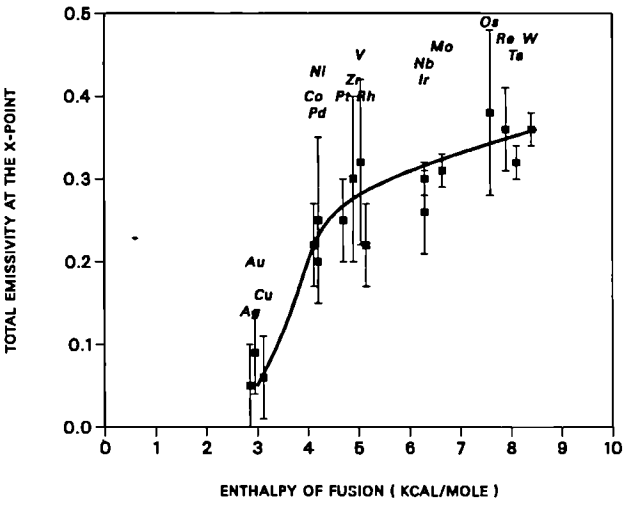

Fig. 1.33 *Total emissivity of various metals as a function of enthalpy of fusion*

calibration.The latter procedure should not represent a source of error because in our experiment the liquid-solid transition plateau provides an unquestionable reference temperature. On the other hand, the assumption of the dependence of ε on λ has an essential implication on the extrapolation of T and ε_λ. In fact, we assume that the spectral emissivity can be written for a sufficiently small λ-range as

$$\log \varepsilon_\lambda = a(T) + b(T)\lambda \qquad (1)$$

This has as a direct consequence that the derivative

$$\frac{d\varepsilon_\lambda}{d\lambda} = b(T)\,\varepsilon_\lambda$$

has a λ-independent zero, defined by the equation

$$b(T) = 0$$

Now, b(T), as well as a(T), is evaluated experimentally from the six independent measurements of the intensities $I(\lambda_i, i = 1 .... 6)$ of the pyrometer by means of a best-fitting procedure of eq. (1). Possible discrepancies are thus reduced to a statistical significance test, after the acceptance of which the parameters T and a(T) and b(T) are formally regarded as λ-independent. If in the explored temperature range b(T) changes sign or becomes sufficiently near to zero, the presence of a well-defined X-point is ensured. Yet strictly speaking, the X-point should be experimentally defined as an interval $\lambda_x \pm \delta\lambda_x$, $T_x \pm \delta T_x$, where the significance of the variances, in the context of our evaluation procedure, has a rather complex definition.

However, independent of the question whether an X-point or an X-interval exists, the essential result is that this coincides with (or is centered around) the melting point of the investigated metals. That a metal at the transition solid/liquid behaves as a grey body is intuitively reasonable if one thinks that near the melting point the electronic states - and in particular the Fermi surface gradually merges into a configuration where the interaction with the electromagnetic waves is mainly affected by the localized electrons.

The theoretical models are well established, but rather difficult to apply. In the simplest case, if the electrons interacting with light are described in terms of simple conduction following Ohm's law, the emissivity can be written as

$$\varepsilon_\lambda = \frac{4v}{1 + v^2 + 2v + \chi^2} \qquad (2)$$

where v is the real and χ the imaginary parts of the refraction index.

The Maxwell theory enables the values of v and χ to be expressed as functions of the d.c. conductivity σ and the dielectric constant ε_o:

$$v^2 - \chi^2 = \varepsilon_o \qquad (3)$$

$$v\chi = \frac{2\pi}{\omega}\sigma \qquad (4)$$

where ω is the electromagnetic wave frequency.

If ω is small (large λ's) the product $v\chi$ becomes large, whereas the difference $v^2 - \chi^2$ remains constant, so that the fractional difference of these two quantities becomes negligible and:

$$v = \chi = \sqrt{\frac{2\pi\sigma}{\omega}}$$

where from one obtains the Rubens-Hage formula

$$\varepsilon_\lambda = 0.365\sqrt{\frac{r}{\lambda}} \qquad (5)$$

where $r = 1/\sigma$ is the resistivity.

Since r increases with temperature

$$\frac{\delta\varepsilon_\lambda}{\delta\lambda} < 0 \quad \text{and} \quad \frac{\delta\varepsilon_\lambda}{\delta T} > 0$$

which excludes any X-point effect.

Actually, these two conditions are only experimentally satisfied for $T < T_x$ and $\lambda > \lambda_x$, (i.e. in the solid range and large wavelengths).

This discrepancy is ascribed to the assumption of the simple dispersion model, by which all the electrons have an unified velocity

$$\frac{ds}{dt} = \frac{eE}{r} \quad . \quad (E = \text{electric field})$$

Let us now more generally suppose that the conductor contains different types of carriers and/or internal polarizable charges with $\Sigma k_i s_i = eE$.

In this case a more complex expression for v and χ is obtained:

$$v^2 - \chi^2 = v_o^2 - 4\pi\,\Sigma_i \frac{N_i e m^2}{r_i^2 + m^2\omega^2} \qquad (6)$$

$$2v\chi = \frac{4\pi}{\omega}\Sigma_i \frac{N_i e r_i}{r_i^2 + m^2\omega^2} \qquad (7)$$

where m = electron mass N_i = electron density and v_o is a constant grouping all the real parts of the dielectric constant.

The last equation can be written as:

$$v\chi = \frac{2\pi}{\omega}\Sigma_i \frac{N_i e^2}{r_i} \frac{1}{1 + \dfrac{4m^2\omega^2}{r_i^2}}$$

and, since

$$\Sigma_i \frac{N_i e^2}{r_i} = \sigma\,,$$

this expression of $v\chi$ becomes much smaller for short wavelengths (large ω's) than that given by (5), whereas for $\omega \rightarrow 0$ converges to (5).

It can be seen that ε_λ obtained from (2) with (6) and (7) has variation domains which, for certain values of r_i and/or k_i, satisfy for small λ's the conditions

$$\frac{\delta\varepsilon_\lambda}{\delta\lambda} > 0 \quad \text{and} \quad \frac{\delta\xi_\lambda}{\delta T} < 0,$$

for $\lambda < \lambda_x$ and $T < T_x$.

In conclusion, the emissivity X-point effect is strictly dependent on the electronic structure and can be hardly described with simple models. In view of the future temperature and emissivity measurements in rapid-cooling experiments on UO_2 this aspect will be further investigated in order to check the validity of the present assessments and their possible extension to non-metallic components.

References

[1] J.P. Hiernaut et al, High Temp.-High Press. 18 (1986) 627

[2] TUAR 86 p. 38 (1987)

[3] J.P. Hiernaut et et al, High Temp.-High Press. 18 (1986) 617

[4] A.G. Worthing, Phys. Rev. 28 (1926)174

[5] W. Weniger, A.H. Pfund, Phys. Rev. 14 (1919) 427

[6] L.N. Latyev, V. A. Chekhovskoi and E.N. Shestakov, Phys. Stat. Sol., 38(1970) K149

X-Ray Shadow Imaging Device

An x-ray shadow technique was adopted to measure the thermal expansion coefficient of nuclear fuels in laser-pulse heating experiments [1].

With the practicable specimen sizes, to obtain a measurement precision of better than 1 % an image resolution of at least 5 µm is required. Furthermore, due to the rapid cooling conditions, the image must be acquired within a few milliseconds.

In the first attempt this objective was pursued by magnifying the x-ray shadow image by 40 times. This implied a positioning of the x-ray/light converter foil at a distance of about 3 m from the sample. The experimental setup led to an important weakening of the x-ray intensity arriving on the converter: A light amplifier was therefore needed to produce an usable image. However, the sensitivity of the amplifier was not very high for the green-blue light emitted by the converter, so that the signal-to-noise ratio was eventually rather low. Furthermore, other losses were produced in the optical path between the converter and the TV-camera.

A new setup was therefore implemented consisting of a simpler construction and providing higher performances. The improvement is based on the utilisation of a converter-foil which is directly adapted onto a 1:2 taper. The optical resolution of the new foil is better than 30 lines/mm, so that a magnification of only 8x is needed to obtain an image resolution of ~2 µm. Furthermore, the optics between the converter and the TV-camera was replaced by optical fibers

which directly convey the light into a green-blue sensitive tube.

The distance between the specimen and the camera could thus be reduced to 260 mm and hence the signal-to-noise ratio increased by two orders of magnitude. A sketch of the old and of the new setup is respectively shown on top and at the bottom of Fig. 1.34. In Fig. 1.35 a converted x-ray picture of a Tungsten sphere is shown. The contrast is very good and enables a suitable measurement of the object contours to be made and a microdensitometric determination of the zones of half-darkness can be carried out in order to obtain an accurate evaluation of the specimen linear size.

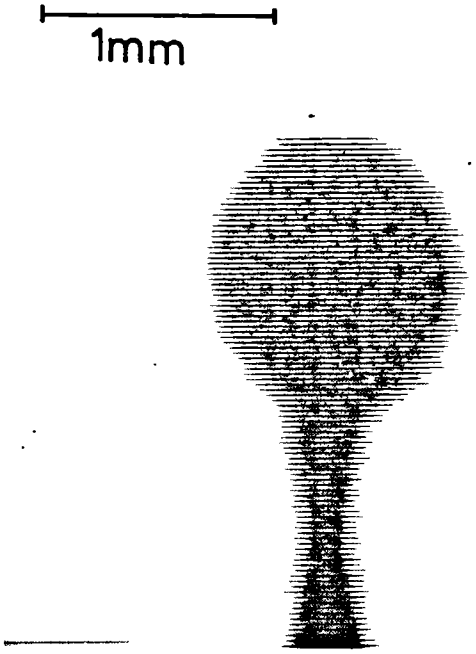

Fig. 1.35 *X-ray converted picture of a W-sphere*

Reference

[1] TUSR 40 p. 26 (1986)

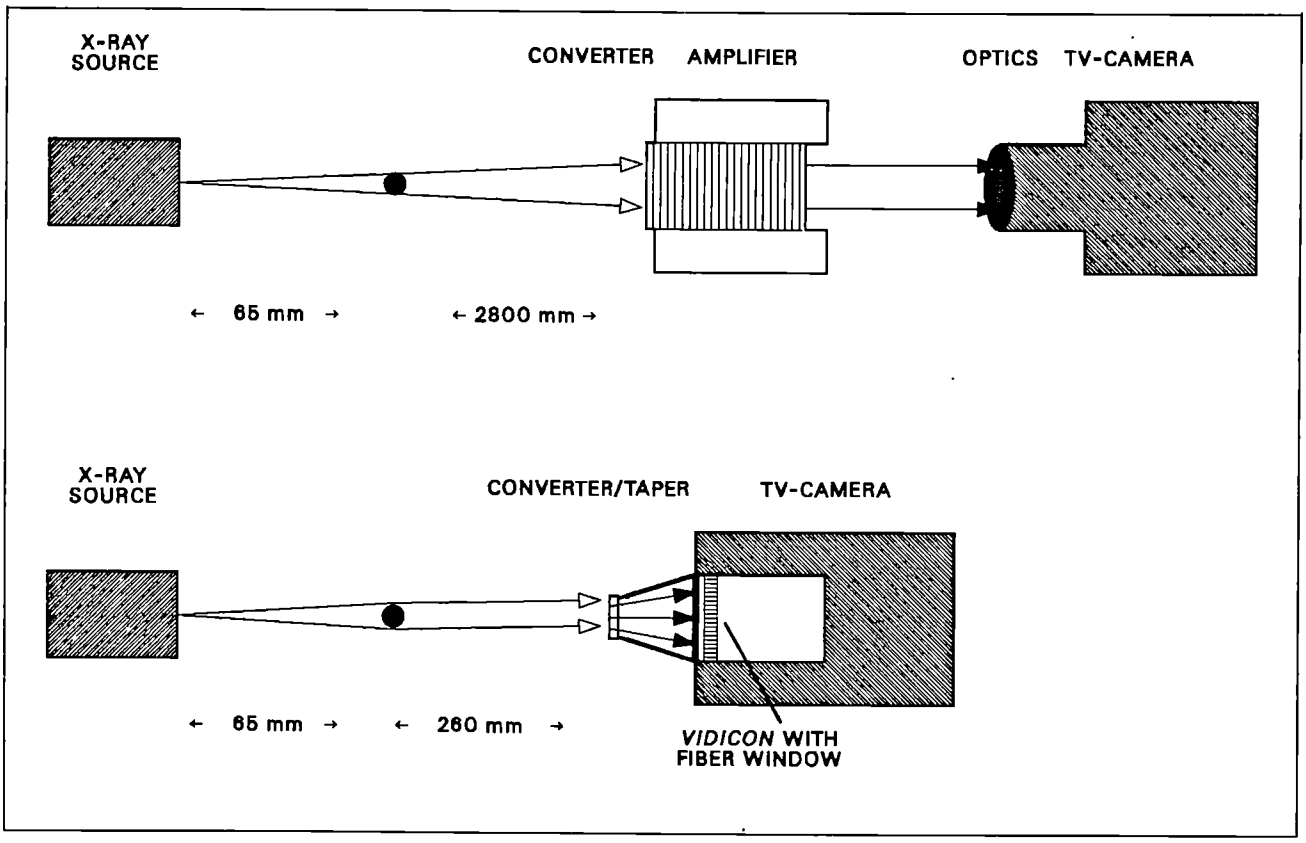

Fig. 1.34 *Top: old setup for the X-ray shadow imaging. Bottom: new setup*

Acoustic Levitation

Uniaxial acoustic positioning of spherical samples in pulsed multibeam laser-heating autoclaves under high inert-gas pressure conditions is a method for specific heat measurements under investigation.

Preliminary experiments have shown that the levitation conditions are strongly perturbed by sudden variations of the sample temperature: In most cases the effect is a rapid ejection of the levitated object in the radial direction. Improvements are being studied to remove this experimental difficulty by designing and testing levitators where stable radial retention forces are created which are less affected by local temperature changes.

Tri-axial levitator

The present apparatus consists of a standing-wave resonant levitator (Ø 10 mm) with reflector, driven by a single ultrasonic horn-transducer. The levitator device is fitted in the center of a high pressure laser autoclave with tetrahedral laser beam configuration. It is required that with a heating pulse duration of 100 ms and inert gas pressures of 100 - 200 bars wavelength changes should be negligible and a stable sound pattern situation should be created. This seems to be feasible under the following three conditions:

1. Absolute homogeneous and symmetrical laser-beam heating of the levitated sphere surface.
2. Perfect uniformity of the intensity of the four tetrahedral configured pulsed laser beams.
3. Negligible disturbance of the sound field pattern by local heat-up of the gas atmosphere around the levitated sphere.

It is very difficult however to prove that the above-mentioned conditions are strictly observed. First tests on levitated spheres heated by pulsed lasers show that short-time heating and maintenance of the resonance conditions are not assured: in some cases the sphere was completely ejected from the laser beam center and in others the sphere returned in position after being ejected to a distance of about 2.5 sphere diameters.

The standing wave resonance is not temperature-compensated because of the extremely small dimensions of the levitation-device. During the short-time heating and cooling of the sphere, the density of the inert gas (Ar, Kr or He) changes in the direct vicinity of the levitated sphere resulting in a change of velocity of sound and resonance frequency.

Experiments [1,2] have shown that the radial positioning force F_{rad} is about 13 % - 22 % of the axial positioning force F_{ax}. The ejection of a levitated sphere caused by short time heat-up and cooling can possibly be prevented by an increase in the radial retaining force F_{rad}.

A tri-axial levitator device to solve the problem is proposed: The scheme of the apparatus in shown in Fig. 1.36. It consists of a rectangular ground plate, three vertical holders and three

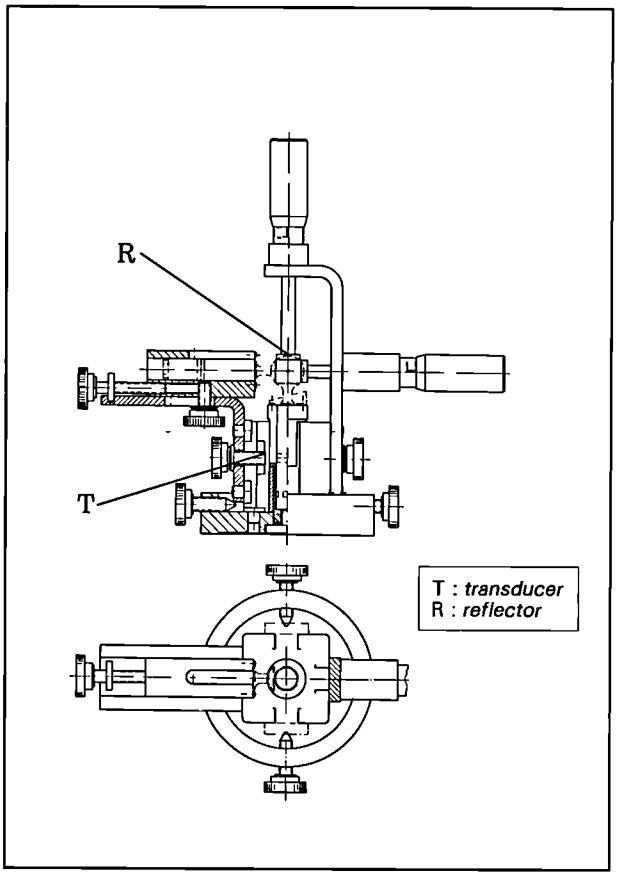

Fig. 1.36 Three-axial acoustic levitation device

transducers with reflectors. Those transducers with reflectors are precisely adjustable in three orthogonal planes and directed to the center by means of three adjusting gauges. Each transducer can levitate the spherical sample alone, so that the positioning forces along the three axes are nearly equivalent. The resulting standing-wave interference should produce well defined 3-D levitation cells whose walls should provide sufficiently strong barriers against sample movements produced by thermal perturbations.

Improvement of the resonance conditions of the ultrasonic transducers

The maximum acoustic radiation intensity of composite pre-stressed transducers is proportional to the square of the maximum permissible dynamic tensile stress amplitude near the nodal plane, where the stress amplitude reaches a maximum. The fatigue strength of the piezo-electric ceramic, the end pieces such as steel, aluminium or titanium and the materials of the screws or bolts should be considered. In most cases the transducer power requirements are severe and require optimal resonance conditions. This can be achieved by mechanically pre-stressing the transducer in the axial direction by means of a high tensile central screw. The useful amount of pre-stress on the piezo-ceramic surface is about 25 N/mm^2. An uncertainty remains when the nuts are simply tightening with the torque spanner. This method is inaccurate, since the torque required for a certain amount of pre-stress depends to a large extent on the finish of the transducer parts and on the quality of the screw thread.

The required pre-stress force P is [3]:

$$P = \frac{Mg}{\frac{d_m}{2} \cdot tg(\alpha+\rho) + r_A \cdot \mu_A} \quad [kg]$$

Mg	=	total torque [kg mm]
d_m	=	$d_2 = d - t_1$ middle thread diameter [mm]
$tg\alpha$	=	$h/(\pi d_2)$ = thread pitch angle
h	=	thread pitch [mm]
t_1	=	0.695 h = thread depth [mm]
μ_A	=	coefficient of fricton on the screw head support [-]
r_A	=	radius of fricton on the screw head support [mm]
μ	=	$tg\rho$ = coefficient of friction [-]

The estimated coefficient of friction μ is about 0.15. In this estimation lies a large uncertainty which causes different forces taken up by the screw for each transducer. This method can only be used if the piezo-ceramic disks are protected from shear stress by a tool that takes up the torque. Otherwise the piezo-ceramic disks may be severely (though invisibly) precracked: this results into an unexplainable power loss with overheating of the piezo-ceramics.

To solve the problem of the differing pre-stress forces and consequent changes in transducer power a hydraulic operated press was designed (Fig. 1.37) to obtain precise pre-stressing of the transducer with the piezo-ceramic disks.The system consists of a ground plate on which the device is mounted, a hydraulic movable piston in which a turnable shaft with spanner for square head screws has its bearing, a cylinder, a counter holder, a hydraulic hand pump and a manometer.

The non-pre-stressed and non-tightened transducer is introduced into the hydraulic press between counterholder and piston. After assembly, a direct connection for tightening the cylindrical screw head at the metal endpiece of the transducer presses the transducer against the counterholder and produces the desired pre-stress force on the piezo-ceramic disks. The stress can be controlled with the fitted manometer (0 - 100 bar). As soon as the desired force is reached the screw head can be tightened to maintain the established pre-stress conditions.

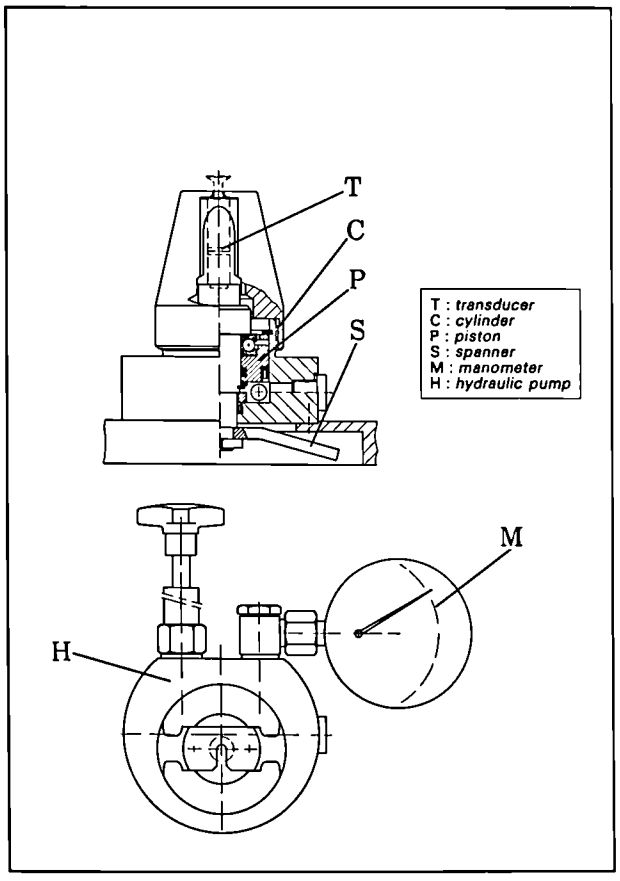

Fig. 1.37 Fixed pre-stressing device for ultrasonic transducers

References

[1] I. Rudnick "Measurements of the Acoustic Radiation Pressure on a Sphere in a Standing Wavefield", J. Acoust. Soc. Am. **62**, (1977) 20-22

[2] E. Leung, N. Jacobi and T. Wang, "Acoustic Radiation Force on a Rigid Sphere in a Resonance Chamber", J. Acoust. Soc. Am. **70**, (1981) 1762-1767

[3] Hütte, Maschinenbau, Teil IIA, "V Schraubenverbindungen" edited by Akademischer Verein Hütte, E.V. Berlin (1954)

Collaboration with External Organisations

CEA - CEN, Cadarache
CEA - CENG, Grenoble
National Laboratory of Metrology, Japan
JRC Ispra

2 Transient Behaviour of Oxide Fuels and Fission Product Release (under Severe Fuel Damage Conditions)

Introduction

The OFT project has three objectives:

- to determine and understand mechanisms which occur in commercial LWR fuel under normal and transient conditions and to provide a quantitative description of these mechanisms up to high burn-up and extending to hypothetical accident conditions

- to investigate fundamental mechanisms such as diffusion, precipitation and release of volatile fission products at high temperatures

- to establish models for the mechanisms important for gas release and fuel swelling under normal and off-normal conditions as well as for the technological treatment of fuel pin performance.

Progress was achieved with this combination of basic and technological approaches in all these fields.

TU has now very extensive data bases on transient-tested LWR fuel up to high burn-up and on the behaviour of volatile fission products, and two powerful fuel performance codes are available. Besides describing the progress in the above three fields, some additional new results are reported in the following on oxygen potential measurements of $(U,Pu)O_2$ at very high burn-up and on UO_2 leaching in water as a preliminary to studying problems connected with direct storage of high burn-up spent fuel.

Irradiation Experiments

Irradiation Experiment VOLEX (VOLume EXpansion)

For details of this irradiation, see TUAR 86, 58. Due to safety problems, the irradiation in the HFR had to be postponed. The experiment started in December 1987.

Irradiation Experiment BUMMEL (BUbble Mobility MEasurement Level)

The aim of this experiment is to study the migration of fission gas bubbles in UO_2 single

crystal specimens in a predeterminated temperature gradient. Two sets of 10 discs of UO_2 single crystals, ø : 7 mm, 1 mm thick are stacked with molybdenum spacers and sealed in two cans with welded end-plugs (Fig. 2.1).

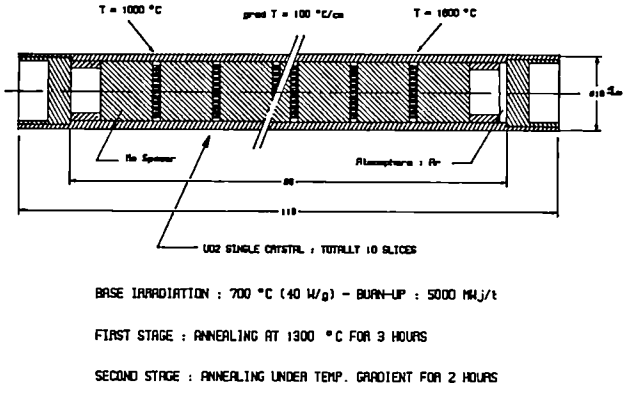

Fig. 2.1: BUMMEL, fuel pin

The experiment will be carried out in different phases. First, the two cans are irradiated at 700° C until a burn-up of about 5000 MWd/t is achieved. One can is then unloaded, the second one is submitted to a heat treatment - 1000° C for 3 hours - and to an irradiation for 2 hours in a thermal gradient of 1000° C to 1800° C. The irradiation, carried out in the HFR reactor, is conceived to be operated in a TRIO capsule using gamma heating, gas mixture temperature control and a vertical displacement unit.
Fabrication of capsule and structural parts is completed, and the assembly of the fuel pins was made in December 1987. Start of irradiation is foreseen for March 1988.

Post-Irradiation Experiments on LWR Fuel Samples Irradiated to Increasing Burn-up under Base and Transient Conditions

Hot Cell Fission Product Release Studies

The apparatus developed for hot cell studies of fission gas-release under constant temperature and transient conditions has been used for the analysis of the release of non-volatile fission products and particulates.

The only modification of the previously described apparatus (TUSR 35, 27-40, 39) for hot cell fission gas analysis on irradiated materials is shown in Fig. 2.2. In the new set-up the sample is placed in a HF furnace in a crucible extended by an impactor/condenser tantalum tube located outside the furnace coil. The temperature of the tantalum tube decreases along its axis from a value near to that of the sample down to a few hundreds degrees.

Samples (200-400 mg) of uranium dioxide irradiated to a burn-up of 53000 MWd/t at a rating ranging between 200 and 300 W/cm have been used for these tests. During the annealing the capsule is swept by a stream of He/2 % H_2 flowing at 16 ml/s.

The fission gas evolved from the sample is swept away and measured in a beta flow-counter of 10 cc capacity. Integral measurements of fission gas

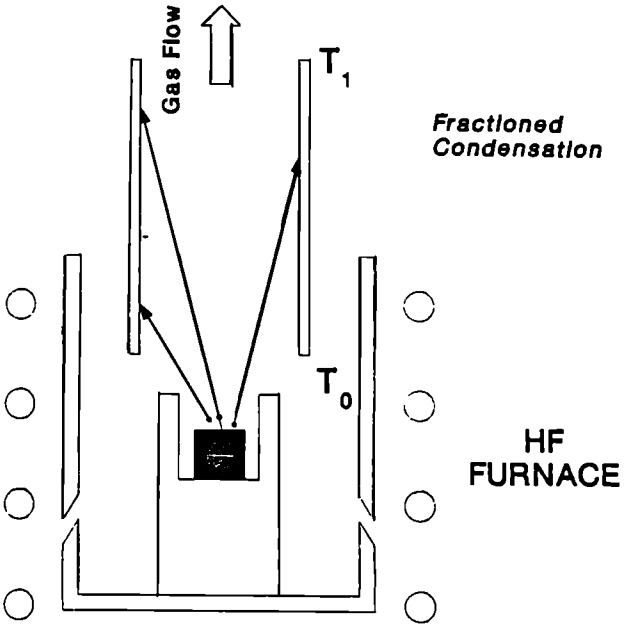

Fig. 2.2: Hot cell fission product release studies. Experimental set-up for fractional condensation of non-volatile fission products

release are carried out by trapping Xe and Kr with liquid nitrogen and by determining the amount of ^{85}Kr with a NaI counter at the bottom of the trap and also by analysing an aliquot of Xe using a quadrupole mass-spectrometer.

The less volatile fission products are mostly collected on the condenser tube and partly on the outlet filters. After the heating the tube is removed and γ-scanned. The isotopes ^{134}Cs, ^{137}Cs, ^{145}Eu, ^{106}Rh are detected. Their axial distribution on the impactor is then analyzed using a scanning-electron microscope provided with a shielded EDAX.

From preliminary experiments carried out in a Ar/H_2 atmosphere, three effects were noted out:

1) the total γ-activity decreases with increasing temperature in the hot part of the impactor/condenser (Fig. 2.3);

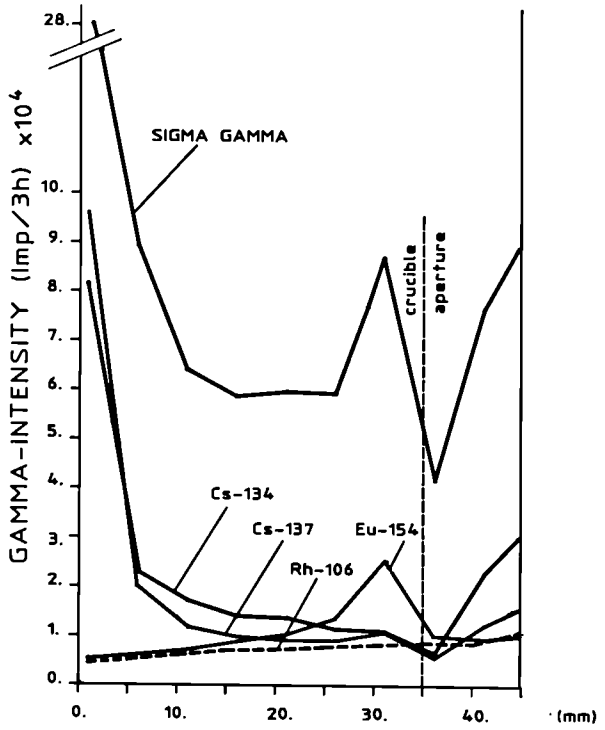

Fig. 2.3: Axial distribution of gamma activity on the tantalum condenser tube

2) in a temperature range around 1100-1200°C two peaks are detected on the tube, the first, at higher temperature, corresponding to ^{154}Eu, the second one to the Cs isotopes:

3) the concentration of ^{106}Rh (the daughter of ^{106}Ru) decreases continuously with temperature.

Scanning-electron microscope analysis of the deposited and condensed phases suggests that release of the less volatile fission products takes place both by homogeneous evaporation and by ejection of solid (fuel particulates) and molten phases. The results are preliminary, since the EDAX analysis of the deposits is still in progress. Tab 2.1 provides an overview of the analysis

Table 2.1: Characteristics of the deposits observed on the tantalum condenser tube

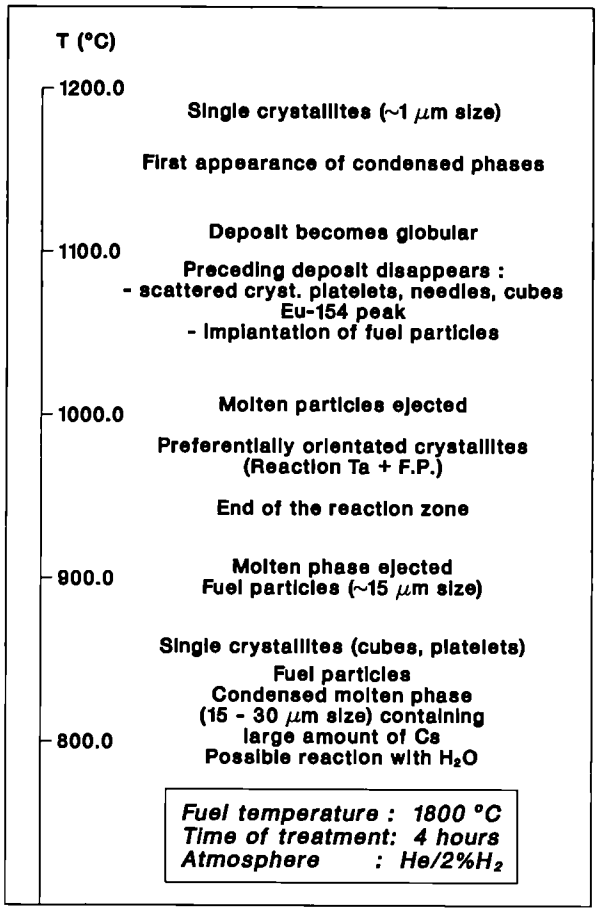

results of the condensed phase release from a high burn-up LWR fuel submitted to a ramp up to 1800°C for 4 hours. The results are preliminary and EDAX analysis of the deposits (from the SEM analysis 6 different phases are anticipated) will be reported in the next issue

Post-Irradiation Examination of Transient-Tested UO_2 and MOX Fuel

Transient-Tested UO_2

The systematic investigation for fuel restructuring on UO_2 samples irradiated to increasing burn-up and under base and transient conditions has been continued. Samples B1 and B1T3 corresponding to the low burn-up samples of the series analysed were characterized (see Tab. 2.2).

Table 2.2 Irradiation scheme of LWR fuels transient tested UO_2 and transient tested MOX fuel

I. UO_2 fuel available for analysis

Designation of fuel	Burn-up GWd/to	Final power level during transient kW/m
B 1	16.4	-
B1T3	12.9	53
B2	31.5	-
B2T1	35.4	41.5
B2T2	35.6	47.5
B3	45.2	-
B3T1	45.2	41
B3T2	44.6	48
B4	53.1	-

B = Base irradiated fuel
BT = Base irradiated and transient tested fuel

II. MOX fuel

MB1	25	-
MB1T3	26.2	?
MB2	35.8	-

The main elements of comparison are collected in tables 2.3 and 2.4. B1 indicated as expected a lower temperature regime for the fuel irradiated with lowest burn-up. B1T3 was transient tested at a higher power than the other fuels available

for the comparison and from the characterisation results alone no final conclusion can be reached.

Table 2.3 *Irradiation and microstructure data*

	B1	B1T3
Burnup (GWd/t)	16.4	12.9
Transient terminal power (W/cm)	/	530
Gap (µm)	17-80	20-50
Average value	42	33
Depth of reaction zone UO_2 + Cs (sum) (µm)	/	/
Onset of precipitation of intergranular porosity (mm)	2.199	1.248
Onset of zone with elongated grains (mm)	/	2.694

Noteworthy is the absence in the case of B1T3 of intragranular pores by optical microscopy and for both B1 and B1T3 the absence of reaction UO_2 + Cs at the outer rim of the fuel pellet.

The other structural features are in good agreement with the observations made on previously analysed samples.The preliminary conclusions presented in TUAR-86 on the microstructure analysis of transient tested fuels are in good agreement with the present results and are still valid.

Transient-Tested MOX Fuel

Two further materials were analysed and the onset of the structural features are collected in Tab. 2.5. No basic difference to the corresponding UO_2 fuels was observed.

EMPA Investigation of MOX Fuel Irradiated under Normal and Transient Conditions

The redistribution of Pu and the behaviour of Xe and Cs have been investigated in two segments of MOX fuel supplied by the German fuel vendor Kraftwerk Union. One segment had been irradiated under steady state conditions to a burn-up of 23.2 GWd/tU ; the other had been transient tested to 42 kWm^{-1} for 52.5h at a burn-up of 26.2 GWd/tU. The power schedule for the transient test incorporated two power dips to 24 kWm^{-1}, each of 0.5h duration. The fuel was fabricated by the AuPuC process. This involved mechanically blending a master mix of 70/30 UO_2-PuO_2 with commercial grade natural UO_2 powder. The product, which contained nominally 3.2 wt% Pu, consisted of agglomerates of master mix particles less than 100 µm in size irregularly dispersed in a matrix of UO_2.

Redistribution of Plutonium

During irradiation not only was the Pu in the master mix agglomerates burnt but it also diffused into the UO_2 matrix at a rate that was dependent on the local fuel temperature. The MOX agglomerates in the fuel irradiated under steady-state conditions had apparently lost little of their Pu by diffusion and consequently the UO_2 matrix contained only about 1 wt% Pu. The high temperatures in the transient tested fuel had caused the MOX agglomerates in the central region of the pellet to dissolve completely and locally this had raised the Pu content of the UO_2 matrix to about 3 wt% (Figs. 2.4 and 2.5).

Table 2.4: Nature and extent of structural features observed in base irradiated and transient tested UO_2 fuels

				1	2	3	4	5	6
		Burn-up (Gwd/t)							
Base Irradiation	B1	16.4			1.00-0.30	0.30-0.00			
	B2	31.5			1.00-0.59	0.59-0.00			
	B3	45.2		1.00-0.97	0.97-0.75	0.75	0.75-0.00		
	B4	53.1		1.00-0.91	0.91 ——— 0.00				
		Burn-up (Gwd/t)	Final Bump Power (W/cm)						
Transient	B1T3	12.9	530		1.00-0.73	0.73-0.40			0.40-0.00
	B2T1	35.4	415		1.00-0.71	0.71	0.71-0.36	0.36-0.00	
	B2T2	35.6	475	1.00-0.99	0.99-0.79	0.79	0.79-0.52	0.52-0.35	0.35-0.00 C
	B3T1	45.2	410	1.00-0.97	0.97-0.76	0.76	0.76-0.45		0.45-0.00 C
	B3T2	44.6	480	1.00-0.97	0.97-0.83	0.83	0.83-0.66	0.66-0.46	0.46-0.00
		T_{fuel} (°C)				900	900-1250	(1700) 1250-1600	

Table 2.5: Nature and extent of structural features observed in base irradiated and transient tested MO_2 fuels

				1	2	3	4	5	6
		Burn-up (Gwd/t)							
Base Irradiation	MB1	25.0			1.00-0.55	0.55-0.00			
		Burn-up (Gwd/t)	Final Bump Power (W/cm)						
Transient	MB1T3 (a)	26.2	419		1.00-0.77	0.77-0.41			0.41-0.00
	MB1T3 (b)	26.2	419		1.00-0.78	0.78	0.78-0.39		0.39-0.00
		T_{fuel} (°C)				900	900-1250	(1700) 1250-1600	

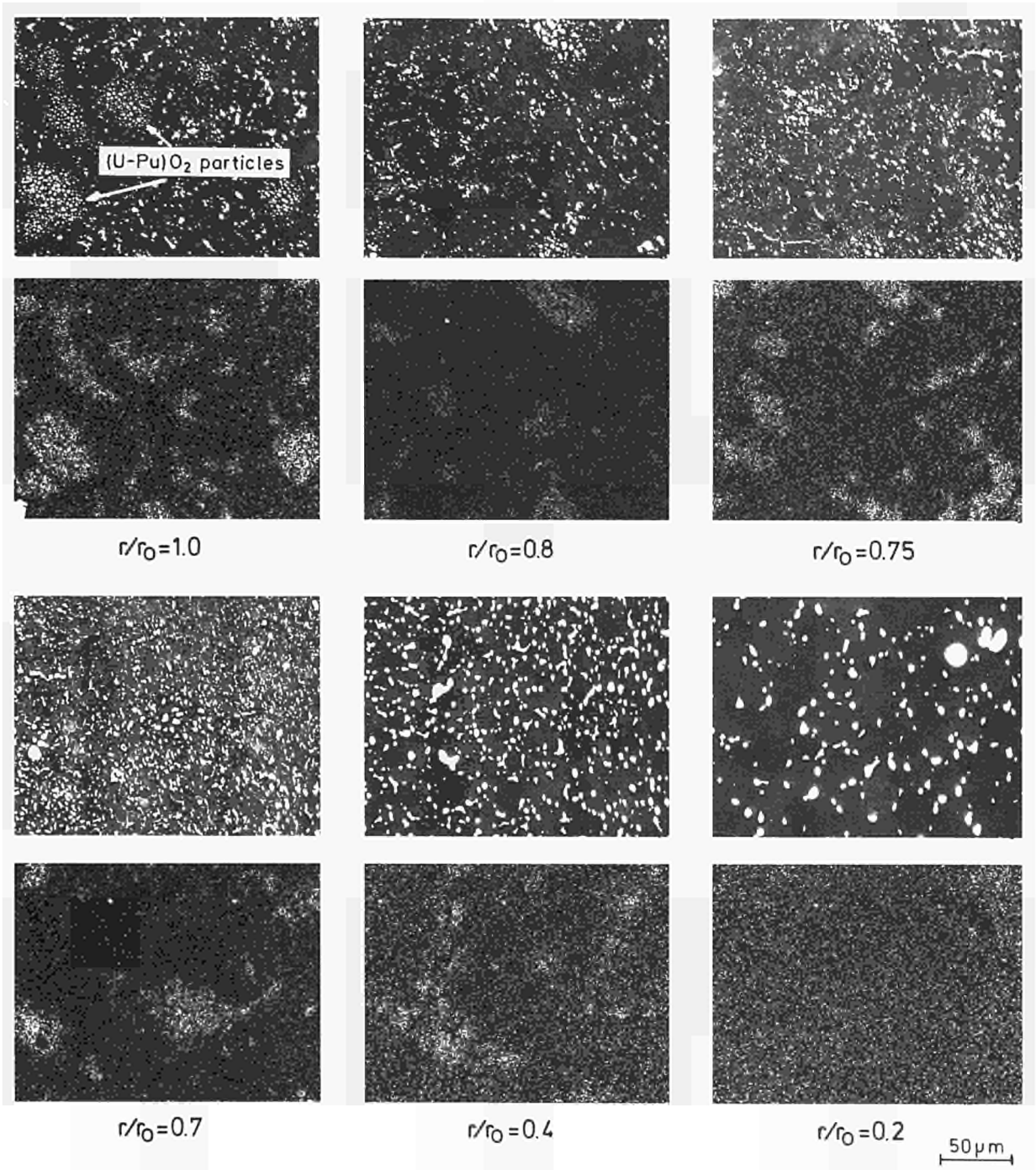

Fig. 2.4. Electron absorption and X-ray scanning micrographs showing the fuel microstructure and the local distribution of Pu in the transient-tested fuel segment. MOX agglomerates are absent at $r/r_o = 0.2$.

Behaviour of Xe and Cs

The MOX agglomerates became highly porous in the course of irradiation. The porosity is assumed to be a consequence of vacancy supersaturation caused by the high fission density in the agglomerates. A contributing factor, however, could be the diffusion of Pu to the UO_2 matrix. This can cause the formation of pores via the Kirkendall mechanism.

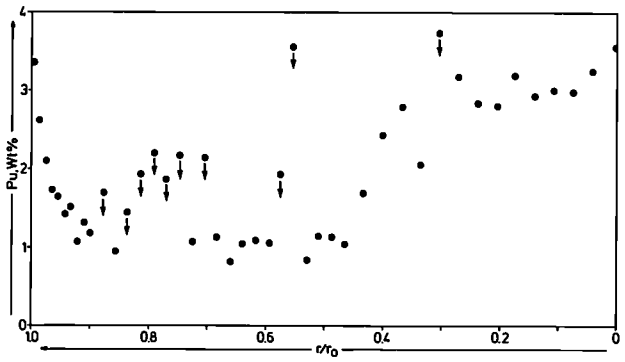

Fig. 2.5. Radial distribution of Pu in the UO_2 matrix of the transient-tested fuel segment. The concentration of Pu increases in the central region of the fuel due to the dissolution of MOX agglomerates. High concentrations are attributed to the pick up of Pu in the MOX agglomerates.

Quantitative image analysis indicated that the porosity in the agglomerates in the outer region of the fuel may have been as high as 50%. At this location an appreciable fraction of the Xe created had probably precipitated in the pores. With increase in the fuel temperature, however, sintering occurred and with decrease in the percentage of porosity more gas was found in the $(U,PU)O_2$ lattice (Fig. 2.6).

Caesium behaved differently to Xe in that it did not collect in the pores. As a result, more than half of the Cs created was retained in the lattice of the MOX agglomerates in the outer region of the fuel segments. The high level of Cs retention suggests that during irradiation the oxygen potential in the MOX particles was much higher than in the surrounding UO_2 matrix.

Appreciable amounts of Xe and Cs were found in the UO_2 matrix in both fuel segments. Since commercial grade natural urania was used in the fabrication of the fuel, part of these fission products must have diffused out of the MOX agglomerates. Nevertheless, their radial distributions in the UO_2 matrix (Fig. 2.7) were not significantly different from those found in conventional LWR fuel with similar power histories.

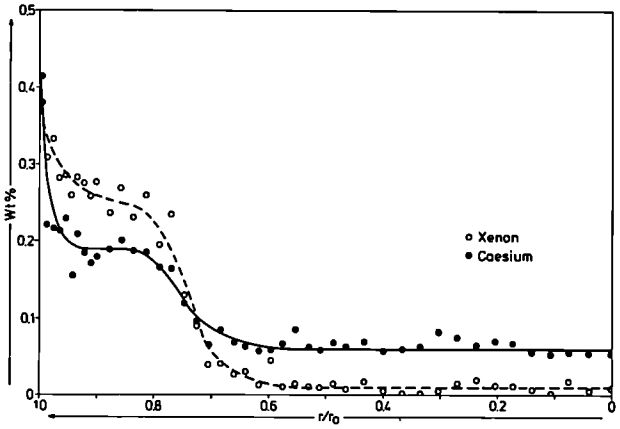

Fig. 2.7. Radial distributions of retained Xe and Cs in the UO_2 matrix of the transient tested fuel segment. Similar profiles are found in conventional LWR fuel following a power transient to 42 kWm^{-1}

Release of Xe and Cs to the pin free volume occurred via the UO_2 matrix. As in conventional LWR fuel, the release of Xe involved the interlinkage of gas bubbles on the grain boundaries and the subsequent formation of escape tunnels (see electron absorption micrographs in Fig. 2.4). The UO_2 grains in the steady-state irradiated fuel had released about 15% Xe and 1-2% Cs whereas about 40% Xe and 30% Cs had been released from the UO_2 grains in the transient-tested fuel. Similar release values would be expected for conventional LWR fuel. Apparently, not all the fission gas released from the UO_2 grains had reached the pin free volume. Puncturing gave a release value of about 2% for the steady state irradiated fuel. Hence, it is assumed that in this fuel most of the gas released from the UO_2 grains was retained on the grain boundaries.

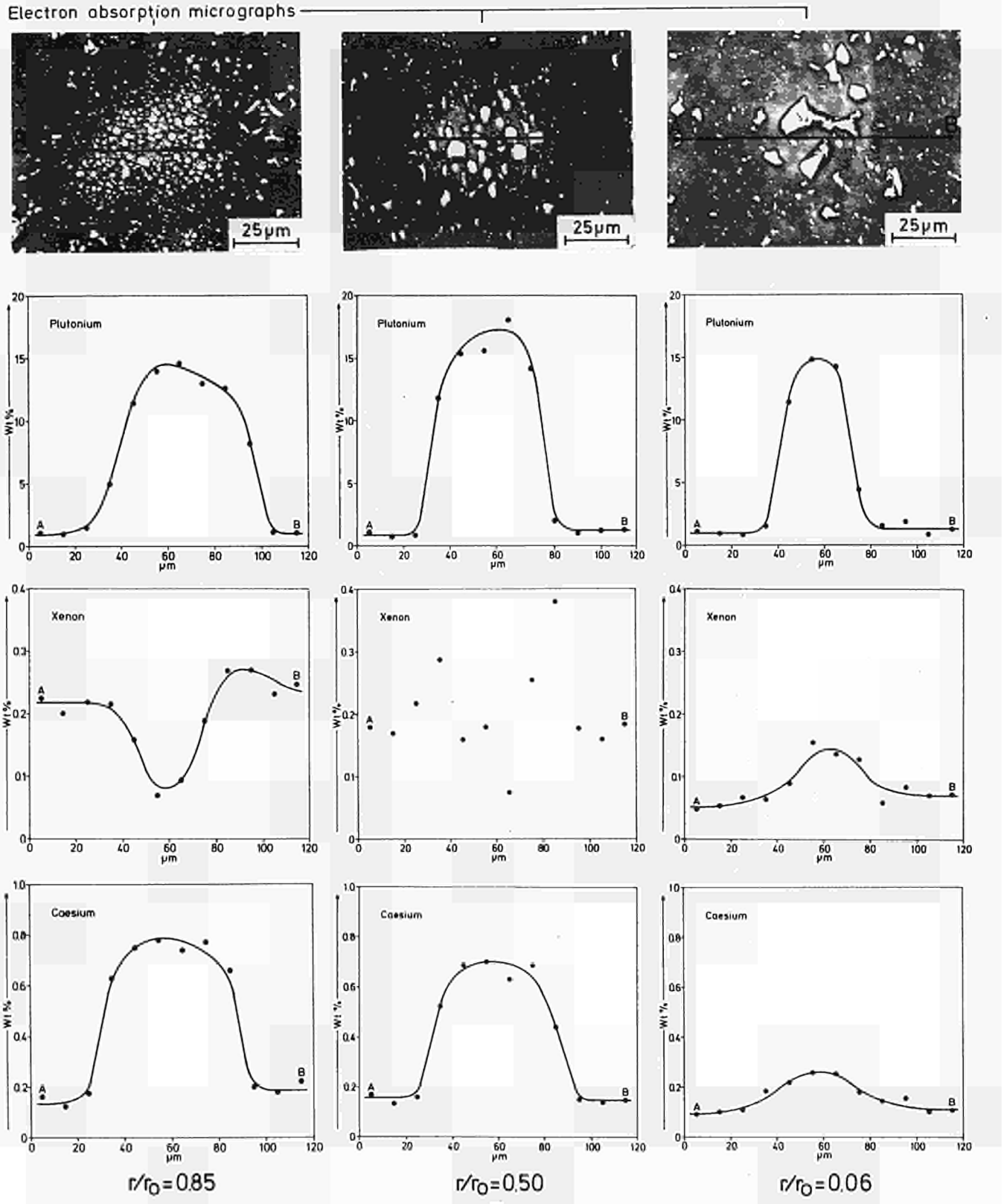

Fig. 2.6. *Concentrations of Pu, Xe and Cs in MOX agglomerates at three radial locations in the fuel segment irradiated under normal conditions. With increase in the fuel temperature the concentration of Xe in the $(U,Pu)O_2$ lattice increases whereas the concentration of Cs decreases.*

TEM and REM Investigation of Transient-Tested UO_2 Fuel

Introduction

In the framework of the Oxide Fuel Transients Project electron microscopy is being used to study the microstructure of fuel samples which have been subjected to various combinations of burn-up and transient. Tab. 2.2 shows the combinations which are being examined.

Transmission Electron Microscopy (TEM) is used on small thinned samples of fuel to show the defect structure (dislocations, small loops) and the nucleation, density and size distribution of small solid precipitates and fission-gas bubbles. Scanning Electron Microscopy (SEM) and Replica Electron Microscopy (REM) are used to examine the size distribution and density of large-fission gas bubbles (>50nm diameter) and the grain boundary porosity. Both of these techniques are used on suitably prepared cross-sections of fuel, giving a complete radial distribution. With TEM it is unfortunately only possible to examine a small number of radial positions because of the limitations imposed by specimen preparation, though these radial positions can be measured very precisely by comparing SEM images of the sample surface with the optical macrographs of the full cross-section.

The results reported here represent a full analysis of a B3T1 sample by REM and TEM.

Results of the Replica Analysis

The replicas on this fuel showed no fission gas bubbles at the periphery , but a strong growth of intergranular and intragranular bubbles between the radial positions $R/R_0 = 0.75$ and $R/R_0 = 0.46$ could be seen. However, for $R/R_0 < 0.45$ both populations disappear rapidly and no bubbles can be seen at the centre. The bubble distribution within the inner half radius of the fuel cross section was very inhomogeneous, some grains showing a very high density of bubbles with neighbouring grains totally bubble free. An example of this is shown in Fig. 2.8 taken at a radial position of $R/R_0 = 0.43$. Fig. 2.9 shows an example of the micro-structure at the periphery, and Fig. 2.10 at the point of maximum microswelling at $R/R_0 = 0.61$. Tab. 2.6 summarises the results obtained by the replica analysis, and Fig. 2.11 shows the resulting microswelling curve calculated for this

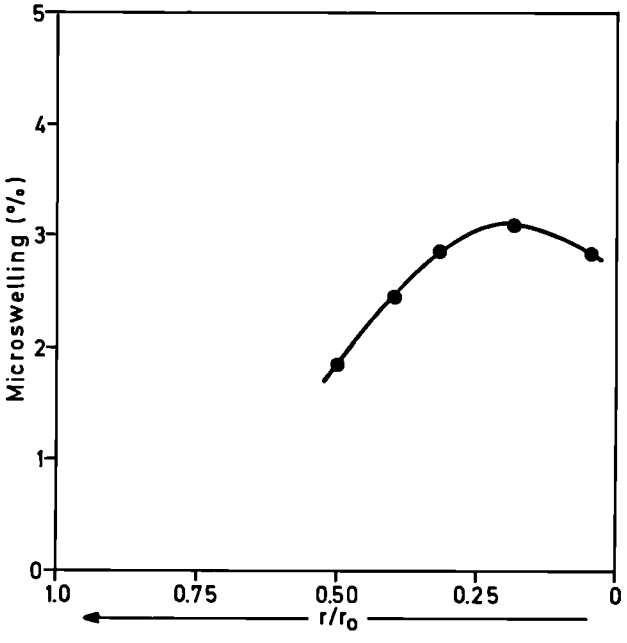

Fig. 2.11 Microswelling radial profile calculated from the replica analysis for the sample B3T1

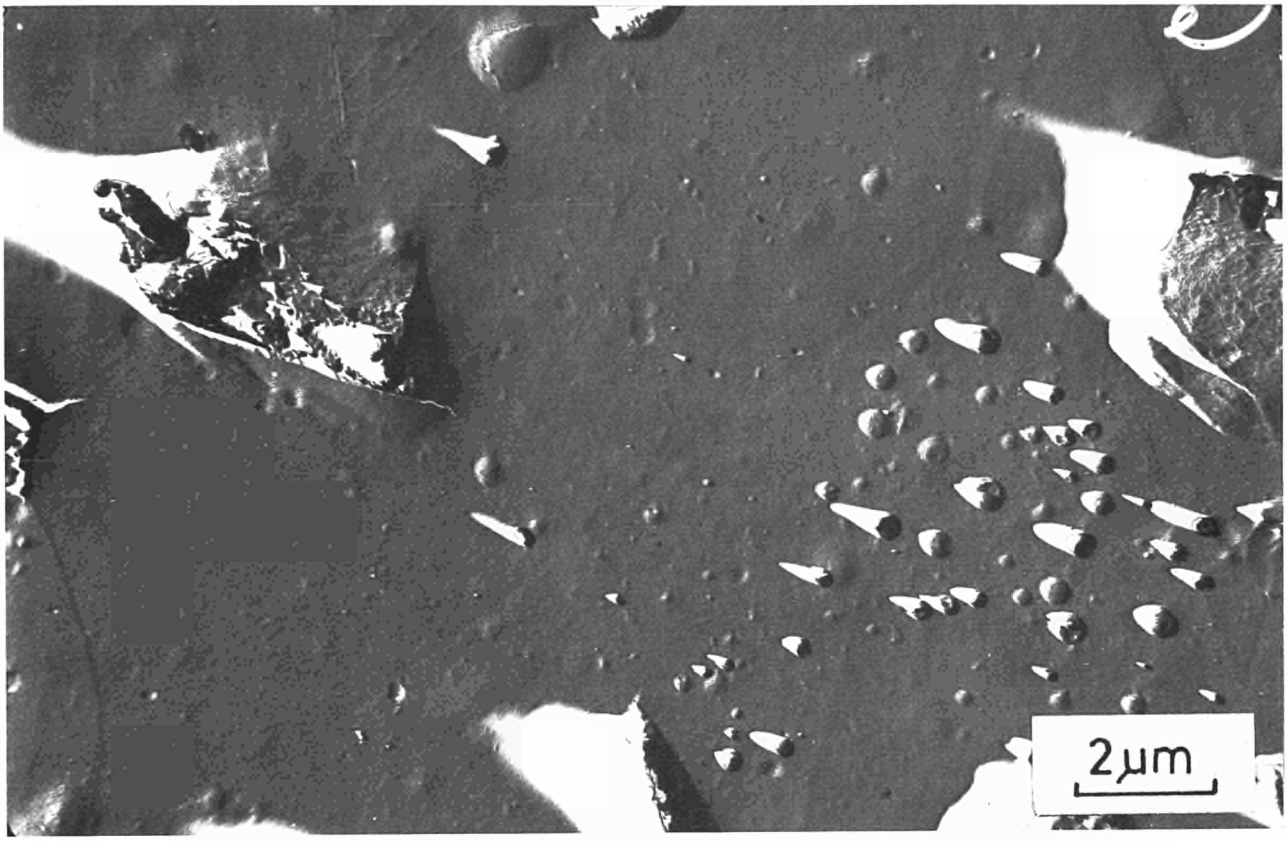

Fig. 2.8 *Replica micrograph of the B3T1 sample taken at the radial position R/Ro = 0.43*

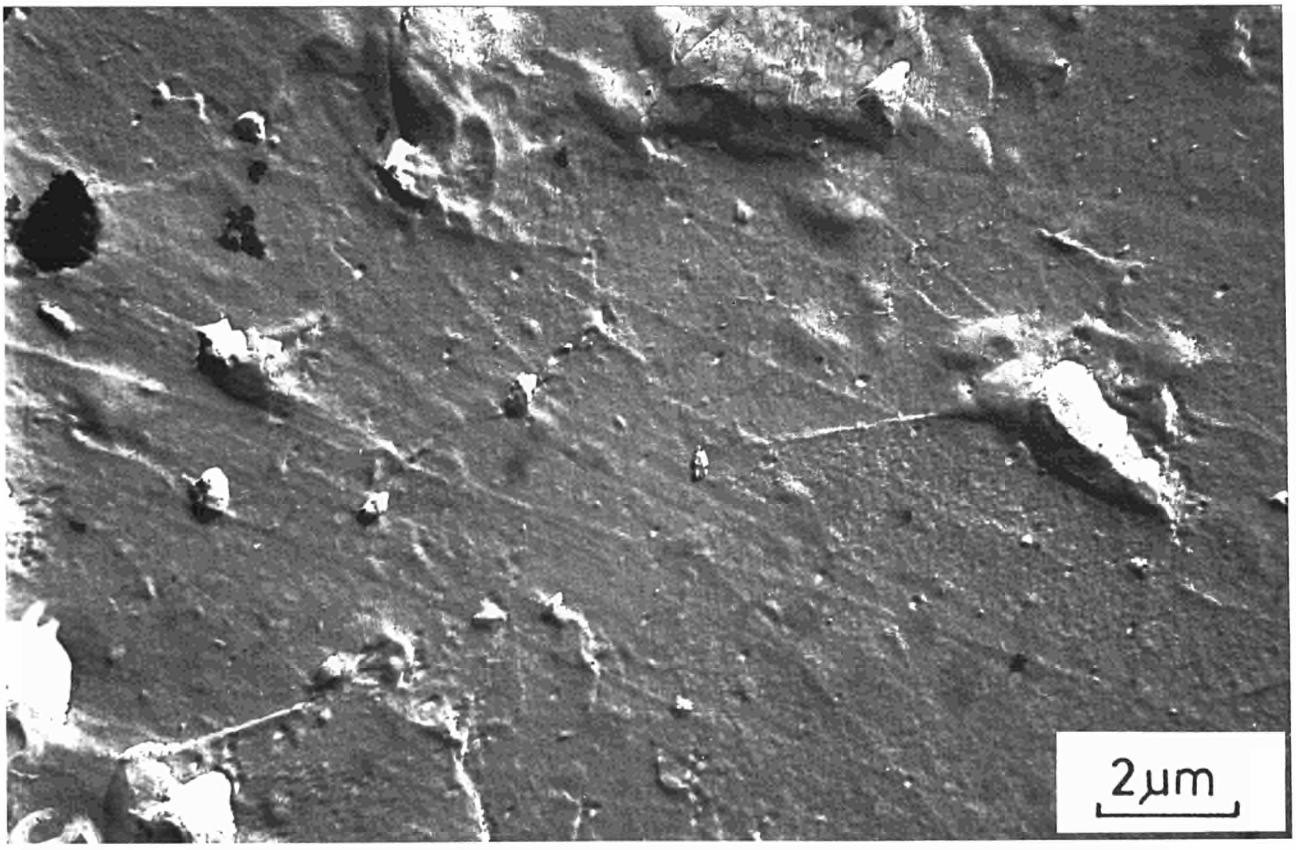

Fig. 2.9 *Replica micrograph of the B3T1 sample taken at the periphery, radial position R/Ro = 1*

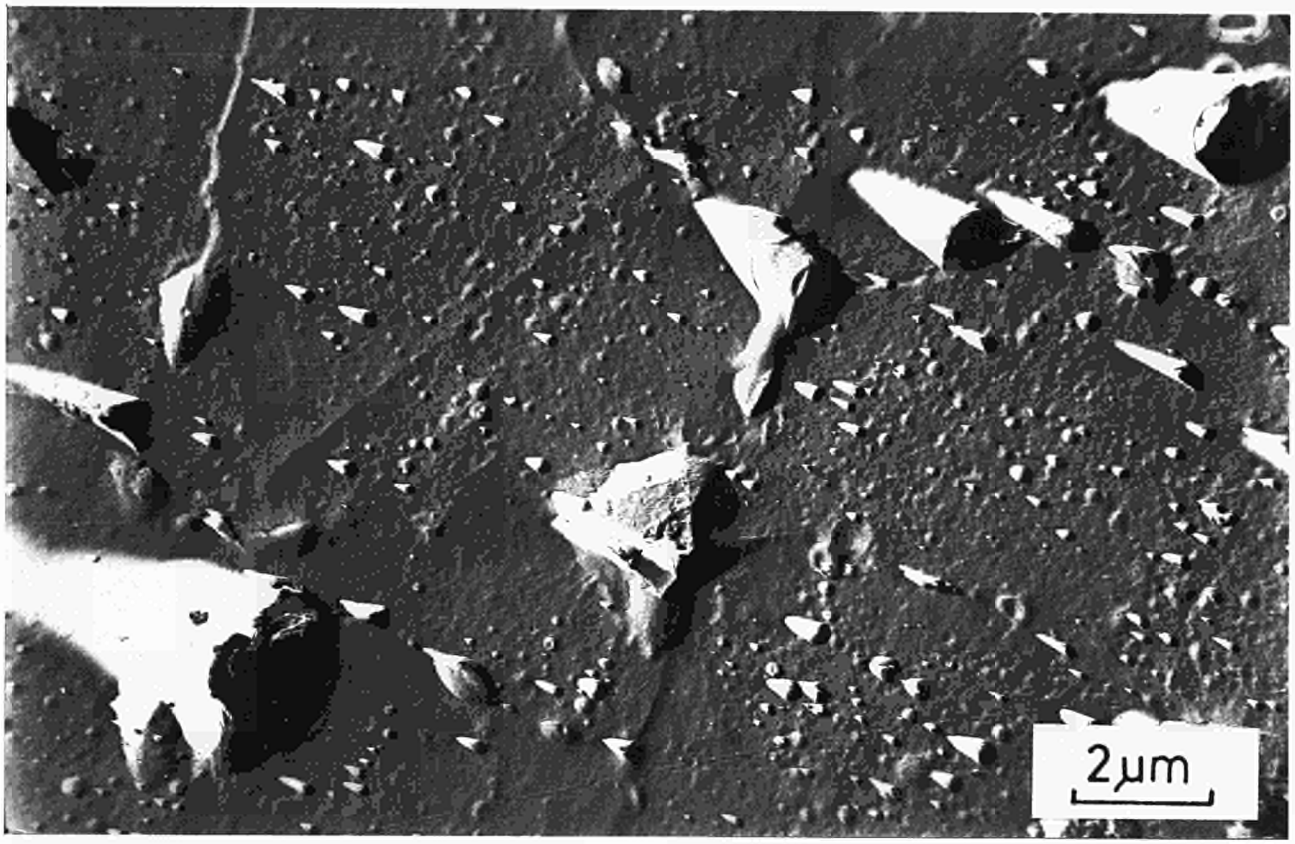

Fig. 2.10 *Replica micrograph of the B3T1 sample taken at the radial position R/Ro = 0.61, corresponding to the point of maximum swelling*

Table 2.6 *Replica analysis of B3T1*

	Feature	Radial Position R/R_0
1.	No bubble growth:	1.0 - 0.79
2.	Start of grain boundary decoration:	0.79
3.	Start of intragranular bubble growth:	0.78
4.	Strong development of both bubble populations:	0.75 - 0.46
5.	Microswelling maximum:	0.66
6.	Bubble populations disappear rapidly and become very inhomogeneous:	0.46 - 0.38
7.	No fission gas bubbles:	0.38 - Centr

section.Fig. 2.12 (a to c) shows for comparison the appropriate SEM micrographs from equivalent positions. It is interesting to note the strong agreement between the two types of image, but that the SEM micrographs also reveal a high density of solid fission-product precipitates associated with the bubbles. Though probably extracted by the replica these precipitates are subsequently lost in the decontamination process which is essential for the preparation and handling of the replicas. It is proposed to examine replicas which have not been decontaminated in the Hitachi TEM and to try to determine the composition of the precipitates using energy dispersive X-ray analysis.

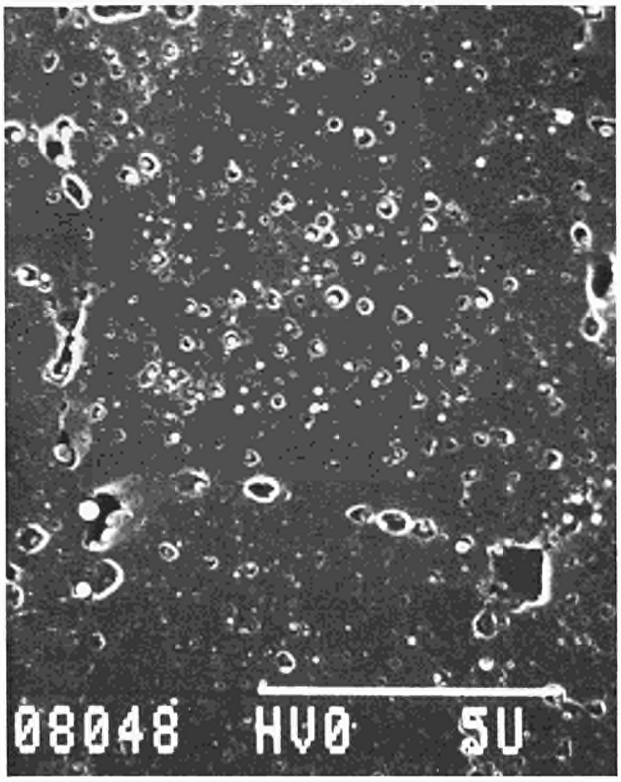

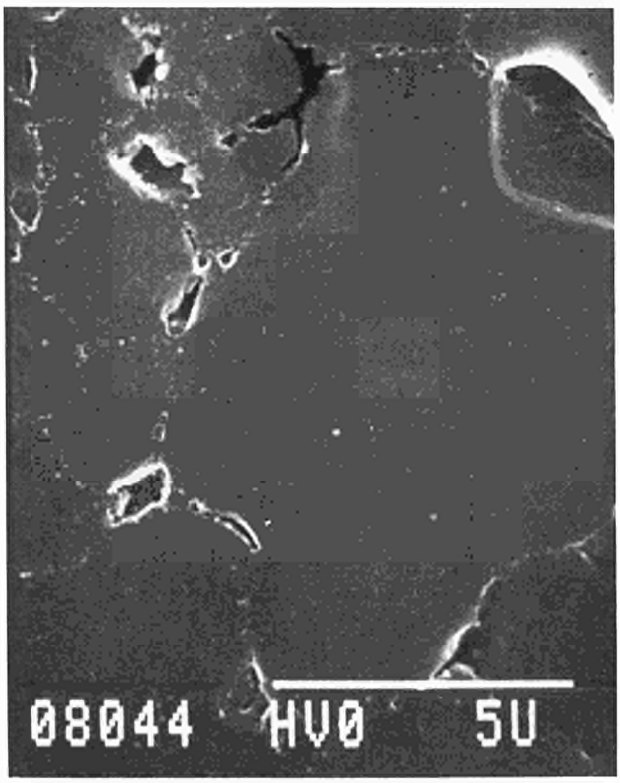

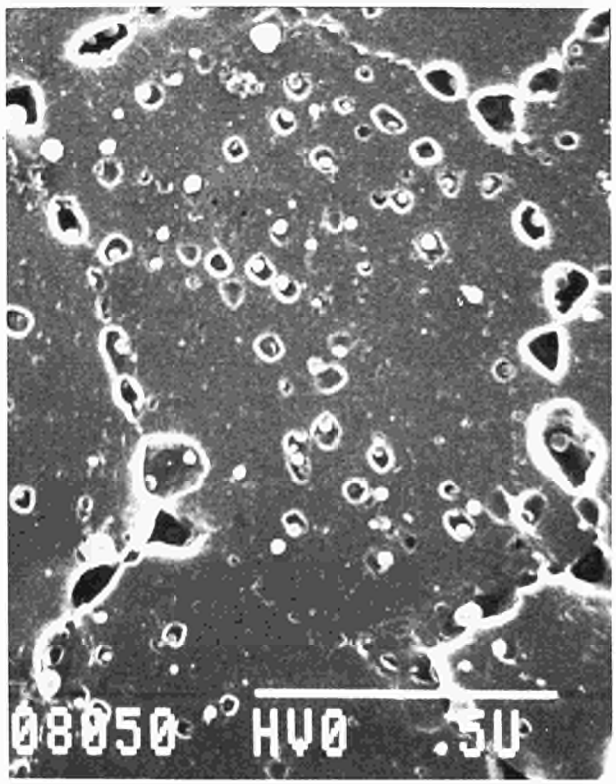

Fig. 2.12 *Scanning electron micrographs of the surface of the B3T1 sample, taken at the approximate positions (a) periphery, (b)R/Ro = 0.43 and (c) R/Ro = 0.61*

Results of the Transmission Electron Microscopy Analysis.

A specimen of the fuel was successfully prepared for transmission microscopy covering the range 0.4 to 1.1 mm from the periphery. Interestingly this sample showed two polishing holes parallel to the radius, allowing not only a radial study of the microstructure to be made but, also, a check of the consistency of the structure tangentially. It was confirmed that there was no significant difference in the structure observed at equivalent radial - but different circumferential - positions.

The microstructure over this radial range showed a high dislocation density and a high concentration of small precipitates and defect clusters. For $R/R_0 < 0.85$ a low density of very small fission gas bubbles (diameter < 5nm) was observed, usually in association with small precipitates of the same size range. All of these microstructural features showed an inhomogenous local distribution at any particular radial position; thus, for example, some subgrains showed a very high dislocation density while neighbouring subgrains were almost dislocation free despite careful diffraction contrast adjustments to maximise the dislocation visibility. Tab. 2.7 summarises the average values of dislocation density, precipitate density and fission-gas bubble density at chosen radial positions in the range $0.91 > R/R_0 > 0.76$ examined by TEM. The dislocation density remains almost constant over this radial range, while the precipitate density and bubble density increase.

It was not possible to prepare successfully a specimen of this fuel taken from the centre of the cross section for TEM.

Table 2.7 Summary of the TEM results on B3T1

R/R_0	Dislocation Density (cm^{-2})	Precipitate Density (cm^{-3})	Bubble Density (cm^{-3})
0.90	3.3×10^{10}	1.4×10^{16}	-
0.87	1.4×10^{10}	0.9×10^{16}	-
0.84	2.0×10^{10}	2.4×10^{16}	0.9×10^{16}
0.80	2.2×10^{10}	2.4×10^{16}	3.3×10^{16}

Fission Product Behaviour and Microkinetics

Diffusion and Precipitation of Fission Product Atoms in UO_2

Introduction

The technique of controlled ion implantation of interesting fission products into UO_2 and so-called SIMFUEL, i.e. UO_2 with added inactive fission products to simulate 3 % burn-up was further used to extend the data reported in TUAR 86, 58 ff. In the reporting period, UO_2-based SIMFUEL produced at AECL, Chalk River was used; the fabrication procedure was that successfully developed for ThO_2 based SIMFUEL (see previous report). The channeling technique with Rutherford backscattering of 2 MeV He-ions of the van de Graaff accelerator of the Institut für Nukleare Festkörperphysik, KfK, was employed to study radiation damage and lattice location of the implanted fission products. The study on the location of Te by channeling was reported in TUAR 86. In the present period, a transmission electron microscopy study of Te in UO_2 was made and the behavior of Cs was investigated in detail with channeling.

Channeling Study of Cs-Implanted UO_2

A number of <100> oriented UO_2 single crystals have been implanted with 40 keV Cs ions in a random direction in order to study the damage and impurity behavior. Fig. 2.13 shows the aligned and random spectra of a UO_2 single crystal implanted with Cs ions. The impurity

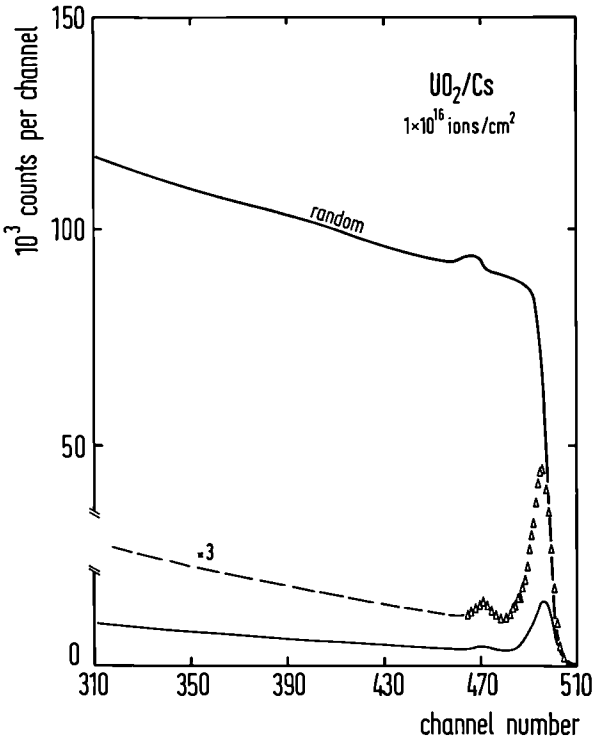

Fig. 2.13: Random and aligned Rutherford backscattering, RBS, spectra of a UO_2 single crystal implanted with Cs-ions

peak is clearly visible in both cases which makes it possible to estimate the amount of implanted Cs atoms. The total amount of Cs atoms as determined from the random spectrum (4×10^{15} at/cm^2) is significantly smaller than the preselected implantation dose: 1.0×10^{16} at/cm^2. This indicates that the sticking factor for Cs ions in UO_2 is much less than unity. In order to prove this hypothesis, an aluminium foil was implanted with Cs ions in the same time as the UO_2 sample. The ion beam was swept across both samples which thus were implanted with equal current density. Fig. 2.14 shows the backscattering spectra obtained for Al samples

implanted with Cs ions. The preselected doses were $2x10^{15}$ Cs/cm^2 (full line) and $1.0x10^{16}$ Cs/cm^2 (stars). The Cs peak is now well separated

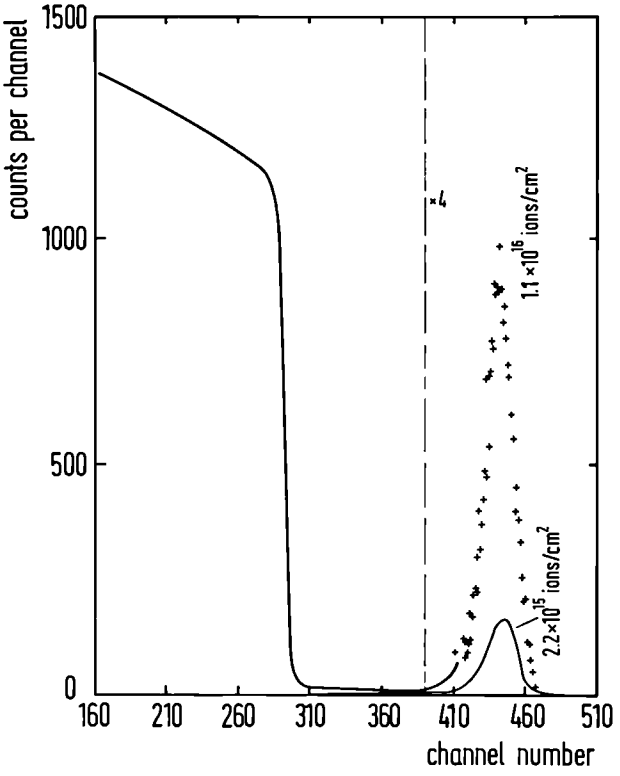

Fig. 2.14: RBS spectra of an Al-foil implanted with $2x10^{15}$ (full line) and $1x10^{16}$ Cs-ions/cm^2 (stars)

from the substrate portion of the spectrum, i.e. the low-mass Al. The number of implanted Cs ions can easily be determined and amounts to $2.2x10^{15}$ Cs/cm^2 and $1.1x10^{16}$ Cs/cm^2, respectively. These numbers are very close to the preselected Cs-ion fluences thus indicating that the deficiency in the accumulated Cs ions in UO_2 is apparently due to their small sticking factor. The number of retained Cs atoms was found to be almost independent of implantation dose. It ranged from 3.4 to $4.0x10^{15}$ at/cm^2 for implantation doses between $5x10^{15}$ to $5x10^{16}$ at/cm^2. A large fraction of Cs can thus be released during implantation, a phenomenon never observed for implantation of Te, Kr or Xe.

The comparison of the amounts of Cs ions determined from the aligned and random spectra (cf. Fig. 2.13) yields the substitutional fraction of the implants. It amounts to about 40%. This is a very surprising result because a substitutional fraction for the largely oversized Cs atoms would not be expected. Unfortunately, the channeling results obtained for one crystallographic direction only do not allow an unambiguous lattice site determination. The apparent substitutionality of Cs atoms may also be due to the formation of defect-impurity complexes in which a part of the Cs atoms is shadowed by the<100> atomic rows of the host crystal. To solve this problem, channeling measurements along other directions (<111> or <110>) are necessary. These are planned in future work.

The pronounced damage peak corresponds to about 1.7×10^{16} displaced U atoms/cm^{-2}. Thus the number of displaced atoms per incident ion (Displacement Efficiency) amounts to 4.3 which is very close to the values obtained previously for Te and Kr implantation. The analysis of two other samples implanted with a smaller dose, i.e. $3.5x10^{15}$ Cs-ions cm^{-2} reveals a somewhat higher displacement efficiency, i.e. 5.8. This is also in accordance with the previous results.

One notes that the numbers given above concern the accumulated atoms as determined from the random spectra. This leads to the conclusion that the impurity atoms which were released from the sample contributed to a much smaller extent to the damage creation than the retained ones. Such an effect can be due to the stabilization of radiation damage via stress fields due to the incorporation of oversized impurity atoms.

The evolution of aligned spectra for Cs implanted UO_2 upon thermal annealing is shown in Fig. 2.15 (plus signs - as implanted, 500 °C - dots, 800 °C - triangles, 1000 °C - circles, 1300 °C - reverse triangles). It can be seen that there is no change

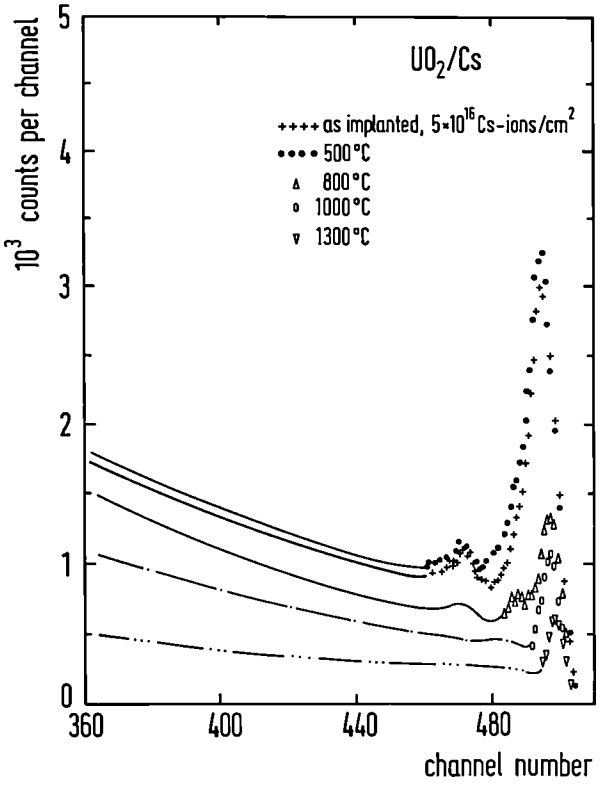

Fig. 2.15: RBS spectra of an aligned UO_2 single crystal implanted with Cs-ions following implantation and following annealing at 500, 800, 1000 and 1300 °C

in the spectra up to 500 °C. The χ_{min} begins to decrease after annealing at 800 °C. This decrease is accompanied with the release of 70% of the accumulated Cs. The impurity signal is no longer visible after annealing at higher temperatures. Annealing at 1300 °C leads to the complete restoration of the crystal structure - no residual damage can be detected. The annealing behavior of UO_2 single crystals implanted with different fluences of Cs ions is summarised in Fig. 2.16, where the fractional release of Cs atoms, F, and channeling minimum yield, χ_{min}, are plotted as a function of annealing temperature, T. Again, the release fractions are compatible with previous work using radioactive Cs[1] or Rb[2].

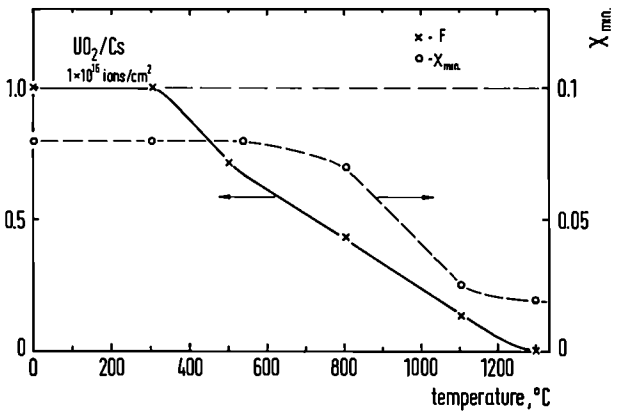

Fig. 2.16: Fractional release, F, and minimum aligned yield, χ_{min}, of UO_2 implanted with Cs

The channeling study has thus shown that significant amounts (up to 1 at.%) of Te and Cs can be located in substitutional sites or, for Cs, at least on <110> atomic ions, a fact so far not incorporated in any consideration of O/M-ratio development with burn-up. Also, for Cs, a surprising mobility and release during implantation at ambient temperature was seen. This, again, should be considered in considerations of the behavior of reactor irradiated UO_2.

References

[1] Hj. Matzke, J. Nucl. Mater. 23 (1967) 209

[2] Hj. Matzke, I.L.F. Ray and R.A. Verrall, Proc. Techn. Comm. Water Reactor Fuel Behavior and Fission Products Release in Off-Normal and Accident Conditions, IAEA, Vienna (1987) IWGFPT/27, p. 183

Transmission Electron Microscopy of Ion-Implanted UO_2

Introduction

Transmission Electron Microscopy (TEM) studies of UO_2 specimens ion- implanted with Rb and I and subjected to progressive annealing treatments were reported in TUAR 86. This work has been extended in the present reporting period by the examination of similar samples implanted with Te ions at 40kV. The specimens were prepared from prethinned (100) oriented UO_2 discs. Two samples were used for heat treatment and TEM analysis with total doses of 6×10^{15} and 2×10^{16} ions.cm^{-2}.

The specimens were observed as received, then following annealing treatments for one hour at 500, 700, 1100 and 1350°C in an argon-hydrogen atmosphere. The microscope used was the Hitachi H700 HST operating at 200kV. The projected in-situ annealing experiment using the microscope heating stage was unfortunately not possible following accidental damage to the apparatus.

Results

Both samples as-received showed an irresolvably high density of dislocation tangles and point defect clusters. Even at very high magnification (300000x) no bubbles could be seen indicating precipitation of Te. Fig. 2.17 shows an example of the microstructure of the high dose sample. Annealing at 500°C produced very little change in the microstructure.

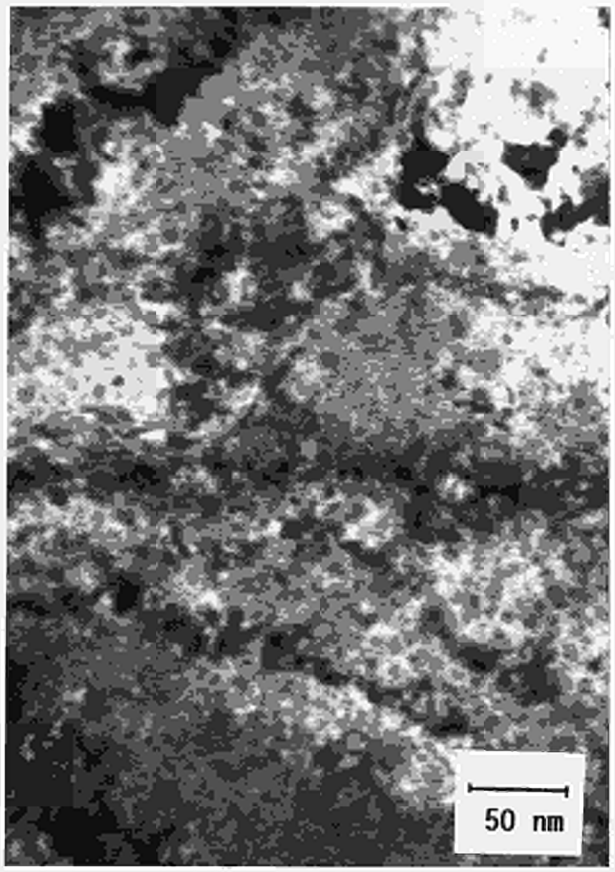

Fig. 2.17 *Transmission electron micrograph of a Te-implanted sample in the as-received state*

Annealing out of the dislocation tangles to form resolved networks was observed at 700°C in the high dose sample, and this was accompanied by the formation of a high density of very small bubbles. An example of this microstructure is shown in Fig. 2.18. A comparison with the low dose sample at this temperature was complicated by the formation of a dirt film on the sample surface which proved very resistant to cleaning.

The density of the small bubbles at this temperature was measured to be 2.5×10^{17} cm^{-3} with an average size of about 2.3nm.

At 1100°C the dislocation tangles had annealed out in both samples to give large scale networks,

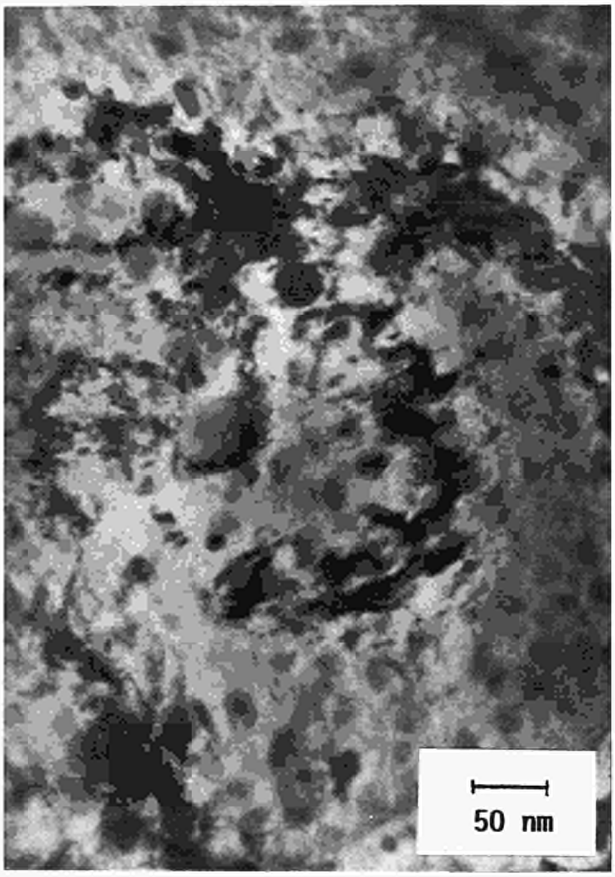

Fig. 2.18 *Transmission electron micrograph of a Te-implanted sample after annealing at 700°*

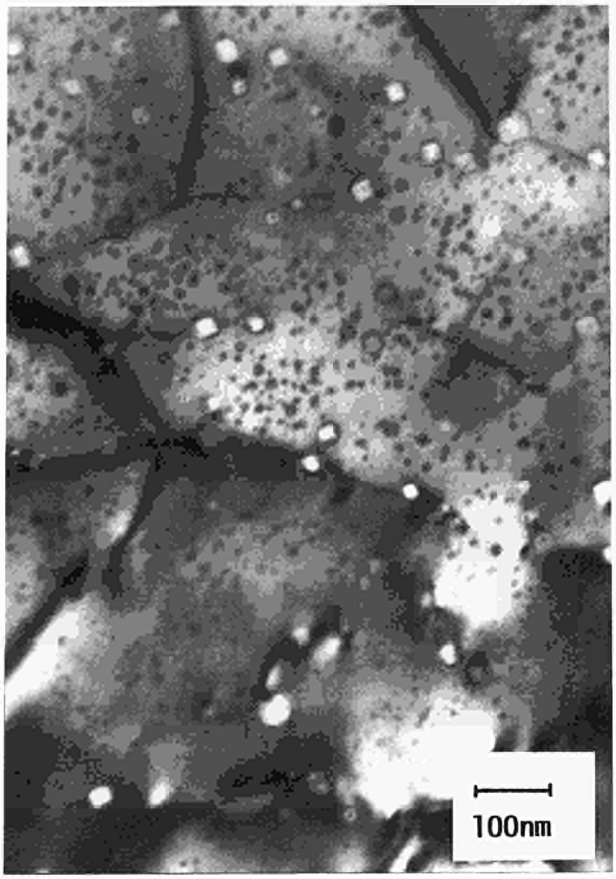

Fig. 2.19 *Transmission electron micrograph of a Te-implanted sample after annealing at 1100°*

a typical example for the low dose sample being shown in Fig. 2.19. At this temperature two distinct bubble populations develope - a population of large, often facetted bubbles on the dislocation networks and nodes, and a high density of small bubbles within the matrix. The measured parameters for these populations are given in Tab. 2.8, together with measurements of the dislocation density.

Both samples were further treated at 1350°C. At this temperature the dislocation networks had almost entirely disappeared. This is a surprising result, since the normal development on annealing is the formation of a stable Frank network which is constant with increased annealing temperature, and the result almost certainly reflects surface effects in the very thin areas examined. Two bubble populations remained in both samples, and an example of the microstructure is shown in Fig. 2.20 for the high dose sample. The measured bubble densities are given in Tab. 2.9.

Discussion

A preliminary comparison of the results presented here with those obtained on the Rb-irradiated samples in TUAR 86 reveals some interesting results. The starting material for both experiments was the same, and the development of the dislocation structure is

Tab. 2.8 *Analysis of Te-implanted and annealed UO_2*

High-Dose Sample: Temp.	Dislocation Density (cm^{-2})	Matrix Bubble Density (cm^{-3})	Disl. Bubble Density (cm^{-3})
700	-	2.5×10^{17}	-
1100	1.4×10^{10}	9.9×10^{16}	2.8×10^{15}
1350	*	1.7×10^{16}	*
Low-Dose Sample:			
1100	1.0×10^{10}	8.0×10^{15}	6.5×10^{14}
1350	1.0×10^{9}	1.7×10^{16}	2.4×10^{13}

(* Too low to be measured reliably, $< 10^9$ cm^{-2})

Table 2.9 *Input parameters and calculated properties of the trajectory of a fission fragment in UO_2*

Input parameters for fission product: E = 67 MeV, A = 137, Z = 56			
Input parameters for matrix:		U-lattice	O-lattice
atomic density (atoms/Å^3)		0.024	0.048
displacement energy, eV		50	20
heat capacity, W/g deg		0.34	
Properties of trajectory			
total range, µm		5.7	
projected range, µm		5.5	
transverse straggling parameter (dR_t), µm		0.84	
fraction of nuclear stopping, MeV		6	
number of displaced atoms,	U-lattice	16000 - 30000 *	
	O-lattice	46000 - 90000	

* The high values are for the theory of Brandt and Kitagana (7), the low ones for the LSS theory. The former theory gives also a larger range R = 8.1 µm and yields 11.1 MeV nuclear stopping. The results for U_4O_9 are very similar to those for UO_2.

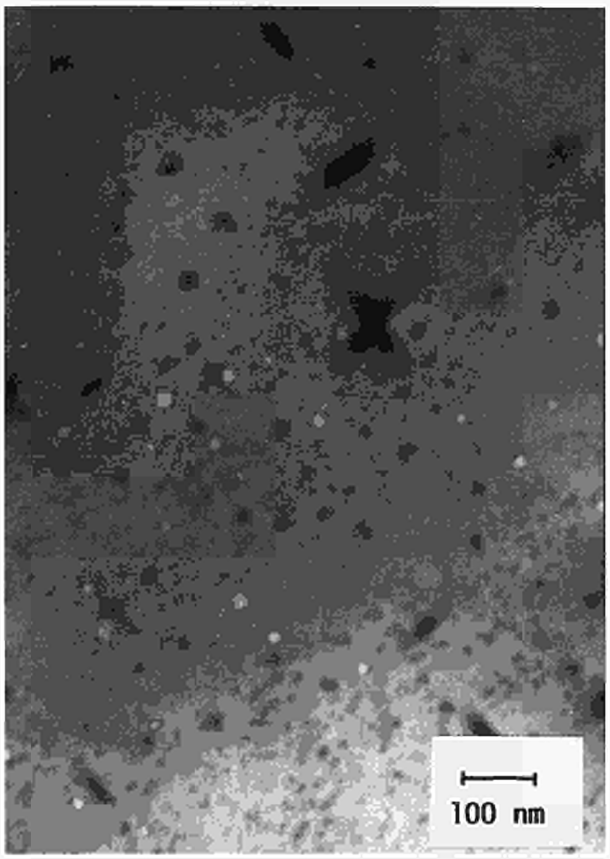

Fig. 2.20 *Transmission electron micrograph of a Te-implanted sample after annealing at 1350°*

similar in that dense irresolvable tangles were observed up to 700°C, followed by the development of a uniform dislocation structure up to 1100°C on which large bubbles are nucleated and grow. Above this temperature the dislocation density drops and sub-grain boundaries are observed with relatively defect-free sub-grains. This result is consistent with the channeling measurements on Te-implanted samples reported in TUAR 86, which show the recovery of most of the lattice defects at this temperature.

However, the bubble growth observed previously in the Rb implanted sample, with a dose of 5 x 10^{15} ions cm^{-2}, resembles more closely that observed here in the high dose Te implanted sample (dose = 2 x 10^{16} ions cm^{-2}). This can be seen, for example, in the almost identical results obtained for the densities of matrix bubbles and bubbles on dislocations observed at 1100°C. At these temperatures the bubbles were relatively homogeneously distributed and the measured figures can be taken to $\pm$ 25%. Thus this similarity of behaviour for a factor of 4 difference in dose must be a consequence of the higher lattice solubility and the fast release of Te. Both phenomena must contribute to this observation. Otherwise it would be difficult to explain that the dislocation density drops with temperature in the same way, since a high level of Te in solution in the matrix might be expected to stabilise the dislocation network.

Simulation Study of Grain Boundary Venting. Cooling Bursts (In cooperation with P. Bailey and S.E. Donnelly, Univ. Salford, U.K.)

Sintered UO_2 was annealed at high pressure (1500°C, 1000 bar) in an argon atmosphere. This hot pressing procedure leads to closure of open pores which are filled with Ar at the experimental pressure of 1000 bar. The UO_2 was subsequently annealed in a UHV mass-spectrometer with different heating rates and terminal temperatures up to 2500 K. Gas bursts were observed during heating and during cooling. The total amount of gas released corresponded to 7.9 x 10^{19} Ar-atoms/cm^3 UO_2, or 1.3 x 10^{-4} mole (NPT), or a volume of 3 x 10^{-3} cm^3 at 1000 bar. The gas was released in a large number of individual bursts. On heating, these occurred between 900 and 1500 K at a heating rate of 3000/s and comprised between 1.8 x 10^{12}

and 8 x 10^{13} atoms per burst. The corresponding volume of gas is in the range of 10 to 350 μm^3. Therefore, one to a few pores are vented per burst. More gas was, however, released on cooling. Cooling bursts were observed in the temperature range of 800 and 1500 K. Most cooling bursts occurred between 1000 and 1100 K, and none above 1500 K. Fig. 2.21 shows the release rate (not to scale) for two heating and one cooling rates, indicating how the bursts could be

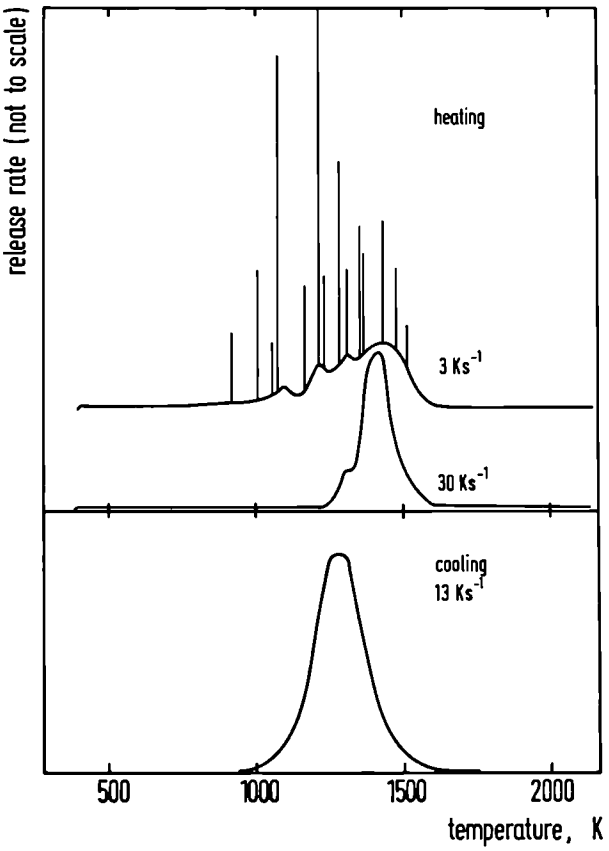

Fig. 2.21 Argon release spectra from UO_2 for two heating and one cooling rate

resolved as individual events at low rates of temperature changes.

Cooling bursts are known to occur in operating fuel and are explained as cracks venting grain boundary bubbles. The present results indicate, for the first time, the temperature range of cooling bursts, and they show that individual venting events occur in a rather narrow temperature range at rather low temperatures.

Oxygen Potential of High Burn-up Mixed Oxide Fuel (U, Pu)O_2.

The relationship between oxygen potential, $\Delta G(O_2)$, temperature T and composition (or O/M-ratio) for unirradiated $UO_{2\pm x}$ for water reactors and $(U,Pu)O_{2\pm x}$ for fast breeder reactors is rather well established. Much less work has been done on irradiated fuel or fuel with chemically simulated burn-up (SIMFUEL), and the available results are not consistent. Previous results on both slowly cooled and quenched (U, Pu)O_2-pins [1,2] with burn-ups up to 5.4 at. % showed pronounced increases in $\Delta G(O_2)$ with burn-up and confirmed the oxidative nature of fission, in particular that of Pu-239. These results were obtained with a miniature solid state galvanic cell developed at TU about 10 years ago. The results obtained are contained in the progress reports of 1977 to 1980.

Due to the increased burn-ups achieved more recently in LWR's and LMFBR's, there is a revival in the interest in the development of $\Delta G(O_2)$ with burn-up in oxide fuels; this is due to rather unexpected effects obtained in fuel chemistry and fission-product behaviour at higher burn-up in LWR fuel and because exact data are needed to understand and model fuel compatibility with clad and with Na for LMFBR fuel.

The miniature emf-cell was therefore re-activated. It was shown to still work reliably in test measurements with unirradiated (U,

$Pu)O_{2-x}$. Subsequently, a set of measurements was performed on fuel specimens from pins irradiated in the PHENIX reactor. These had Pu/(U+Pu) ratios between 0.194 and 0.206, initial O/M-ratios of about 1.98 (range 1.979 to 1.983) and 3 largely different burn-ups of 3.8, 7.0 and 11.2 at %. The U was natural uranium, and the fuel had been cooled slowly. The radial oxygen profiles known to exist during irradiation will therefore have been levelled out and are not expected to exist in the fuel pins after cooling. Fig. 2.22 shows the results. Excellent reproducibility without hysteresis is seen, except for one pin with the highest burn-up of 11.2 at. % where radiation damage affected the performance of the Y_2O_3-doped ThO_2 crucible used as solid state electrolyte in the emf-cell. A linear increase of $\Delta G(O_2)$ with burn-up is obvious.

Since radial oxygen profiles are not expected to exist, the results show the effective combination of

i) the oxidative nature of Pu-fission increasing both O/M-ratio and $\Delta G(O_2)$
ii) the effect of dissolved fission products (f.p.), such as the rare earths, increasing $\Delta G(O_2)$ even at constant O/M-ratio
iii) the buffering action of the stainless steel clad

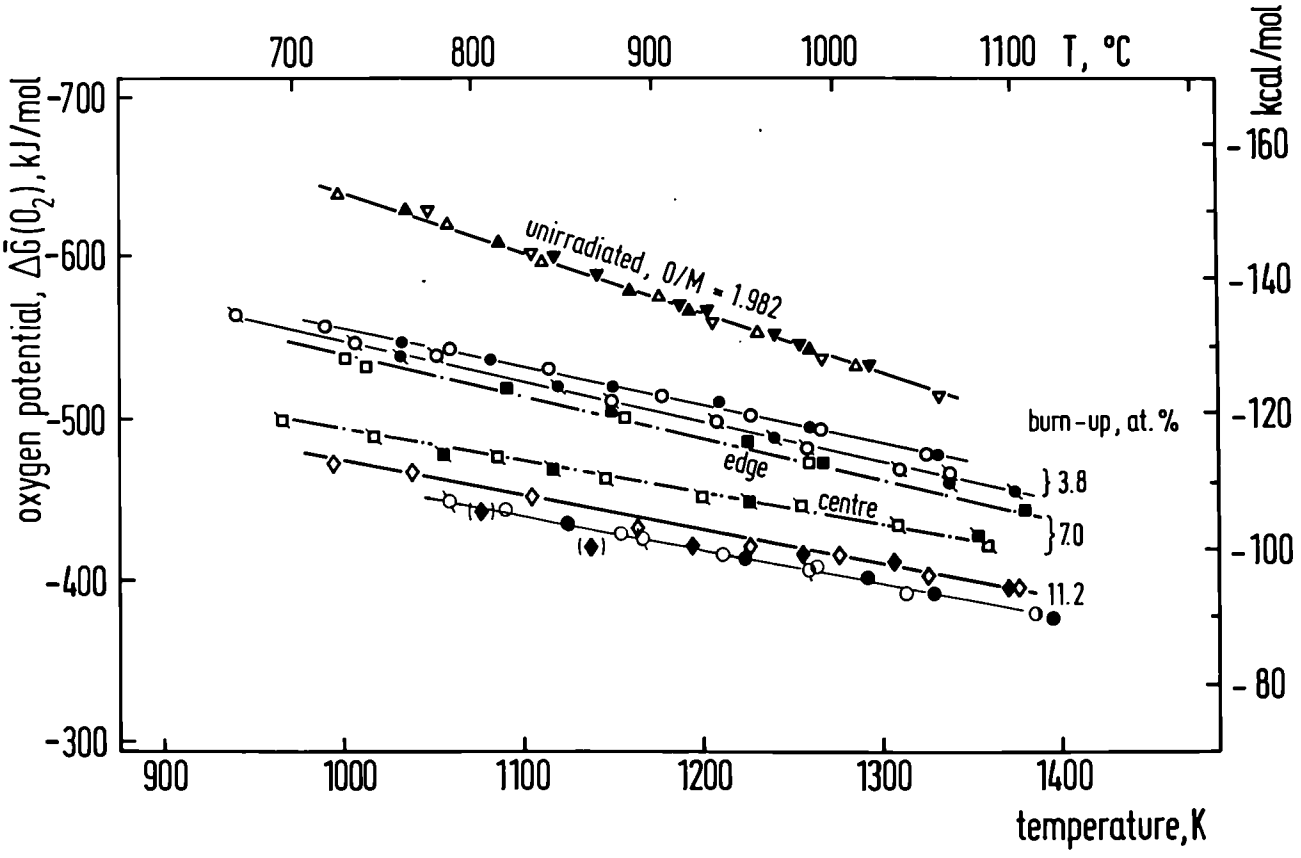

Fig. 2.22 : Oxygen potential measurements with the miniature emf-cell developed at TU on irradiated PHENIX fuel of initial composition $(U_{0.8}Pu_{0.2})O_{1.98}$

Fig. 2.23 shows the present results compared with the most recent published predictions of changes in O/M-ratio [3] and the work on $\Delta G(O_2)$ on simulated fuel by Woodley [4] and previously performed at the Institute [5].Though the *trend* of all results is identical, the increase of $\Delta G(O_2)$ with burn-up in the real PHENIX fuel is faster than that of the chemically simulated burn-up fuel containing some 5 fission products only.

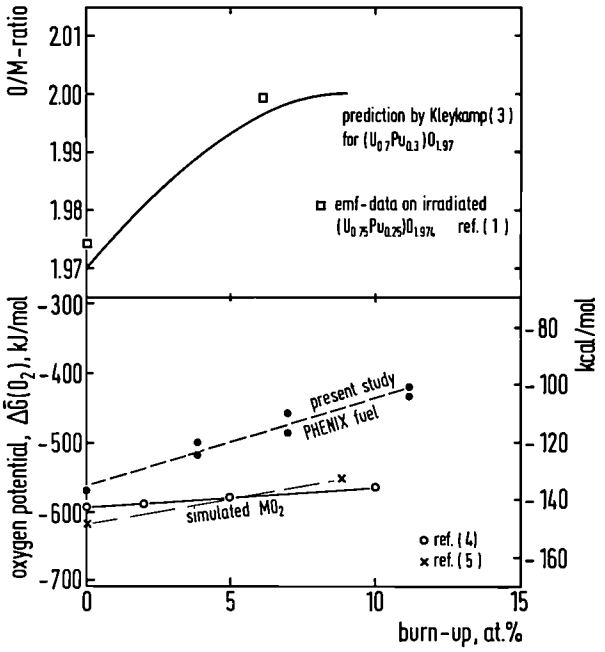

Fig. 2.23 : Development of $\Delta G(O_2)$ with burn-up at constant temperatures, compared with published predictions of changes in O/M-ratio due to the oxidative nature of fission and with previous measurements on simulated burn-up oxides.

Lattice parameter measurements performed at CEA Cadarache [6] on the PHENIX fuel indicate a constant O/M-ratio of 1.985 ± 0.005. If this result is accepted, the present data indicate that the effect of *all* f.p.'s in increasing $\Delta G(O2)$ at constant O/M is larger than that of the few f.p. added to the simulated fuel.

A last point needs discussion: for 7.0 at. % b.u., a fuel piece from the edge showed a higher $\Delta G(O_2)$ than another piece from the centre. This is opposite to the trend expected and found for in-pile oxygen gradients where the lowest $\Delta G(O_2)$-values exist in the centre. However, the result is compatible with the larger-than-expected increase in $\Delta G(O_2)$ due to the total concentration of f.p. A larger amount of f.p.'s is dissolved in the fuel centre compared to the edge, due to the higher operating temperatures in the centre. At the lower operating temperatures of the fuel surface, the f.p.'s have smaller diffusion rates and are less likely to form the compounds or precipitates they form in equilibrium. They are therefore expected to take up a larger share of oxygen than would be expected by equilibrium. An exact prediction of f.p. chemical behaviour needs inclusion of both rate equations and chemical equilibria of a large variety of possible f.p. and f.p.-MO_2-compounds into a fuel performance code like the MITRA-code. This may be done in the future. Other reasons for different $\Delta G(O_2)$-values along the radius of slowly cooled fuels are radial Pu-migration and radial f.p. migration and segregation during irradiation.

Summary

The oxygen potential of PHENIX mixed oxide fuel $(U_{0.8}\ Pu_{0.2})O_{1.98}$ was shown to increase linearly with burn-up up to 11 at % b.u.; the total increase being about 160 kJ/mol at 1100 K. This important increase is largely due to the combined effect of all fission products increasing $\Delta G(O_2)$. It must be considered in studies of fuel compatibility with clad and Na in case of clad failure at high burn-up. More measurements are

planned with PHENIX fuel and also with the SIMFUEL described elsewhere in this report.

References

[1] F.T. Ewart, C.M. Mari, S. Fourcaudot, Hj. Matzke, L. Manes and F. Toci, in "Thermodynamics of Nuclear Materials 1979", IAEA, Vienna I (1980)369

[2] F.T. Ewart, K. Lassmann, Hj. Matzke, L. Manes and A. Saunders, J. Nucl. Mater. 124 (1984)44

[3] H. Kleykamp, J. Nucl. Mater. 66 (1977)292

[4] R.E. Woodley, J. Nucl. Mater. 74 (1978)290

[5] Hj. Matzke and S. Fourcaudot, TUSR 30 (1980)31

[6] M. Trotabas, internal report CEA Cadarache

A Monte-Carlo Simulation Study of Fission Damage (In cooperation with A. Mazzone, LAMEL, Bologna)

The effects of the stopping of fission fragments in UO_2 have been studied at the Institute for a long time [1-4]. Important phenomena such as fission gas re-solution, radiation enhanced diffusion and creep are due to the energy deposition in the UO_2 lattice during the slowing down of the fission fragments. To achieve a better understanding of the underlying phenomena, a simplified version of the Monte Carlo method used before successfully to study ion implantation and thermal spike damage in semiconductors [5, 6] was developed. The cascade region was examined on a fine scale to define the location of zones of high and low deposited energy density. The fission fragments were assumed to originate a few nm below the surface and to penetrate in a direction normal to the surface. Both primary and secondary (recoil) particles were followed until the energy fell below the threshold energy, E_d, for displacements. Both elastic (nuclear stopping) and inelastic (electronic stopping) processes were calculated. For most calculations, the standard LSS theory was used. The case of a medium heavy fission fragment (67 MeV, A = 137, Z = 56) and UO_2 and U_4O_9 as matrices were used. E_d was assumed to be 50 eV for U and 20 eV for O defects.

As first results, the total and projected range, range straggling, number of displaced (secondary) atoms etc. were calculated, and are summarised in Tab. 2.9.

The evaluating of the connection between collisional and post-collisional phases, i.e. lattice relaxation, is a field open to speculation and controveries. The phenomena occurring during lattice relaxation are determined by the density of deposited energy. The transverse oscillations of the trajectory will play an important role in this post-collisional phase. The point is best illustrated in Fig. 2.24 showing the spatial distribution of electronic (a) and nuclear (b) energy losses in x/y planes at distances of 0.5 μm. The rectangles represent elementary volumes of 0.2x0.2x0.5 μm^3. It is obvious that the f.p. acquires transverse momentum in nuclear collisions. Similar results were obtained for atomic displacements. A rather crude approximation based on the model of a free electron gas suggests that the observed track is formed in two parts. The initial part is characterised by a high electron excitation in closely connected volumes, and, with reasonable assumptions

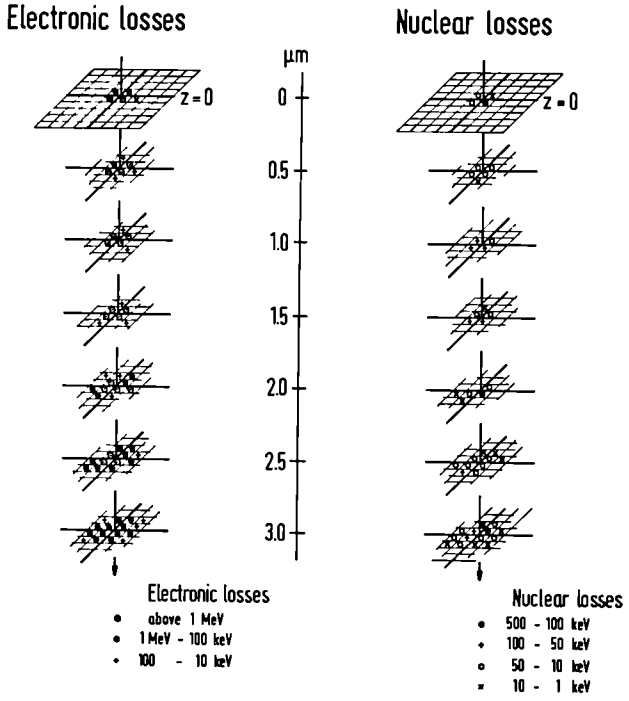

Fig. 2.24: Calculated stopping of a median heavy fission product in UO_2 a) electronic losses b) nuclear losses

(uniform sharing of energy in the elementary volumes, free electron gas etc.), temperature increases of 1500 ± 500 due to electron-lattice collisions are obtained, in agreement with previous results [1, 2]. At larger depths (≥ 2 to 3 µm), effective ionisation is less plausible; the projectile acquires transverse momentum; the primary energy is more widely distributed within the lattice leading to a reduced increase in lattice temperature. Note, however, that processes connected with ion mixing are still important in this region.

These first attempts to apply Monte Carlo techniques to better understand the stopping of fission fragments in UO_2 are promising and are planned to be continued with calculations of the light medium fission fragments.

References

[1] H. Blank, Phys. Stat. Sol. a10 (1972) 465

[2] H. Blank and Hj. Matzke, Radiation Effects 17 (1973)57

[3] C.Ronchi, J. Appl. Phys. 44 (1973)3575

[4] Hj. Matzke, Radiation Effects 64 (1982)3

[5] A.M. Mazzone, Radiation Effect Letters 87 (1985)91

[6] A.M. Mazzone, Appl. Phys. A 42 (1987) 193

[7] W. Brandt and M. Kitagawa, Phys. Rev. 1325 (1982) 5631

Modelling

TRANSURANUS Sytem Development Application

The general concept of the TRANSURANUS code has been described in the report TUAR 86. Furthermore, an extensive documentation of all basic aspects of the code including the most important details will be published in February 1988 [1]. Consequently, no general introduction of the TRANSURANUS code is given and this report is limited to the work actually performed in 1987.

TRANSURANUS System Maintenance and Improvements

The TRANSURANUS system is continually being improved (reliability of numerics, structure of code components, incorporation of new models and numerical techniques). All changes are continuously documented in the "TRANS-

URANUS-Änderungsprotokoll" [2]. Basically, improvements were made in the following areas:

1. general revision of the LWR stress-corrosion cracking model SPAKOR,
2. general revision of the Fast Breeder Reactor version (densification models, pore migration, formation and closure of the central void and incorporation of a Pu-redistribution model),
3. incorporation of an interface to couple the TRANSURANUS code with the in-pin motion model URADYN (in connection with the European Accident Code EAC).

This new version is still being tested with approximately 50 very different test data cases (FBR and LWR conditions) using the special test compiler WATFIV. The new version will be released to the different users (KfK, JRC Ispra, TÜV-Bayern, TÜV-Baden, TÜV-Norddeutschland, JEN-Spain) by the end of spring 1988.

General Revision of the LWR Stress-Corrosion Cracking Model SPAKOR

The stress-corrosion cracking (SCC) model SPAKOR incorporated in the TRANSURANUS code is basically that of Mattas, Yaggee and Neimark [3]. The model is based on the observation that iodine SCC failures usually begin as an intergranular fracture which becomes a "cleavage and fluting" fracture at some point in crack growth. It is assumed in the model that the intergranular portion of the failure is due to chemical attack which is independent of applied stress, while the cleavage and fluting portion of the failure can be described by linear elastic fracture mechanics. The time to failure, t_f, in an SCC test can thus be divided into the time t_{ch} required to chemically grow an intergranular crack and the time t_{cf} required to propagate the crack to failure by cleavage and fluting:

$$t_f = t_{ch} + t_{cf} \qquad (1)$$

The chemical crack-growth rate da/dt is assumed to have an initial value A_o, and to decrease exponentially as the crack depth increases:

$$da/dt = A_o \exp(-a/B) \qquad (2)$$

where a is the crack depth and B is a rate constant. Eq.(2) can easily be integrated and put into an incremental form:

$$a(t) = B \ln \{ A_o/B \, \Delta t + exp[a(t-\Delta t)/B] \}. \qquad (2a)$$

Chemical crack growth is assumed to continue until a critical stress intensity for cleavage and fluting, K_{ISCC}, is reached. At this point, cleavage and fluting fracture initiates and continues to failure:

$$da/dt = 1/C \, K^4 \qquad (3)$$

where K is the stress intensity factor ($K^2 = \sigma^2 y^2 a$), C is a constant, y is a geometric factor and

σ is the applied hoop stress. Eq.(3) can also be cast in incremental form to give

$$a(t) = \{ a(t-\Delta t)\, C \} / \{ C - a(t-\Delta t)\, \sigma^4 y^4 \Delta t \} \qquad (3a)$$

For steady state conditions the times t_{ch} and t_{cf} can be obtained in closed form from eqs. (2a) and (3a).

Chemical crack growth is assumed to initiate if the following conditions are satisfied:

1. the burn-up must exceed a critical value (5000 MWd/tU),
2. the cladding temperature must exceed a critical value (270°C),
3. the strain rate in the cladding must exceed a critical value which is temperature dependent,
4. the hoop stress must be positive.

Once a crack has been initiated, the eqs. given above apply, i.e. new formation of an protective layer is not considered.

The SPAKOR model evaluates the incremental formulation Eqs.(2a) and (3a) as well as a global cumulative damage concept where the cumulative damage fraction D is given by

$$D(t) = \Sigma\, \Delta t_i / t_f \,. \qquad (4)$$

In eq.(4) t_f is the time to failure under the conditions in time step Δt_i.

Zircaloy properties (yield strength σ_{ys} and rupture strength σ_{fs}) are needed to be known precisely in order to apply the model correctly. At present the approximate values

$$\begin{aligned} \sigma_{ys} &= 560 \text{ MPa and} \\ \sigma_{fs} &= 690 \text{ MPa} \end{aligned} \qquad (5)$$

are used.

SPAKOR has been extensively tested by randomly generated test cases. Under steady state conditions it was proved that the time to failure calculated by the incremental formulations (2a) and (3a) and the closed form solution were in agreement, i.e. that the cumulative damage fraction $D(t=t_f) = 1$.

General Revision of the FBR Version

The Fast Breeder Reactor version was generally revised and improved. However, the validation will not be completed before 1988 and consequently the planned detailed validation report [4] cannot be published before the end of 1988. The most important changes were made in the area of the general material conservation equations. In the following the new, consistent scheme valid for all processes is given.

General Material Conservation Equation

The basic equation of material conservation written in vector notation is

$$\frac{\partial c}{\partial t} = - \nabla \cdot J + Q \qquad (6)$$

where

c = concentration of species (atoms per unit volume)
∇c = spatial gradient of the concentration
J = vector flux of the species (atoms per unit area and unit time)
Q = net rate of atoms created (atoms per unit volume and unit time)

Eq. (6) is independent of the physical phenomena that produce the flux J. Since in the present model only radial transport in cylindrical geometry is considered eq. (6) can be simplified:

$$\frac{\partial c}{\partial t} = \frac{1}{r} \frac{\partial}{\partial r} (rJ) \qquad (7)$$

where J is the flux in radial direction.

Eq.(7) is solved by a finite difference technique. The fuel is divided into m radial zones which need not to be equidistant. In the following, a superscript (i) indicates a radial zone whereas a subscript indicates the value at the node r_i. For each zone the balance equation is written in a conservative form:

$$c^{(i)} = - \frac{2(r_{i+1} J_{i+1} - r_i J_i)}{r_{i+1}^2 - r_i^2}, \quad i = 1, m \qquad (8)$$

where $c = \partial c / \partial t$

For the processes considered here, it is assumed that the fuel is a closed system with the boundary conditions

$$J_1 = J_{m+1} = 0 \qquad (9)$$

which can easily be incorporated into eq.(8). Eq.(8) is the general scheme applied to pore migration and Pu redistribution.

Plutonium Redistribution

Plutonium redistribution in nuclear fuel is important as it can change the thermal conductivity of the fuel significantly. The main mechanisms of the Pu transport are

1. solid-state transport by thermal diffusion

2. vapor transport by pores and cracks.

Both processes have different time constants. Compared with the redistribution through vapor transport thermal diffusion is a long term process which produces a continuously growing redistribution effect. After longer periods of irradiation this effect becomes dominant.

Therefore, the model of Bober et al. [5] has been incorporated into the TRANSURANUS code. Special emphasis was given to the numerical treatment. Explicit and implicit treatments were compared and showed perfect agreement. However, since the explicit solution did not result in significant reductions of the computational costs but suffered from timestep limitations due to stability problems, only the fully implicit treatment was incorporated into the TRANSURANUS code.

The numerical algorithm was tested against an analytical, asymptotic solution given by Clement [6] which is valid as long as the change from the initially constant Pu concentration is relatively small. However, since the Pu diffusion constant decreases rapidly with r, this solution is an excellent approximation in the cold parts of the fuel.Thus, deviations between the analytic and the numerical solutions will be seen first at the inner parts of the fuel. The general tendency will be that the asymtotic solution overestimates the plutonium redistribution the larger the time step is. Comparisons between numerical and the analytical solutions are shown in Fig. 2.25 for two different time steps. An excellent agreement can be stated. By way of example plutonium redistribution in a reference FBR rod is given in Fig. 2.26

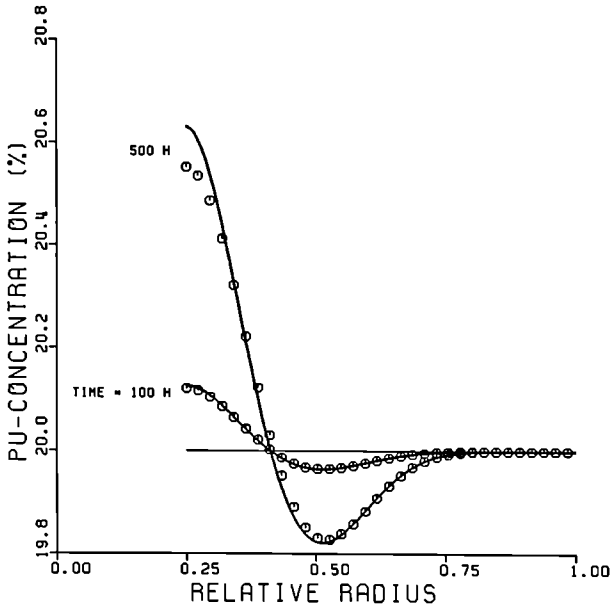

Fig 2.25: Comparison between the analytic, asympotic solution of Clement [6] (solid line) and the numerical solution (open circles): inner and outer fuel radii 0.75 and 3 mm; centre temperature 2550 K, fuel surface temperature 1100 K, initial plutonium concentration 0.2

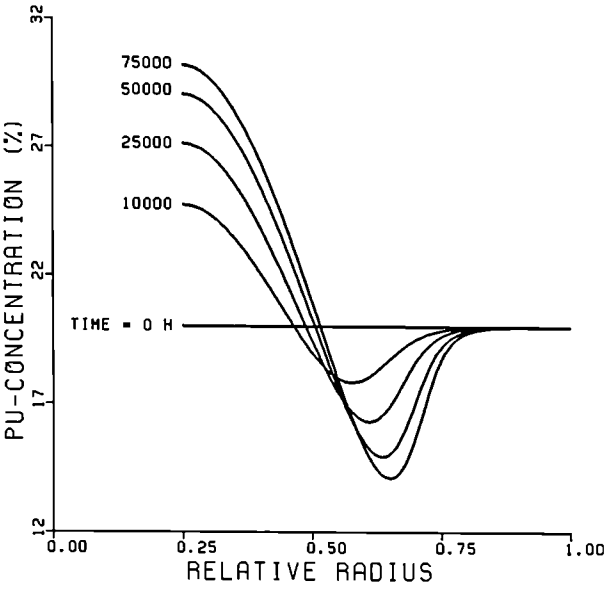

Fig. 2.26: Radial plutonium distribution at different times: the fuel data are the same as in Fig. 2.25

It has to be stressed again that the algorithm chosen can easily be extended to include Pu migration due to pores and cracks. However, the present version should already give the correct Pu redistribution for medium and high burn-up fuel which is of importance in accident analyses.

Pore Migration

The general pore conservation eq. is given by

$$\frac{\partial P}{\partial t} = \frac{1}{r}\frac{\partial}{\partial r}(rJ) \qquad (10)$$

where

$J = v_p P$
v_p = pore velocity
P = porocity

which can easily be solved utilizing the general scheme (8). Pores migrate in a temperature gradient due to an evaporation-condensation

mechanism which can be described by

$$v_p = a\ T^{-5/2}\ \nabla T\ e^{-(Q/RT)} \qquad (11)$$

The discretization of the flux equation by a fully implicit formulation is trivial and leads to a bidiagonal system of equations.

As in the case of the Pu redistribution due to thermodiffusion, the numerical algorithm to calculate the pore migration was tested against an analytical asymtotic solution given by Clement. This asymptotic solution is valid as long as the change from the initially constant pore distribution is relatively small. The comparison between numerical and analytical solutions is shown in Fig. 2.27. An excellent agreement is found.

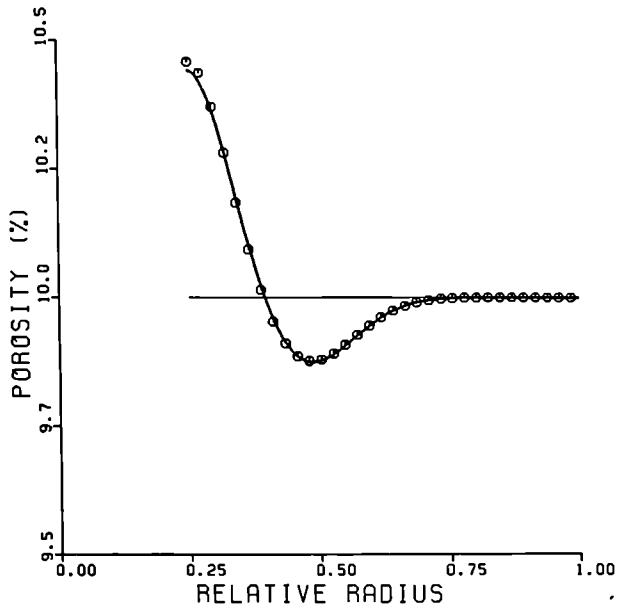

Fig. 2.27: Comparison between the analytic, asympotic solution of Clement [6] (solid line) and the numerical solution (open circles): the fuel data are the same as in Fig. 2.25, time = 360 s

Assessment of the Axial Friction Force Model URFRIC

The mechanical pellet-cladding interaction (PCI) has been the subject of many investigations. Of prime importance is the prediction of the cladding deformation or cladding failure if the loading of the cladding exceeds a certain threshold or if the cladding has been weakened by corrosion or other processes. Another area of importance is the prediction of fuel expansion during a Fast Breeder Reactor accident. Here the fuel expansion is affected by the complicated interaction with the cladding and provides an important negative reactivity feedback mechanism which determines the severity of the accident.

Within this context an important aspect of PCI, namely the calculation of axial friction forces between fuel and cladding has been analysed.

The problem of the quasi two-dimensional fuel rod models is that the local axial friction forces, which must be considered in the axial equilibrium balance, are unknown when a section of the fuel rod is analysed for the first time in a new time step. Consequently, the axial friction forces can only be calculated iteratively from the axial deformations of fuel and cladding. In other words, the calculation of all fuel rod sections has to be embedded in an axial iteration loop which increases the computational costs. In order to avoid this axial iteration loop sometimes **"simple local slip or noslip models"** are applied which substitute for a calculation of the local friction forces but at the expense of physical meaningful results as will be shown below.

A **simple noslip model** is based on the assumption that in all sections with radial contact the fuel and the cladding are considered as one single continuum, i.e. fuel and cladding stick together.

A **simple slip model** is based on the assumption that the friction coefficient between fuel and cladding is always zero, i.e. fuel and cladding can move axially without any restraint.

It is evident that the simple slip or noslip models suffer from severe limitations: the simple slip model underestimates the loading on the cladding, whereas the noslip model can account neither for a trapped fuel stack situation nor for a correct treatment if the fuel sticks to the cladding and the cladding expansion exceeds that of the fuel.

In order to avoid these limitations a theory was developed which allows the calculation of friction forces taking all different modes of interaction between fuel and cladding into consideration. The model for calculating the local axial friction forces incorporated in the TRANSURANUS code is the URFRIC model [9].

During different steady-state or transient irradiations of different pins the local contact condition may vary over a wide range of situations. In order to check all possible situations, a Monte Carlo technique was selected to test the URFRIC model in some 10^4 data cases. Agreement was found in all cases thus confirming the correct formulation of the URGAP model. Some selected data cases were documented in more detail [10].

In the following, predictions of the TRANSURANUS code with the URFRIC model and experimental data from rod 11 of the IFA-508 experiment performed in the Halden Boiling Water Reactor [11] are compared to assess the URFRIC model. In addition, the results of the **simple noslip** and the **simple slip model** which are optional in the TRANSURANUS code will also be discussed.

The characteristic details of IFA-508, rod 11 are :

Diametral gap (mm)	0.100
Total column length (mm)	420
Enriched column length (mm)	390
Filling gas (MPa)	0.1 pure helium

The rod was equipped with an axial elongation detector. The maximum peaking factor was 1.08 and occurred at the top of the rod. The rod power was increased in a step-ramp manner. Constant holding times, which ranged from 4 to 48 h, were imposed at 30, 40 and 50 kW/m in order to study fuel relaxation at the different power levels.

The comparison between the axial expansion of the cladding and the experimental results is shown in Fig. 2.28 as a function of the average rod power. Here, fuel relaxation during the holding times results in a decrease of the axial expansion. The simple noslip model and the detailed URFRIC model give essentially the same results. The reason for this agreement is that due to the nearly constant axial power shape all sections reach radial contact at the same time. Consequently, any trapped stack situation is avoided and both models must give

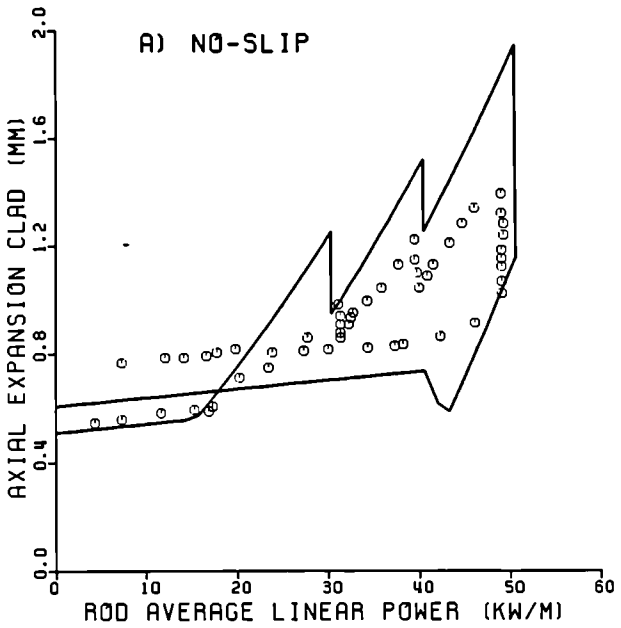

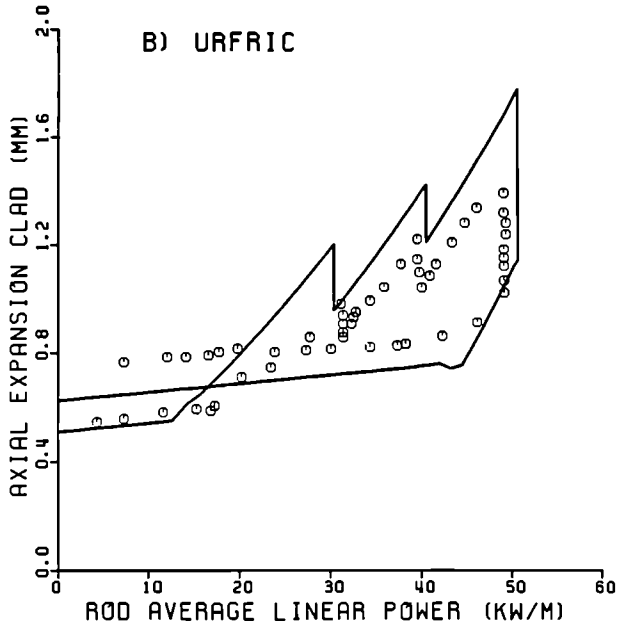

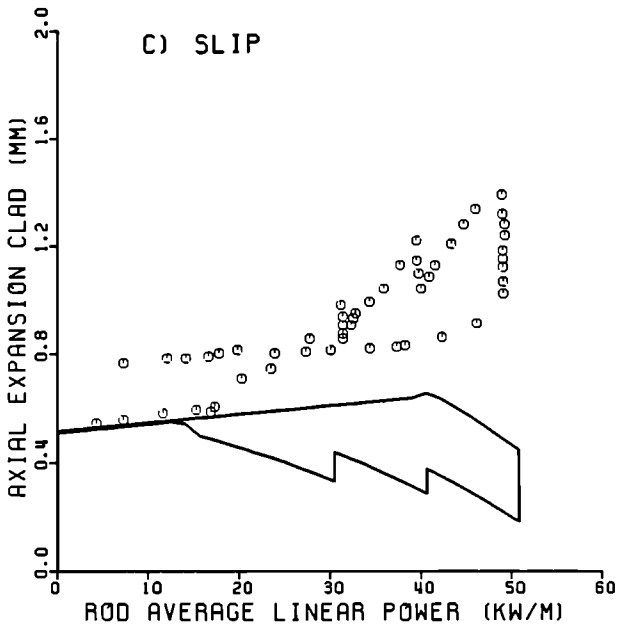

Fig. 2.28: IFS 508, rod 11: axial expansion of the cladding as a function of the rod average linear power. a) simple noslip model, b) detailed URFRIC model, c) simple slip model. The symbols indicate the data, the line is the prediction of the TRANSURANUS code.

the same results. Fig. 2.28a a shows some undershooting during shutdown which is due to tensile forces in the fuel. Fig. 2.28b demonstrates that the more detailed URFRIC model can better cope with such a situation. The overall agreement between the predictions and the data in both cases is acceptable if it is taken into account that some details of the fuel behaviour cannot be obtained from the open literature. On the other hand, the performance of the simple slip model is extremely poor. Due to the Poisson effect this model is not even able to predict correct tendencies (Fig. 2.28c).

The TRANSURANUS code offers three model options for taking axial friction forces into account: a simple slip model, a simple noslip modeland the detailed URFRIC model. All models offer some advantages in specific situations. However, for the majority of failure analyses or safety related analyses under normal, off-normal and accident conditions a detailed model which takes all different modes of interaction between fuel and cladding into account is indispensible. The URFRIC model is such a model. It is formulated in an extremely efficient numerical algorithm which saves computational costs. The URFRIC model has been applied successfully over 2 years in the TRANSURANUS code and may in principle also be used in other quasi two-dimensional fuel performance codes.

References

[1] K. Lassmann, Nucl. Eng. Design, Vol. 106 (1988) 291

[2] K. Lassmann, TRANSURANUS Änderungsprotokoll, Version 2, Modifikation 1 Jahr 1987 ("V2M1J87"), Technical Note K0287109 (1987)

[3] R.F. Mattas, F.L. Yaggee, L.A. Neimark, Portland, Oregon (1979), CONF-790441-7

[4] K. Lassmann, G. van Goethem, to be submitted to RES MECHANICA

[5] M. Bober, G. Schumacher, D. Geithoff, J. Nucl. Mater., 47 (1973) 187-197

[6] C.F. Clement, J. Nucl. Mater., 68 (1977) 54-62

[7] G. van Goethem, K. Lassmann, 9th International Conference on Structural Mechanics in Reactor Technology, Lausanne (1987), Transactions Vol. C, Invited Paper C 4

[8] Ispra report

[9] K. Lassmann,

a. 9th International Conference on Structural Mechanics in Reactor Technology, Lausanne (1987), Post-Conference No. 9: 6th International Seminar on Mathematical/Mechanical Modeling of Reactor Fuel Elements, Kippel, Switzerland, August 24-25 (1987)

b. Nucl. Eng. Design (1987), accepted paper

[10] K. Lassmann, TU, Technical Note K0287103 (1987)

[11] K. Yanagisawa, Nucl. Technol., Vol. 73 (1986) 361-377

The Final Version of the Code MITRA

Introduction

The main improvements of the computer code MITRA are listed here. This program calculates the release of radionuclides from a nuclear fuel during steady state and transient conditions.

Though some difficulties still persist, the code is now much more powerful than in the past, though its size has been increased very slightly, due to the structured way in which it has been rewritten (about 4500 lines, including copious comments). It is now able to simulate an irradiation history and the speed of its performances have been increased by about a factor 200. This allows to use it on relatively complex cases at reasonable cost.

A guide to use the code is available [1] . It also explains the mathematical model used.

Present State of MITRA

The preliminary version of the computer code was used to calculate the release for nuclides included in the ORIGEN [2] library of Fission Products, with the decay trees present in [3] and furnished numerical results not much different from the present ones.

A flow chart of the main program is shown in Fig. 2.29. More information can be found in reference [1].

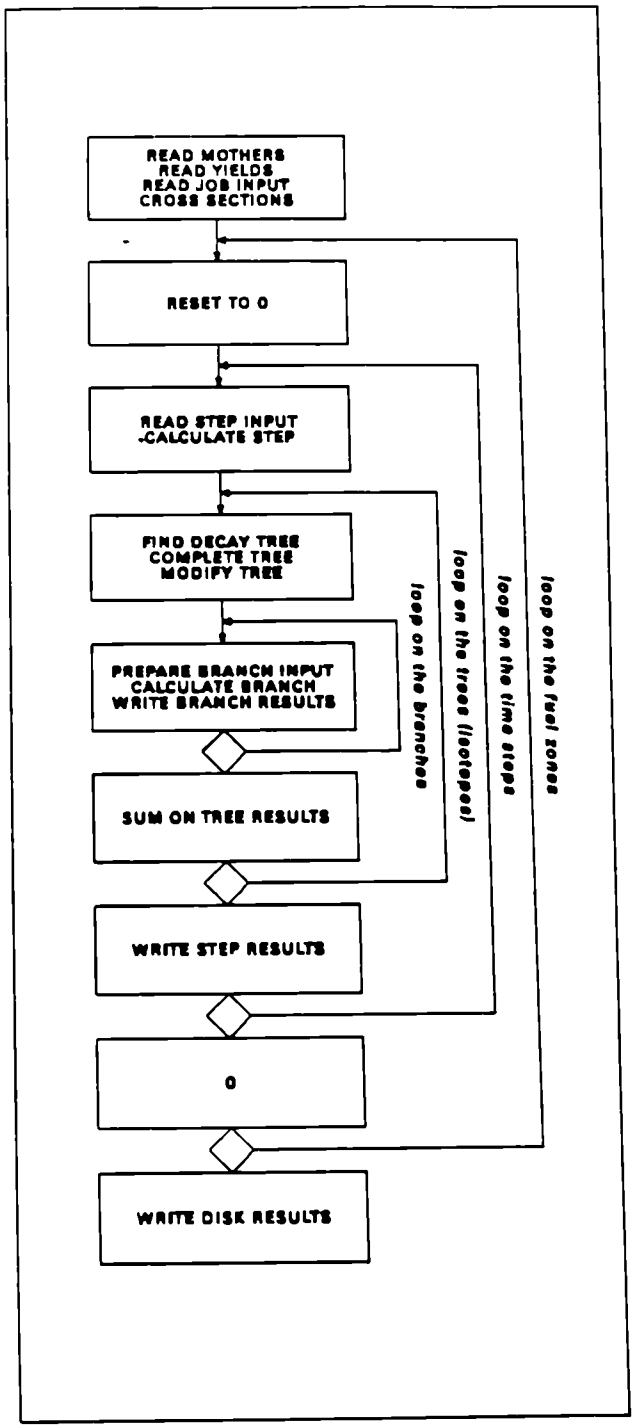

Fig, 2.29 *Flow chart of the main routine of Mitra. For every line in the flow chart there is a routine or a group of instructions in the program.*

Fuel Zones

It is now possible to specify a subdivision of the fuel in different annular zones. For each of them the program gives separate results which, at the end, are summarised over the fuel cross section.

Time Steps

The possibility of using MITRA to simulate any irradiation history is by far the main improvement of the code. This achievement implied the complete revision of the differential transport and rate equations in a new form, keeping in consideration the possibility of having variable initial values for the amounts created, dissolved and trapped in bubbles [1] , their transposition on the computer and the check of the subroutines for various cases.

Change of Treatment for the Term H

The code used a Fourier-type solution for the determination of the boundary loss term "H", that substitutes for the Laplacian term in the transport equation. This feature proved to be the most expensive part of the program, in a check of the CPU time used from the various subroutines. Analytical functions instead of series are now used [4], and this increases the execution speed very much and yields sometimes better results, due to the greater precision offered from the internal functions of the compiler, compared with the Fourier solution.

Output: Two output files on paper and one on a dataset for the plotter have been established.

The primary output on paper contains the most important data for every nuclide calculated, as decay constant, amounts created, dissolved in the lattice and trapped in "bubbles", birth rate and release rate. It also gives the total results for chemical species, but only for the contributions of the isotopes actually calculated, i.e. if one wants to know the global amounts of a chemical species then it is necessary to run MITRA for all the known (important) isotopes of that species.

The secondary output on paper contains the detailed calculations for all the nuclides. It also contains detailed information on the contribution to the release rate and birth rate due to diffusion, bubble migration or decay from mother nuclei.

The plotter output contains the same information as the primary output, apart from a summary of the chemical species.

Limitations

- The data on diffusion coefficients are still incomplete and with uncertainties due to differences between the various references.

- For MITRA, "Release" is the amount diffused out of the fuel grain, and this is not exactly that measured as released from the pin, because of delay effects due to trapping in open pores or chemical reactions.

- The code considers a zero solubility for all the chemical species in the lattice, that is they precipitate as soon as they physically interact. In fact, the equilibrium solubility of a chemical species, that is the maximum allowable amount of that species dissolved within the lattice, should be split between all the isotopes that belong to that species. But MITRA is a code that works on a variable subset of isotopes for each chemical species, and it is difficult to ascribe the correct fraction of equilibrium solubility to each isotope, without having to calculate the dissolved amount of all the isotopes for that chemical species.

  The development of a parallel program treating the basic aspects of the fission product chemistry is a useful complementary study for the implementation of MITRA in large codes evaluating the source term during reactor accidents.

- Furthermore, if the absolute amounts of the nuclides and not the percentages are required, then one should remember that MITRA considers only the main nuclear reactions, so there can be usually an error of up to 20 %. It can be worthwhile to compare these results with the more correct by created amounts furnished from the ORIGEN code.

Applications

Calculations have been carried out for the only available experiments for which the irradiation and release conditions were well established, taking into account precipitation and resolution in bubbles of fission product atoms. These experiments, already examined in [4] , have

been performed in the SILOE reactor in Grenoble and in the DIDO reactor in Harwell.

Grenoble Experiment "Contact" [5]

This experiment concerned the behaviour of PWR fuel rods under irradiation and its aim was to require informations on fuel cladding gap evolution and fission gas release.

In order to calculate the release of a few species, our program had to calculate the release of all the decay trees containing these nuclides (about 70 nuclides). The results are presented together with the measured quantities.
Some input data of the program are listed here:

^{235}U enrichment	=	4.95	%
Fuel grain radius	=	10	µm
Irradiation time	=	261	days
Linear reactor power	=	36	kW/m
Temper. inner zone	=	1300	°C
Inner temper.gradient	=	2000	°C/cm
Temper. outer zone	=	900	°C
Outer temper. gradient	=	3300	°C/cm

In the following figures the amounts of about 70 nuclides with atomic numbers between 32 and 56 (Ge to Ba) and atomic masses between 83 and 139 have been plotted versus the decay constants.

Fig. 2.30 shows the fractions of the created amounts of nuclides still in solution within the UO_2 lattice after the irradiation, and Fig. 2.31 the corresponding amounts trapped in intra-

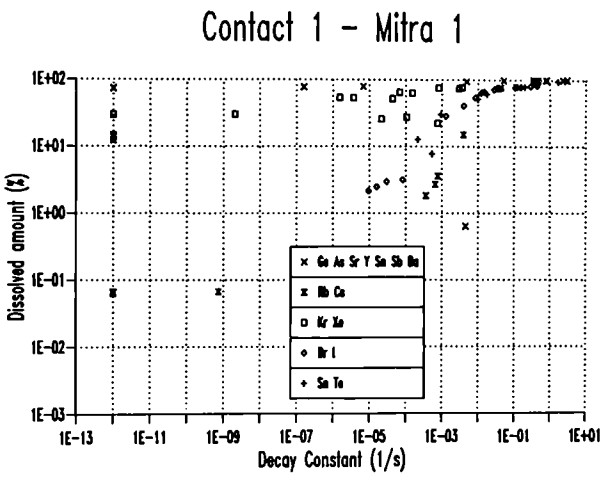

Fig. 2.30 *Fractions of the created amounts still in solution within the UO_2 lattice after the irradiation. The atoms that have a decay constant less than 10^{-12} (comprising stable ones) have been plotted with this decay constant. Nuclides from Ge to Ba.*

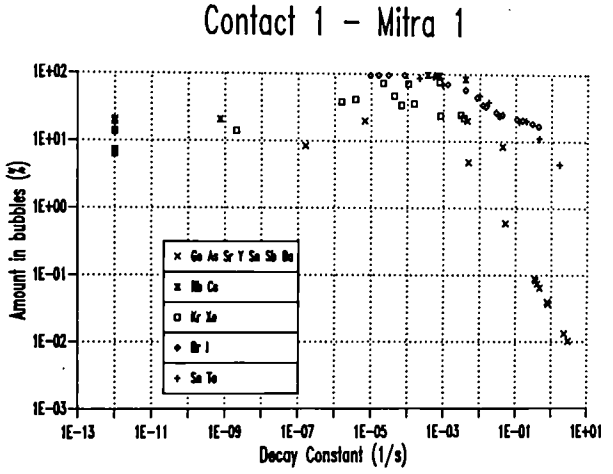

Fig. 2.31 *Fractions of the created amount trapped in intragranular bubbles after the irradiation. Bubble characteristics are taken from the FUTURE [6] code output.*

granular bubbles. Bubble characteristics were taken from the FUTURE [6] output.

Fig. 2.32 gives the fractions of the nuclides released which are complementary to the

fractions shown in Fig.2.29 and 2.30. These data are of special interest since they can be directly compared with the experiment. The agreement is not too bad, if one considers the uncertainties in the input parameters and the experimental error.

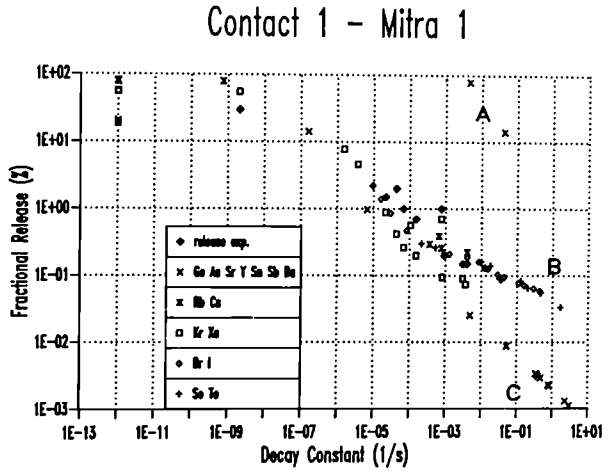

Fig. 2.32 *Percentual release versus the decay constant.*

There is a decrease in the release while melting , in Fig. 2.32, towards high decay constants (short half lives) because the atoms decay before having the time to diffuse out of the grain.

The two points on the top right (A) correspond to atoms that have a short life and a great amount of released atoms of one mother (^{137}Ba* from ^{137}Cs and ^{89}Y* from ^{89}Sr). In this way they are created mainly outside the grain, and their release fraction is abnormally high. Although this contribution to the release does not come from direct physical and/or chemical processes inside the fuel grain, it is necessary to keep it in consideration because, in in-pile experiments, it can be hardly distinguished whether an atom comes directly out of the fuel or is generated by the decay of an already released mother nuclide. (Actually, the term "Release" has to be suitably defined in view of the considered practical application).

It can be seen in Fig. 2.32 that the released atoms are arranged roughly along two distinct curves in the short life range of the diagram (bottom right). They are due to two distinct classes of nuclides, with a different diffusion coefficient. The higher curve (B) is due to nuclides with higher diffusion coefficients, such as Se, Te, Br, I, while (C) is due to those with low diffusivity. These nuclides are those for which no reliable data on diffusion coefficients are available and the UO_2 self-diffusivity has been assumed.

Fig. 2.33 presents another aspect: the connection between release of atoms in a decay tree, where nuclides are generated by natural decay or neutron capture, until a stable nuclide is reached.

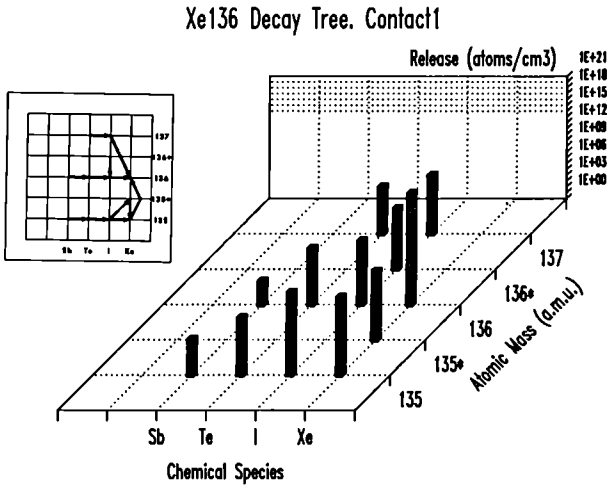

Fig. 2.33 *Connection between release of atoms in the ^{136}Xe decay tree. Nuclides are generated by natural decay or neutron capture (here only ^{135}Xe becomes ^{136}Xe for capture). Stars indicate an atom in excited state. Arrows indicate the successive decay/capture processes.*

Arrows indicate the successive decay/capture processes; see also reference [3].

In the ^{136}Xe decay tree, among the nuclides that contribute to this tree, the branch can be observed that comes from the "poison" ^{135}Xe for neutron absorption.

Harwell Experiment [7]

In this experiment the release of rare gas fission products and their halogen precursors from polycristalline uranium dioxide was measured during irradiation.

Here some input data of the program are listed:

^{235}U enrichment	=	20	%
Fuel grain radius	=	25	µm
Irradiation time	=	157	days
Linear reactor power	=	23	kW/m
Averaged temperature	=	1400	°C
Temperature gradient	=	400	°C/cm

The Harwell experiment was simpler than Contact, as in the fuel the temperature gradient was very small. The agreement of the MITRA calculations with the experiment is much better.

In Fig. 2.34 the same trend of release as a function of decay constant can be seen: a marked decrease of release with half life, except for an intermediate range where the release becomes nearly independent of the decay constant. This behaviour is characterised better by predominant precipitation into bubbles, followed by a limited migration of the bubbles to the grain boundaries. It is also possible to recognize the

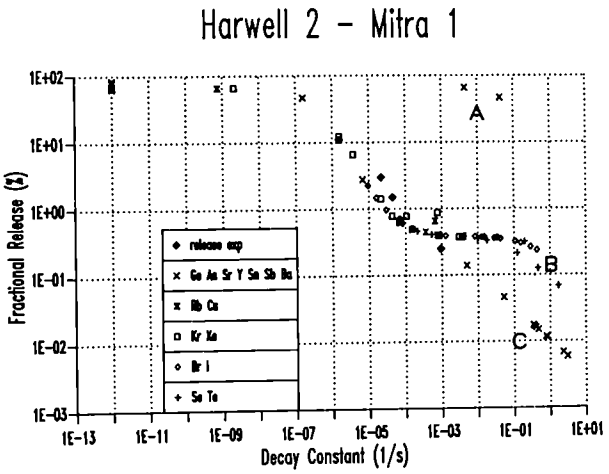

Fig. 2.34 Percentual release versus the decay constant

same points (A), (B) and (C) already discussed in Fig. 2.32.

References

[1] M. Gardani, C. Ronchi, Joint Research Centre (Karlsruhe), Report K0287098 (1987).

[2] A. Croff, ORNL-5621 (1980).

[3] A. Tobias, CEGB Report CNDC(73)P4 (1973).

[4] J. Sakellaridis, Doctoral Thesis, JRC Karlsruhe, Institute for Transuranium Elements, Germany - University of Patras, Faculty of Engineering, Greece (1986).

[5] M. Charles, P. Chenebault, and P. Melin, ANS Topical Meeting on Light Water Reactor Fuel Performance, Orlando, Florida (Apr. 22-24 1985).

[6] C. Ronchi, J. van de Laar, Joint Research Centre (Karlsruhe), Report K0287101 (1987)

[7] J.A. Turnbull, C.A. Friskney, J.R. Findlay, F.A. Johnson, and A.J. Walter, J.Nucl.Mater. 107, (1982) 168.

Spent Fuel Direct Storage

A new activity has been started to investigate spent fuel as barrier for long time storage of radioactive elements. If the used nuclear fuel is to be disposed of in an underground nuclear waste repository, the interaction of the UO_2 with the ground water could be crucial in determining the release of radionuclides from the fuel. Typically, a few percent of the fission products are located in the gap between fuel and clad. These are released within a few days following rupture of the clad and access of water. Depending on fuel operating conditions, a certain percentage of the radionuclides are located at grain boundaries. Preferential leaching releases much of this "grain boundary inventory "within relatively short times (months to years) as well. The steady state release rate for long periods of time of typically over 90 % of the fission products and the actinides which are located within the UO_2 grains, is controlled by matrix dissolution of UO_2 (Fig. 2.35). It is known that the type of ground water is a crucial factor. UO_2 is very insoluble in water under reducing conditions, but under oxidising conditions, its solubility increases. Many data have been collected in different laboratories on the effects of temperature, pH and composition of aqueous solutions (concentration of O_2, H_2O_2, CO_3^{2-}-ions etc.) on the dissolution of unirradiated UO_2. However, there are still no data on the effect of radiation damage on UO_2-dissolution and on UO_2 at high burn-up. To fill these gaps, three sets of experiments were performed within the reporting period.

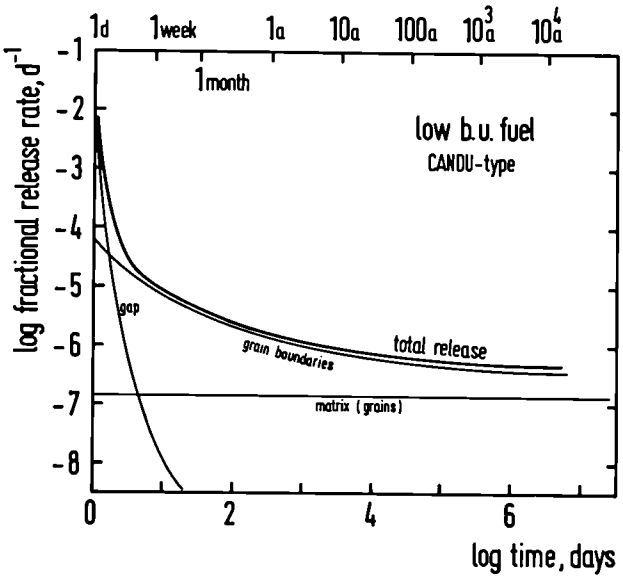

Fig. 2.35: Sketch of the three different contributions to release radioactivity from defected fuel, based on observations at low burn-ups [1]

Measurements of Very Small Leach Rates of UO_2

In the first set of experiments, some experience was gained in leaching UO_2 in distilled water at room temperature and in autoclaves at 100 and 200° C. As expected, weight change measurements were no reliable indication of U-dissolution because three processes occur concurrently:

i) UO_2 oxidation
ii) UO_2 dissolution
iii) UO_2 redeposition from the solution.

Fig. 2.36 shows the redeposition of crystalline uranium oxides on the underlying leached sinter in an impressive way (SEM picture, UO_2 leached for 26 d at 200° C).

Because of the low solubilities, a tracer technique was used to determine surface dissolution of UO_2. Reactor-grade sintered UO_2

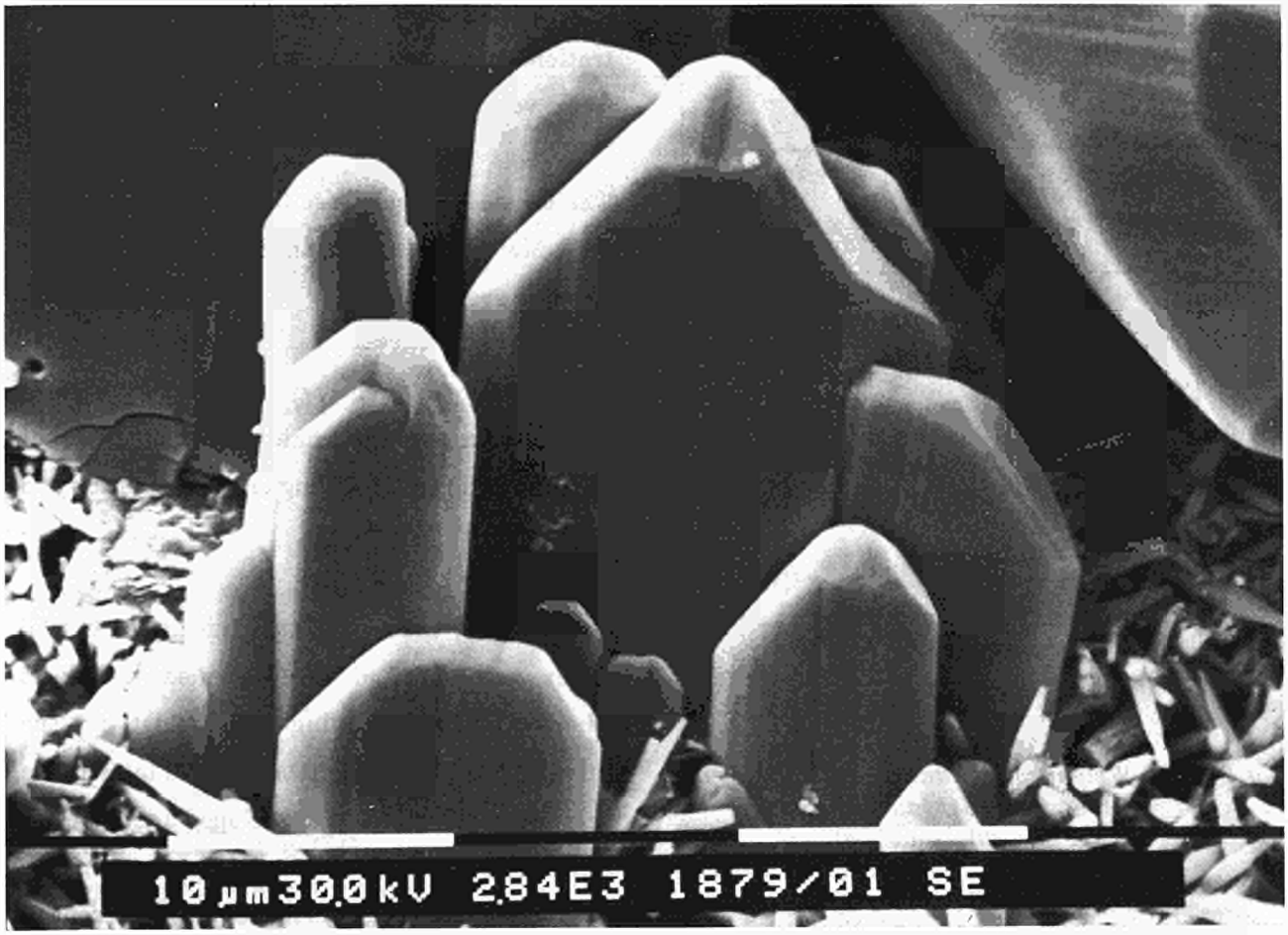

Fig. 2.36: SEM picture of UO_2 leached at 200° C for 26 d showing redeposition of single crystalline needles of uranium oxide on the leached sinter

was implanted with a trace-amount of radioactive Rb-84. The range of these ions is very small: ~ 200 Å..The remaining activity was determined following leaching as a measure of the UO_2 which was dissolved. The amount of UO_2 dissolved was confirmed to be very small

- at 20° C and up to 36 days, only 4 % of the Rb was lost corresponding to about 20 Å UO_2 dissolution, or less than 1 Å/day,

- at 90° C, about 15 % Rb was lost in one week, corresponding to about 75 Å UO_2 dissolution.

The time dependence is given in Fig. 2.37, together with the weight changes.

Effect of Radiation Damage on UO_2 Dissolution

A parallel set of UO_2 specimens was prebombarded with stable Rb-85 before the tracer Rb-84 was introduced. The prebombardment with $4x10^{14}$ ions/cm^2 caused about 1 displacement per atom damage in UO_2, a dose corresponding to a relatively low burn-up of < 1 at%. Nevertheless, an important increase in loss of Rb, and thus in UO_2 dissolution was observed

- at 20° C, 50 % Rb was leached out in 10 days
- at 90° C, about 93 % was leached out in 3 days.

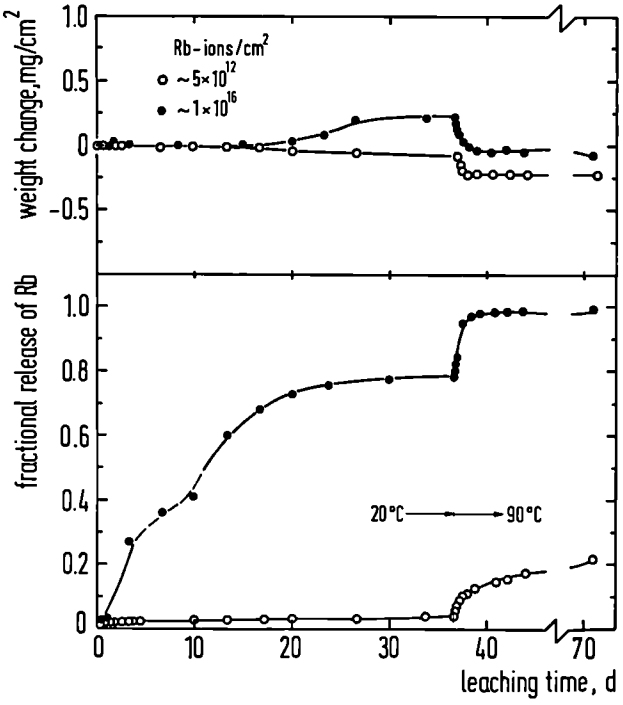

Fig. 2.37: Weight change and loss of implanted Rb-84 from UO_2 during leaching in H_2O at 20 and 90° C. The predamaged specimens show increased Rb-loss indicating a significantly increased leach rate of damage UO_2

These results are included in Fig. 2.37. Besides the radiation-induced increased solubility, an increased oxidation at 20° C is also seen as indicated by the weight increase of the prebombarded specimen.

Leaching of SIMFUEL

The fuel with simulated burn-up of 3 at. % (see TUAR 86,59) was leached at 20, 100 and 200° C. In addition to this ThO_2-based fuel, UO_2-based SIMFUEL became available towards the end of the reporting period. It was included in the experiments and will be used for future work. As expected, Th could not be detected in the solution (< 0.02 ppm). However, appreciable amounts of the fission products were dissolved.The concentrations found for 400 h leaching for a surface to water volume ratio of 1:20 are given in Tab. 2.10.

The dectection limits are (in ppm) Ba: 0.01, Ce: 0.08, Mo: 0.04, Nd: 0.02 and Sr: 0.0004. No La or Ru were ever found.

These first results show preferential leaching of some fission products, mainly Sr and Ba, either by grain boundary leaching or by dissolution and redeposition of the matrix.

In summary, first results on the interaction of water with UO_2 fuel were obtained in 3 areas where no corresponding data exist in the literature: a microanalytical method to measure very low leach rates was developed and tested, a significant effect of radiation damage in enhancing matrix leaching was found, and preferential fission product leaching with fuel simulating elevated burn-up was observed.

References

[1] L. H. Johnson, Whiteshell Report AECL-6837 (1982)

Tab. 2.10 Leach data for SIMFUEL

UO_2-based SIMFUEL					
	Ba	Ce	Mo	Nd	Sr
20° C	-	-	-	-	0.006
190° C	0.004	-	-	-	0.019
200° C	0.03	-	0.80	-	0.020
ThO_2-based SIMFUEL					
	Ba	Ce	Mo	Nd	Sr
20° C	-	-	-	-	0.002
100° C	0.05	-	0.07	-	0.030
200° C	0.76	0.09	0.09	0.19	1.24

Collaboration with External Organisations

- Risø National Laboratory, cooperation in the international fission gas release project.
- Siemens-KWU, Erlangen (transient-tested LWR fuel, MOX fuel).
- Technical University of Darmstadt (modelling) further collaboration (TRANSURANUS) with KfK Karlsruhe, University Stuttgart, JRC Ispra, CIEMAT, Spain, TÜV Bayern, TÜV Baden and TÜV Hamburg.
- Max Planck Institut für Chemie and University of Salford (fission gas solubility).
- Atomic Energy of Canada Ltd and KfK, INFP (fission product behaviour in UO_2).
- LAMEL, Bologna (Radiation Damage Calculations).

3 Actinide Cycle Safety

3.1 Formation of Actinides (FACT)

Introduction

In Sub-project FACT (Formation of Actinides), the build-up of actinides, and in particular the so-called minor actinides - Np, Am, Cm are investigated. Experiments such as TACO [1] have been carried out to measure the integral cross-sections of pure actinides in fast reactors. Such experiments are of great importance for checking microscopic cross-section libraries: predictions of the nuclear composition of irradiated samples can be made using standard calculation methods of various degrees of sophistication and which require as input data the starting (isotopic) composition of the irradiated material, the reactor characteristics (such as irradiation history and neutron flux intensity and energy dependence) and the cross-sections of the various nuclides as a function of the neutron energy spectrum.

Two irradiation experiments of actinides in the fast reactor KNK II (MTE 2) are being carried out and one in PHENIX. Of the former, one consists of 10 actinide mixtures and the other of 38 smaller actinide samples to be irradiated to a higher burnup. The position of the analysis of the former irradiation, i.e. the 10 actinide mixture samples is first reported here,then the status of the SUPERFACT irradiation , followed by a report on the interaction between uranium-americium oxides and liquid sodium.

Before minor actinide mixed oxide fuel can be recycled in fast reactors the physical and chemical properties of the proposed fuels must be studied. The fuel / coolant interaction is one of the main chemical problems within these studies. Because of its strong reaction with sodium the uranium-americium mixed oxide is of special interest.

Post-irradiation Examinations of Irradiated Pellets from the KNK II / MTE Experiment

10 actinide fuels with different nuclide compositions (for description,see TUSR **34**, 52) have been irradiated in KNK II (TUSR **31**, 59). After irradiation the 10 capsules - each one containing 3 pellets of one specific composition - were transferred to the Institute's hot cells for post-irradiation examination.

The results of the first examinations were described in a previous report (TUAR **86**, 85). The results of the experimental investigation are summarised here.

The present state of this work is as follows:

- Samples for radiochemical analyses have been prepared from the 10 capsules.
- Samples for quantitative optical microscopy of the 10 fuels were prepared. A summary of the characteristics of the in-pile fuel

restructuring is given in Tab.3.1. The radial porosity distribution has been measured and the experimental results are illustrated in Fig. 3.1. Two major conclusions can be pointed out from this characterisation work:

a. There was no apparent corrosion of the internal surface of the capsule.
b. A strong densification effect was

Table 3.1 Characterisation data of KNK II - MTE 2 fuels

Sample No.	Chemical composition	Secondary phase	Fissuration mode	Porosity, %		gap, µm	
				starting value	after irradiation	min.	max.
0P 43	$^{232}ThO_2$	none	pattern of diametral and radial cracks	10	8.10	33	125
0P 44	$^{238}UO_2$	none	no diametral crack	7,6	6.46	50	140
0P 45	$(^{232}Th, Pu)O_2$	dark ceramic phase at fuel periphery	1 diametral + 1 radial crack	12±3	n.d.	25	132
0P 46	$(^{233}U, ^{238}U)O_2$	none	2 diametral cracks + pattern of eccentric small cracks	10±3	3.04	25	235
0P 47	$(Pu^{2nd}, U)O_2$	centre: two-phase ceramics intermediate radial position: intergranular ceramic phase	2 diametral cracks	10±3	3.11	73	113
0P 48	$(^{239}Pu, ^{238}U)O_2$	none	pattern of radial cracks	10±3	3.68	32	284
0P 49	$(Pu, ^{237}Np, U)O_2$	none	1 diametral crack	10±3	2.40	21	217
0P 50	$(Pu, ^{241}Am, U)O_2$	none	2 eccentric circumferential cracks	10±3	2.54	20	150

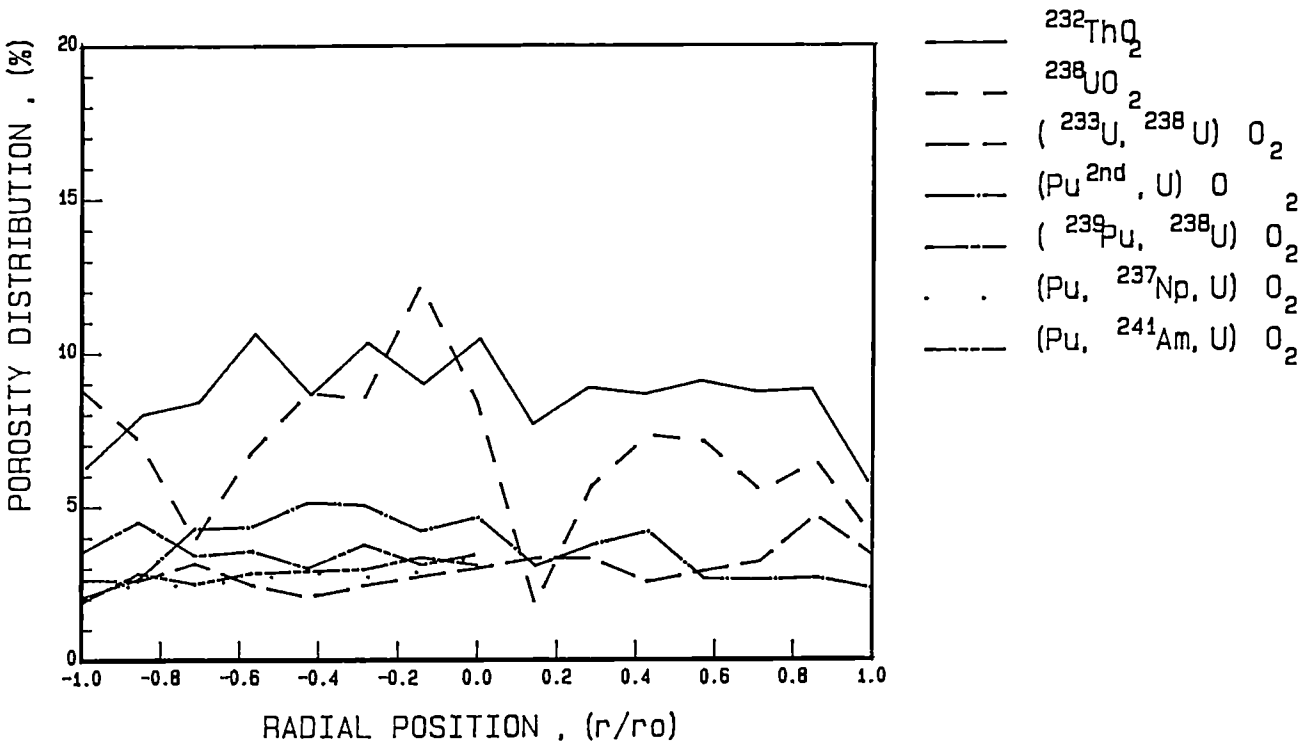

Fig. 3.1 Radial porosity distribution in KNK II / MTE 2 samples

observed from the irradiation; this effect appears more pronounced in the oxides UO_2, MO_2, (M, Np/Am)O_2.

The fuel relocation during the irradiation led sometimes to a strong eccentricity of the fuel pellets and the variable thermal transfer conditions between clad and fuel resulted in fuel temperature profiles dependent upon the azimuthal concentration.

Radiochemical Analysis of Irradiated Pellets from KNK II

The compositions of the actinide mixtures before analysis were reported previously (TUAR 86, 85). Pellets of each of the mixtures have been dissolved and analyses of the total composition carried out. The present situation is shown in Tab. 3.2 where the elements for each capsule to be analysed are listed. It can be seen from the table that the analyses for thorium and neptunium are not complete: these must be made by chemical titration methods for those samples where they are a major component. The mass-spectrometric isotope dilution analyses for U and Pu are to a large extent complete. Certain analyses have to be repeated to reach the expected measurement accuracy. These occur for the most part when an interference is present, for instance for sample 8 where ^{233}U - used as spike in the determination of uranium concentrations - is produced during the irradiation by the reaction ^{232}Th (n, γ) ^{233}U.

For certain elements, more than one analytical method has been or will be employed. Thus for measuring the concentrations of the major components, K-edge absorption spectrometry can also be used. These measurements are not yet complete but will provide an independent check on the concentrations in these cases and will also allow experience to be gained in the application of the K-edge absorption instrument for elements other than uranium.

^{241}Am is measured routinely by α-, γ-spectrometry and mass-spectrometric isotope dilution (MSID). The results from MSID are the most accurate and reliable and have the advantage of giving values for the ^{243}Am nuclide and - when the americium has been separated from curium - ^{242}Am as well. The γ-spectrometry determinations of ^{241}Am have the advantage of being relatively quickly carried out and are normally in good agreement with those from MSID, but provide no information on the other americium isotopes.

Small amounts of ^{237}Np will be measured by gamma-spectrometric isotope dilution (GSID). It may be possible to use the internal spike technique [2] for sample 9, where measurable quantities of ^{243}Am are to be expected, but otherwise ^{239}Np as external spike must be used. These analyses have yet to be carried out.

Measurement of Burn-Up

The burnup per capsule is relatively small, lying between 1 and 2%. For such low burnups, Nd measurements are difficult and so γ-spectrometric determinations of the ^{137}Cs content were made.

Table 3.2 Analyses of actinide capsules irradiated in KNK-II/MTE 2

	Sample	Element analysed	Method	State of analysis
1	ThO_2	Th	titration	incomplete
		Pu	MSID	complete
2	$^{238}UO_2$	U	MSID	complete
		Pu	MSID, α-Spect.	complete
		Np	GSID	incomplete
3	$^{237}NpO_2$	Np	titration	incomplete
		Pu	MSID	to be repeated
4	$(Pu, U)O_2$	U	MSID	to be repeated
		Pu	MSID	complete
		Am	MSID	to be repeated
		Cm	α-Spect.	complete
5	$(Am, U)O_2$	U	MSID	to be repeated
		Pu	MSID	complete
		Am	MSID, α-Spect.	incomplete
		Cm	α-Spect.	complete
6	$(^{233}U, ^{238}U)O_2$	U	MSID	complete
		Pu	MSID	complete
7	$(Pu, U)O_2$	U	MSID	complete
		Pu	MSID	complete
		Am	α-Spect.	incomplete
		Cm	α-Spect.	incomplete
8	$(Th, U)O_2$	Th	titration	incomplete
		U	MSID	incomplete
		Pu	MSID	complete
9	$(U, Pu, Np)O_2$	U	MSID	complete
		Pu	MSID	complete
		Np	GSID	incomplete
		Am	MSID, γ-Spect.	complete
		Cm	α-Spect.	complete
10	$(U, Pu, Am)O_2$	U	MSID	complete
		Pu	MSID	complete
		Am	MSID, γ-Spect.	complete

MSID : mass-spectrometric isotope dilution
GSID : gamma-spectrometric isotope dilution

Measurement of Flux Monitor Capsules

As reported in TUAR 86, the neutron flux monitor capsules have been shipped to CEN-Mol where they are being analysed. These results will define the total flux and the neutron energy distribution at the actinide pellets.

Calculation of Results

An important part of the experiment is the

calculation of the actinide concentrations and the burnups in the irradiated samples and comparing them with the measured values. The calulations are to be carried out by INR,KfK. Input data for the calculations will be the microscopic cross-section libraries, the starting composition of the pellets and the precise neutron flux as determined from the analysis of the monitor capsules (see above). First results of the calculations are expected in 1988.

Dose Measurements on Irradiated Capsules

The estimation of radiation doses incurred by handling fuel containing minor actinides is important and could invoke financial penalties from extra shielding precautions which may have to be taken in certain cases. The doses from all actinide samples, pellets or pins, have been measured before and after irradiation, and comparisons with calculated values have been previously published for samples prior to irradiation (TUSR 40, 53).

When the compositions of the irradiated KNK II samples are finally determined, the dose-rates from the samples can be calculated. The dose-rates were measured in January 1986 before the pellets were dissolved. Each pin (containing 3 pellets) was held at 1 and 2 metres distance from a 'Babyline' dosimeter and the dose-rates read through a lead glass wall using a telescope and recorded. Neutron doses were also measured although in all cases except for sample 5 containing 50% ^{241}Am which gave 0.006 mSv/h at 1 metre and 0.002 mSv/h at 2 metres, the measured doses were at the background level (< 10^{-3} mSv/h).

The measured gamma doses as described are given in Tab. 3.3.

Table 3.3 Emitted γ-dose-rates from the KNK - MTE 2 irradiated actinide capsules

	Sample	Dose rate (mSv/h)	
		1 metre	2 metres
1	ThO_2	6.7	1.8
2	$^{238}UO_2$	5.3	1.4
3	$^{237}NpO_2$	7.0	2.0
4	$(Pu, U)O_2$	30.0	8.0
5	$(Am, U)O_2$	6.5	1.7
6	$(^{233}U, ^{238}U)O_2$	45.0	12.0
7	$(Pu, U)O_2$	31.0	8.0
8	$(Th, U)O_2$	26.0	7.0
9	$(U, Pu, Np)O_2$	25.0	6.5
10	$(U, Pu, Am)O_2$	26.0	7.0

Background: 0.17 mSv/H

Irradiation Experiment SUPERFACT

As reported previously (TUAR 86,82) the irradiation of the 8 minor actinide fuel pins was started in October 1986. In February 1987 the power of the PHENIX reactor was reduced and therefore the irradiation experiment was unloaded. The pins were reloaded again in May 1987 and irradiated for the rest of the year without problem.

At the end of the reporting period the pins had reached a maximum burnup of about 4 atom%. The end of the irradiation is expected in mid-1988.

The Reaction of Uranium-Americium Mixed Oxides with Sodium

Thermodynamic Aspects

It was assumed that $(U,Pu)O_{2-x}$ could be taken as a starting point in understanding the behaviour of $(U,Am)O_{2-x}$ although some differences in the thermodynamics of the mixed oxides were known. As a result of this we attempted to prepare the most probable reaction product $Na_3(U, Am)O_4$ and some related compounds Na_3AmO_4, Na_2AmO_3. The preparation of $Na_3(U, Am)O_4$ proved to be very difficult, normally yielding as products Na_2UO_4 and AmO_{2-x}. The desired product could only be obtained when the reaction conditions were exactly fulfilled. It was not possible to measure the oxygen potential of $Na_3(U, Am)O_4$ with the solid state e.m.f. cell because of its thermal decomposition to Na_2UO_4 and americium oxide before having reached the measuring temperature.

The measured oxygen potentials of the americium compounds and the ternary oxides of uranium with sodium are shown in Figs. 3.2 and 3.3.

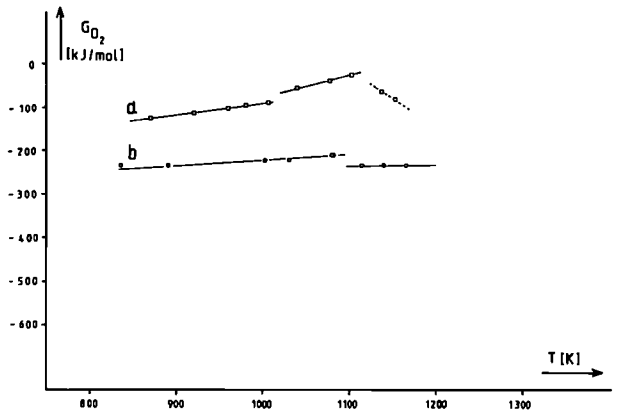

Fig. 3.2 Measured potential of Na_3AmO_4 (a) and Na_2AmO_3 (b)

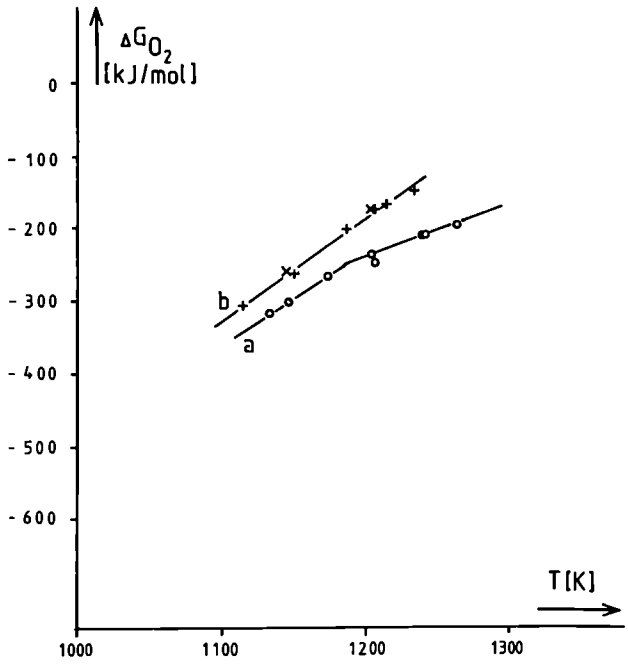

Fig. 3.3 Measured oxygen potential of Na_2UO_4 (a) and $Na_2U_2O_7$ (b)

Starting Material Characteristics

The $(U, Am)O_{2-x}$ shows a fluorite structure with vacancies on oxygen sites. The difference in oxygen potential between $(U, Am)O_{2-x}$ and $(U, Pu)O_{2-x}$ or $(U,Np)O_{2-x}$ can be clearly seen in Fig. 3.4. These differences cannot be explained by the slightly different energies of formation of the dioxides.

The bonding model of the U-Pu mixed oxides is based on the assumption that the uranium atoms are in the tetravalent state, whereas the plutonium atoms are partly trivalent and partly tetravalent. The ratio Pu^{3+}/Pu^{4+} depends on the stoichiometry of the mixed oxide [3]. This

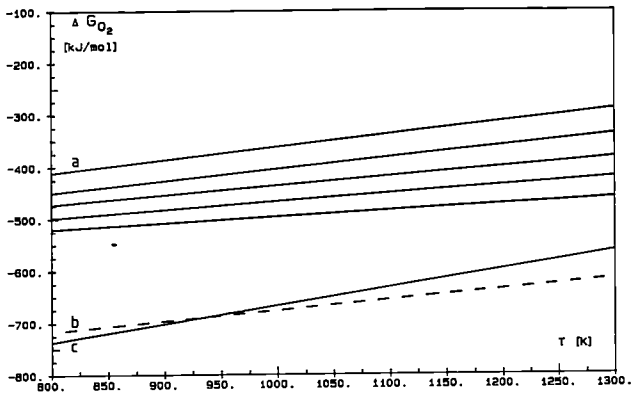

Fig. 3.4 Oxygen potential of $(U_{0.5}Am_{0.5})O_{2-x}$, $(U_{0.5}Np_{0.5})O_{2-x}$ and $(U_{0.8}Pu_{0.2})O_{2-x}$ as a function of temperature

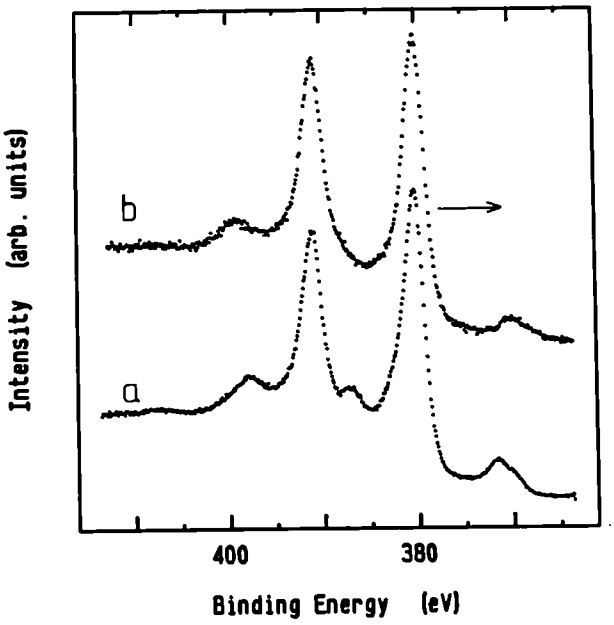

Fig. 3.5 XPS spectra of the U 4f level for $UO_{2.00}$ (a) and $(U_{0.5}Am_{0.5})O_{1.95}$ (b). The spectra (b) is shifted 0.8 eV towards lower binding energy, so the relative satellite position is easier to compare.

formalism when applied to the U-Am mixed oxide gives no explanation for its high oxygen potential and is in contradiction to the experimental results given here.

Structure and Bonding in $(U_{0.5}Am_{0.5})O_{2-x}$

XPS measurements performed with $(U_{0.5}Am_{0.5})O_{1.95}$ showed clearly that the americium was in the trivalent state while the uranium appeared in a valency state higher than 4+. The photoelectron spectra are given in Figs. 3.5 - 3.7 and the binding energies in Tabs. 3.4 and 3.5. These experimental results agree with a bonding model applied to uranium-lanthanide mixed oxide systems, e.g. Nd_2O_3 - UO_x ($2 \leq x \leq 3$) [5].

$(U_{0.5}Am_{0.5})O_{2.0}$ shows a positive deviation from Vegard's law, when the calculation is based on the crystallographic data of UO_2 and AmO_2. For $(U_{0.5}Np_{0.5})O_{2.0}$ the same calculation results in perfect agreement with the experiment. Applying the assumption given by Wadier [6] that is based on Nd_2O_3 - U_2O_5 to the U-Am-O system yields a much better agreement.

The XPS data, the structural aspects and the thermodynamic behaviour of the U-Am mixed oxide are easier to understand when the system is formally considered as a mixture of Am_2O_3 and UO_x ($2 \leq x \leq 3$). There is a strong tendency for the americium to pass over to the more stable trivalent oxidation state. Therefore it is more similar to the lanthanides than to the actinides neptunium or plutonium.

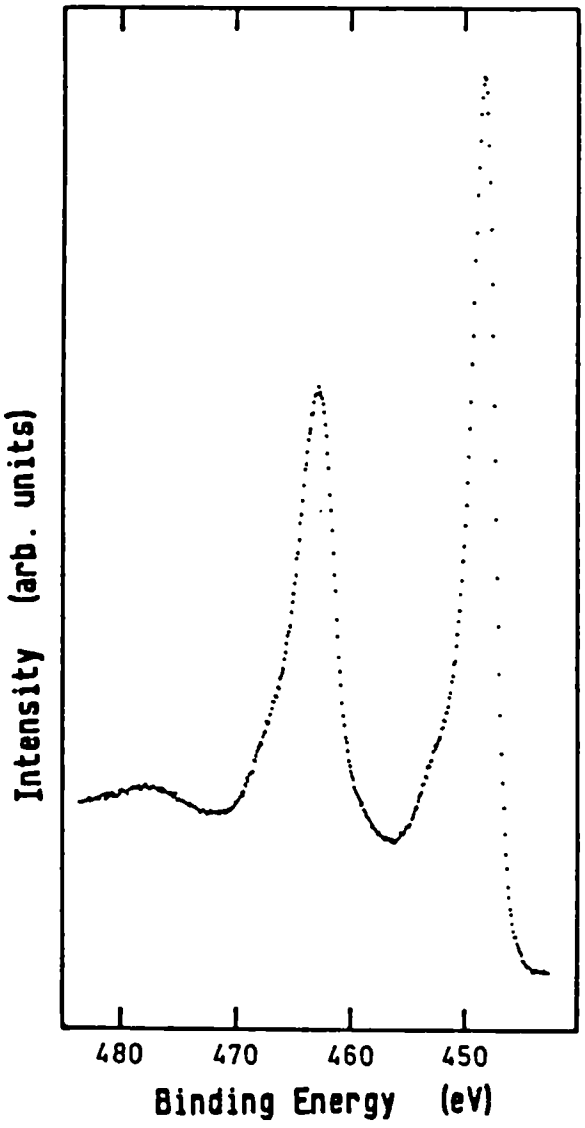

Fig. 3.6 XPS spectra of the Am 4f level for Am_2O_3 [4]

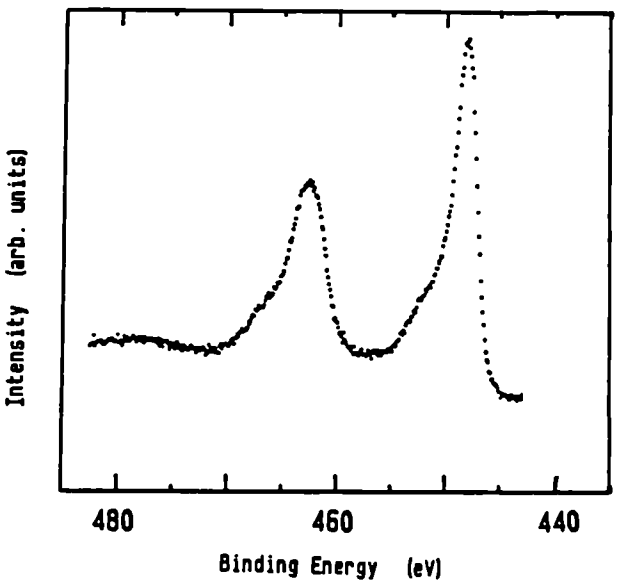

Fig. 3.7 XPS spectra of the Am 4f level for $(U_{0.5}Am_{0.5})O_{1.95}$

Conclusion

The presence of Am^{3+} in $(U_{0.5}Am_{0.5})O_{2-x}$ forces the uranium in a valency state higher than 4+. Following this the high oxygen potential, the reaction with sodium and the deviation from Vegard's law can be explained by a behaviour which is more similar to the U/Ln mixed oxides (Ln= lanthanide element) than to the UO_2/PuO_{2-x} solid solutions.

References

[1] A. Crichio, R. Ernstberger, L. Koch, R. Wellum, "The TACO Experiment for the Determination of Integral Neutron Cross-Sections in a Fast Reactor", Proceedings of the International Conference on Nuclear Data for Science & Technology, p. 175-177, Antwerp, 6-10 September 1982

[2] T. Adachi, K. Kammerichs, L. Koch, "Inherent Isotope Dilution Analysis of 237Np in Spent Nuclear Fuels", J.Radioanal. Chem., Letters 117, (1987), 233-241

[3] R.E. Woodley, J. Nucl. Mater.,96 (1981) 5

[4] J.R. Naegele, J. Ghijsen, L. Manes in:"Structure and Bonding", 59/60 (1985) 197
Eds: M.J. Clarke, J.B. Goodenough, Springer Verlag Berlin (1973)

[5] K. Une, M. Oguma, J. Nucl. Mater., 115 (1983) 84

[6] J.F. Wadier, CEA-R-4507

[7] G.C. Allen, P.M. Tucker, J.W. Tyler, J. Phys. Chem., 86 (198) 224

[8] J.J. Pireaux et al., Chem. Phys. 22 (1977) 113

Table 3.4 Binding energies of the U $4f_{5/2}$, U$4f_{7/2}$ levels and the relative satellite position (eV) in various compounds

-	U $4f_{5/2}$	relative satellite position	U $4f_{7/2}$
$(U_{0,5}Am_{0,5})O_{2-x}$	391.6	8.4	380.9
$UO_{2,000}$ [5]	391.2	6.7 ---	380.3
UO_2 [6]	391.1	5.8 8.2	380.1
UO_{2+x} [5]	391.6	6.3 8.2	380.7
UO_3 [6]	391.9	--- ---	380.9

Table 3.5 Binding energies of the Am $4f_{5/2}$ and Am $4f_{7/2}$ level (eV)

	Am $4f_{5/2}$	Am $4f_{7/2}$
$(U_{0.5}Am_{0.5})O_{2-x}$	462.7	448.2
Am_2O_3 [2]	462.6	448.2

Collaboration with External Organisations

CEA, Cadarache

KfK, INR

Univ. Karlsruhe

3.2 Safe Handling of Nuclear Fuels (SHAPE)

Introduction

Sub-Project **SHAPE** is concerned with the safe handling of plutonium, plutonium compounds, and other heavy elements.

SHAPE studies deal with saftey aspects in fuel fabrication and with plutonium bearing aerosols, their formation and dispersion under normal and off-normal working conditions in a plutonium laboratory or a plutonium fuel manufacturing plant.

These investigations are being pursued along several lines:

- Studies aimed at reducing the amount of materials lost by evaporation during sintering;
- Development of instrumentation and methods for controlled plutonium aerosol generation and detection;
- Sampling and analysis of aerosols in plutonium fuel fabrication glove boxes, accompanied by appropriate model calculations;
- Study of the generation and dispersion of plutonium bearing aerosols in glove box fires, both on a small scale, involving plutonium, and on a full-size laboratory scale (with Pu-simulants).

During the reporting period

- the particle distribution in simulated agglomerations was studied,
- alpha-recoil experiments were performed in order to evaluate the amount of material becomming air-borne due to this phenomenon,
- fire experiments under realistic laboratory conditions to investigate the dispersion of radioactive material in case of an accident in a plutonium laboratory or a plutonium fuel manufacturing plant were continued,
- new insight into the mechanism of resuspension of uranium-plutonium oxide particles from burning plexiglas was obtained.

Particles Distributions in Simulated Agglomeration

In highly concentrated populations of small particles, such as smokes, Brownian motion leads to the rapid formation and growth of particle agglomerates. Particle clusters of this type have a characteristic low density "chain agglomerate" structure. The morphology of such clusters can be described using the concept of "fractal dimension" and the growth kinetics and agglomerate size distribution can be studied conveniently by numerical simulation [1]. Even

small computers can be used for such simulations providing the particle concentration is not too low. The results of such a simulation are reported here for the evolution of the particle size distribution in an initially monodisperse population subjected to cluster-cluster agglomeration.

Fig. 3.8 shows how a population of monodisperse particles evolves by diffusion to form a single cluster and gives a plot of the radius of gyration of the cluster against the number of primary particles in the cluster from which the fractal dimension is obtained. The open and irregular structure of this type of cluster is clearly visible. The model can simulate the Brownian diffusion of an initially monodisperse population of particles on periodic two or three dimensional lattices. Typically populations of 5000 particles were studied at concentrations of 0.2 to 0.02 particles/lattice site, i.e. at rather high concentrations. A mass dependent cluster mobility of the form $m_n = m_1/n^x$ was assumed where m_n is the mobility of a cluster containing n particles and m_1 is the mobility of a cluster consisting of a single particle. A sticking coefficient of 1 was assumed for colliding particles. As mentioned above, the fractal dimension of individual clusters was calculated from the dependence, for each cluster, of the radius of gyration on cluster size i.e. the individual points on the plot consti-

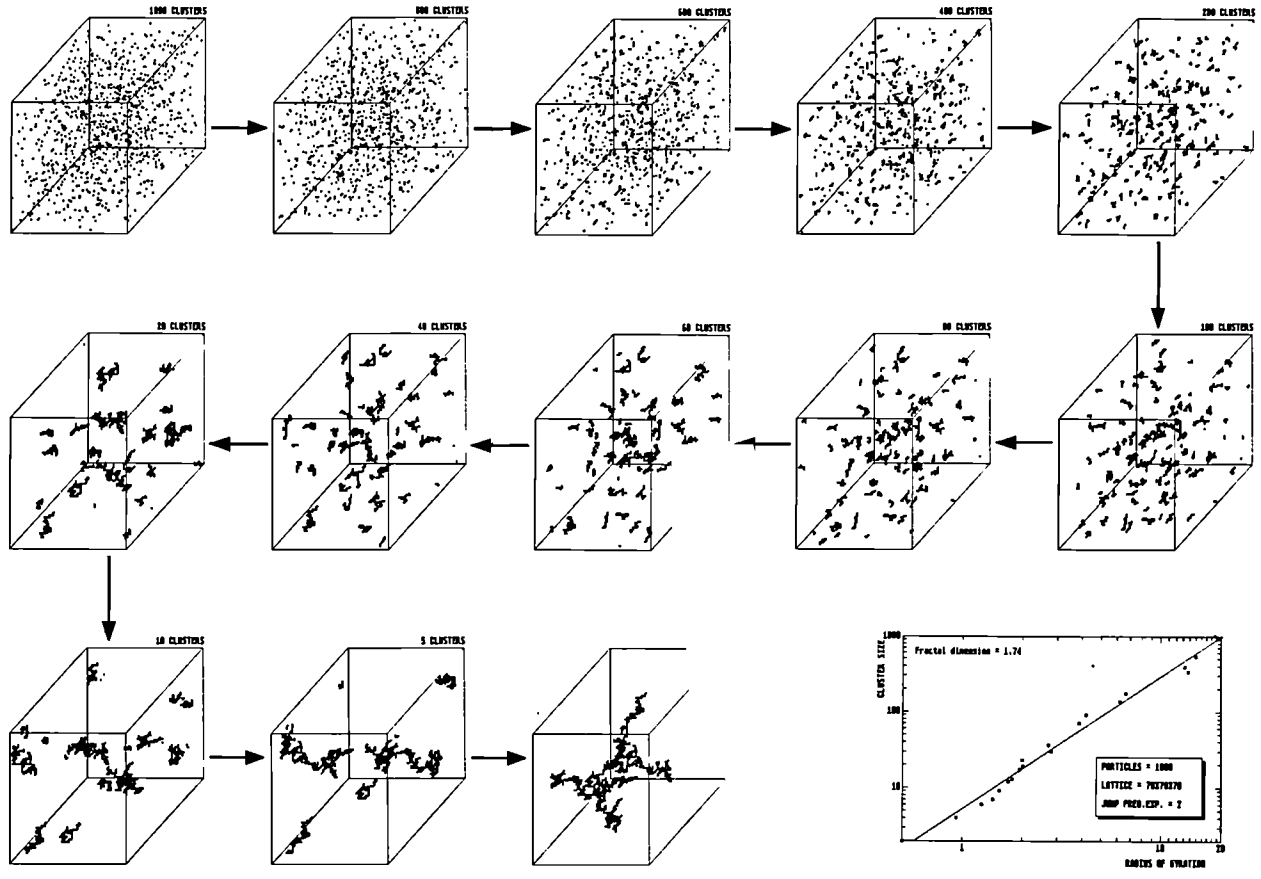

Fig. 3.8 *Formation of clusters by diffusion limited agglomeration*

tute a record of the growth of the cluster. The straight line of this plot, i.e. the independence of fractal dimension of cluster size, is the criterion for the self-similarity of the structures of the cluster during growth.

The fractal dimension of clusters grown by cluster-cluster agglomeration was lower than that found for the growth of clusters by the accretion of single particles i.e. by the Witten-Sander model (the Witten-Sander model is not discussed here as it is not applicable to aerosol populations except perhaps at very low particle concentration that are not of practicle interest). The considerable dispersion found in the values for fractal dimension for small clusters decreases rapidly with increasing cluster size and at the same time the average value of the fractal dimension increases slightly. This slight dependence of fractal dimension on cluster size is linear and the slope of the line is the parameter termed "sensitivity" in Fig 3.9. Except in the very early stages of agglomeration however the fractal dimension of all the clusters in the population is almost constant indicating that the clusters are self-similar. This is the self-similarity of the population in contrast to the self-similartity of individual clusters mentioned above. Because of this self-similarity of the population of clusters it is possible to calculate a fractal dimension for the whole population of clusters at any given time by plotting on a single diagram the current value of the radius of gyration against cluster size for each of the clusters. The fractal dimension of the population obtained in this way was found to increase from values of about 1.25 to values around 1.7 for median cluster sizes of 60-70 particles. As shown

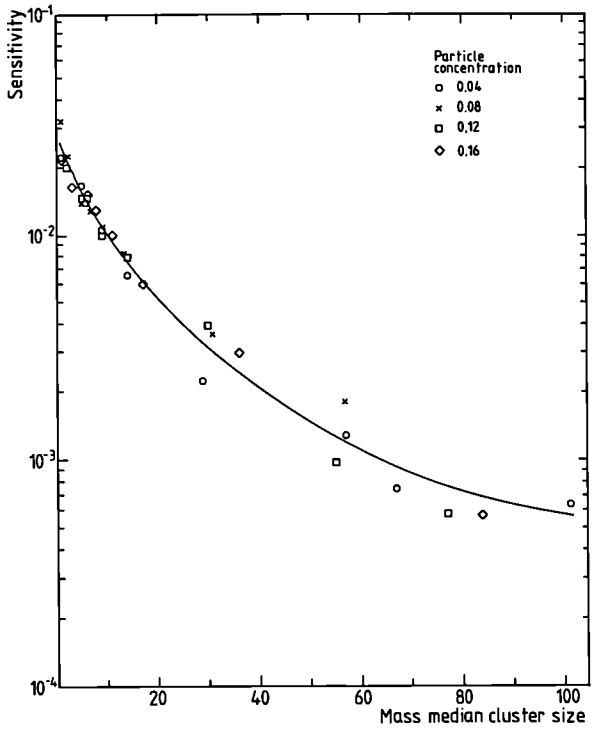

Fig. 3.9 *Dependence of the sensitivity of the fractal dimension to cluster size within a population on the median cluster size of that population*

in Fig 3.10 the fractal dimension of the clusters was independent of the initial particle concentration in the range studied.

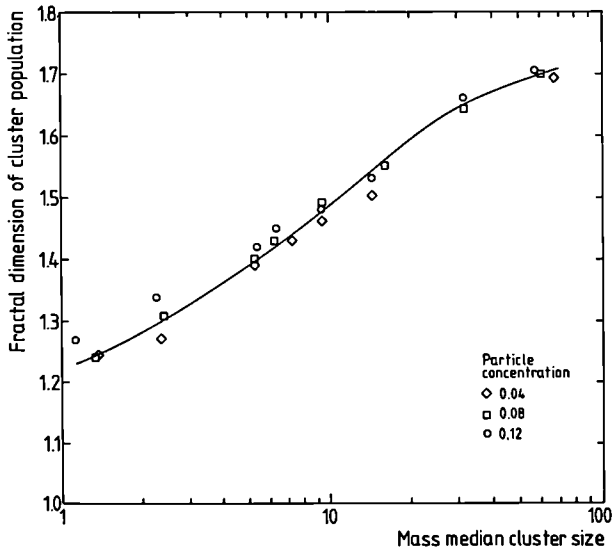

Fig. 3.10 *Agglomeration kinetics*

As shown in Fig 3.11, the agglomeration kinetics were studied using the variation with time of the number concentration and the median cluster size. The decrease in concentration and the increase in median size were nearly identical exponential functions of time. These exponents (0.41 -0.45) were independent of the initial particle concentration in the range studied.

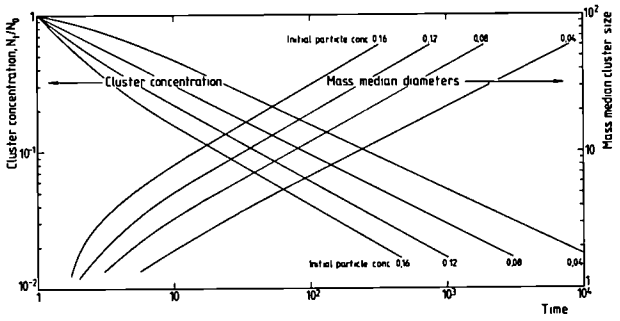

Fig. 3.11 Dependence of fractal dimension on median cluster size

The distribution of cluster sizes depended strongly on assumptions made on cluster mobility but for the case of m=2, i.e. for a cluster mobility inversely proportional to the square of the mass, the cluster sizes were log-normally distributed with geometrical standard deviations in the range 1.6 - 1.7. The log-normal distribution is established quite rapidly i.e. by the time the number concentration reaches about 30% of the initial value. An example of the development of the particle size distribution is shown in Fig 3.12.

References

1. P.Meakin Phys.Rev.B 31 (1985) 564

Alpha Recoil Experiments

Filtration is the most frequently used method of separating particles from gases. Most aerosol filters are not sieves however. A sieve of the fineness required to trap all aerosol particles would have too high a flow resistance and would clog too rapidly to be of practical use. Instead, the commonly used high efficiency filters consist of porous membranes or fibre mats having relatively open structures and relying mainly on impaction and diffusion processes for particle capture. Particle capture in these filters is thus a statistical process dependent on factors such as particle size, shape and electrostatic charge; complete filtration cannot be expected. The degree of filter penetration that is acceptable depends on the application but in the case of radioactive aerosols, in the nuclear industry for example, very high efficiencies are required.

It is thus a matter of practical concern as well as of theoretical interest that alpha-active aerosol particles are reported to penetrate filters more efficiently than inactive particles. The enhanced penetration meant here is not that relatively innocuous increased penetration resulting from the reduced particle capture efficiency of filters for radioactive particles due to their ability to neutralize electrostatic charge [1], but is the much more insiduous phenomenon of the migration of radioactive material through a filter subsequent to the initial capture. Published experimental evidence for such enhanced filter penetration exists [2,3,4] and the enhancement was ascribed to "aggregate recoil" a phenomenon attributed only to alpha-active substances.

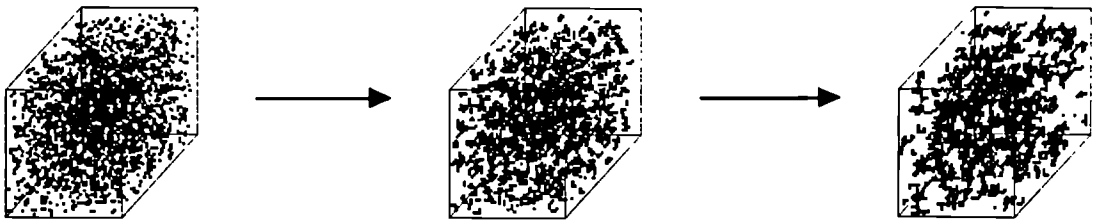

A: Cluster-Cluster Agglomeration

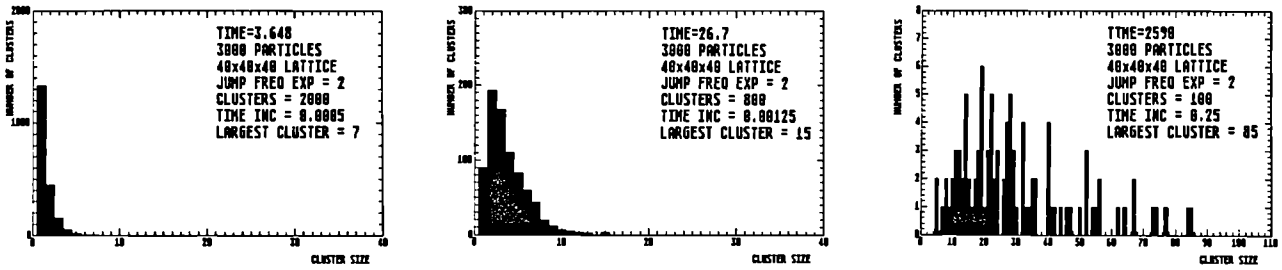

B: Cluster Size Distribution

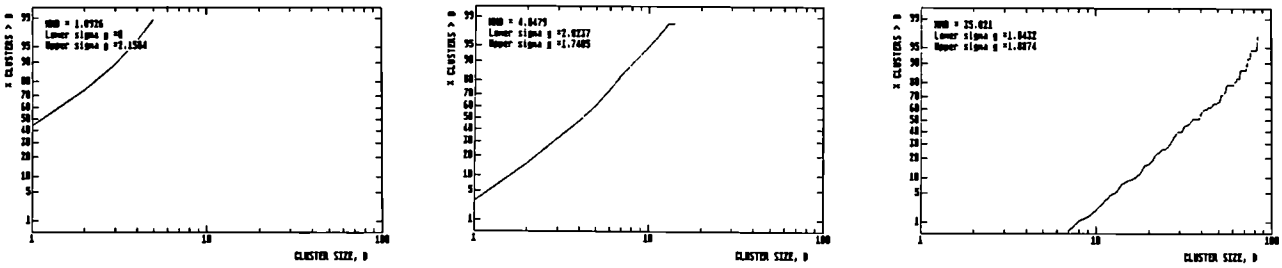

C: Log-Normal Plot of Size Distribution

Fig. 3.12 Development of a log-normal distribution

Usually, an aerosol particle that lands on a filter is totally immobilized. Known exceptions to this rule are a) particles of substances with high vapour pressures and b) particles of substances that are water soluble. Particles of these two classes of substances can show an apparent enhanced filter penetration. These classes of substances can thus be detected downstream of filters in quantities in excess of those expected on the basis of quoted filter efficiencies.

The above type of filter penetration mechanism can apparently also apply to highly radioactive aerosols in the nuclear industry. A study of filter penetration histories in nuclear installations found that episodes of enhanced filter penetration coincided with periods when the moisture content of the air flowing through the filters was abnormally high [5]. This correlation is consistent with the presence on the filters of particles of class b) above. The aggregate recoil hypothesis suggests yet a further mechanism for enhanced filter penetration.

According to the aggregate recoil hypothesis, alpha-active aerosol particles, or fragments of

such particles (Fig. 3.13), are repeatedly resuspended by recoil from alpha decays and so, by a series of jumps, migrate through the filter. Calculations indicate that even for HEPA filters with a penetration factor of 10E-7 only 10 jumps would be necessary for a particle to penetrate the filter [6]. Two versions of this hypothesis may be found in the literature: alpha-recoil resuspension and alpha-recoil fragmentation.

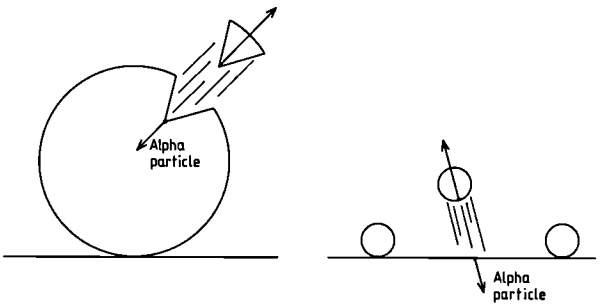

A: Alpha recoil fragmentation B: Alpha recoil resuspension

Fig. 3.13 Hypothetical alpha recoil mechanisms

Alpha-recoil resuspension is the earliest version of the alpha-recoil hypothesis and is due to Makower and Russ [7]. It maintains that when a member of an aggregate of radioactive atoms ejects an alpha-particle in the direction of the substrate upon which the aggregate sits, not only the parent atom, but the entire aggregate containing this atom may be thrown off the substrate by recoil. This mechanisms thus deals with the resuspension of existing particles and applies only to very small, i.e. colloidal size, particles.

Alpha-recoil fragmentation is the more recent version of the alpha-recoil hypothesis and is due to Fleischer [8]. It asserts that a single alpha-recoil nucleus originating in the near surface region of any solid can tear out aggregates of up to 10000 atoms as it erupts from the surface. This version of the hypothesis is thus different from the first in that it proposes the creation of recoil agglomerates from any solid surface e.g. from a large aerosol particle deposited on a filter.

The experimental results presented here concern only alpha recoil fragmentation and indicate that only certain alpha emitting nuclides penetrate filters. This finding is not consistent with the aggregate recoil fragmentation hypothesis. It is suggested that Radon is the only alpha emitting nuclide that penetrates filters in appreciable amounts.

Experimental

Uranium-232 was chosen as the source nuclide because both it and its daughter nuclides all have relatively short half-lives and nearly all are alpha emitters (Fig. 3.14). The alpha-emitters in the decay sequence are: U-232 -> Th-228 -> Ra-224 -> Rn-220 -> Po-216 ->Bi-212/Po-212. The source was prepared by allowing a nitrate solution to evaporate to dryness on a membrane filter. The source did however already contain some daughter products

As a first experiment material ejected from the source by alpha recoil was collected on a filter positioned 1mm away from the source for a period of 15 days. The alpha spectrum of this filter was then measured for 7 days. All the alpha-emitting daughter nuclides down to Bi-212/Po212 were detected but not the source

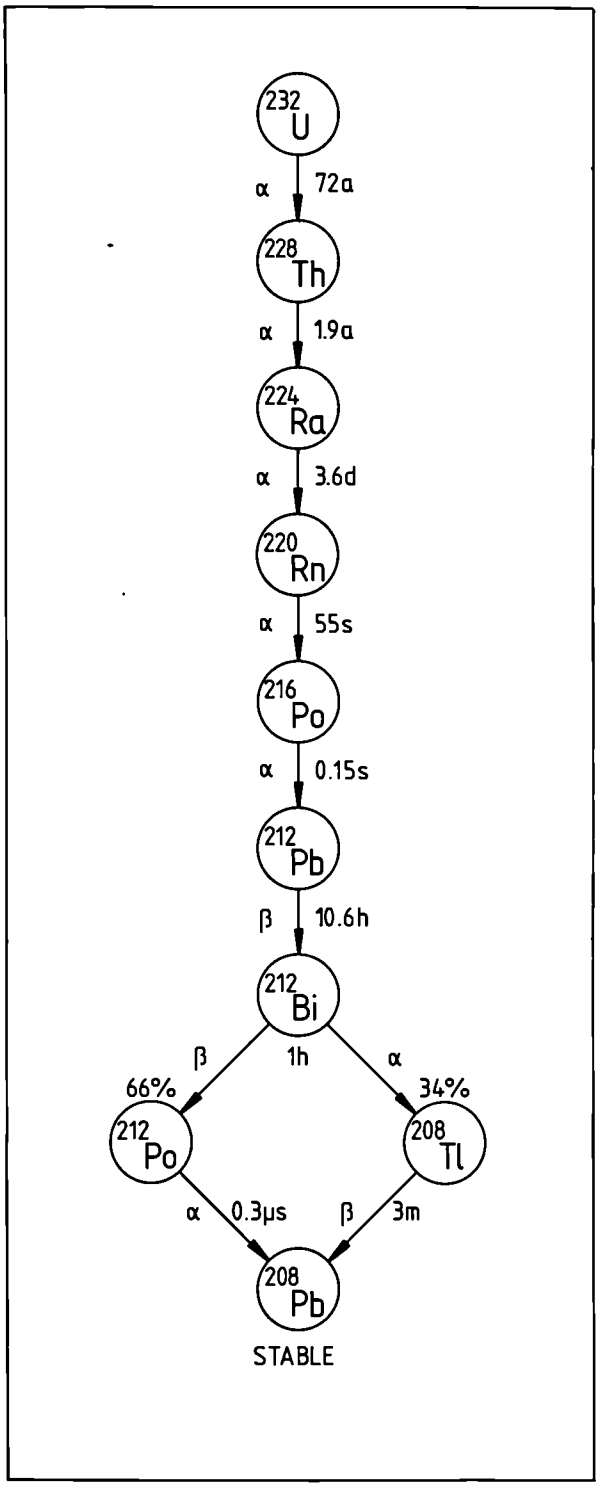

Fig. 3.14 Decay chain for U-232

nuclide U-232 see Fig. 3.15a. If both the source nuclide and daughter nuclides had been detected it would have indicated that aggregates of atoms were ejected from the surface. However, the fact that no parent nuclide was detected does not mean that none was present. The limit of detection in this experiment for the amount of source nuclide was 167% of the sum of the number of atoms of daughter nuclides so that it cannot be excluded that on average 1 to 2 atoms of parent nuclide were transferred with each atom of daughter nuclide. The average size for aggregate recoil particles must therefore be less than 3 atoms. The unfavourably detection limit for the parent nuclide in these measurements was due to the much longer half-life of the parent nuclide compared with the daughter nuclides.

In a second experiment U-232 was deposited on the surface of a high efficiency membrane filter and air was drawn through onto a second similar filter placed behind to collect material penetrating the first filter. After a 7 day exposure the collecting filter was measured for 3 days using an alpha spectrometer. This time only 2 nuclides were detected: Po-212 and Bi-212; see Fig 13.5b. These nuclides are both below Rn-220 in the decay sequence. Rn-220 is the only gaseous nuclide in the sequence indicating that the only species ejected by alpha recoil that was capable of penetrating the absolute filter was the gaseous Radon.

Conclusions

It is concluded from these results that the alpha recoil process ejects daughter nuclides from the source as single atoms but that these single atoms because of their high mobility and high sticking coefficient are rapidly trapped while still inside the labyrinthine passageways of membrane or fibrous filters. Only in the case where the ejected nuclide is Radon, i.e. an inert gas with a low sticking coefficient, is filter

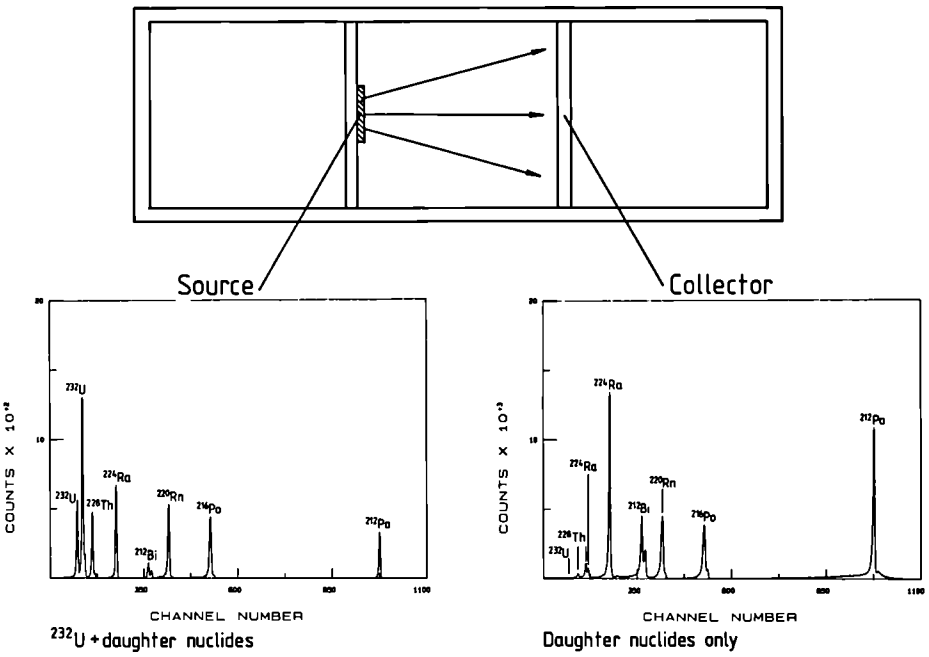

A. Direct collection of alpha recoil species

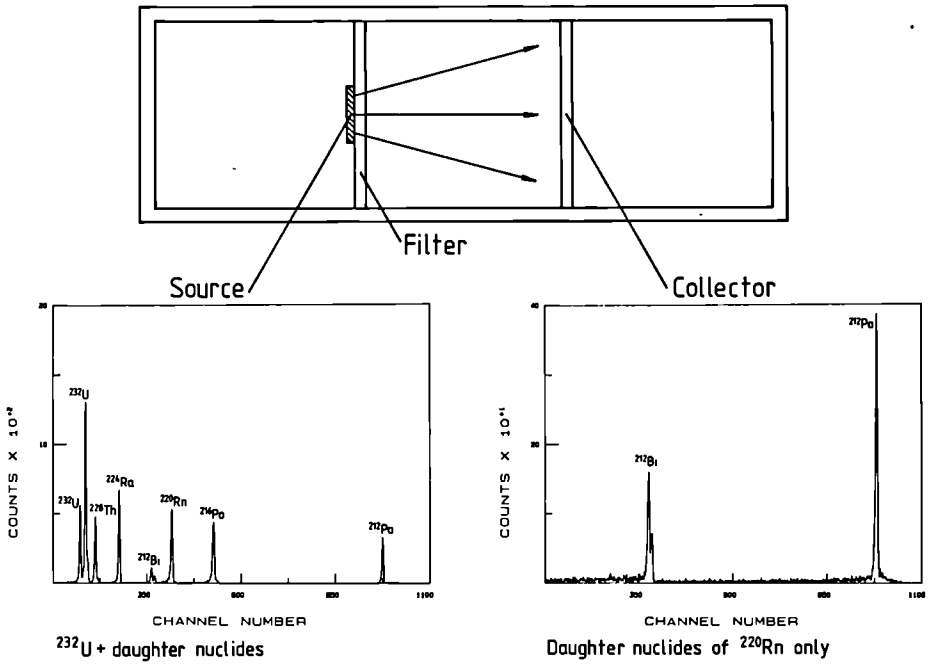

B. Filter penetration of alpha recoil species

Fig. 3.15 Identification of alpha recoil nuclides by alpha spectrometry

penetration possible. Radon subsequently decays so that Radon daughters are also detected downstream of the filter. No evidence was found to suggest that other possible filter penetration mechanisms by alpha active materials e.g. the repeated hopping of nanometer sized clusters, is of any significance compared with Radon penetration.

References

[1] B. Binek, B. Binkova and F. Kepak Jad. Energ. (CS) 32 (1986) 41

[2] H.T. Ryan, K.W. Skrabble, G. Chabot Health Phys. 29 (1975) 796

[3] W.J. McDowell, F.G. Seeley, M.T. Ryan Proc. 14th ERDA Air cleaning Conf., Sun Valley, Idaho (1976) 662

[4] W.J. McDowell, F.G. Seeley, H.T. Ryan Health Phys. 32 (1977) 445

[5] N.A. Frigerio and R.S.S towe Proc. Seminar High Efficiency Air Filtration, EEC Luxembourg (1976) p457

[6] J.A.M.M. Kops, L.C. Scholten, J.P. Deworm and T. Zeevaert Proc.Conf."Gaseous Effluent Treatment in Nuclear Installations" Luxembourg, Oct. 1985, p73

[7] W. Makower and S. Russ Phil.Mag. Series 6, Vol 19 (1910) 100

[8] R.L. Fleischer Health Phys. 29 (1975) 69

Fire Experiments

Fire Experiments under Realistic Laboratory Conditions

Introduction

During the reporting period, the development of the procedures for a standard contaminated PMMA-fire was finished, a high reproducibility of the characteristics of the fire and of the heavy-metal mass inventory having been obtained. On the other hand, the series of fire experiments, in which contaminated specimens of other materials (both combustible and not combustible) are burned in or exposed to the flames of a standard PMMA-fire, were continued.

The complete knowledge of the spreading process was still hampered by the lack of a device suitable to measure, in the actual conditions of concentration, the aerodynamic diameters of the aerosol particles containing the Ce-Eu oxide. For this purpose, a high volume (34 m^3/h) cascade impactor was ordered in march 87, but due to technical problems this instrument was not available during the reporting period.

The Standard PMMA-Fire

Table 3.6 shows thermal data collected during a number of test fires using the standardized five-plate fuel assembly previously described (**TUSR 36**), except for experiment Nr.36 which had only

Table 3.6 Thermal data from a series of test fires

Experiment Nr.	Rate of ventilation [m^3h^{-1}]	M Initial weight of PMMA [kg]	P Maximum Rate of Pyrolysis [$g\ s^{-1}$]	P/M [$g\ s^{-1}\ kg^{-1}$]	Maximum temperature at ceiling [°C]
28	3000	4.9	23.4	4.8	178
29	3000	4.9	23.9	4.9	176
30	2000	4.9	25.0	5.1	208
31	2000	4.9	23.2	4.7	194
32	1000	4.9	22.3	4.6	206
34	450	5.0	21.3	4.3	216
35	500	4.9	24.0	4.9	217
36	3000	1.0	4.5	4.5	53
37	3000	4.9	23.7	4.8	163
38	2000	5.0	21.8	4.4	207
39	1000	4.9	22.3	4.6	218
44	1000	5.0	21.7	4.3	219
45	2000	4.9	21.5	4.4	191
46	2000	4.9	22.3	4.6	200
47	2000	4.9	22.9	4.7	195
48	2000	4.9	23.3	4.8	205
49	2000	4.8	22.7	4.7	209
53	2000	4.9	23.3	4.8	200
54	2000	4.8	22.7	4.7	203
58	2000	4.7	23.8	5.1	220
61	2000	4.9	21.3	4.3	190
62	2000	4.8	22.5	4.7	196
64	2000	4.9	22.0	4.5	201
65	2000	4.8	21.8	4.5	211
66	2000	4.6	21.0	4.6	181
67	2000	4.5	23.3	5.2	196
68	2000	4.6	23.8	5.2	208
70	2000	4.5	21.8	4.8	194
71	2000	4.7	23.9	5.1	216
72	2000	4.9	21.0	4.3	199
76	2000	5.2	23.1	4.4	208
78	2000	5.0	23.6	4.7	200

one plate. The peak value of the pyrolysis rate always occurred between 280 and 380s after ignition of the fire. The parameter P/M (maximal rate of weightloss per initial weight of fuel) is quite important for the prediction of the material spreading power of a fire. Its mean value from 32 fires (including Nr.36) amounts to 4.7 g s-1 Kg-1 with a standard deviationof 0.3 (relative SD of 6 %). This result shows that our standard fire is very reproducible.

As previously shown from continuous CO and CO_2 analysis in the ventilation outlet channel, the combustion of PMMA, under the conditions of the test fires, is practically complete, and the fire power can be calculated from the rate of pyrolysis on the basis of 26 Kw for 1 g s-1. Thus the test fires listed in Tab. 3.6 (except Nr.36) had a thermal power between 0.55 and 0.65 Mw.

The carry-over of contamination from one fire experiment to the next is now minimized with the improved technique described in **TUAR 86**(p.98). The Table 3.5 of **TUAR 86** (p.99) could be completed with the results from 3 further experiments carried out under the same conditions. In this way, data collected in 11 contaminated standard fires are now available, all showing a quite normal time pattern (premature outflow of cerium less than 1 mg, i.e. less than 0.3 % of the initial contaminant). Statistical analysis shows that the mean percentage of cerium transported into the exit channel is 1.4 with a standard deviation of 0.5and the mean percentage of cerium left in the residue is 33 with a S.D.of 6.

In conclusion, apart from a few deviations, which are easy to identify (e.g. Nr.71 and 72 in **TUAR 86**, p.98) and related to extraneous and typically non-reproducible transfer of contamination from preceding experiments (which of course cannot occur in a single accidental fire), the reproducibility of the heavy-metal mass inventory after a standard experimentis quite high.

Other Contaminated Materials Exposed to a Standard Fire

Studies of the transport of Ce-Eu oxide particles from surfaces of combustible or non-combustible materials contaminated with this oxide, and exposed to a PMMA-fire, are being pursued and first results are reported here. As described in **TUAR 86**, one plate of the test material, with a five-fold increased contamination level (0.5 mg cm-2), is put on top of the usual stack of 5 uncontaminated PMMA-plates, burning under the same conditions as the standard fire studied up to now.

The following materials, widely used for the construction and equipment of glove boxes, have been separately tested : stainless steel and aluminium, polycarbonate, polyethylene and neoprene. Polyvinylchloride (PVC) will be studied at a later stage because of the toxicity and the corrosiveness of its combustion products.

Data measured up to now are presented in Tab. 3.7 Further experiments are necessary for some materials, but at the present stage, the following points can be observed :

- the somewhat higher spreading of contamination from painted than from uncovered

Table 3.7 Transport of heavy metal from fires involving contaminated plates of different materials

Type of Contaminated Material	Percent of Original Contaminant Cerium		
	Transported into vestilation exit channel	Left on the surface	Left in the residue
Stainless steel	1.7	90	*
Stainless steel	0.2	86	0.3
Painted stainless steel	0.3	78	0.3
Painted stainless steel	2.0	62	0.4
Painted aluminium	2.1	*	20
Polycarbonate (1.5 kg)	0.5	-	*
Polycarbonate (0.9 kg)	0.4	-	63
Polyethylène (1 kg)	1.0	-	23
Polyethylène (1 kg)	1.3	-	42
Neoprene (87 g)	5.9	-	13
Neoprene (32 g)	2.3	-	19

Contamination level 0.5 g/cm²
(*) not measured

surfaces due to the combustion of the paint,

- the results for contaminated polyethylene, not significantly different from those obtained with contaminated PMMA,

- the specific behaviour of the poorly igniting polycarbonate, where the greater part of the Ce-Eu oxide remains in the voluminous residue,

- the greater spreading of contamination from neoprene, which ignites quasi flashlike.

Resuspension of Uranium-Plutonium - Oxide Particles from Burning Plexiglas

Nuclear fuel materials such as Uranium-Plutonium oxide must be handled remotely in gloveboxes because of their radiotoxicity. These gloveboxes are frequently constructed largely of combustible Plexiglas sheet. To estimate the potential airborne spread of radioactive contamination in the event of a glovebox fire, the resuspension of particles from burning Plexiglas must be quantified.

A combustion chamber 500mm tall with a cross-section 100 x 100mm was installed in a glovebox to enable Plexiglas contaminated with uranium-plutonium oxide particles to be burnt under controlled conditions (Fig 3.16). A constant combustion rate was achieved by burning hollow cylinders of Plexiglas in a controlled upward air flow (Fig 3.17). The weight loss of the specimens with time was recorded continuously with an electronic balance, the O_2, CO and CO_2 content of the filtered combustion gases was measured by infra-red absorption and the combustion temperature was monitored with a vertical array of thermocouples.

As shown in Fig 3.18 surface bubble formation is a prominent feature of Plexiglas combustion and is believed to be the mechanism of particle resuspension. The resuspension efficiency of bursting bubbles is a function of the product of the number of bubbles and the energy with which they burst. Fig 3.19 shows that this product is appreciably above zero only in the

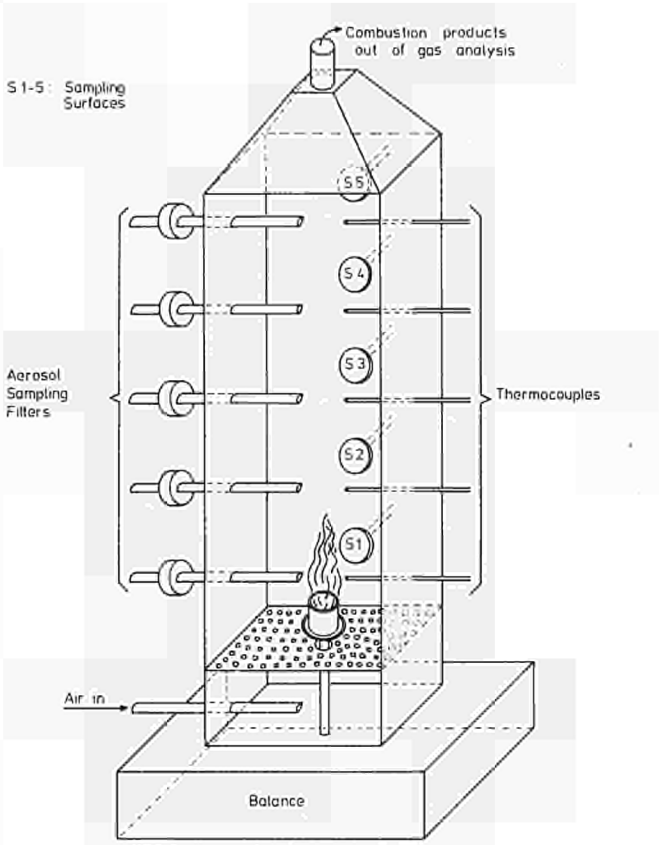

Fig. 3.16. *Apparatus for burning contaminated Plexiglas under controlled conditions*

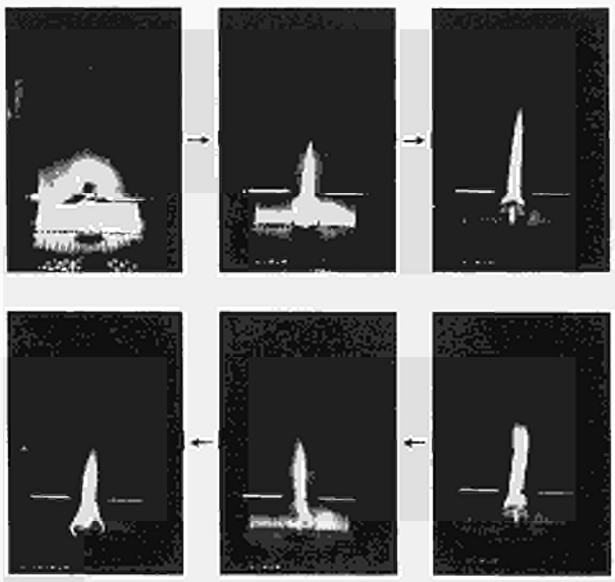

Fig. 3.17. Constant rate combustion of contaminated Plexiglas

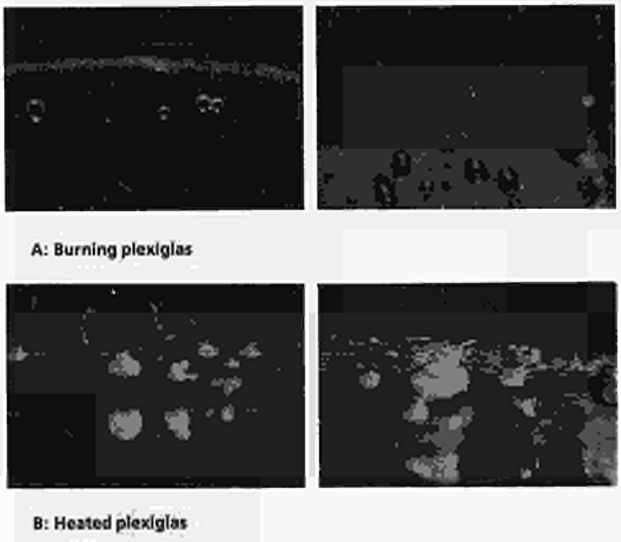

Fig. 3.18. Bubble formation in a) burning Plexiglas and b) heated Plexiglas

relatively narrow temperature range of 180-210C.

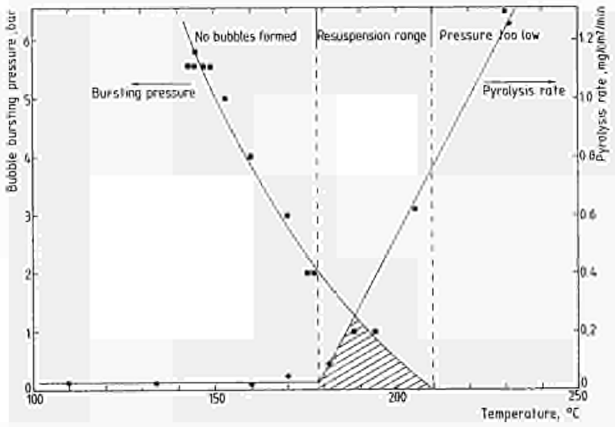

Fig. 3.19. Dependence of bubble bursting pressure and pyrolysis rate on temperature

The degree of resuspension of the uranium-plutonium oxide was determined by taking filter samples of soot and resuspended contaminant. The amount of radioactive material on the filters was determined by alpha counting. In a similar way the amount of contaminant deposited on the walls and floor was determined from measurements on deposits collected on removeable sampling surfaces placed in the combustion chamber for this purpose.

The duration of these experiments was rather short at about 7 minutes but temperatures of 600-700C were achieved which is not untypical of a large scale fire and the reproducibility was good. The amount of contaminant used was generally 3mg on a 3g Plexiglas specimen i.e. 1mg/g Plexiglas which corresponds to a very high level of contamination.

Experiments were made both with polydisperse dusts obtained by abrading sintered oxide fuel pellets and on size fractions of such dusts obtained with a cascade impactor. There was a strong dependence of the degree of resuspension on particle size as shown in Fig 3.20. The apparent minimum in the degree of resuspension at 4-5

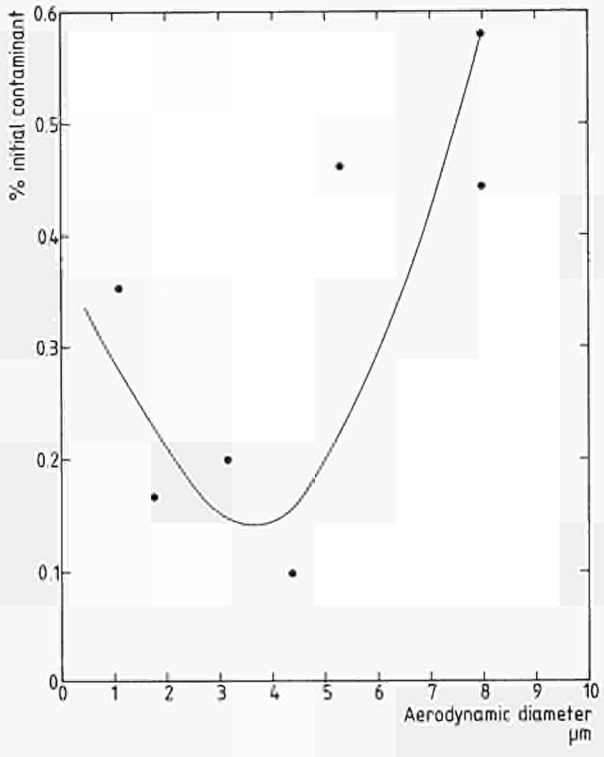

Fig. 3.20. Dependence of degree of resuspension on particle size

microns particle diameter is at first sight surprising. A continuous decrease in resuspension for increasing particle size was expected. Two possible explanations for the enhanced resuspension of the larger particles are: 1) The large particles obtained with the cascade impactor are in fact agglomerates of smaller primary particles which separate from each other in the fire and are resuspended independently, 2) The large particles, whether agglomerates or not, are resuspended and act as agglomeration centres for soot particles thus aquiring a fluffy coating which reduces their sedimentation velocity and enables them to be transported by the air stream. Further experiments are required to clarify this question.

For polydisperse uranium-plutonium oxide dust, the material balance made after the experiments yielded the following typical values: 75% in the solid residue, 5% on the floor, 18.5% on the walls and 1.5% airborne. It thus appears that about 80% of the contaminant remains in the immediate vicinity of the source and that 20% can be transported some distance in aerosol form. The amount of contaminant that remains airborne or deposits on surfaces by thermophoresis or diffusion depends of course on many parameters such as flow rates, temperature gradients and the geometry of the experiment and cannot be generalized easily. Nevertheless the value of 1.5% for airborne material is very similar to the values obtained in other experiments in this laboratory for large scale fires (5kg Plexiglas, 160m^3 fire room) using Ce/Eu oxide as a substitute for U/Pu oxide.

Collaboration with External Organisations

Lavoro e Ambiente, Bologna and University of Bologna

University of Antwerp

Kernforschungszentrum Karlsruhe

3.3 Reprocessing of Nuclear Fuels (REPRO)

Introduction

One activity in sub-project REPRO is devoted to the head-end processes for advanced fuels; a feed solution compatible with the requirements of the Purex process is to be obtained. The studies aim at a description of the head-end reactions taking place upon dissolution of nitrides in nitric acid. Here, the composition of the off-gas is being studied with special interest in the evolution of elemental N_2. Comparisons are made with the behaviour of oxide fuels. The formation of ammonium ions in the dissolver solution is a further subject of investigation; these ions could have adverse effects in the Purex process. The exchange reactions taking place between ^{14}N and ^{15}N upon dissolution of MN in nitric acid - in the case the fuel has been fabricated with nitrogen enriched in ^{15}N - are also being examined.

Another activity is concerned with separation of actinides from fuel or waste solutions. The aim is to recover the actinides before they enter the waste streams. The chemical behaviour of Np is of particular interest in these studies.

Fuel Dissolution Studies

Analyses of Off-gas Composition and of Ammonium Ions in the Solution

The formation of gases (N_2, N_2O, NO and NO_2) and of NH_4^+ ions have been investigated as functions of temperature and nitric acid concentration. Fig. 3.21 shows the dependence on the temperature of dissolution of UN in 6 M HNO_3.

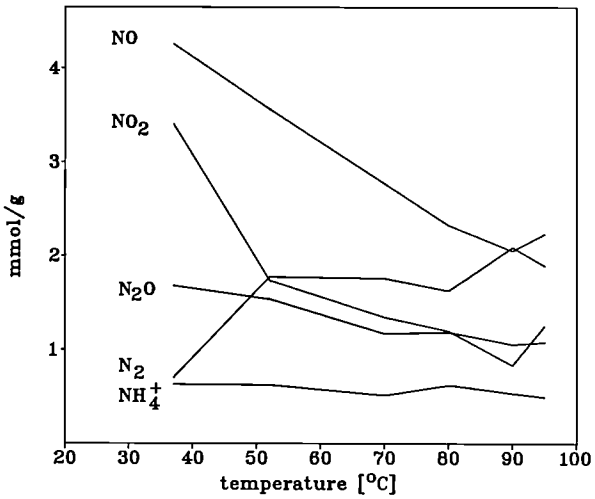

Fig. 3.21 The concentration of the off-gas components NO, NO_2, N_2 and N_2 as well as the concentration of ammonium ions in the dissolver solution in mmol/gramme upon dissolution of UN in 6 M nitric acid as a function of the temperature in °C.

The amounts of nitrogen oxides decrease with temperature increase, whereas the elemental nitrogen amount increases. The NH_4^+ value is constant at about 0.6 mmol/g UN dissolved, corresponding to about 15 % of the nitride nitrogen. The NH_4^+ amount found in the case of (U,Pu)N dissolution is similar to that of the UN dissolution (≈ 17 % of the nitride nitrogen).

Similarly, Fig. 3.22 shows the dependence on the nitric acid molarity; the concentrations of all the gases decrease at higher acidity (N_2 and N_2O only slightly). Again, the ammonium concentration is not much affected.

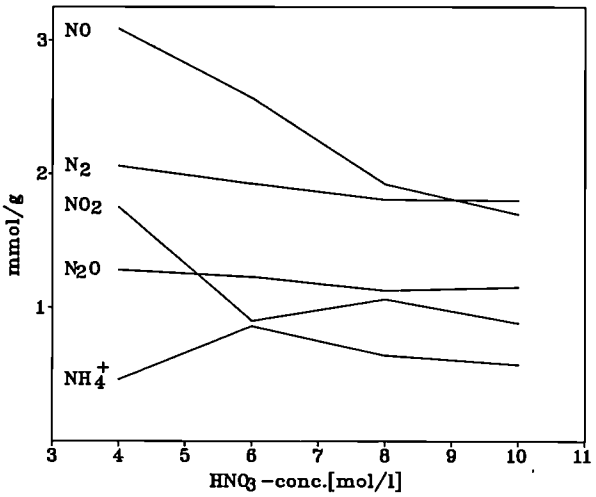

Fig. 3.22 The concentration of the off-gas components NO, NO_2, N_2 and N_2 as well as the concentration of ammonium ions in the dissolver solution in mmol/gramme upon dissolution of UN in nitric acid as a function of the acid molarity.

Activation Energy of Dissolution of Uranium Dioxide

Data on the dissolution of UO_2 in nitric acid at various temperatures allow to calculate the activation energy of the reaction. Fig. 3.23 shows the reaction rates as a function of time for the dissolution of UO_2 in 6 M HNO_3.

In contrast to UC and UN (see TUAR 86,104), the curves from UO_2 have an irregular shape probably due to phase inhomogeneities in the starting material. The linear part around 20% allows to calculate the reaction rate constant at 20 % dissolution and to draw the Arrhenius plot.

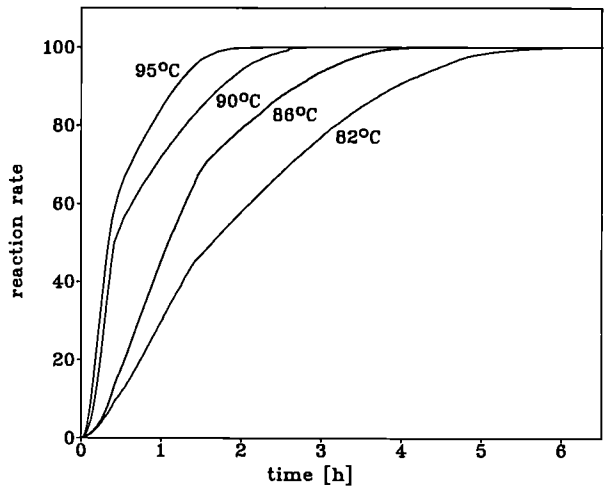

Fig. 3.23 The reaction rate of dissolution of UO_2 in 6 M HNO_3, expressed as percent dissolved, as a function of time.

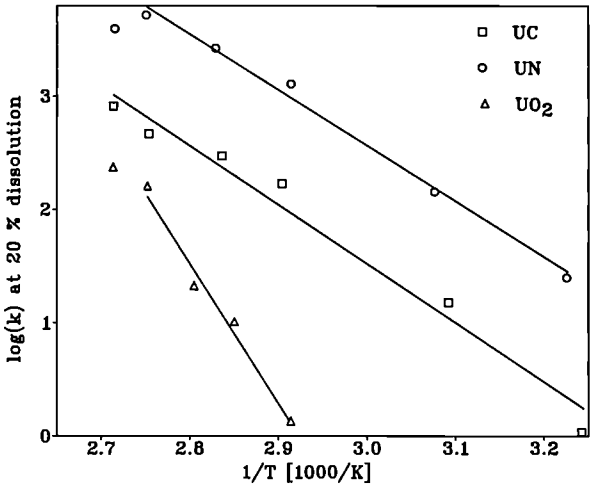

Fig. 3.24 The log of the reaction rate constant, k, at 20 % dissolution for the dissolution process of UN, UC, and UO_2 in 6 M nitric acid as a function of reciprocal temperature (Arrhenius plots).

In Fig. 3.24 the log(k) values as a function of 1/T are given for UN, UC and UO_2.

A summary of dissolution parameters for the dissolution of UN, UC and UO_2 in 6M HNO_3 at 90 °C is given in Tab. 3.8.

Table 3.8 Dissolution parameters, gas volumes and activation energies for the dissolution of UN, UC,and UO_2 in 6 M HNO_3 at 90 °C.

Fuel	Sample weight [g]	Dissolution time [h]	Gas volumes [ml/g]					E_a [kcal/mol]
			N_2O	NO	NO_2	CO_2	N_2	
UN	1.478	0.22	23.5	46.8	18.5	0.3	46.8	9.9
UC	1.904	0.65	9.1	127.5	64.8	24.5	-	10.4
UO_2	1.031	3.00	-	52.5	94.4	-	-	22.8

As described in the literature [1] the Arrhenius plot is linear up to 90 °C. Above that temperature, the reaction velocity does no longer increase significantly, for nitrides it even decreases.

Dissolution of UN in Nitric Acid Highly Enriched in N-15

Upon dissolution of UN in HNO_3 the following nitrogen compounds could be identified: NO_2, NO, N_2O and N_2 in the gas phase and NH_4^+ ions in the solution. To get further information about the formation of these compounds and the dissolution mechanisms, UN is dissolved in ^{15}N enriched HNO_3, a gas sample is taken at the time of the maximum gas evolution rate and the isotopic composition of nitrogen is analysed by GC-MS.

The gas chromatographic separation of nitrogen oxides causes some problems, because the most suitable column materials require a pre-conditioning of the solid phase with NO_x. This gives rise to an isotopic exchange during separation, making these columns useless for our experiments. A compromise is an inert OT column, which needs no pre-conditioning. Unfortunately, this type of column does not separate the nitrogen compounds completely.

In a first test Cu was dissolved in nitric acid; the chromatogram obtained is shown in Fig. 3.25. The relevant mass abundances in the four peaks are given in Tab. 3.9.

The peak at 5.1 min contains only NO_2, the peak at 1.6 min contains NO and NO_2 and the peak at 0.9 min contains N_2O, NO and N_2. N_2 comes from the original atmosphere in the dissolver tube and is the main constituent in the 0.6 min peak. In some cases, when 2 or 3 gases contribute

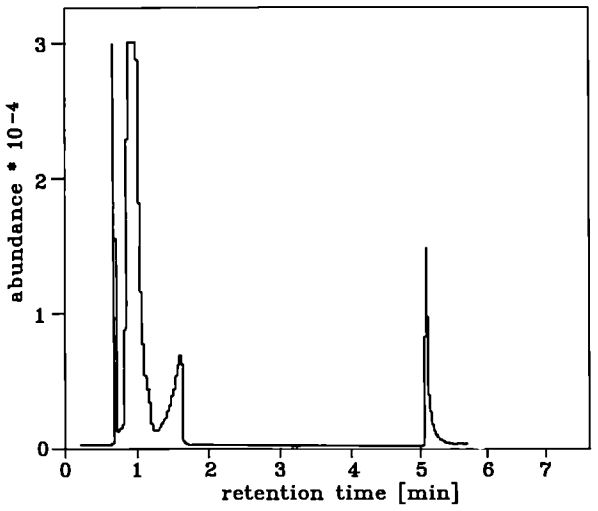

Fig. 3.25 Gas chromatographic separation of nitrogen compounds in the off-gas from the dissolution of copper in 5 M HNO_3.

to the same mass, a deconvolution of the chromatographic peak is necessary in order to calculate the isotopic composition of nitrogen in the different components.

Table 3.9 Dissolution of copper in 5 M HNO_3. Mass abundances in the four chromatographic peaks, shown in Figure 3.25, in relation to their retention time, t_R, in minutes. Reference mass: 30

T_R [min] Mass	0.6	0.9	1.6	5.1
14	30.7	38.2	6.8	3.8
15	0.4	0.4	0.4	0.4
28	158.9	106.7	0.4	0.5
30	100.0	100.0	100.0	100.0
31	0.8	0.7	0.8	1.3
44	0.1	3.6	0.4	0.9
46	0.0	0.1	10.6	125.2
47	0.0	0.0	0.1	1.1

The same experiment with nitric acid highly enriched in ^{15}N gives a chromatogram similar to the one in Fig.3.25; the corresponding mass abundances are listed in Tab. 3.10.

Table 3.10 Dissolution of copper in 5 M HNO_3 highly enriched in ^{15}N. Mass abundances in the three chromatographic peaks, see Figure 3.25, in relation to their retention time, t_R, in minutes. The first peak at 0.6 minutes, containing only N_2 was left out of the Table. Reference mass: 31.

T_R [min] Mass	0.9	1.6	5.1
14	6.9	0.6	1.4
15	16.6	7.6	5.4
30	3.7	2.7	10.2
31	100.0	100.0	100.0
44	1.1	0.3	1.7
46	0.1	0.2	11.0
47	0.1	7.1	111.0

Although the column used in these experiments needs no pre-conditioning an adsorption especially of NO_2 was observed and about 5 consecutive injections are required to give a stable isotopic composition (Fig. 3.26).

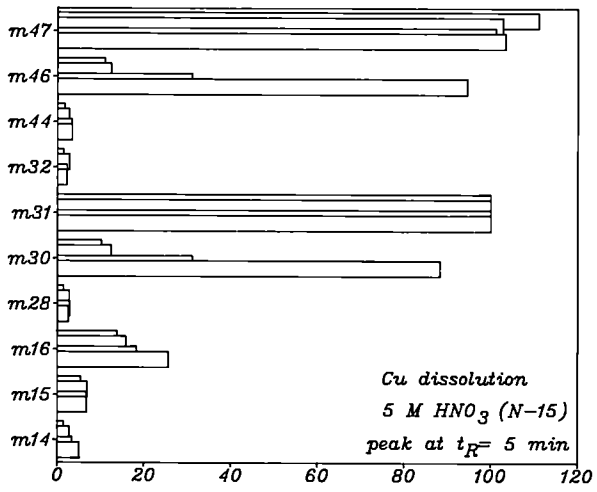

Fig. 3.26 Evolution of the relevant mass positions upon 5 consecutive injections of the same gas composition onto a column previously loaded with another gas composition. Dissolution of copper in 5 M HNO_3 enriched in ^{15}N.

A first experiment with UN dissolved in HNO_3 of normal isotopic composition gave the chromatogram shown in Fig.3.27.

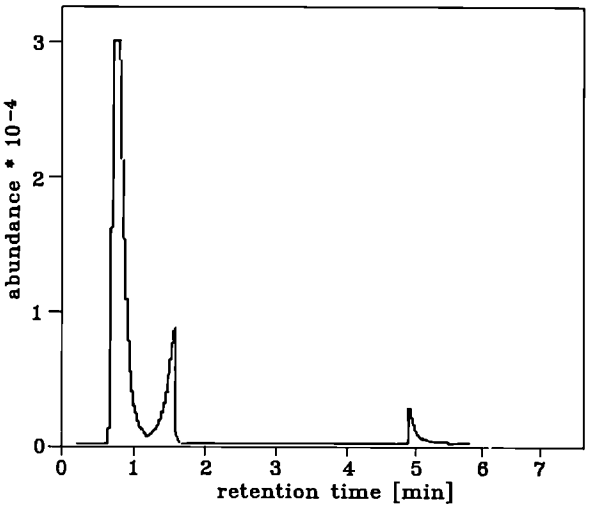

Fig. 3.27 Gas chromatographic separation of nitrogen compounds in the off-gas from the dissolution of UN in 5 M HNO_3.

The first peak in the chromatogram has disappeared (cf Fig. 3.25). Table 3.11 gives a summary of the ^{15}N contents in the different nitrogen containing constituents for the three dissolutions mentioned above.

Table 3.11 Content of ^{15}N, in percent, in the nitrogen compounds in the off-gas from dissolutions of Cu and UN in 5 M HNO_3. The acid contained nitrogen of the natural isotopic composition or it was highly enriched in ^{15}N.

Dissolution		Cu in N-14 HNO_3	Cu in N-15 HNO_3	UN in N-14 HNO_3
Constituent	t_R			
N_2	0.9	-	-	0.43
N_2O	0.9	-	-	0.33
NO	0.9 1.6	0.77 0.72	96 98	1.00 0.80
NO_2	5.1	0.87	91	2.80

The copper dissolution produces only NO and NO_2 and the values for NO_2 indicate that the column shows memory effects for this gas. The NO values obtained from two different peaks correspond quite well.

The next step in these studies will be the separation of off-gas compounds from UN dissolution in ^{15}N enriched HNO_3. Furthermore the isotopic composition of the ammonium ions in the dissolver solution has to be determined either after precipitation or after transformation into gaseous NH_3.

Actinide Separation and Purification

Absorption Spectroscopy of Neptunium

The data treatment programme for the Cary 17 spectrophotometer has been changed to cater for the acquisition of data in the near infrared, this wavelength region is of particular interest in the analysis of Np in its higher oxidation states. The multicomponent analysis matrix was correspondingly extended to include also Np.

The dependence of the molar extinction coefficient on the acidity of nitric acid has been published for solutions of uranium, plutonium and americium [2, 3, 4]; however there is a lack of such data on neptunium.

Extensive series of absorption spectra of the elements U, Np, Pu and Am in their various oxidation states have been recorded using the remote Cary 17 installation; one of the aims of these efforts being to re-evaluate the absorption spectra of these species in nitric acid medium (spectral fine structure) and to re-measure the molar extinction coefficients. Surprisingly enough, such spectra are not very well described in the existing literature. The data acquisition and treatment system developed in our group and applied over the years to actinides should be especially well suited to this kind of investigations. An example of such a spectrum is shown in Fig. 3.28.

The behaviour of Np(V) has been investigated as a function of the strength of HNO_3. The complete spectrum in the range 350-1350 nm is shown in Fig. 3.29; whereas Fig. 3.30 presents the molar extinction coefficient for the most intense absorption band at 981 nm, e, as a function of the nitric acid acidity. As the strength of the acid increases, a strong decrease in e is seen, which is assignable to changes in the coordination in the room around the NpO_2^+ ion, water being replaced by NO_3^-.

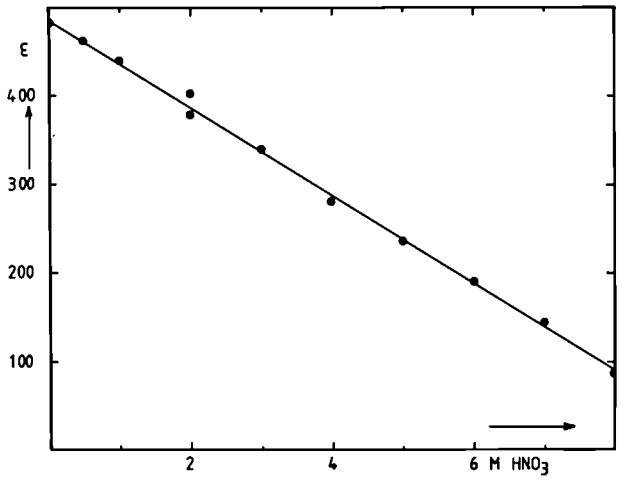

Fig. 3.30 The molar extinction coefficient, e, of Np(V) at the principal absorption band at 981 nm as a function of the nitric acid molarity.

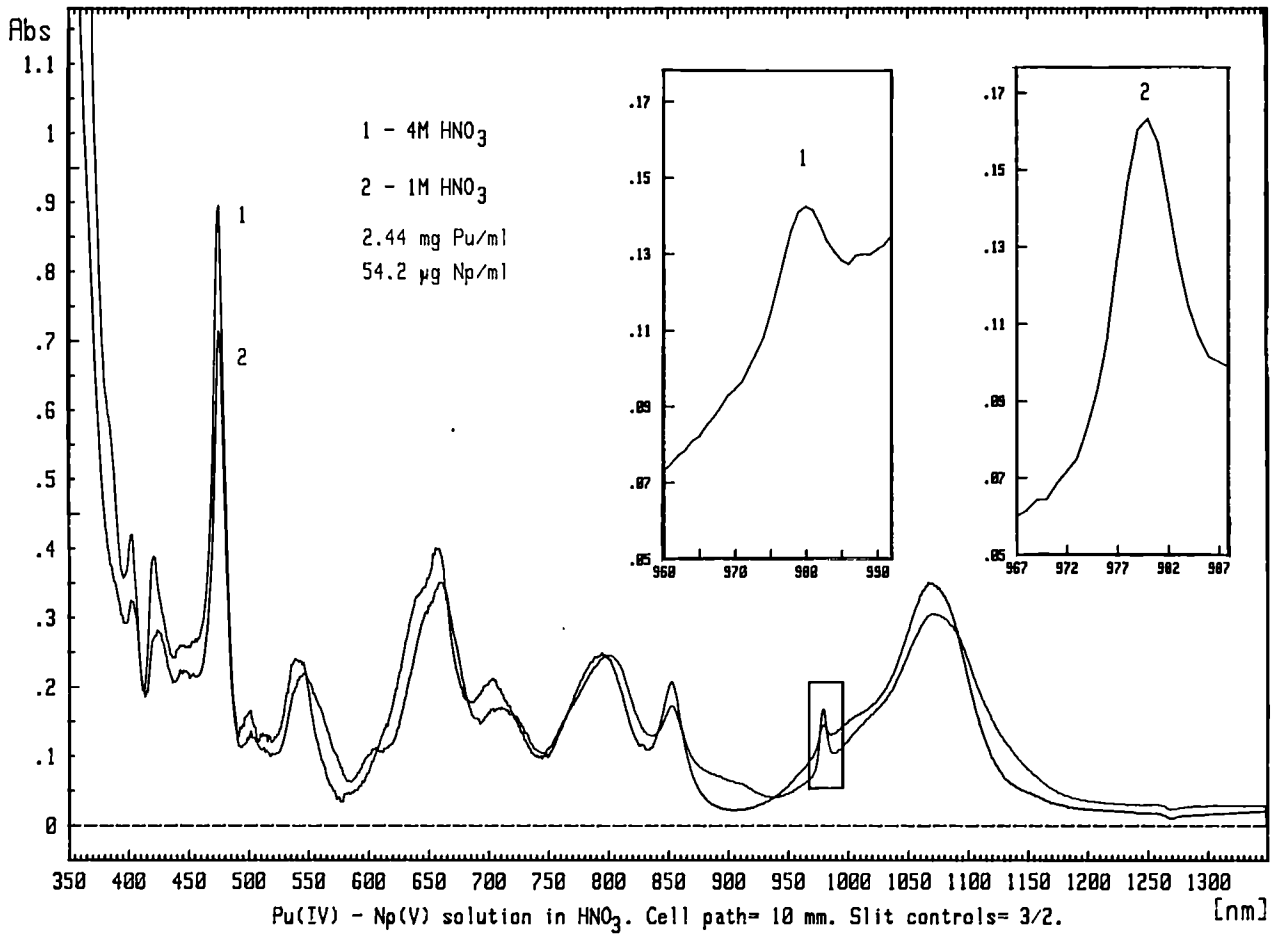

Fig. 3.28 Absorption spectrum of Np(V) and Pu(IV) in nitric acid. Curve 1: 4 M HNO_3, curve 2: 1 M HNO_3.

The curve in Fig. 3.30 can be used for a fast estimation of the concentration of Np in nitric acid, when the molarity of the acid is known.

In connection with the above study an analytical method was developed for the determination of neptunium in the presence of plutonium; the method is based on spectrophotometry and uses the characteristic absorption band of Np(V) at 981 nm in 4 M nitric acid medium.

Integral Separation Scheme by the Use of TBP and Ion Exchange (HPLC)

The work on actinide separations from fuel or from waste solutions was continued. A small ion exchange column (HPLC-I) has been placed between the bigger columns to obtain a certain pre-concentration of the Np species and of the fission products and to save capacity on the main column. The tests show that the monovalent ions pass through the column in 1 M HNO_3, whereas ions in higher oxidation states are retained. Cs^+

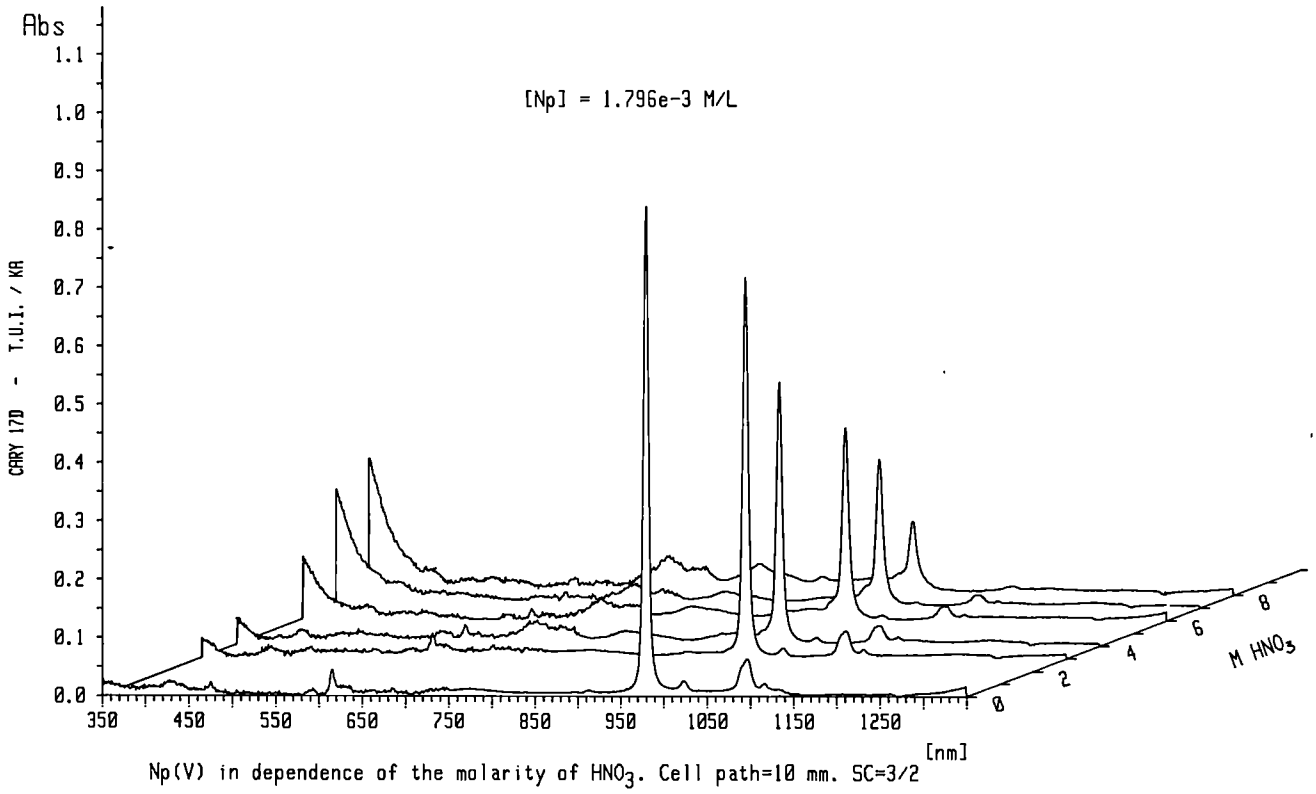

Fig. 3.29 The absorption spectrum of Np(V) in the wavelength range 350-1350 nm as a function of the nitric acid molarity. The cell path was 10 mm, and the slit control of the Cary 17 spectrometer was set at 0.26 mm (at peak intensity)

and NpO_2^+ can thus be separated already on the pre-column.

The effects of combining columns containing TBP impregnated beads and ion exchange resin, respectively were studied with the aim of further improving the Ln/An separation. Fig. 3.31 shows a complete separation of U, Nd and Ho in 4 M HNO_3, the solution contained a 150 fold excess of uranium. The concentrations were measured with the OMA-2 spectrometer using a flow-through

set-up and assigning the wavelengths 415 nm, 571 nm and 439 nm to UO_2^{2+}, Nd^{3+} and to Ho^{3+}, respectively.

All the four columns (2 of each type) are quasi neutral in their reaction at the outset. The TBP-I column is then pre-loaded with 0.5 litre

1M HNO_3, while the outlet from the column is kept open. Thereupon, the feed solution is loaded onto the column, a washing step with 1 M HNO_3 follows; at the appearance of Nd/Ho at the outlet of TBP-I the stream is led into TBP-II. Similarly, only when Nd/Ho is seen at the outlet of TBP-II the HPLC-I column is brought into service. At the same time it is verified, if the rare earth ions have left the TBP-I colunm completely, and if they remain on the HPLC-I column. If so, the washing with 1 M HNO_3 is stopped and the elution of uranium from TBP-I with water is started (see bottom right side part of Fig. 3.31). Alternatively, the washing could continue until uranium is starting to leak out of the TBP-I column. Now, the lanthanides and the higher actinides are situated in the HPLC-I column; the connection to HPLC-II is established and the lanthanides and the higher actinides of interest

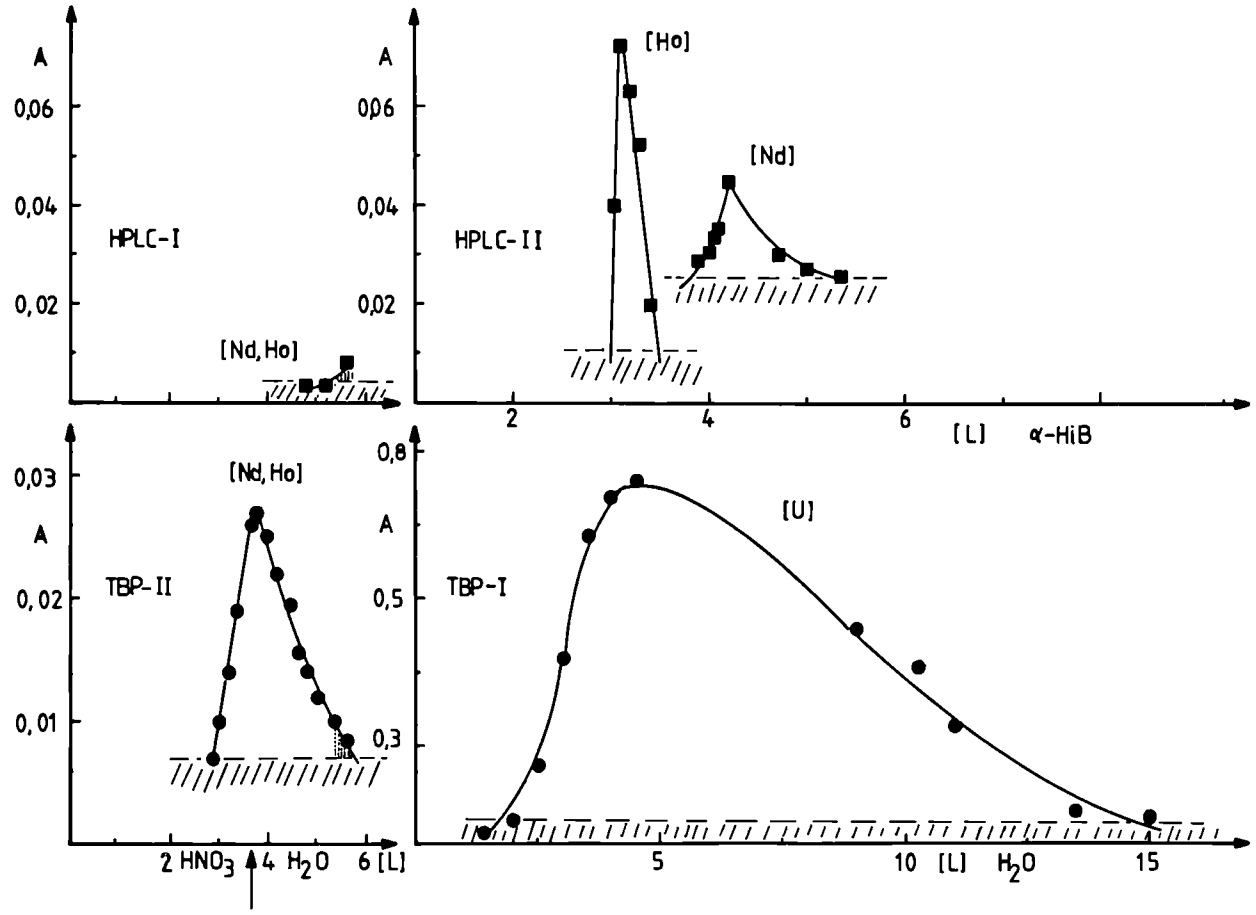

Fig. 3.31 Absorption spectra taken with the OMA-2 spectrometer during washing andelution of the four chromatographic columns TBP-I, TBP-II, HPLC-I, and HPLC-II, as explained in the text. The elements Nd, Ho, and U were followed on their way through the system as a function of the volume of the washing and eluting fluids, respectively.

are eluted from HPLC-II with alpha-hydroxyisobutyric acid, as described earlier, e.g. in [5] or in TUAR-86, p 105.

The HPLC separations were supplemented with a few tests on real highly active waste. With the inclusion of the elution spectrum of Pu(III) in the array of spectra the actinides Np, Pu, Am, and Cm in their various oxidation states have all been covered and the work was stopped for the time being. Sufficient data on and experience with the separation scheme are available to warrant a successful resumption of the work in due course.

Comparison of Different Separation Methods for Plutonium

The three separation methods for plutonium: TBP-extraction, TTA-extraction and ion exchange have been compared with respect to their capabilities of removing very small amounts of plutonium from uranium. The aspects of scaling-up were also considered. TTA-extraction gave the most promising results and provided a decontamination factor of about 800 at the 30 ppm level of plutonium. Details will be given elsewhere.

Study of Colloids of Plutonium

The generation of colloids of plutonium is an important process in the chemical behaviour of plutonium in natural aqueous solutions. In neutral solution the tetravalent plutonium ion readily becomes hydrolyzed and hence gives rise to colloid formation. A number of factors has influence on this process, such as the pH, the specific activity of the plutonium, the aging of the solution, etc.

The formation of Pu(IV) colloids and their stability with time have been investigated by spectroscopy using the Cary 17 instrument; furthermore different pH conditions were used. Liquid-liquid extraction with TBP was also employed to verify the presence of collodial plutonium in very low concentrations, beyound the limit of spectroscopic detection. The specific activity of the plutonium, i.e. its isotopic composition also plays a significant role in the colloid formation through its influence on the valency of the plutonium.

The results, published elsewhere [6], were compared with those from plutonium in higher concentration as used in the Purex process, in which a tailing in the extraction is often triggered by the formation of non-extractable colloids.

The Behaviour of Technetium and Neptunium in Natural Aquatic Systems

In a co-operation with IHCh, KfK and Institut für Radiochemie, TU München contribution was given to a study on the above mentioned subject [7]. The following subtopics were of special interest: The solubilities of NpO_2 and $NpO_2(OH)$ in water, NaCl solutions and in carbonate solutions, the hydrolysis of $NpCl_4$ in NaCl solutions, the oxidation of the Np(IV) to Np(V), and speciation of the pentavalent neptunium in HCO_3^-/CO_3^{2-} solutions at different pH values.

Alpha- and Gamma Spectroscopy

The determination of the nuclides Np-237, Pu-238, Pu-239, Am-241 and Cm-244 by alpha-spectroscopy has been optimized as regards the sample preparation, especially the heat treatment of the counting discs and other parameters; series of calibration curves were run. These operations were all carried out in a new special glovebox, dedicated to alpha- and gamma spectroscopy. The box contains 4 interconnected compartments, in which the sample preparation and the alpha counting on a multichannel analyzer take place.

References

[1] B. Herrmann, KfK Report 3673 (1984).

[2] H. Schmieder, E. Kuhn, W. Ochsenfeld, KfK Report 1306 (1970).

[3] P. Pascal, Nouveau Traite de Chimie Minerale, Masson et Cie 1962.

[4] W. W. Schulz, The Chemistry of Americium, TID 26971 (1976).

[5] C. Apostolidis, H. Bokelund, A. Moens, M. Ougier, Inorg. Chim. Acta 140 (1987) 253.

[6] C. Apostolidis, P. Dressler, B. Kanellakopulos, J. I. Kim, Conference on Chemistry and Migration Behaviour of Actinides and Fission Products in the Geosphere, Munich September 1987, Proceedings p 159.

[7] C. Apostolidis, B. Kanellakopulos, J. I. Kim, F. Klein, J. Müller, J. T. Vida, Conference on Chemistry and Migration Behaviour of Actinides and Fission Products in the Geosphere, Munich September 1987, Proceedings p 143

Collaboration with External Organisations

Institut für Heisse Chemie, KfK

Institut für Radiochemie, TU München

4 Actinide Research

Objectives

The aim of the project is the understanding of the properties of actinide-containing solids in terms of the electronic structure of their constituents and of the 5f electron contribution to the bond. The objective is attained by the experimental and theoretical investigation of selected properties of, especially, intermetallics and binary actinide compounds, with emphasis on the less known elements Pa, Np, Am, Cm, Bk, and Cf. This requires the availability, hence preparation of well characterised samples (often as single crystals) of known composition, crystal structure and impurity content.

The effectiveness of the actinide project is much enhanced by extensive collaborations throughout Europe and strong connections with a number of US laboratories. In a real sense the Institute acts as a focal point for actinide research in Europe and most of our research initiatives, such as the preparation of new compounds and materials, comes as the result of extensive discussion with outside collaborators.

In Sub-Project Actinide Chemistry, specific compounds of minor and major actinides with very high purity and reproducible physical and chemical characteristics are prepared by suitable crystallisation methods. This is a necessary condition not only for the Sub-Project Actinide Physics, but also for the combined efforts on actinide research of the Member States of the Community. In addition, basic physico-chemical properties like crystal structure, PVT diagram, and stability regions of these compounds are studied.

Sub-Project Actinide Physics deals with the physical characteristics (thermodynamics, magnetic, electronic properties, also under high pressure) of well defined metals and actinide compounds, representative for certain bonding types. Joint programs between chemistry and physics involve studies of organometallics and surface properties. These are performed in the double context of understanding the influence of 5f electrons on the chemical bond, but also of producing a basis for a possible catalytic application of actinide compounds.

4.1 Actinide Chemistry

Introduction

This effort focusses on materials preparation and characterisation. Materials preparation includes a number of techniques as shown in Tab. 4.1 and new techniques such as splat cooling and melt spinning to prepare thin films and amorphous

materials are being developed. Characterisation techniques include X-ray diffraction and electron microscopy, which are performed by members of the Physics Division. X-ray diffraction studies also include collaborative studies on the structures of organometallic compounds.

Progress in Materials Synthesis and Characterisation

The compounds prepared and encapsulated for physical property measurements during 1987 are listed in Tabs. 4.1 and 4.2.

Table 4.1 New compounds prepared during 1987

Compounds		Preparation technique	Comments
NaCl Structure	PuP	M	size suitable for magnetic investigations (few mm^3)
	$Pu_{1-x}Y_xSb$ ($x=0.05,0.1$)	M	large single crystals
	NpP	M	small single crystals ($<1mm^3$)
	NpAs	M	large size
	AmBi AmTe	M M	small single crystals
Laves Phases	UFe_2	Cz	large size suitable for neutron diffraction studies
Ternary inter-metallic compounds	$NpRh_2Si_2$	AcM	polycrystalline material with small single crystals ($<1mm^3$)
	$Np(Ru_{0.5}Rh_{0.5})_2Si_2$	AcM	
	$Np(Ru_{1-x}Tc_x)_2Si_2$ ($x=0.2, 0.4$)	AcM	

M = Mineralization
Cz = Czochralski
AcM = Arc Melting

Single crystals of PuP were prepared for the first time by the mineralization technique, completing the plutonium monopnictide series. The effort on the synthesis of pseudobinary plutonium monopnictides was continued with the preparation of single crystals of $Pu_xY_{1-x}Sb$ ($x=0.05$, 0.1). Single crystals of NpP were obtained for the first time and search for optimal growth conditions is in progress. Optimal growth conditions were found for NpAs and large single crystals were obtained.

In order to prepare single crystals of the transplutonium monopnictides and monochalcogenides, the mineralization technique was adapted to synthesis with small quantities ($<1g$). The technique was successfully tested on AmBi and AmTe and small single crystals of both compounds were obtained.

UFe_2 single crystals were pulled from the melt (levitation) by the Czochralski method. The single crystals were cut and oriented for neutron diffraction studies.

To search for new materials with interesting magnetic or superconducting properties, new ternary or pseudoternary compounds were prepared and characterised such as $NpRh_2Si_2$, $NpRuRhSi_2$, $Np(Ru_xTc_{1-x})_2Si_2$ ($x=0.2$, 0.4).

The investigations on $(U_{1-x}Np_x)Pt_3$ and $(U_{1-x}Pu_x)Pt_3$ ($x=0.01$, 0.05 and 0.1) by X-ray powder diffraction show that these intermetallics are isostructural with the hexagonal UPt_3 compound ($SiNi_3$ structure type) and having the lattice parameters reported in Tab. 4.3. For comparison, the lattice parameters determined for UPt_3, $NpPt_3$ (hexagonal $TiNi_3$ structure type) and $PuPt_3$ ($AuCu_3$ structure type) are also reported. The sample of $PuPt_3$ analysed several times revealed either a mixture of two phases (cubic

Table 4.2 Samples prepared, characterised, and encapsulated for indicated measurements during 1987.

Specific heat	AERE Harwell	PuS, PuSe	GSC-Powder
		$PuSb_{0.96}Te_{0.04}$	GSC-Powder
		NpSb	GSC-Powder
Magnetization	ETH Zurich	$Pu_{0.95}Y_{0.05}Sb$	M-SC
		$Pu_{0.90}Y_{0.10}Sb$	M-SC
		PuP	M-SC
		AmTe, AmBi	M-SC
Neutron scattering	Riso Nat. Lab.	$NpCo_2$	Cz-SC
		UFe_2	Cz-SC
	ILL Grenoble	$^{242}Pu_2O_3$	Powder
		NpO_2	Powder
		NpSb	M-SC
		$PuFe_2$	Cz-SC
	CEN Saclay	UCp_3Cl	Powder
		UCp_3Cl	SCS-SC
Susceptibility	CEN Grenoble	$NpRu_2Si_2$	ACM-SC
L_{III} Absorption	TU Berlin	Cs_2UCl_6	Powder
		NpSe, NpSb	GSC-Powder
		$NpPt_3$, $NpCo_2$	GSC-Powder
		PuS	GSC-Powder
Moessbauer Spectroscopy	CNR Strasbourg	NpP	GSC-Powder
		$NpPt_3$, $NpTc_2$, $NpCo_2$	ACM-Powder
		$NpRh_2Si_2$	ACM-Powder
		$Np_2Tc_3Si_4$	ACM-Powder
		$Np(Ru_{0.5}Rh_{0.5})_2Si_2$	ACM-Powder
		$Np(Ru_{0.8}Tc_{0.2})_2Si_2$	ACM-Powder
		$Np(Ru_{0.6}Tc_{0.4})_2Si_2$	ACM-Powder
		$Pu_{0.95}Y_{0.05}Sb$	GSC-Powder
		$Pu_{0.90}Y_{0.10}Sb$	GSC-Powder
		AmTe, AmBi	GSC-Powder
Muonic Spectroscopy	Uni. Bonn	ThO_2	Powder

Symbols are: GSC-ground single crystals; M-SC-mineralization, single crystal; Cz-SC-Czochralski, single crystal, SCS-slow coding solution growth; ACM-SC-arc melting, single crystal.

Table 4.3 Cell dimensions of materials synthesized in the UPt_3-$NpPt_3$ and UPt_3-$PuPt_3$ alloys

compounds	Lattice parameters	
	a in (pm)	c in (pm)
UPt_3	576.0(1)	490.16(9)
$(U_{0.99}Np_{0.01})Pt_3$	575.9(1)	490.02(9)
$(U_{0.95}Np_{0.05})Pt_3$	576.1(1)	489.77(8)
$(U_{0.90}Np_{0.10})Pt_3$	576.2(1)	489.48(9)
$NpPt_3$	580.6(2)	953.0(5)
$(U_{0.99}Pu_{0.01})Pt_3$	575.9(1)	489.90(10)
$(U_{0.95}Pu_{0.05})Pt_3$	575.7(1)	489.54(3)
$(U_{0.90}Pu_{0.10})Pt_3$	576.3(2)	490.4(4)
$PuPt_3$	410.7(1)	

phase and an unknown phase) or a complex structure. Single crystals are necessary to clarify this problem.

By X-ray diffraction on single crystals, the following new compounds $NpRh_2Si_2$, $Np(Ru_{0.5}Rh_{0.5})_2Si_2$, $Np(Ru_{1-x}Tc_x)_2Si_2$ ($x = 0.2$ and 0.4) and $Np_2Tc_3Si_4$ were identified and their crystallographic data established (Tab. 4.4).

The full structure of the following new intermetallics $U_4Tc_7Si_6$, $U_2Tc_3Si_5$, $NpRu_2Si_2$ and $Np_2Tc_3Si_4$ has been determined. In $U_4Tc_7Si_6$ the U atoms are surrounded by a cuboctahedron formed by six Tc(1) atoms, all in the same plane, and six Si atoms. Therefore, the coordination number is twelve. The U-Tc(1) and U-Si distances are of 289.7(2) and 293.9(9) pm respectively. The shortest U-U distance is of 409.7(2) pm corresponding to the half length of the a-axis. In $U_2Tc_3Si_5$, the U atoms are surrounded by four Tc atoms (two at 311.7 pm and two at 326.0 pm) and nine Si atoms at distances ranging from 286.8 to 316.4 pm. The shortest U-U distance is of 382.1 (1) pm.

In $NpRu_2Si_2$, which is isostructural with

Table 4.4 Structural parameters of Np-based ternary compounds

Compounds	Space group	Structure type	Lattice parameters pm	Z
$NpRh_2Si_2$	I4/mmm	$ThCr_2Si_2$	a = 401.0(5) c = 1002.2(7)	2
$Np(Ru_{0.5}Rh_{0.5})_2Si_2$	I4/mmm	$ThCr_2Si_2$	a = 408.8(1) c = 980.3(3)	2
$Np(Ru_{0.8}Tc_{0.2})_2Si_2$	I4/mmm	$ThCr_2Si_2$	a = 414.3(1) c = 960.2(2)	2
$Np(Ru_{0.6}Tc_{0.4})_2Si_2$	I4/mmm	$ThCr_2Si_2$	a = 414.2(1) c = 964.8(2)	2
$Np_2Tc_3Si_4$	$P2_1/c$		a = 680.8(1) b = 808.1(1) c = 556.7(1) β = 103.61°	2

URu_2Si_2, the Np atoms are surrounded by eight Ru atoms at 316.3(2) pm and eight Si atoms at 314.4(5) pm, then the coordination number is sixteen. The shortest Np-Np distance corresponds to the length of the a axis (412.9(2) pm). In $Np_2Tc_3Si_4$, the Np atoms are surrounded by four Tc atoms (from 294.2 to 327.4 pm) and eight Si atoms (from 287.5 to 309.0 pm), reaching in this way a coordination number of twelve (Fig. 4.1). The shortest Np-Np distance is 341.3(1) pm.

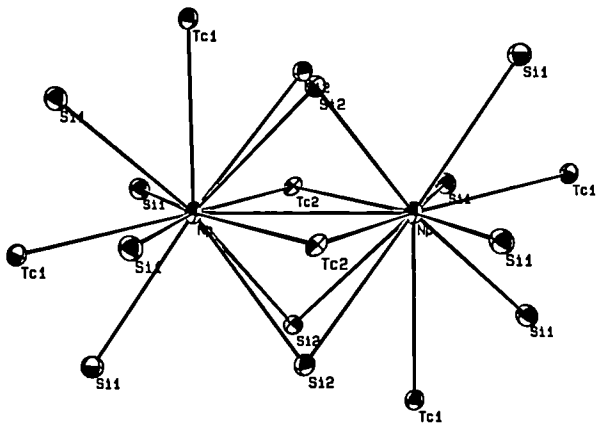

Fig. 4.1 Environment of Np (up to 345 pm) in the new compound $Np_2Tc_3Si_4$.

Structure of Organometallic Compounds

The detailed knowledge of the molecular structure of the organometallic compounds is fundamental for the interpretation of several physical measurements. Therefore, the determination of the crystal structures of several new organometallic compounds is reported (Table 4.5). This work is in collaboration with the Institut für Heiße Chemie KfK and University of Liège, which supply the crystals.

To continue the systematic investigation of the U Cp_3 X compounds the structure of complex with X=O-(C_6H_5) has been determined. This compound presents an arrangement similar to that of U Cp_3 X with a bond distance U-O of 211.9 pm.

In the compound U $(C_9H_7)_2$ $(BH_4)_2$, the coordination polyhedron about the uranium atom is a slightly distorted tetrahedron. From

Table 4.5 Summary of crystal and molecular parameters for organometallics.

compounds	Space group	Z	Lattice parameters (pm)	Coordination Number	U-X distances (pm)
U Cp_3 O(C_6H_5)	P 2 2 2	4	a = 833.1 b = 899.9 c = 2333.7	4 tetrahedron	U-O = 211.9
U $(C_9H_7)_2(BH_4)_2$	P $2_1/c$	4	a = 863.6 b = 2635.1 c = 776.5 β = 102.69^0	4 tetrahedron	U-B_1 = 250.7 U- B_2 = 253.4
U $(C_9H_7)_3$ I	P $2_1/c$	4	a = 1445.4 b = 1041.6 c = 1815.6 β = 128.87^0	4 tetrahedron	U-I = 304.1
Th Cl [(C_9H_6)-C_2H_5]$_3$	P $2_1/c$	4	a = 765.1 b = 1175.0 c = 3023.4 β = 94.18^0	4 tetrahedron	Th-Cl = 267.3
Th CH_3 [(C_9H_6)-C_2H_5]$_3$	P $2_1/c$	8	a = 991.4 b = 3095.3 c = 1817.5 β = 95.21^0	4 tetrahedron	Th_1-CH_3 = 248.0 Th_2-CH_3 = 250.0
La Cp_3	P $2_1/c$	8	a = 1523.7 b = 979.0 c = 1672.1 β = 93.93^0	4 tetrahedron	La_1-C = 297.2 La_2-C = 299.9
Gd [ODOTRA.H_2O].4 H_2O	P b c a	8	a = 1283.9 b = 2153.3 c = 1530.2	9 capped square antiprism	

the U-C distances it appears that the U atom is *pentahapto* coordinated to the five-membered rings of the indenyl moities. The two U-B bond lengths are 250.7 and 253.4 pm.

In the compound U $(C_9H_7)_3$ I, the atom I and the five-membered rings of the three indenyl moities are arranged tetrahedrally about the U atoms. The U atoms is bonded to the C atoms of the five-membered rings of the three indenides at distances ranging from 257.2 to 298.2 pm. In each case, the closest U-C approach is observed for the three non-bridging atoms of the five-membered rings (*trihapto*-bonding). The U-I bond length of 304.1 pm is comparable to the length reported for U Cp_3 I.

In the complex $ThCH_3(C_9H_6\text{-}C_2H_5)_3$ the crystal structure consists of eight discrete molecules per unit cell of which two are symmetrically independent. The coordination polyhedron about the Th atom is similar for the two independent molecules (Fig. 4.2) and can be described as a trigonally compressed tetrahedon along the Th-

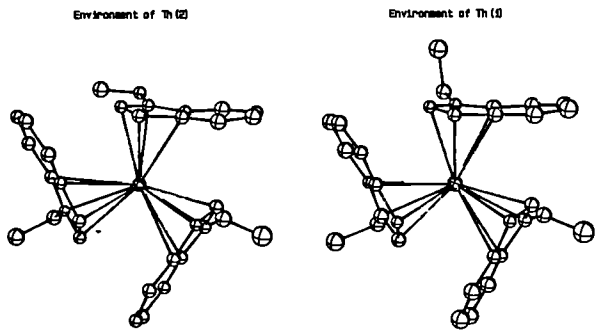

Fig. 4.2 Structure of $(C_9H_6\text{-}Ch_2CH_3)_3ThCH_3$ showing the environment of the two different Th atoms.

CH_3 bond. Each Th atom is *trihapto*-bonded to the three non-bridging C atoms of the five-membered ring of the indenyl moities. The Th-CH_3 distances of the two independent molecules are 248.0 and 250.0 pm, respectively, in agreement with the Th-C σ-bond length reported in the literature. The only difference between the two independent molecules arises from the position of the ethyl groups (bonded to position 1 of the five membered ring). In one molecule, the ethyl groups possess the same arrangement with the C atoms non-bonded to the indenyl ring oriented in opposite direction of the Th-C bond, whereas in the other molecule an ethyl group is almost planar with the indenyl ring and oriented toward the five-membered ring (Fig. 4.2).

In the compound Th $(C_9H_6\text{-}C_2H_5)_3$ Cl, the Th atom presents the same arrangement as in the previous Th $(C_9H_6\text{-}C_2H_5)_3$ CH_3. The Th-Cl distance of 267.3 pm corresponds to the value expected for a single covalent bond. On the other hand, the ethyl groups are almost in the same plane as the indenyl ring and oriented toward the five-membered ring.

In the compound $LaCp_3$, the crystal structure exibits two symmetrically independent $LaCp_3$ molecules in the assymetric unit. They are bridged through one cyclopentadienyl ring, to form infinite zig-zag polymeric chains parallel to the b axis of the crystal (Fig. 4.3). This compound is a new polymorphic form of $LaCp_3$ that differs markedly from those reported in the literature [1], not only by the cell dimensions and the space group but also by the molecular geometry and by the packing. From the La-C distances, it appears that each La atom is *pentahapto*-coordinated to three Cp rings (La-C averaged to 285 pm) and *monohapto*-coordinated to a neighbouring Cp through only one C atom (La-C σ-bond averaged to 298 pm).

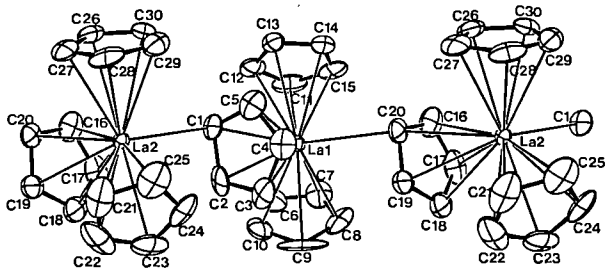

Fig. 4.3 Structure of $LaCp_3$ showing how the two symmetrically independent molecules in the unit cell are bridged through one cyclopentadienyl ring.

The investigation of the crystal structure of the lanthanide macrocyclic complexes has been continued by a determination of the structure of Gd [ODOTRA. H_2O]. 4 H_2O (where ODOTRA stands for 1-oxa-4.7, 10-triazacyclododecane-4.7, 10 triacetato). ODOTRA forms a shell around the Gd ion which is linked to the four non C atoms of the macrocycle (three N and one O atoms) and to the three carboxyl oxygen atoms of the ligand. The Gd ion is also associated with one water oxygen atom and one carboxyl oxygen atom of another molecule in order to form infinite

polymeric chains. Therefore, the coordination number is nine. The variations among Gd-N, Gd-O (carboxyl) and Gd-O (O of macrocycle and of water) are statistically not significant. These distances range from 264.4 to 267.4 pm, from 232.7 to 235.7 pm and from 255.9 to 257.4 pm respectively for the three types. As expected, the Gd-N bands are much longer than those of the Gd-O. The coordination polyhedron about the Gd is described in terms of a distorted capped square antiprism; the eight-coordinated donor atoms of the ODOTRA macrocycle are at the vertices of the two square bases and one water oxygen atom is in the axial position.

References

[1]. S.H. Eggers, J. Kopf and K.D. Fischer, Organometallics 5(1986)383

Surface and Catalytic Studies of Uranium Systems

Knowledge of the chemical reactivity of uranium is needed in the study of its catalytic properties and that of its compounds. In this work, ultra-violet and X-ray Photoelectron Spectroscopy (UPS and XPS) have been used to investigate the reaction of uranium with O_2 and CO. UPS is very useful because it allows the evolution of the valence electrons (which are responsible for the chemical reactivity) to be followed.

A high purity sample (<100 ppm metallic impurities) was cleaned in-situ by argon ion sputtering at 573 K and photoemission measurements were performed using HeII radiation (40.81 eV)).

UPS spectra of a clean uranium sample exposed to an increasing oxygen dosage at 573 K are shown in Fig. 4.4. O_2 adsorption leads to the growth of two peaks at about 2 and 6 eV, also found in UO_2 and attributed to the O(2p) band and to the localized U($5f^2$) level of UO_2. The peak

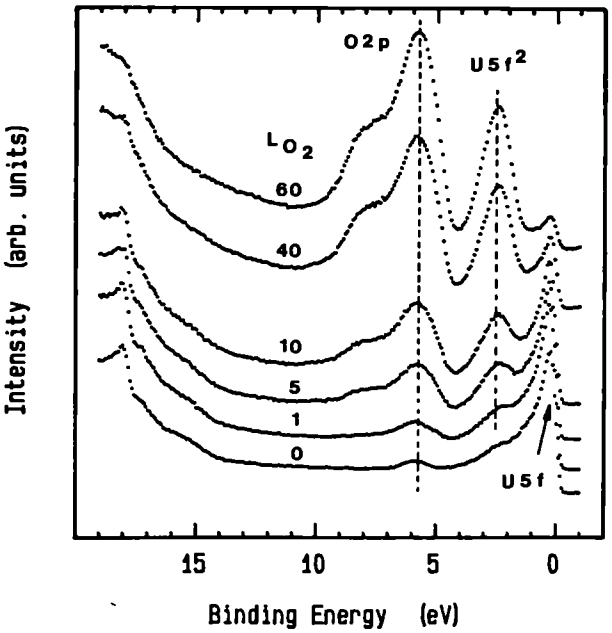

Fig. 4.4 Ultra-violet photoemission spectra using He_{II} light of uranium with oxygen absorption at 573K. 1L (=Langmuir) corresponds to complete coverage of the surface.

at 6 eV is asymmetrical, having a shoulder on its high energy side, exactly as in UO_2. The emission at the Fermi-level becomes smaller as the oxide signals grow, indicating a decrease of the uranium metal concentration within the depth probed by UPS (about 2 monolayers). This shows that surface oxidation by O_2 is not limited to the topmost surface but that also the bulk is affected. The XPS O(ls) and U(4f) core-level spectra also indicate the formation of UO_2.

Figure 4.5 shows UPS spectra of an uranium sample exposed to CO at 573 K. CO adsorption

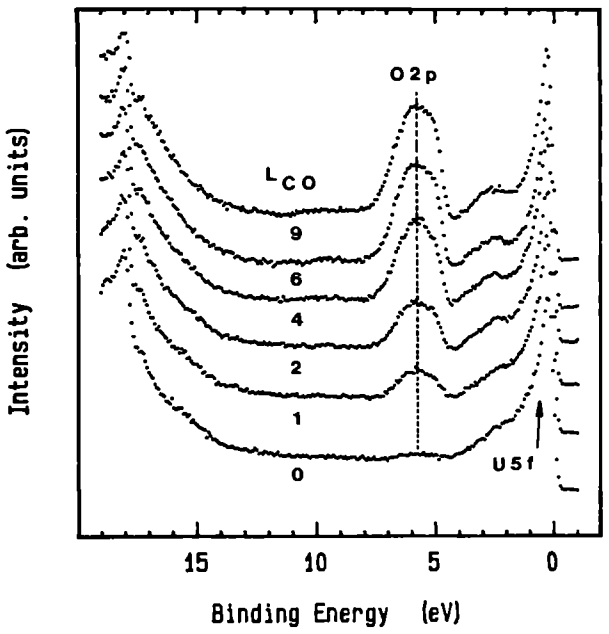

Fig. 4.5 As in Fig. 4.4 but showing the spectra as a function of CO absorption at 573K.

leads to the growth of a peak at about 5.5 eV again attributed to an O(2p) emission. But, in contrast to the O(2p) emission of UO_2, it is almost symmetrical pointing to the presence of a surface oxide different from UO_2. Similarly, the U($5f^2$) emission at about 2 eV, which was characteristic for UO_2, is also missing. The broad structure at 3 eV is attributed mainly to an emission from a C(2p) level [1] and possibly small amounts of UO_2. The intensity at the Fermi-level does not decrease pointing to the self-limiting feature of the reaction to the topmost surface layer, or to the formation of a compound with metallic properties. The XPS C(1s) and O(1s) core-level spectra indicate the presence of an oxide and a carbide or an oxycarbide.

The formation of another oxide containing compound by CO reaction with U can be due only to the presence of carbon. We think the new compound is UO_xC_{1-x}; this is the simplest possible assumption to explain the influence of C on the O(2p) and the U($5f^2$) emissions. It was shown by difference spectra [2] that the new compound has a f-d density-of-states ratio higher than that of uranium. This could be attributed to the formation of UO_xC_y, which is a solution of UO in UC [3].

References

[1] R. Panzner and W. Diekmann, Surface Sci. 160 (1985), 253

[2] T. Gouder, Thesis, University of Namur/Belgium (1987)

[3] H. Holleck and K. Kleykamp, in Gmelin Handbook of Inorganic Chemistry, Springer-Verlag (Berlin) (1987), U. Suppl. Vol. C12, 1

4.2 Actinide Physics

Introduction

The actinide physics effort brings a large number of sophisticated research probes, both in-house and at outside facilities, to bear on problems in actinide materials science. Most of the experiments are performed on the samples prepared by the sub-project actinide chemistry and there is thus a close relationship between the efforts in the two sub-projects. As well as containing reports on the in-house experimental efforts this report contains sections on work done at large central facilities and a short overview of some of the work performed by our European collaborators on encapsulated samples produced at TU. The group's efforts are also strengthened by theory performed in-house and with outside collaborators.

High Pressure Studies on Actinide Systems

HPXRD work was continued during 1987 for metals, alloys, NaCl type and An_3X_4 compounds. First results were obtained with the study of X-ray absorption under pressure using the synchrotron radiation of LURE. The equipment for measuring optical reflectivity under pressure became operational and has supplied first results for B1 (NaCl) type uranium compounds, indicating correspondences between structural phase transitions and reflectivity maxima associated with electronic transitions. This work at LURE is described under the section at large central facilities.

Structural Phase Transition in Alpha-Plutonium under Pressure

With the heavier actinides Am to Cf, pressure induces phase transformations to structures of lower symmetry, accompanied by volume decreases from 6 to 21 %. The decrease in symmetry, together with the observed decrease in atomic volume, indicates that these transitions correspond in fact to the delocalisation of the 5f electrons. In the earlier actinides, which have their 5f electrons already in an itinerant state, pressure can not induce this type of phase transition. A phase transition in alpha-plutonium was thus not expected, except perhaps at very high pressures. Previous HPXRD work on plutonium metal up to 21 GPa was reported by Roof [1]. No phase transition was observed. We have extended the HPXRD work up to 59 GPa in order to give a complete picture of the behaviour of the light actinides under very high pressure, and to determine the compressibility of this material. Up to 38 GPa, a single monoclinic phase is observed. Increasing pressure to 41 GPa modifies the diffraction pattern in a way characteristic of a phase transition. The transformation is complete at 47 GPa. When releasing pressure, hysteresis to transformation is observed down to 5 GPa, where the metal becomes again single-phase monoclinic. The bulk modulus of the low pressure phase and its pressure derivative were determined by fitting the standard equations giving the bulk modulus $B_0 = 43 \pm 1$ GPa, and its pressure derivative $B_0 = 15 \pm 4$. These results show that α-plutonium becomes unstable at moderately high pressure and transforms to a previously unknown high-pressure structure. The exact crystal structure

and implications for our understanding of the electronic structure of α-Pu will have to be elucidated by further work, but the phase transition in itself is further evidence that pressure effects do not stop once the f's are delocalised.

HPXRD studies on uranium metal had indicated that a structural phase transition occurs in this metal below or around 71 GPa [2]. The high pressure phase has not been identified up to now. With the next actinide, neptunium, we have performed HPXRD studies up to 52 GPa [3] and did not detect a phase transition in this pressure range. But the results for uranium, and the present study on plutonium, suggest that the intermediate metal neptunium could well exhibit a phase transition at a pressure somewhat higher than 52 GPa. It thus seems useful to extend the study of the compression of neptunium to higher pressures.

References

[1] R.B. Roof, Adv. X-ray Anal., 24 (1981) 221

[2] J. Akella, G. Smith, H. Weed, J. Phys. Chem. Solids, 46 (1985) 399

[3] S. Dabos, C. Dufour, U. Benedict, M. Pagès, J. Magn. Magn. Mat., 63 & 64 (1987) 661

Formation of Np_2O_3 on Np-Metal Studied by Photoemission Spectroscopy

Photoemission spectroscopy (UPS/XPS) is a powerful technique to obtain direct information on the electronic structure and chemical state. The pronounced surface sensitivity of 0.5 to 3nm enables the examination of the topmost surface layers. As part of the investigation to study the electronic structure of actinide metals, photoemission data for the surface oxidation of clean Np-metal are presented.

Recent phase diagram studies for the Np-O system exclude the existence of bulk NpO and Np_2O_3. On the other hand, the deviation of the electronic structure of the surface from that of the bulk may stabilize surface phases that do not exist as bulk materials. The analysis of conduction band spectra recorded by UPS on Am-metal recently [1] indicated that divalent Am atoms exist at the surface of bulk trivalent Am metal.

The measurement (UPS/XPS) were performed on polycrystalline high-purity (doubly electrorefined at Los Alamos National Laboratory) Np-metal plates, which had already been used previously for electronic structure studies [2]. The samples were first cleaned by 'in-situ' Ar ion sputtering and then oxidized slowly by segregation of residual bulk oxygen impurities to the surface.

Fig. 4.6 shows the XPS 4f core lines for clean (curve a) intermediate (curves b and c) and completely (curve d) oxidized Np-metal surfaces. For intermediate oxidation two distinct emission

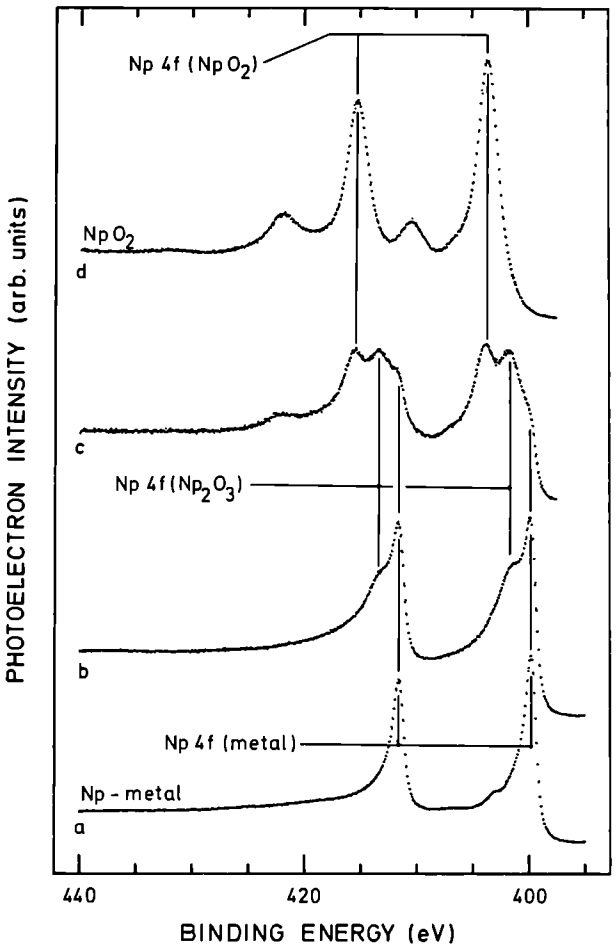

Fig. 4.6 X-ray induced 4f core level photoemission spectra (XPS, E=1253.6 eV) for increasing surface oxidation of Np-metal: (a) clean metal, (b), (c) intermediate oxidation, (d) complete oxidation.

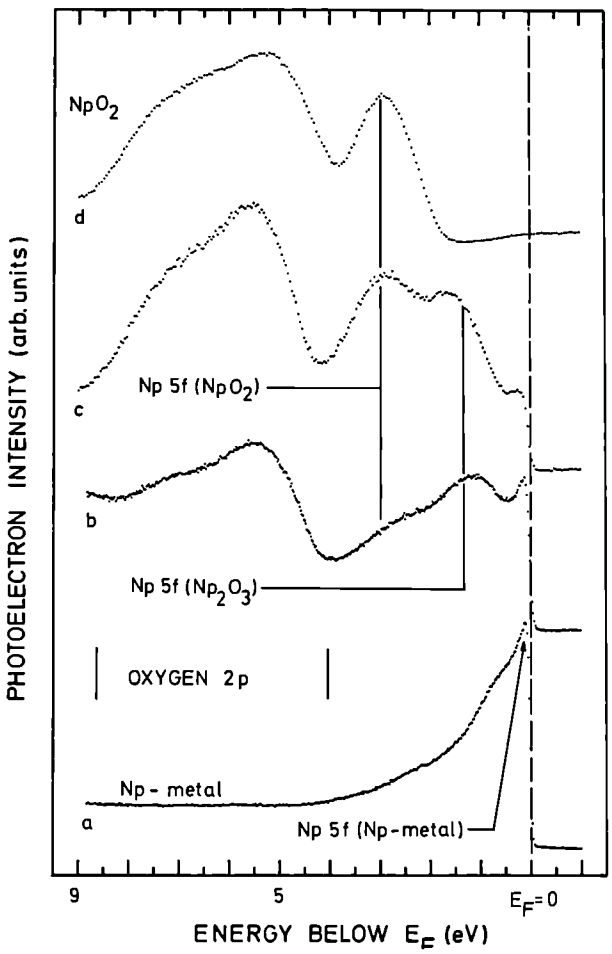

Fig. 4.7 UV-light induced valence band photoemission spectra (UPS, E= 40.8 eV) for increasing surface oxidation of Np-metal (a) clean metal, (b), (c) intermediate oxidation, (d) complete oxidation.

signals appear at about 1.9 and 3.9 eV higher binding energy in addition to the metal line. The line shifted by about 3.9 eV is clearly due to the formation of NpO_2 because of the characteristic actinide dioxide signal with a satellite at 6.8 eV higher binding energy, as found for bulk UO_2, NpO_2 and PuO_2. Thus, for intermediate oxidation a lower Np oxide, which does not exist as a bulk phase, must be formed on the surface in the presence of metal. This is confirmed by UPS valence band spectra for the same stage of surface oxidation (Fig. 4.7). With the increase of the oxygen 2p signal at about 6 eV two distinct 5f electron derived structures appear at about 1.5 and 3 eV as long as the metal signal at E_F is observed. The spectrum for complete surface oxidation (curve d) is again characteristic of NpO_2. The only difference between the XPS and UPS data is seen for curves b; whereas in XPS (Fig. 4.6) the NpO_2 signal is not clearly seen, the related UPS spectrum (Fig. 4.7) shows this signal clearly. This is explained by the higher surface sensitivity in UPS (0.5 nm) in which even very small amounts of surface NpO_2 can be detected, in contrast to XPS, which has a surface sensitivity of about 3 nm.

To determine the oxidation degree of Np for the lower oxide phase one can use the linear relationship between the oxidation state and the binding energy shift, ΔE (chemical shift), measured for the XPS 4f core lines. With $\Delta E = 0$ eV and the oxidation state 0 for clean metal, and $\Delta E =$ 3.9 eV with the oxidation state 4 for NpO_2, an oxidation state close to 2 is found, i.e. the lower oxide would be a monoxide. Taking into consideration that the linear relationship is valid only for fully ionic compounds, the lower oxide is attributed to the hypo-stoichiometric Np_2O_{3-x}. In addition, NpO should be metallic because of a $5f^4(6d7s)^1$ electron configuration, which results in a small chemical shift due to screening of the 4f core hole by conduction electrons. A comparison with the surface oxidation of Pu-metal [3] also shows a considerably lower formal oxidation state of 2.4 instead of 3, as expected for Pu_2O_3, which is clearly identified on the surface of Pu-metal, and which exists also in the bulk.

In conclusion, we have observed for the first time a layer of a lower oxide, attributed to normally unstable Np_2O_3, that forms as a thin layer at the interface between the metal and the dioxide.

References

[1] N. Märtensson, B. Johansson and J.R. Naegele, Phys. Rev. B 35 (1987) 1437

[2] J.R. Naegele, L.E. Cox and J.W. Ward, Inorg. Chim. Acta 139 (1987) 327

[3] R. Baptist, D. Courteix, J. Chayrouse and L. Heintz, J. Phys. F 12 (1981) 2103

Calculated Electronic Structure of $U(Rh_{1-y}Pd_y)_3$ Alloy

The pseudobinary alloys $U(Rh_{1-y}Pd_y)_3$ crystallise in the cubic Cu_3Au-structure for y smaller than 0.9 and in the hexagonal $TiNi_3$-structure when y is greater than 0.93. To study the change of the 5f electron character in these systems, we have extended our previous calculations [1] to include the ternary compounds $URhPd_2$ and URh_2Pd. Although these ordered compounds themselves do not exist, our purpose is to use a knowledge of their electronic structure to study 5f localization in the pseudobinary alloys. The main features of the density of states for URh_3 can be described by a "bonding" 4d band separated by approximately 6 eV from an "antibonding" 6d band. The 5f states are located at the top of the "bonding" d states and hybridize strongly with them. This hybridization is crucial for the 5f bandwidth - an estimate of the unhybridized 5f bandwidth in URh_3 is only 0.3 eV, which is much narrower than the calculated fully hybridized 5f bandwidth of about 3 eV. As the concentration increases the "bonding" d states move down in energy decreasing their overlap with the 5f levels. This causes a reduction of f-d hybridization and 5f bandwidth. In the UPd_3 system the 5f states are situated in the gap between the "bonding" and the "antibonding" d states. Consequently the 5f bandwidth is far narrower than in URh_3, strongly increasing the tendency of the 5f electrons to localize. It is the nearest neighbour environment of the uranium atom which determines the nature of the 5f-states, which is consistent with the fact that for all these systems the U-U distances are considerably larger than the Hill limit.

From the calculated state densities at the Fermi-level, $D(E_F)$, of the four ordered compounds we have calculated the Stoner product $I \cdot D(E_F)$ where I is the Stoner parameter for the multi-band system [2]. Stoner theory predicts URh_2Pd and URh_3 to be paramagnetic since the Stoner product is less than one, and the contrary for $URhPd_2$ and UPd_3. In good agreement, we find directly from our self-consistent spin-polarized calculations ferromagnetic states for both for UPd_3 and $URhPd_2$, the spin-polarization in these two compounds being almost saturated, which we again interpret as consistent with localized 5f electrons. However, an interpolation of the state density, between UPd_3 and URh_3 does not yield satisfactory values of $I \cdot D(E_F)$. The calculations for the ordered intermediate compounds (albeit with a spurious long range order) give a more exact description of the environment of an uranium atom surrounded by eight Rh and four Pd atoms (and vice versa) in the alloys, and it is this near neighbour environment which is important. Further, the intermediate compounds are both close to the Stoner limit of $I \cdot D(E_F) = 1$, which we wish to use to identify the critical concentration for localization of 5f electrons on an uranium atom. Therefore we have interpolated $D(E_F)$ for intermediate concentrations and from the results calculated the Stoner product which, when equal to one, gives the critical concentration for localization.

The experimental lattice constants of the alloys (Fig. 4.8) change continously from URh_3 to UPd_3. However, the change deviates from Vegard's linear law. For comparison, we have also plotted the experimental volumes for the $Zr(Rh_{1-y}Pd_y)_3$ systems which obey Vegard's law over the entire

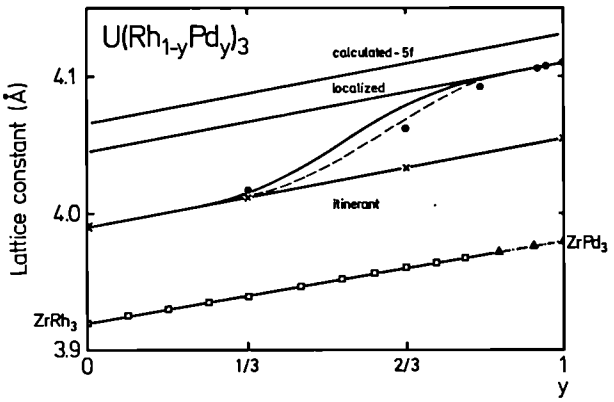

Fig. 4.8 Experimental (filled circles) and theoretical lattice constants for $U(Rh_{1-y}Pd_y)_3$. The dashed and full drawn curves correspond to a localization criterion of 8 and 7 palladium atoms surrounding an uranium atom, respectively. The calculated lattice constants with chemically bonding 5f electrons are shown by crosses and the curve labelled "ITINERANT" is obtained by interpolation. The lattice constants calculated by subtracting the 5f contribution to the bonding and for the chemically inert $5f^2$ configuration are labelled "CALCULATED-5f" and "LOCALIZED", respectively. The experimental lattice constants for the $Zr(Rh_{1-y}Pd_y)_3$ alloys are also plotted, where the full drawn and broken lines refer to the Cu_3Au and $TiNi_3$ crystal structures, respectively.

concentration range despite the crystallographic change from Cu_3Au to the hexagonal $TiNi_3$ structure (indicated as a dash-dotted line in the figure).

The calculated lattice constants - with the 5f states treated as band states - for the ordered compounds are shown in Fig. 4.8, from which it is evident that they are in agreement with Vegard's law (full line marked ITINERANT). Also plotted are the lattice constants for the $U(Rh_{1-y}Pd_y)_3$ system when the partial 5f contribution to the electronic pressure has been

subtracted from the calculated equation of state (this curve is called "CALCULATED-5f"). The agreement between the "ITINERANT" volume and experiment for URh_3 is very good. In contrast, for UPd_3 it is the "CALCULATED-5f" volume that agrees with experiment to within 2% - consistent with localized 5f-electrons. Since the pseudo-binary system is homogenous each uranium site has its twelve nearest neighbour positions occupied randomly by both Rh and Pd atoms. We now assert that the nature of the 5f states - i.e. local (non bonding) or itinerant (bonding) - on a particular uranium site is dependent primarily upon the 5f-bandwidth which, as we have already mentioned, is influenced mainly by its nearest neighbour atoms because hybridization with the 4d states determines the width of the 5f band. Stoner theory predicts ferromagnetism when y is larger than 0.6. When $y=2/3$ we found for the ordered compound that the spin-polarization is complete and we have associated this with a localized 5f behaviour. This means that somewhere in the range $0.6<y<0.67$ localized moments are formed. Let us assume first that $y=0.6$, which is close to 7/12, is the critical concentration for the formation of localized moments, then when an uranium atom is surrounded by 7 or more Pd atoms its 5f states are localized. We can then go on to calculate the volume of the pseudo-binary alloy $U(Rh_{1-y}Pd_y)_3$ for any value of y, by first considering the probability P(n) of having n Pd atoms surrounding an uranium atom with M nearest neighbours (=12). The corresponding lattice constant of the cell, a(n) is obtained from a linearly interpolated value along the itinerant curve in the figure, when $n<7$, and along the localized curve when $n>7$.

The results are shown in Fig. 4.8. If we assume that $y=2/3$ is the critical value for localization, the critical number of nearest neighbour Pd atoms becomes 8. Then the "ITINERANT" lattice constants are used for $n<8$ and the "LOCALIZED" lattice constants for $n>8$. A slightly better agreement with experiment is obtained.

In conclusion, although the linear specific heat coefficient might at first sight suggest that the transition from itinerant to localized 5f states is gradual in the $U(Rh_{1-y}Pd_y)_3$ system, the lattice parameters do not obey Vegard's law. This we can better understand in terms of an abrupt Mott transition for those uranium atoms in the alloy for which the criterion for localization is fulfilled.

References

[1] B. Johansson, O. Eriksson, M.S.S. Brooks and H.L. Skriver, J. Less. Comm. Metals, 133 (1987) 25-29

[2] M.S.S. Brooks, O. Eriksson, B. Johansson, Physica Scripta, 35 (1987) 52

Studies of Intermetallic Actinide-Iron Systems

We have started recently a study of the An-Fe intermetallic systems with both experimental and theoretical band-structure methods. Our initial studies have focussed on the Laves phases, formula $AnFe_2$, which are often cubic. The analogous rare-earth (Ln) systems, e.g. $TbFe_2$, have been extensively studied and are in fact used in magnetostrictive devices. However, a

fundamental difference between the $LnFe_2$ compounds and the $AnFe_2$ is that in the former the rare-earth atom is truly localised and is only weakly coupled via exchange interactions with the Fe 3d electrons. However, in the actinides this is not the case, and we expect to have to consider all the electrons as itinerant.

One way to tackle such problems is through energy-band calculations. We will start by investigating UFe_2. The observed moment per formula unit is 1.1 μ_B, of which the 3d moments are ~0.6 μ_B and the uranium moment is ~0.06 μ_B, and oppositely directed to the Fe moment. In the initial calculations without spin-orbit coupling we find a moment of 0.75 μ_B/Fe and -0.51 μ_B/U. The total moment is in reasonable agreement with experiment, as is the lattice parameter, but the individual moments are not.

We therefore investigated the effect of spin-orbit coupling by adding it to the Hamiltonian. The main effect is an induced orbital moment which is calculated according to the scheme suggested by Brooks & Kelly [1]. The calculation was iterated to self consistency and gives an iron moment little changed from before (~ 0.8 μ_B/Fe) but a spin uranium moment $\mu_s = +0.47\ \mu_B$ and an orbital uranium moment $\mu_l = +0.47\mu_B$. Thus, we find that the magnetism in UFe_2 contains large spin moments on both U and Fe sites, coupled antiparallel, but that the orbital and spin moments almost cancel on the U site. We can also calculate the pressure dependence of the moment, which is in better agreement with experiment when spin-orbit coupling is included. One of the most sensitive techniques for determining the ratio of orbit and spin contributions is the magnetic form factor as measured by neutron diffraction. This form factor reflects the spatial extent of the magnetisation density, and is particularly sensitive to the cancellation of orbital and spin components because these do not have exactly the same spatial extent of their magnetisation density. Thus we may write the form factor as

$$f(Q) \approx \langle j_0\rangle \mu_s + (\langle j_0\rangle + \langle j_2\rangle)\mu_l \qquad (1)$$

where Q is the momentum transfer ($Q = 4\pi\sin\theta/\lambda$), and $\langle j_0\rangle$ and $\langle j_2\rangle$ are averages of spherical Bessel functions over the 5f spin density (Fig. 4.9a). The terms μ_s, μ_l, and μ are the

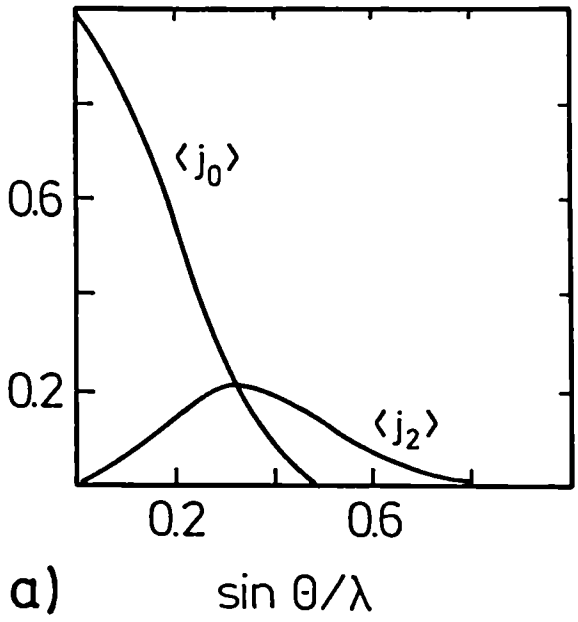

spin, orbital, and total moments on the actinide atom, respectively. We can now write

$$\begin{aligned} f(Q) &= (\mu_s + \mu_l)\langle j_0\rangle + \mu_l\langle j_2\rangle \\ &= \mu(\langle j_0\rangle + C_2\langle j_2\rangle) \end{aligned} \qquad (2)$$

since $\mu=\mu_s+\mu_l$ and $C_2=\mu_l/\mu$ conveniently measures the ratio of the orbital to total moment. Note that since μ_s and μ_l have opposite sign for less than half-filled f systems, C_2 diverges as μ approaches zero. From our calculations we find $C_2=4.\dot{3}$. This has the wrong sign because $|\mu_s|>|\mu_l|$, but a glance at Fig. 4.9b shows that we are in a very sensitive part of the (C_2, μ_l) plot. The most we can say is that $|C_2|$ should be large.

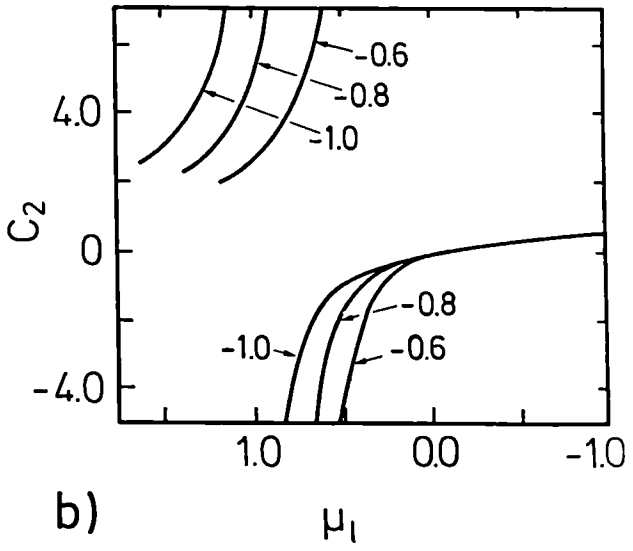

The experimental situation in UFe_2 is by no means clear and we plan to measure f(Q) on a crystal of UFe_2 grown and characterised at the Institute. The magnetic moment is known to be a function of stoichiometry [2] and the only published form factor [3] has been averaged so that no individual points remain. Taking more recent work on UNi_2, where indeed a large value of C_2 was found [4], we find that the UFe_2 form factor does suggest the presence of a large orbital moment and the high-angle curve from UFe_2 and UNi_2 agree very well. We suspect that the characteristic down turn (Fig. 4.9c) in f(Q) was not found in UFe_2 because at that time no such form factors had been seen.

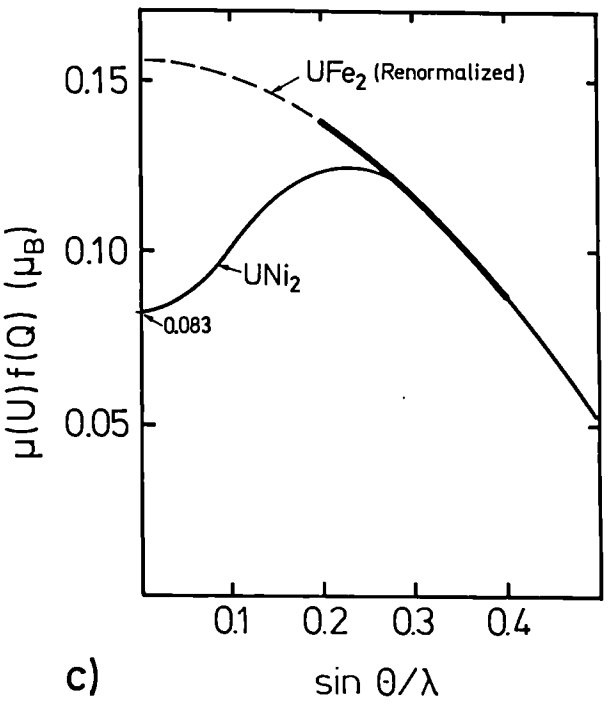

Fig. 4.9 Form factor analysis. (a) The calculated spin density averages over spherical bessel functions. (b) The dependence of C_2 upon orbital moment for several values of the spin component. (c) The published 5f form factor of UFe_2 (Yessik 1969), renormalized to a 5f moment of 0.155μ_B, and the measured 5f form factor of UNi_2 (Fournier et al 1986). The shape of the two form factors matches for $0.2<\sin\theta/\lambda<0.4$, whereas the composition of the 5f moment is sensitive to the form factor at $\sin\theta/\lambda<0.2\text{Å}^{-1}$.

Whereas experiments on UFe_2 still wait to be done, we have completed a study [5] on a single crystal of $PuFe_2$. An initial experiment was performed at Risø National Laboratory to characterise the crystal and determine its stoichiometry. The crystal was then examined with the polarized-diffractometer at the Institut Laue-Langevin, Grenoble. The form factor of the small (0.39 μ_B) Pu moment is shown in Fig. 4.10. We can see immediately the maximum in the form factor near $\sin\theta/\lambda\simeq0.3\text{Å}^{-1}$ that is charac-

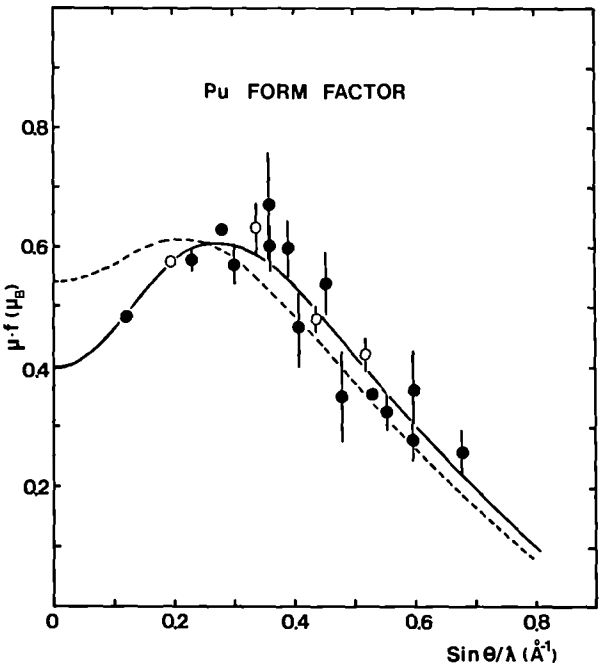

Fig. 4.10 The Pu form factor (open and closed circles) measured in $PuFe_2$. The solid line is the best fit with $C_2=6.0$, giving a moment of 0.39(2)μ_B. The dashed line uses $C_2=3.8$, the value found for PuSb, and is clearly a poor fit to the data.

teristic of a large C_2 in Eq. (2). We can compare this form factor with that found in a more "localised" Pu system such as PuSb. This is shown by the dashed curve in Fig. 4.10, which is clearly not nearly such a good fit as the solid line (for which $C_2=6.0$) Following the discussions above, the large C_2 value in $PuFe_2$ can only come from a smaller orbital component μ_l than is normal in localised systems, but which is still greater than μ_s. The band structure calculations show a strong hybridisation of the itinerant 5f and Fe 3d electrons, and predict that it is this hybridisation that reduces the orbital moment, in agreement with the neutron experiments.

References

[1] M.S.S. Brooks and P.J. Kelly, Phys. Rev. Lett. **51** (1983) 1708

[2] A.T. Aldred, J. Mag. & Magn. Matls. 10 (1979) 42

[3] M. Yessik, J. Appl. Phys. 40 (1969) 1133

[4] J.M. Fournier et. al., J. Less. Comm. Metals **121** (1986) 249

[5] M. Wulff et al, Phys. Rev. B (in press) 1988.

Actinide Behavior and Radiation Damage in Oxides

In extension of the work on Cm-containing oxides, reported previously in 1986, emphasis in 1987 was placed on a complex mixture of oxides, tailor-made to incorporate high level waste (SYNROC B, consisting of zirconolite $CaZrTi_2O_7$, Ba-hollandite $BaAl_2Ti_5O_{14}$, perovskite $CaTiO_3$ and rutile TiO_2). Such ceramics are being investigated as possible matrices for solidification of special waste streams or as possible second generation matrices.

The partitioning of long-lived ^{237}Np in such a complex matrix has not been investigated previously. Therefore, an electron-microprobe examination was performed on this 4-component matrix after having incorporated a few atom percent of NpO_2 by soaking a green pellet with the Np-solution and subsequent sintering under reducing conditions. Np was about equally partitioned between zirconolite (10.7 wt.%) and perovskite (9.5 wt. %), whereas the remaining two phases of hollandite and rutile only contained $\leq$ 0.2 wt. % Np. An oxidising anneal did not change the Np-partitioning appreciably.

This is understood by assuming Np to be tetravalent to directly replace Zr in zirconolite, and to replace Ca in perovskite by simultaneously reducing two Ti^{4+} ions to Ti^{3+} ions.

The leach rates of the SYNROC-B containing Np were very small. For example, the leach rate for Np at 190 °C in deionised water was $\leq 5 \times 10^{-3}$ g/m²d. As observed for waste glasses, the actinide leach rate is smaller than the bulk leach rate. The actinides (Np, but also Pu and Cm present as impurities) become therefore enriched at the leached surfaces, as is obvious in α-spectra of the leached product.

Because of the long half-life of ^{237}Np ($2.1 \cdot 10^6$ yrs), no radiation damage effects were seen in the waste matrix. Actinide partitioning will, however, cause local damage in part of the matrix. This damage contributes only about 10% to the total displacement damage. To investigate the effects of such partial amorphization, a parallel specimen containing 1 wt.% ^{244}Cm was prepared and is accumulating damage.

In another set of experiments SYNROC B was implanted with 40 keV radioactive ^{85}Kr or ^{133}Xe ions to different doses. It is well known that energetic beams of heavy ions can amorphize anisotropic oxides as easily as α-decay. If rare gases are used to produce this amorphous, metamict state, the fact of its formation and the recrystallization temperatures can easily be detected by a fast gas release process caused by sweeping due to recrystallization starting at the undamaged underlying oxide and proceeding to the surface. Fig. 4.11 shows some typical results: at doses $\geq 10^{15}$ (Kr-or Xe-) ions/cm², a fast release in a very narrrow temperature interval

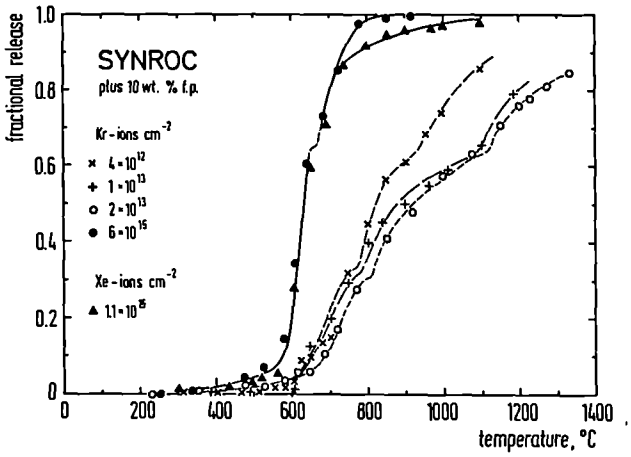

Fig. 4.11 Gas release as a function of temperature for samples implanted with different doses. The sudden release in samples with large dose implantation values signifies that the material is amorphous.

occurs typical of recrystallization of amorphous radiation-damaged ceramics. At low doses, diffusional release from the different phases is seen at significantly higher temperatures. These and other similar results can be taken as proof that SYNROC B becomes amorphous due to radiation damage.

An international workshop on radiation effects in nuclear waste materials was also organised within the reporting point. Within this workshop, held in parallel to the international conference on radiation effects in insulators in Lyon in July 87, a large number of important results on different actinide-containing oxides were discussed and reported. The details will be available in the proceedings [1].

References

[1] Hj. Matzke, Ed., Nuclear Waste Materials, Proc. Int. Workshop on Radiation Effects in Nuclear Waste Materials, Nucl. Instr. Methods in Phys. Res., in print.

Actinide Studies at Large Central Facilities

Modern materials science demands a very large and diverse range of experimental probes, and studies in the actinides are no exception. Personnel from the Project, usually working in collaboration with outside staff, make use of the sophisticated instrumentation available at large European or national facilities in their efforts to increase our understanding of actinide materials.

A variety of neutron experiments are performed at CEN, Grenoble, Institut Laue-Langevin, Grenoble, Risø National Laboratory, Denmark, CEN Saclay, Rutherford-Appleton Laboratory, and Argonne National Laboratory. These studies included single-crystal studies of structure (to look for aspects of hydrogen bonding in organometallics), determination of complex magnetic structures, measurement of high-energy crystal-field states at spallation sources and measurements of the excitation spectra in large single crystals.

Last year we reported work on ^{242}PuSb in which evidence was found for a linearly polarized mode [1]. Although neither experiments nor theory on this material are complete, major progress has been made by Cooper and his colleagues [2] in proposing a model that includes anisotropic hybridisation between the 5f and conduction electrons. An important new element in the neutron inelastic scattering studies of PuSb, which is a ferromagnet, is that we performed the experiments on a single domain sample. We have now extended this technique to the ferromagnet UTe. The important point about having a single domain is that we can then measure independently effects parallel and perpendicular to the unique magnetisation axis. Because all ferromagnetic actinide systems exhibit enormous magnetic anisotropy we have thought for some time that differences in the parallel and perpendicular (with respect to the moment) exchange parameters should be reflected in the excitation spectra, but experiments have always been performed on multidomain samples. The results so far of our experiment on the high intensity IN8 triple-axis spectrometer at the Institut Laue Langevin are shown in Fig. 4.12. The excitation gap at the Γ-point (zone center) is 3.7 THz, in good agreement with earlier work on a multidomain sample [3]. In the q_z direction (excitation propagating along the direction of μ) the dispersion is strong and the spin waves are well defined out to the zone boundary. We expected this

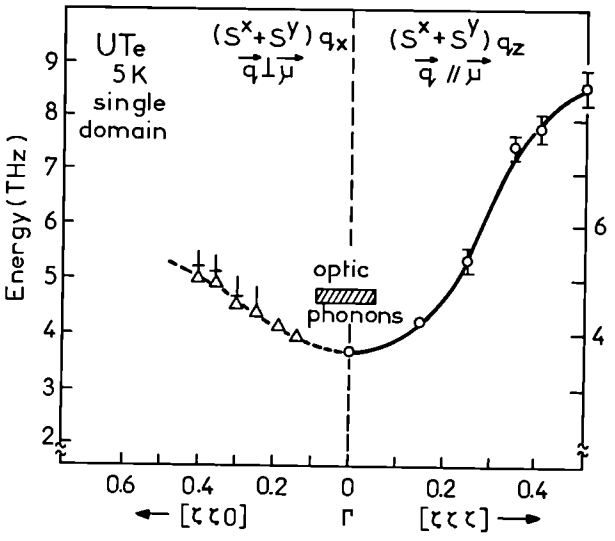

Fig. 4.12 Magnetic excitation spectra of single crystal UTe taken at the Institut Laue Langevin, Grenoble. The crystal has been cooled in a magnetic field to create a single domain. The direction q_z corresponds to excitations propagating parallel to the moment direction, q_x is perpendicular to μ.

behaviour. However, for the q_x direction (excitation propagating perpendicular to the direction of μ) the situation is more complex. First, the dispersion is less - this is a signature of the anisotropy mentioned above. Second, we find strong damping of this excitation, starting at $q_x \simeq 0.25$ and so strong by $q_x = 0.4$ that the excitation can no longer be seen. This feature of excitation damping is found in many actinide systems and indicates interaction between the 5f and conduction electrons, although only recently has the problem begun to be treated in a quantitative way [4].

In summary our experiments on single domain UTe have shown for the first time that not only are the exchange parameters anisotropic but also that the interaction between the 5f moments and the conduction electrons is a sensitive function of direction in the crystal.

Another study that has benefited from the higher intensities available at large central facilities has been X-ray absorption spectroscopy (XAS), particularly those measurements under pressure. An effort involving a collaboration between personnel at the University of Copenhagen, CNRS Villetaneuse, and the Institute has been started at the LURE facility at Orsay, France. The energy-dispersive method has the following advantages for high-pressure applications: i) it is fast, a spectrum frame can be obtained in 1 second; ii) the sensitivity is high (0.1 eV); iii) the beam is focussed, allowing for high diffracted intensity from the small sample volume in the pressure cell; iv) the stability of the beam is excellent because of the lack of any mechanical movement during data collection. The main drawback of such a technique is that the spectra are sensitive to sample inhomogeneities such as thickness variations.

Fig.4.13 shows the spectra for UP as a function of pressure, and the relative shift in the maximum

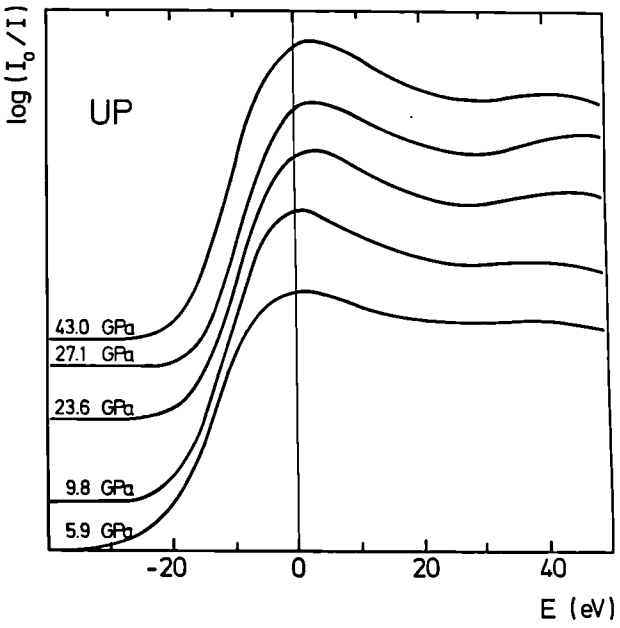

Fig. 4.13 X-ray absorption spectra of UP near the L_{III} edge of uranium at different pressures. Normalized log (Io/I) is plotted as the ordinate, but the numerical scales of individual spectra are shifted against each other to avoid overlapping of the curves, and thus are not indicated in the graph.

is shown together with the volume [5] behaviour in Fig. 4.14. Similar curves were obtained for UC, which has an orthorhombic distortion [6] at about 27 GPa. The energy difference between the absorption edges for the ambient and high pressure phases is 2 eV for UC and 2.6 eV for UP. A shift of the absorption edge to higher energy can be expected when, due to 5f delocalisation, the Coulomb interaction between the 5f electrons and 2p holes decreases and in turn the 6d-2p interaction increases.

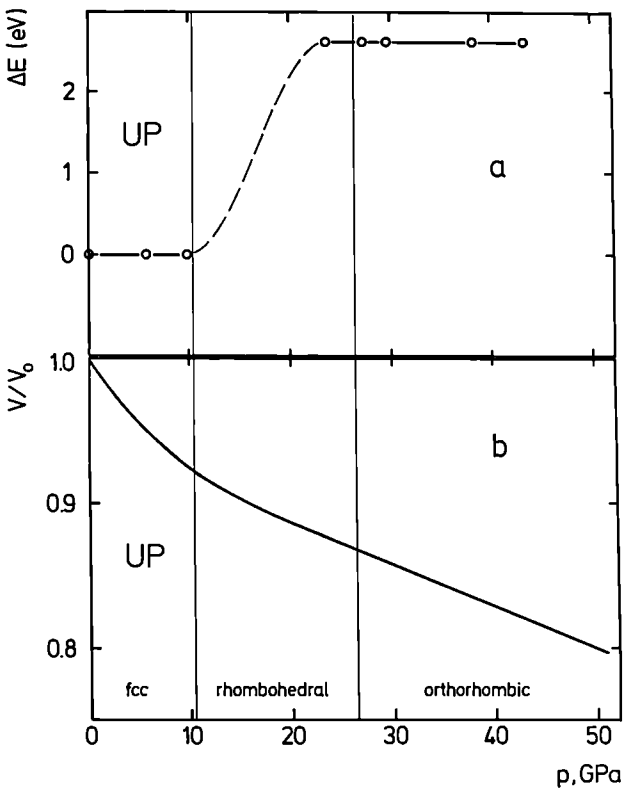

Fig. 4.14 Comparison of L_{III} edge variation with crystal structure and volume for UP under pressure
a) Energy shift of the maximum of the white line
b) Relative volume in the pressure ranges of the different phases

The shift of L_{III} to higher energy observed under pressure in UC and UP can thus be interpreted as an increase in the itinerant character of the 5f electrons (or as an increase of the uranium valence). In UC, the edge starts shifting already at a certain pressure below that of the structural phase transition. This indicates that f-d mixing already increases before this phase transition, and that the latter occurs suddenly when the f-d mixing has reached a certain value, which could be called a saturating value. For UP, in contrast, the shift of the edge is less progressive, except maybe in the range between 10 and 22 GPa where no experimental data are available. The dashed curve (Fig. 4.14) in this area has to be considered as tentative.

For UAl_2, the absorption edge remains constant through the structural phase transition. This can be taken as a confirmation that this phase transition, which was tentatively interpreted as the formation of a modulated lattice of the basic fcc structure [7], is not linked to the 5f electrons.

Both neutron and synchrotron facilities will continue to play a vital role in actinide research efforts in the future. However, because of the excellent penetrating power of the neutrons, encapsulated transuranium samples are routinely examined at neutron facilities but the same is not true for synchrotron facilities. Only in exceptional circumstances, e.g. absorption edges on very thin films, have transuranium samples been examined at synchrotrons. In particular, there seems little hope that such important experiments as high-pressure or photoemission investigations can be carried out at present synchrotron facilities in the near future because of safety requirements. Furthermore, with the increased brightness of new synchrotron machines totally new lines of investigation on very small samples can be envisaged. As a consequence the Institute, together with a number of collaborators has taken the initiative to promote the development of a "hot" beam line at a synchrotron facility. A proposal has been made to the European facility in Grenoble and plans are underway to develop some capability at the Daresbury (UK) source.

References

[1] G.H. Lander et al, Physica **136B** (1986) 409

[2] A. Banerjea and B.R. Cooper, Phys. Rev. B34 (1986) 1607
J. Appl. Physics 61 (1987) 3385

[3] W. Buyers and T. Holden, in "Handbook of Physics and Chemistry of the Actinides", North-Holland, Amsterdam (1985), Vol. 2

[4] G.J. Hu and B.R. Cooper, J. Appl. Phys. **63** (1988) 3826

[5] J. Staun-Olsen, S. Steenstrup, L. Gerward, U. Benedict and J.P. Itié; Physica **139 & 140 B**, (1986) 308

[6] J. Staun-Olsen, L. Gerward, U. Benedict, J.P. Itié, K. Richter; J. Less Common Metals, **121**, (1986) 445

[7] J.P. Itié, J. Staun-Olsen, L. Gerward, U. Benedict, J.C. Spirlet, Physica **139-140B** (1986) 330.

Collaborative Research

Over the last decade expensive and complex equipment has been installed at TU to produce, characterise, and perform certain physical measurements on transuranium samples, often in the form of single crystals. These facilities are unique in Europe. An obligation, therefore, for the Institute is to assure that the maximum use is made from this considerable investment. This is accomplished by an extensive net of collaborators (see separate list); many of whom bring special techniques to bear on samples produced at the Institute. We give a few examples below.

A considerable amount of work has been done at the CEN Grenoble on the material $NpRu_2Si_2$. This is of particular interest because of the heavy-fermion nature of URu_2Si_2. The Np compound has been examined by both Mössbauer spectroscopy and neutron diffraction on a 2 mg single crystal - the crystal having dimensions 1.7x1.0x0.2 mm^3. To our knowledge this is the smallest crystal ever used successfully to determine a complete magnetic structure. The Mössbauer spectra suggest a Np^{4+} state from the isomer shift but the hyperfine field has to come from at least two different Np sites. This ambiguity is resolved by the neutron diffraction that shows the moments (of about 1.5 μ_B) are aligned along the tetragonal c-axis below T_N (27K) but with a linear sinusoidal modulation that is incommensurate. At the lowest temperatures a third harmonic to the sine modulation is seen, but the wave form neither becomes square nor commensurate. At least two different moment values exist on otherwise equivalent Np sites so this is why the hyperfine spectra are so complex. Further measurements of this material in a magnetic field are planned, as well as experiments on mixed $(U\text{-}Np)Ru_2Si_2$ systems.

Collaborators at the CRNS-Strassbourg have been working on $NpRh_2Si_2$, which is isostructural to the $NpRu_2Si_2$ discussed above. The Rh compound orders at $T_c = 73K$ with a reduced moment of 1.4 μ_B and an isomer shift that indicates a Np^{4+} ion, both of which are comparable to those found in the Ru compound. The magnetic moments probably lie in the basal plane in the Rh compound, whereas in the Ru compound they are directed along the unique tetragonal axis.

One of the most extensively studied heavy-fermion uranium compounds is UPt_3. In collaboration with the University of Amsterdam and CEN-Grenoble a new series of experiments

(susceptibility, resistivity, and specific heat) is being undertaken on the pseudo-binary compounds $U_{1-x}Np_xPt_3$ and $U_{1-x}Pu_xPt_3$. Initial studies have shown that the Np doped samples are of good quality and the resistivity shows that with small quantities of Np local-moment behaviour dominates. The Pu doped samples are, unfortunately, of poorer quality due to the impurities of the starting Pu. A small quantity of higher purity Pu should be used for these experiments.

Synchrotron experiments with transuranium samples have, as discussed above, been exceedingly rare, but very small thin samples (~ 1mg) have been used by a group from the Freie Universität Berlin to measure the shape of the L_3X-ray absorption edge on a series of NaCl-structure samples at the DESY synchrotron in Hamburg. The shifts in the L-edge as one moves from U-Np-Pu can be correlated with the increasing localisation of the 5f electrons as more are added to the system. Equally interesting is the difference between the pnictides (e.g. As, Sb) and the chalcogenides (Se, Te). For the pnictides the L-edge positions suggest a trivalent ground state, which is in good agreement with other measurements, but in the chalcogenides they indicate a shift of perhaps ~20% towards divalency. Whether one can actually use this technique as a spectroscopic tool to assign the valency still requires more theory and experiment, but it does highlight the profound difference between these compounds. Further experiments on other Np, Pu, and Am compounds are planned.

In an effort to extend our measurement techniques at the Institute we are planning to install a low-temperature (1.2 K) high-pressure (100 kbar) instrument for measurements of electrical resistivity in 1988. This will be suitable for transuranium samples. The instrument represents a collaboration between Dr. J. Wittig (KFA-Jülich), who will be manufacturing the complex pressure cell, and EITU.

Collaboration with External Organisations

Germany

Max Planck Institute Festkörperphysik Stuttgart: Resonant Photoelectron Spectroscopy and High-pressure reflectivity studies (J. Ghijsen, R.L. Johnson, K. Syassen)

Technical University München: Mössbauer and μSR studies (M. Kalvius, W. Potzel, L. Asch, F. Litterst)

University of Paderborn: High pressure studies (W.A. Grosshans, W. Holzapfel)

KfK, Karlsruhe, Inst. für Heisse Chemie: Susceptibility and crystal preparation (B. Kanellakopulos)

KfK, Karlsruhe, Inst. für Nukleare Festkörperphysik: Low temperature resistivity, magnetization and electron spectroscopies (H. Politis, B. Renker, H. Rietschel, G. Fink))

Freie Universität Berlin: X-ray absorption spectroscopy (G. Kalkowski, G. Kaindl)

KfA Jülich, Inst. für Festkörperforschung: Photoelectron spectroscopy (D. Sarma) and electrical resistivity under pressure (J. Wittig)

Universität Erlangen: Photoelectron spectroscopy (A. Grassman)

Belgium

University of Liège: Single crystal growth, X-ray diffraction, and analysis (J. Goffart, L. Martinot, M.R. Spirlet)

University of Namur: Electron Energy Loss Spectroscopy (P. Thiry, J. Verbist)

Denmark

University of Copenhagen: High pressure X-ray diffraction (J. Staun-Olsen)

Nordita, Copenhagen: Theory (H.L. Skriver)

Risø National Laboratory: Neutron scattering (J. Kjems, B. Lebech)

Technical University Lingby: High-pressure X-ray diffraction (L. Gerward)

France

CEN, Strasbourg: Mössbauer studies, permanent magnet investigations (J. Sanchez, J. Friedt)

CEN, Grenoble: Neutron diffraction, magnetic studies, and transport properties (J. Rossat-Mignod, P. Burlet, J.M. Fournier, A. Blaise, P. Thérond)

ILL, Grenoble: Polarized neutron diffraction and neutron inelastic scattering (W. Stirling, P.J. Brown)

Inst. Curie, Paris: Mössbauer and high-pressure studies (M. Pagès, A. Tabuteau)

University of Strasbourg: Catalysis and surface reactions (G. Maire)

CEN, Saclay: Neutron diffraction and optical spectroscopy (A. Delapalme, P. Delamoye, J.C. Krupa)

CNRS, Villetaneuse and LURE, Orsay: High-pressure X-ray absorption (J.P. Itié, A. Fontaine)

Italy

Istituto Nazionale Fisica Nucleare Frascati: Synchrotron radiation spectroscopy (A. Savoia, P. Perfetti)

University of Parma: Crystallography and theory (G. Amoretti, G. Calestani, G.D. Andreetti)

Netherlands

Philips Eindhoven: Theory (P. Kelly)

University of Amsterdam: Low temperature magnetization and resistivity (J. Franse)

United Kingdom

AERE, Harwell: Low temperature specific heat (R. Hall, M. Mortimer)

University of Birmingham: Prep. of high purity single crystals (D. Fort)

Birkbeck College: neutron and magnetization studies (K. McEwen)

Rutherford-Appleton Laboratory: Neutron spectroscopy (R. Osborne, U. Steigenberger, M. Hagen)

Sweden

University of Uppsala: Photoemission and Theoretical studies (N. Martensson, B. Johansson, O. Eriksson)

Switzerland

ETH, Zürich: Single crystal growth, magnetic, optical and transport properties (O. Vogt, H. Ott, J. Schoenes, P. Wachter)

University of Geneva: Crystallographic computing (E. Parthe, E. Hoverstreydt).

Czechoslovakia

University of Prague: Photoelectron Spectroscopy (v. Sechovsky)

USA

Argonne National Laboratory: Neutron scattering (C.K. Loong; L. Morss, S. Kern)

Oak Ridge National Laboratory: Material preparation, high pressure X-ray and optical studies (R.G. Haire, J.R. Peterson)

Los Alamos National Laboratory: Materials preparation and photoemission (B. Cort, J. Ward, L. Cox, J. Smith)

Lawrence Livermore National Laboratory: Surface reactions (C. Colmenares, J. Schultz)

University of W. Virginia: Theory (B.R. Cooper)

9 Work for the Directorate of EURATOM Safeguards, Luxembourg

Scope

As an ECSAM laboratory (ECSAM: European Commission Safeguards Analytical Measurement) we offer service to the Safeguards Directorate at Luxembourg. Samples taken by EURATOM inspectors are sent to this laboratory to have their fissile material content analysed. The origin of the samples as well as the number of samples analysed are "Safeguards confidential" and will therefore not be reported here.

In order to meet the required accuracy and the increasing demand for analyses new techniques have had to be adapted and applied in the present laboratory.

In the following a description is given of

- the direct IDMS analysis of U and Pu
- the routine analysis of U- and Pu-concentrations in reprocessing output samples by K-edge densitometry
- the determination of ^{242}Pu by isotope correlations
- use of an analytical robot

Direct measurement of U and Pu by Isotope Dilution Mass-Spectrometry

U and Pu can be directly determined in input solutions of dissolved, spent, fast reactor fuel by IDMS [1]. One difficulty arises in the isobaric interference at mass 241 by americium in the analysis of Pu. In order to differentiate between ^{241}Pu and ^{241}Am, ^{243}Am spike is added before the measurement. The results (Tab. 5.1) are not comparable in accuracy to those of the conventional IDMS technique.

Although the technique appears a feasible solution to the analysis of certain ECSAM samples, the technique will not be applied by us because the newly installed laboratory robot has eliminated the previous bottleneck in sample conditioning.

Routine Analysis by a K-Edge Densitometer

A K-edge densitometer developed by KfK [2, 3] has been field-tested at the ECSAM Safeguards Laboratory of the European Institute for Transuranium Elements and is now in use for Nuclear Material Safeguards. The instrument is operated jointly by IAEA and EURATOM to determine the concentration of uranium and

Table 5.1 *Mass-spectrometer measurements on input fuel samples without chemical separation. (Ratios are given relative to measurements made on separated material = 1.0)*

	$Pu\frac{240}{239}$	$Pu\frac{241}{239}$	$Pu\frac{242}{239}$	$Pu\frac{240}{239}$
1 (a)	1.0013	0.9820	------	------
	1.0007	0.9679	------	------
(b)	------	------	0.9982	1.0091
	------	------	0.9986	------
2 (a)	1.0348	0.9493	------	------
	1.0353	0.9720	------	------
(b)	------	------	0.9999	0.9990
	------	------	0.9992	1.0101
3 (a)	0.9637	0.9753	------	------
	0.9645	0.8005	------	------
(b)	------	------	1.0003	1.0038
	------	------	0.9967	1.0042

(a) *unspiked sample*
(b) *spiked sample*

plutonium in the reprocessing output solutions.

For the field-test measurements the concentrations of U and Pu were also determined by conventional redox titration methods in four laboratories. Tab. 5.2 gives the ratio of the densitometric value of the concentration to that obtained by chemical analyses for the different laboratories. The average bias of the Pu determination between the K-edge densitometry results and those from chemical analysis is less than 0.1%. The standard deviations of the means range from 0.15% to 0.49%.

For the corresponding U-analyses the average bias between K-edge densitometry and titration (as obtained by three laboratories) is 0.15%, with a mean standard deviation of 0.14%. It should be noted that, if the laboratory with the highest bias is excluded, the remaining bias between densitometry and titration is reduced to 0.07%, with a standard deviation of about 0.1%.

Samples taken at MOX-fuel fabrication plants could be analysed by the same technique. The most time consuming step is the dissolution of PuO_2 or MOX samples. The total analysis costs are not effected by the method (titration or K-edge) used to determine the uranium or plutonium concentration. However, the K-edge densitometer is restricted to Pu concentrations > 50 mg/ml and therefore the titration method will continue to be used in our laboratory for MOX and PuO_2 samples.

Isotope Analysis of ^{242}Pu by Gamma spectroscopy and Isotope Correlation Technique

The isotopic composition of a plutonium sample can be obtained by γ-spectrometric analysis [4]. The detector of the K-edge densitometer is used for this purpose. The glass cell with the liquid sample is placed inside the glove-box close to the detector at a defined position. The abundance and specific activity of ^{242}Pu are low and the abundance of this nuclide (wt%) is preferably determined by the correlation:

$$^{242}Pu = 52 \times \frac{^{240}Pu\,^{241}Pu}{^{239}Pu\,^{239}Pu}$$

based on the measured weight ratios of the other major Pu isotopes [5]. This correlation is used for BWR and PWR fuels.

The comparison of 13 isotopes analysed with mass spectrometric data is rather good (Tab. 5.2). The deviation for ^{242}Pu can be reduced if a reactor-specific correlation is applied instead of the general correlation given above.

Since the input data are accessible to an inspector, he could calculate the correlation for the particular samples. In this way he could not only obtain a correlation specific for this fuel but also avoid the need to correct the ^{241}Pu to the date of fuel discharge from the power station - a procedure necessary for correlations involving different fuel assemblies and irradiations, and which is very difficult to do when several fuels are mixed in the same output batch. The use of the directly calculated correlation reduces the error of the ^{242}Pu abundance determination from 3.1% to 1.8% (Tab. 5.3). The correlation used in this particular case was calculated from about 100 input analyses pertaining to two BWRs.

Table 5.2 Comparison of Pu and U concentrations determined in reprocessing output samples by K-edge densitometry and titration

	K-edge Lab. 1	K-edge Lab. 2	K-edge Lab. 3	K-edge Lab. 4	K-edge Lab. mean
Pu	0.9996	1.0001	1.0007	1.0002	1.0002
	±0.0038	±0.0027	±0.0049	±0.0015	±0.0016
U	1.0007	1.0033	1.0007		1.0015
	±0.0019	±0.0021	±0.0010		±0.0014

Note: Given are the means of eight Pu and nine U analyses for each laboratory and the mean value of the laboratories with the standard deviation

Table 5.3 Ratio of gamma to mass-spectrometric Pu isotope abundance for 13 output batches

^{239}Pu	^{240}Pu	^{241}Pu	$^{242}Pu^{a}$	$^{242}Pu^{b}$
0.999	1.006	1.005	0.936	1.006
± 0.005	± 0.009	± 0.008	± 0.031	± 0.018

a *^{242}Pu determined by a general correlation*
b *^{242}Pu determined by a fuel specific correlation*

Use of an Analytical Robot in a Safeguards Laboratory

Since October 1986 an analytical robot has been routinely used to condition reprocessing samples coming from different plants.

The robot executes the following steps:

- weighing sample and spike aliquots
- mixing and isotopic exchange
- heating and drying of samples.

The laboratory receives samples from various reprocessing plants which reprocess different fuels and therefore a series of programs has been set up which enables the treatment of (e.g.):

- freshly diluted reprocessing input samples
- already on-site spiked samples, where only the Pu isotope mixing and exchange have to be accomplished
- preparation of dry spikes

In addition the robot is used in the analysis of Pu output samples by isotope dilution analysis.

The robot is surrounded by its periphery devices and a variety of racks for holding the samples (Fig. 5.1). The most important of these devices are the balance, mixer (for liquids), liquid dispenser and heating plate. The layout shows the partitioning of the box into three compartments: one used for the introduction of potentially contaminated samples, the main operation area and an area for the evaporation of liquid samples. The robot possesses two exchangeable hands, one to open and handle the possibly contaminated sample bottles and the second for the subsequent work. To avoid corrosion the robot is flushed internally with argon. As mentioned above, the conditioning of the samples is plant- and fuel-dependent and several standard programmes are used, which allow e.g. for different methods of isotope mixing and exchange in the treatment of the sample with NH_4F, H_2O_2, NH_2OH_2Cl.

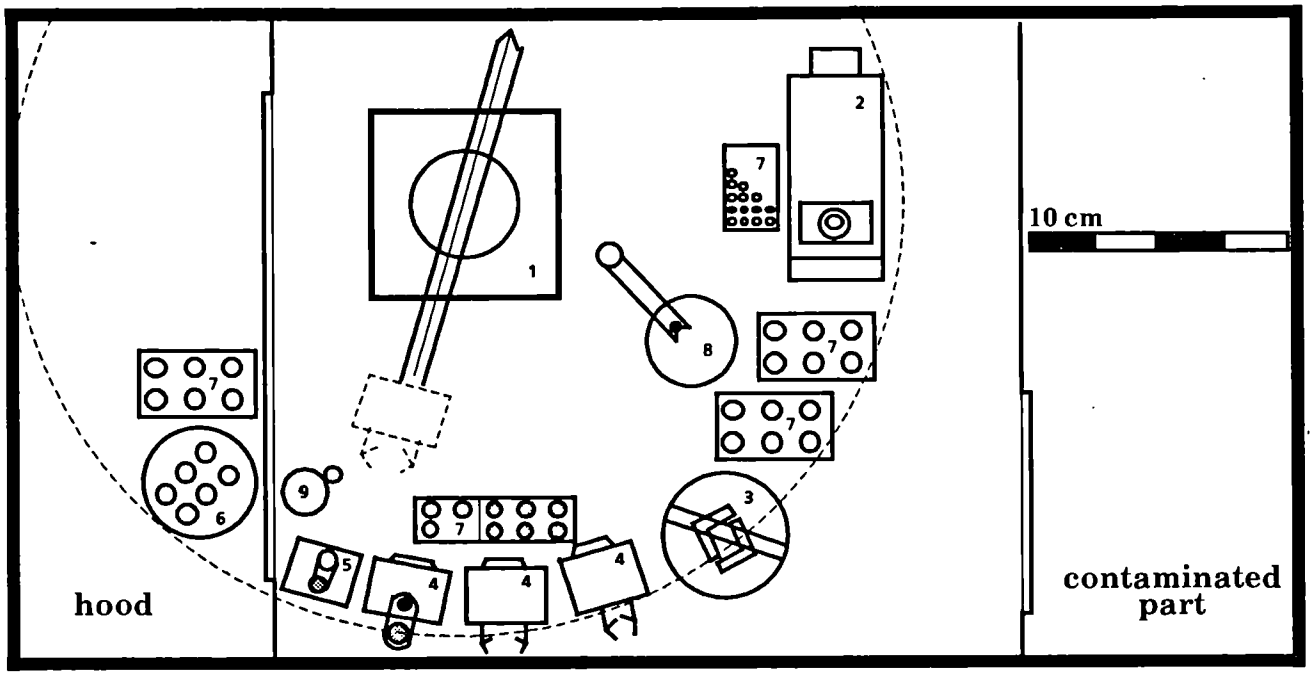

Fig. 5.1 Layout of an analytical robot (1) in a glove-box, balance (2), decapper (3), exchangeable hands (4), mixer (5), heating plate (6), racks (7), waste (pipettes, etc.) (8), liquid dispenser (9)

Performance criteria

In setting up a sample preparation system with robots the following points have to be observed:

- to ensure a steady throughput of samples a certain redundancy in equipment is needed
- quality assurance has to be implemented
- the work throughput of the robot has to be appropriate to the number of samples and/or to the capacity of the mass-spectrometer.

The reliability of the robot up to now has been extremely high and no breakdowns have been observed which could lead to a delay in the analysis. Nevertheless we feel that a standby robot is required especially when further steps of the sample preparation are executed by the robot.

The quality assurance programme applied is not different to that used previously in manual operation. The reproducibility of the sample preparation is controlled by duplicate analyses. The calibration of spikes and balances is routine: non-constant biases are controlled by standard weights and by analysing working standards. The latter consist of secondary standards of mixed $^{233}U/^{244}Pu$ used to monitor cross-contamination. In addition secondary standards of $(U,Pu)O_2$ are used to control the isotope dilution analysis.

The nominal capacity of the analytical robot is designed to process three input samples at the same time. From each of them two parallel dilutions are spiked and conditioned of which after separation, 12 U and Pu samples in total will be obtained (Fig. 5.2). The mass-spectrometer turret holds 13 filaments: 12 samples and 1 isotope standard.

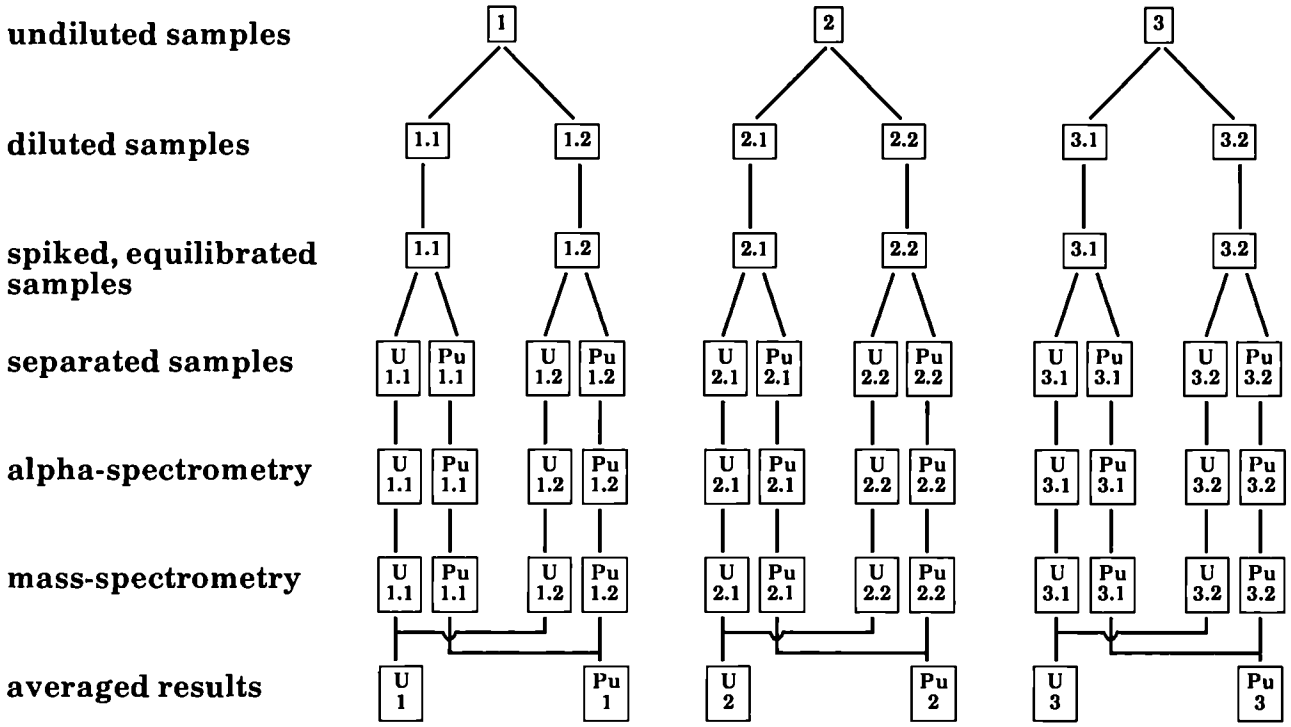

Fig. 5.2 Nominal capacity of the Automatic Laboratory

References

[1] L. Koch, "Possible Verification Methods for the Input Measurements of Fast Reactor Fuel Reprocessing", Proceeding of the 5th Annual ESARDA Symposium on Safeguards and Nuclear Material Management, Versailles, France (19-21 April 1983)

[2] H. Ottmar, H. Eberle, P. Matussek, I. Michel-Piper, KfK 4012 (1986)

[3] H. Ottmar, H. Eberle, L. Koch, R. De Meester, E. Kuhn, "Field Demonstration of an X-ray Densitometer for Uranium and Plutonium Input Verification in Reprocessing", Int. Symposium on Nuclear Material Safeguards, Vienna (10-14 November 1986)

[4] H. Eberle, H. Ottmar, P. Matusssek, JOPAG/04.85-PRG-113, Kernforschungszentrum Karlsruhe (1985)

[5] R. Gunnink, UCRL-84096, Lawrence Livermore Nat. Lab., CA (1980)

6 Prospective Studies

Acoustic Scavenging of Aerosols and Gases

Introduction

The aim of the present studies is to investigate the feasibility of the use of high intensity acoustic waves to combat airborne spreading of accidentally released radioactive or toxic materials. The potential areas of application range from small scale laboratory 'spills' to major releases of hazardous aerosol and gas into the atmosphere [1,2].

Acoustic scavenging of aerosol is foreseen as a two step procedure involving the acoustic agglomeration of very fine particles to larger particles followed by their collection through acoustically induced particle drift. Of particular interest in the agglomeration studies is how quickly submicron particles can be agglomerated as a function of frequency, sound pressure level, and mass loading of the aerosol. These aspects are treated in section 2. With regard to acoustically induced particle drift, details are given in section 4.

Acoustic scavenging of gas is based on a modification of the above procedure. As a first step the gas to be scavenged is sprayed with an aerosol with suitable absorption properties such as activated carbon. The absorption of the gas onto the particles can, under certain circumstances, be enhanced by the action of the sound field. After the absorption process, the injected aerosol can be removed by using the aerosol scavenging technique described above. In section 3 details are given of toxic gas absorption rates as a function of gas concentration , aerosol mass loading and size distribution, and sound field characteristics.

Aerosol Agglomeration

Background

An aerosol may consist either of liquid droplets or solid particles suspended in a gas. When the droplets or particles in the aerosol collide with each other they invariably stick together: the result is termed coagulation for liquid droplets and agglomeration for solid particles. Rapid agglomeration could be applied as a method of eliminating dust clouds because large agglomerates settle rapidly thus removing suspended particles from the air.

Agglomeration requires particles to collide with each other and collisions require relative motion between particles. Such velocity differences always exist because of Brownian motion but, except possibly at very high particle concentrations, Brownian agglomeration is not rapid enough for dust control purposes. Therefore, if it is desired to cause an aerosol to agglomerate rapidly it is advantageous to impart as much

relative motion as possible to the particles. Additional velocity differences, and thus an enhanced collision and agglomeration rate, can result, for example, from the size dependent response of particles to an applied field e.g. gravitational sedimentation.

The motion induced by the forces associated with thermal, gravitational or electrostatic fields however is usually a low velocity unidirectional drift so that the enhancement of agglomeration achievable with such fields is rather limited. An alternating field such as an acoustic field is potentially more effective [3] for enhancing agglomeration because the rapidly alternating force that is applied to the particles is capable of inducing a much greater degree of relative motion between particles.

In fact, the most effective stirring of an aerosol cloud is probably achievable by superimposing a size dependent unidirectional drift and an oscillating motion to the particles.

To achieve a worthwhile agglomeration enhancement it is clear that the velocity imparted by the acoustic field should be much greater than those due to Brownian motion and gravitational sedimentation. The velocities imparted to aerosol particles by various forces are compared in Fig. 6.1. It can be seen that the velocity imparted to a particular size and density of particle depends on the sound frequency and intensity: the inertia of the particles can prevent them from being fully entrained in the sound field if the frequency is too high.

For a monodisperse aerosol (all particles the same size) all the particles are entrained in the

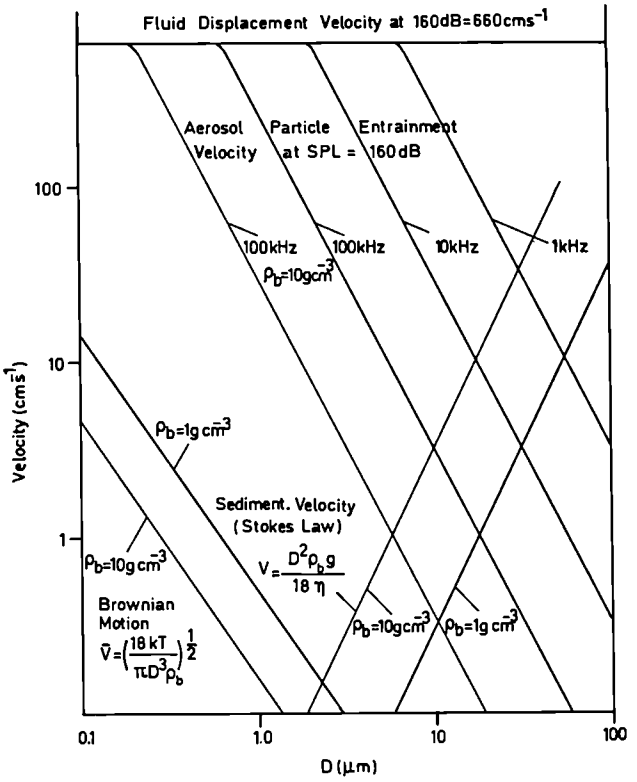

Fig. 6.1 A comparison of particle velocities due to Brownian motion, gravitational sedimentation, and acoustic entrainment.

sound field to the same extent and thus oscillate in parallel with no relative motion and no enhancement of agglomeration. For a polydisperse aerosol however, it is possible to choose a frequency of sound that will induce various degrees of entrainment across the particle size spectrum and thereby ensure relative motion and thus enhance agglomeration.

To achieve acoustic agglomeration the amplitude of oscillation should exceed the average inter-particle spacing. The mass loading of the aerosol cloud should therefore not be below a certain threshold. For particles with a density of $1g/cm^3$, this density is $3.3*10^{-3}$ g/m^3 for 0.1 micron particles and 3.8 g/m^3 for 1 micron particles.

Experimental Agglomeration Studies

From Fig. 6.1 it can be seen that to achieve a suitable degree of particle entrainment for typical aerosols (particle size of the order 1 micron) ultrasonic frequencies are the most suitable. They also have the advantage of lying outside the audible range.

Piezo-electric crystals are the most efficient means of generating high ultrasonic sound pressure levels (SPL). The crystal is driven by the amplified sine wave from a signal generator. With an appropriate acoustic horn design, SPL's in excess of 160 dB can be attained when the crystal is driven at its resonance frequency. The SPL however drops off very rapidly at frequencies only slightly removed from the resonant frequency. To remain exactly on resonance a phase locked loop amplifier is desirable because the resonant frequency drifts as the transducer heats up in operation. A cheaper, but less satisfactory, solution to the problem of drifting resonance frequency is to drive the crystal with a narrow band sweep generator. To maximize the SPL a standing wave is set up with a simple flat plate reflector. One of the acoustic devices used in these experiments is shown in Fig. 6.2.

Rapid acoustic agglomeration has been demonstrated for a number of different aerosol dusts such as Latex spheres, polydisperse alumina and Uranium-Plutonium oxide nuclear fuel. With an aerosol of water droplets, coagulation leads to droplets up to about 1 mm diameter which then remain levitated by radiation scattering at the antinodes of the standing wave pattern [4]. A special apparatus to demonstrate the acoustic coagulation and levitation of water droplets was constructed for use at exhibitions etc. An accompanying video film shows very clearly the very rapid coagulation rate achievable with an acoustic field.

Fig. 6.3 shows agglomerates of the different aerosol materials used in these tests. Certain of the agglomerates formed from polydisperse alumina consist only of relatively large (7 micron) primary particles implying that size segregation has occurred in the acoustic field. This phenomenon is not predictable by theory and demonestrates that the agglomeration process is not properly understood. The images in Fig. 6.3 show that aggomeration of micron size particles up to 0.5 - 1 mm diameter agglomerates is easily achieved.

Acoustically Enhanced Toxic Gas Absorption

Background

Studies on the agglomeration and scavenging of aerosol particles by an acoustic field have been started. The objective of the present work is the widening of this technique to the scavenging of toxic gases, by studying their absorption on aerosol particles, and the effect of an acoustic field on this absorption.

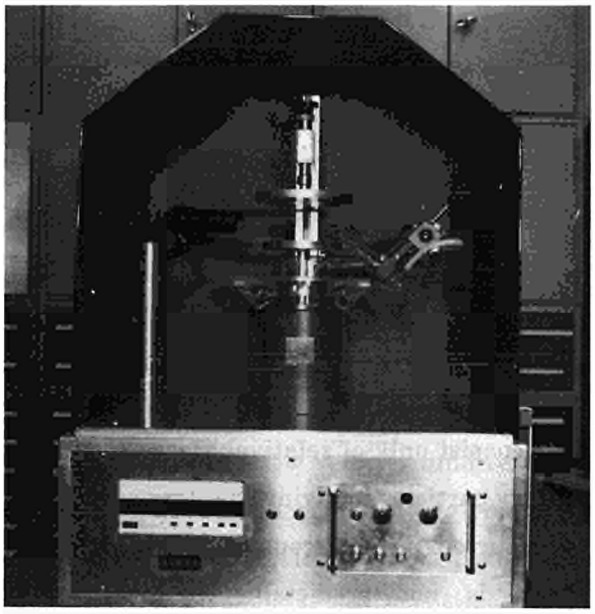

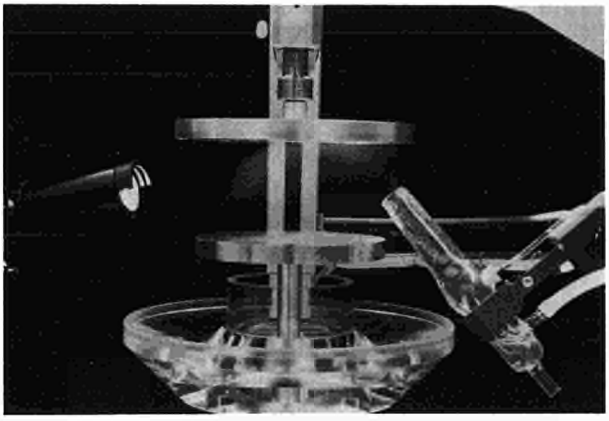

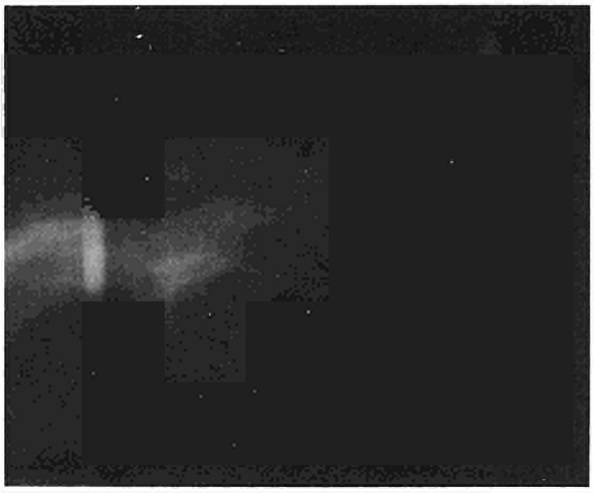

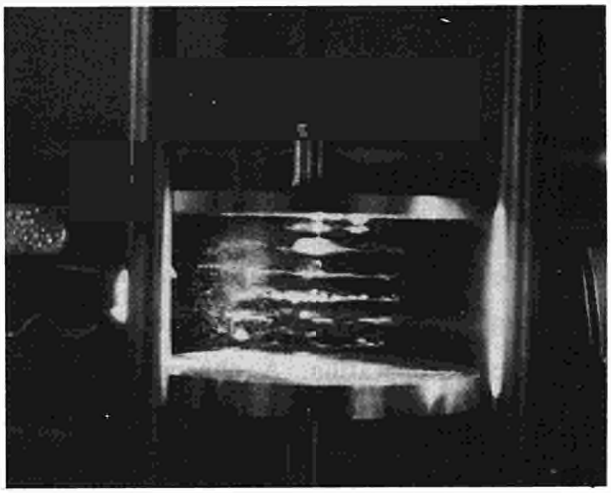

Water aerosol from the left enters the sound field (a 20 kHz standing wave). Initial stages of coagulation lead to the formation of liquid droplets along the vertical axis.

Final stages of coagulation of aerosol and trapping of droplets in the sound field. The structure of the sound field is clearly visible.

Fig. 6.2 An ultrasonic standing wave apparatus for acoustic agglomeration .

Preliminary Experiment: Absorption Capacity of Activated Carbon Samples

In order to roughly quantify the absorption capacity, an air + nitric oxide mixture was blown over activated carbon particles or activated carbon powder. The absorption was indicated by the change of weight of the activated carbon. The results for the powder sample are shown in Fig 6.4 (gas: air + 5000 ppm nitric oxide): the activated carbon powder can absorb up to 20 % of its

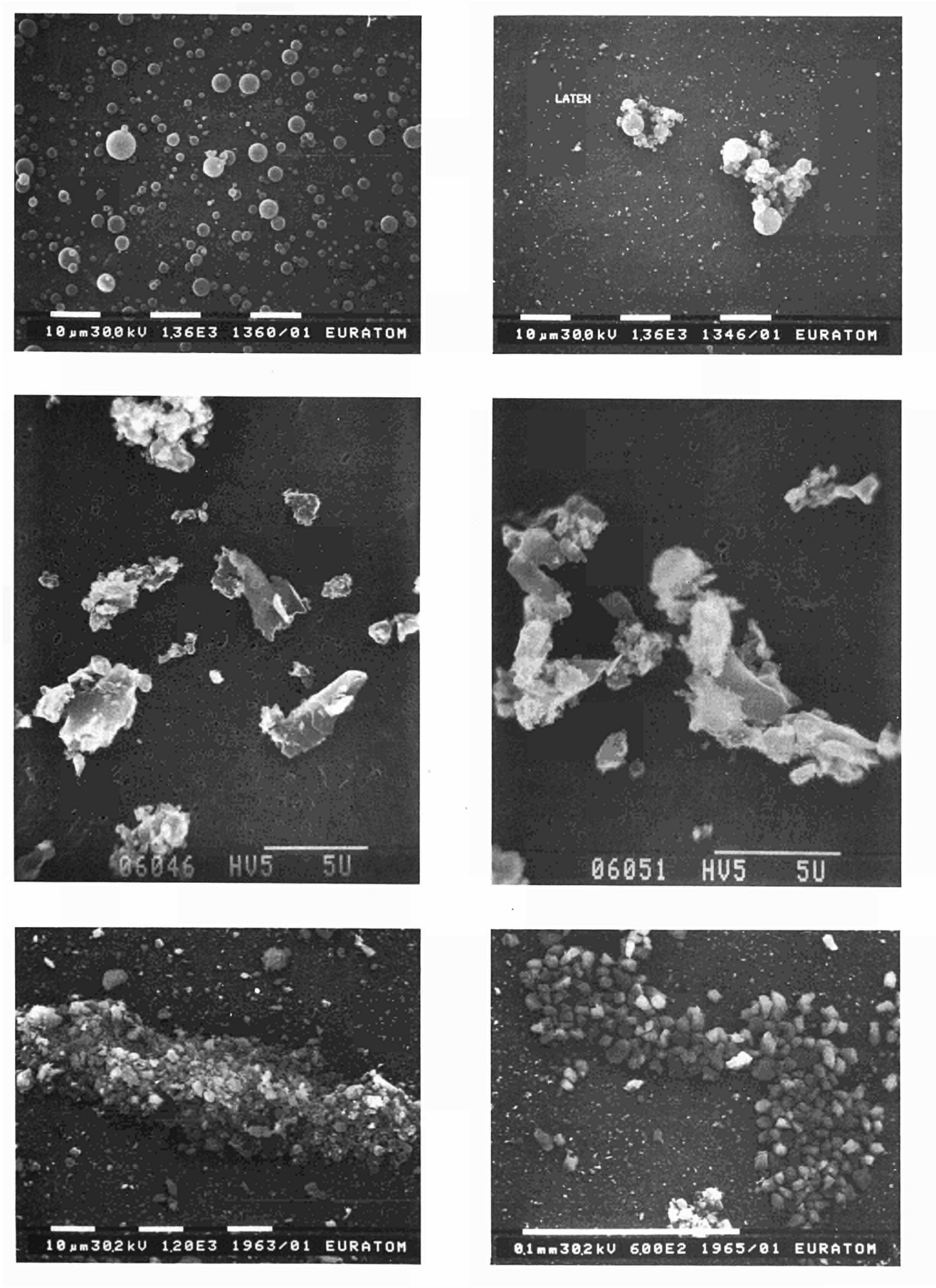

Fig. 6.3 Agglomerates of aerosol particles of various substances produced by an acoustic field

weight, and the absorption is almost completed after 30 minutes.

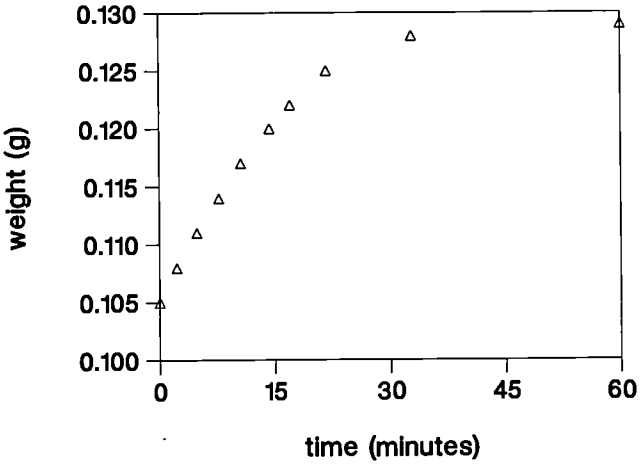

Fig. 6.4 Absorption of nitric oxide by activated carbon powder (no ultrasonic field)

In the second experiment, a flow of air containing 5000 ppm of nitric oxide was continuously blown over a clean piece of activated carbon. The measurements were first done under normal conditions, then with the activated carbon in levitation, i.e. in an acoustic field.

No influence of the acoustic field was found. This could be explained by the dimensions of the activated carbon piece: for such a cylinder (4 mm length, 3 mm diameter), the rate-limiting step of the absorption process is diffusion into pores, which is not affected by the presence of an acoustic field.

Influence of the Acoustic Field on Aerosol Absorption

Principle of the Experiment

The starting point was a cloud of activated carbon powder. The evolution of the aerosol size distribution during the experiment (in the presence of an acoustic field) was measured, and is shown in Fig.6.5. The effect of agglomeration

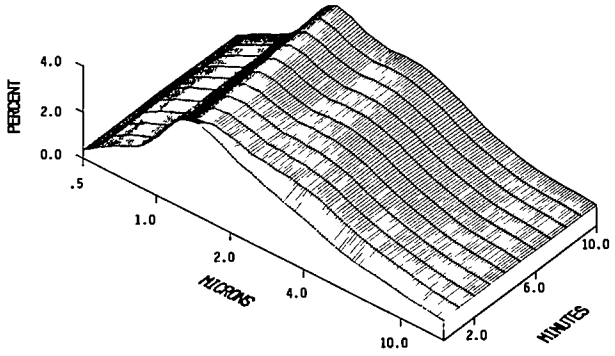

Fig. 6.5 Particle size distribution (in percent) in the cylinder as a function of time

is visible. The aerosol cloud was allowed to fall into a cylinder containing a toxic gas; the resulting absorption was measured with and without the presence of an acoustic field. In this experiment, the change in concentration of the toxic gas was measured because of the difficulty of measuring the change of weight of an aerosol cloud. The concentration was then determined by the Saltzman procedure: a small amount of gas was taken from the cylinder and mixed with a given volume of reactant. The reactant changes its coloration as a function of the nitric oxide concentration.

The experiment was conducted as follows:

- The cylinder was filled with 30 l of air + toxic gas
- Addition of 15 l of air + aerosol (with evacuation of 15 l of the air + toxic gas mixture); this step takes 3 minutes
- A 1.6 ml gas probe was taken at given time intervals
- The filter and the needle were changed
- The gas sample was injected into a closed tube containing 1 cm^3 of Saltzman reactant
- The extinction coefficient was measured (after 15 minutes).

The experimental parameters were determined by the characteristics of the aerosol generator and the volume of the cylinder. The quantities were estimated for an initial nitric oxide concentration of about 250 ppm, which corresponds (for 15 l) to the weight that can theoretically be absorbed by the injected aerosol. A heating plate (35° C) was installed under the bottom of the cylinder, in order to create a convection inside the cylinder and to accelerate the mixing of the air nitric oxide and the air containing the aerosol.

First Results

The first results showed that there is a difference between the absorption with and without the presence of an acoustic field; but it seems that the effect has already occurred when the measurements begin (i.e. 3 minutes after starting aerosol injection). This is due to the long time needed to introduce the required quantity of aerosols into the cylinder. It appeared also that the aerosol quantity produced by the generator was not sufficient to absorb the amount of toxic gas present in the cylinder (because of losses and precipitation of larger aerosol particles onto the bottom of the cylinder).

The original experiment was then modified, as shown in Fig 6.6, to allow the rapid introduction of a significant quantity of aerosol into the cylinder. The aerosol is introduced through a tube at the top of the cylinder, and is quickly blown in by a short blast of air. An advantage of the new setup is the possibility of selecting and varying the size of the injected aerosols.

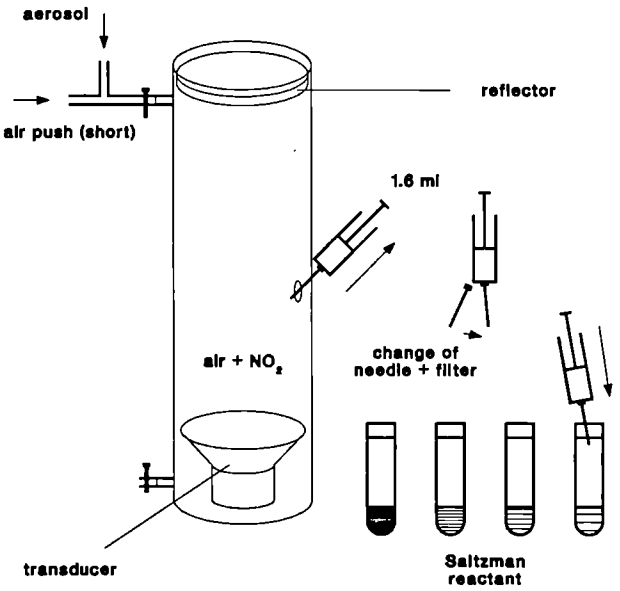

Fig. 6.6 Set-up for the measurement of the effect of acoustic field on the absorption by an aerosol

Conclusions

Typical results obtained with the new set-up are shown in Fig 6.7.

The experiment confirms that the main effect occurs during the first five minutes after introduction of the aerosol. It seems that the

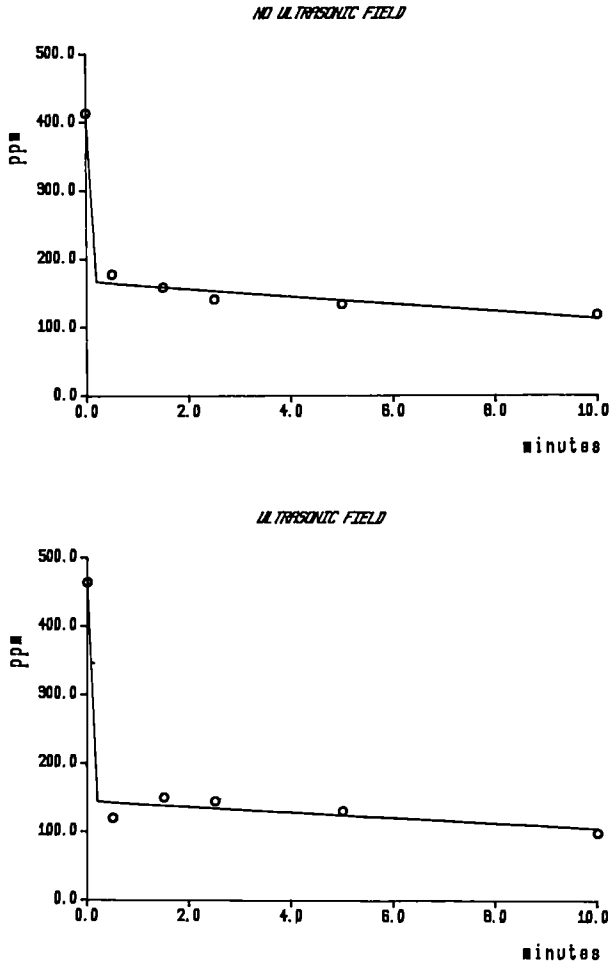

Fig 6.7 Results obtained with the new setup (the gas concentrations are calibrated)

acoustic field slightly improves the absorption of the toxic gas by the activated carbon particles and also that the absorption occurs more quickly in the presence of an acoustic field.

The acoustic field is expected to favour absorption of gases on the aerosol particles, but it has also a number of other effects (agglomeration, turbulence) which may influence the absorption in one or the other direction.

The Reynolds number can be calculated as $5*10^{-2}$, by taking the mean value of 1.5 microns for particle size, and a sound pressure level of 145 db (as measured), at 20 kHz. This is however too low for the acoustic field to have an appreciable effect; in order to see such an effect, the Reynolds number must be greater than 1, which means working with 15 microns particles, and a sound pressure level of 160 db: the sedimentation velocity would then be around 0.4 cm/s. This will be the next experimental step.

Acoustically Induced Particle Drift

Background

When a sound wave interacts with a particle the wave energy is scattered in much the same way as light from particles in the atmosphere. The resulting transfer of momentun gives rise to a force on the particle in the direction of propagation of the wave. This force, known as the 'radiation pressure', is a consequence of the ideality of the medium in which the sound wave is propagating. Normally, however, aerosol dynamics is governed by viscous forces with the particle Reynolds number being much less than unity. Under these conditions very strong forces on the particle can result which are not as intuitively obvious as the radiation pressure. The most important of these forces is the 'averaged Oseen force' discovered by Westervelt in the early 1950's [5,6]. The remarkable feature about this force is that, depending on the shape of the sound wave, the particle can move in the same direction or the direction opposite to that of the wave propagation. This immediately raises the idea of aerosol manipulation by sound waves.

In the following section the averaged Oseen force is described in detail together with preliminary results of an experimental investigation.

The Average Oseen Force

A sphere in a slowly moving fluid will tend to be carried along with the fluid through viscous coupling. The force F acting on the sphere of radius a is given by Stokes' formula

$$F = 6\pi a\eta u \qquad (1)$$

where u is the velocity of the fluid relative to that of the particle and η is the viscosity of the medium. Stokes' formula is valid only for low Reynolds number (i.e. $Re = 2\,|u|\,a/\delta << 1$). At higher Reynolds number, a more accurate expression for the force on the relative speed is given by Oseen's formula

$$F = 6\pi a\eta u\{1 + (3/8)\,(a\,|u|/\delta)\} \qquad (2)$$

Equation (2) can be expressed in terms of the hydrodynamic drag coefficient C which is defined as the force on the sphere divided by the projected area of the sphere and the kinetic energy density of the fluid, i.e.

$$C = 24/Re\,\{1 + (3/16)Re\} \qquad (3)$$

The degree to which equation (3) conforms to experiment can be seen in fig.6.8 [7]. It is seen that for $Re \approx 1$, the drag coefficient obtained from the use of Oseen's formula is more accurate than that obtained from Stokes' formula.

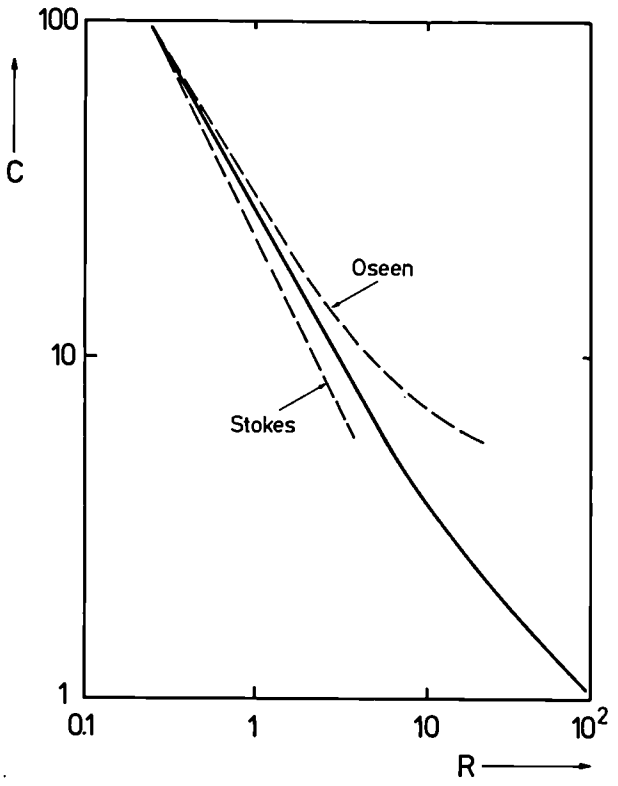

Fig. 6.8 Drag coefficient vs. Reynolds number for a sphere. (– experiment)

It should be remembered that the above relations have been derived for steady flow and it is not clear to what extent these relations are valid for the non-steady flow of fluid past a sphere as produced, for example, by a sound wave. For simplicity Westervelt [6] assumed relation (2) to be instantaneously valid and proceeded to evaluate the consequences of this assumption.

In particular, Westervelt showed that a high intensity sound wave (with zero average fluid velocity) could interact with a small particle in such a way as to lead to a net velocity of the particle either towards or away from the sound source.

To understand this, consider a fluid displacement wave u(t) which is periodic and has zero average

value (e.g. a sound wave). The resulting force on the particle F(t) will also be periodic but will not necessarily have zero average value as is shown in Figs. 6.9a-6.9d. In Fig. 6.9a and 6.9c the force velocity relationship is assumed to be linear (this is equivalent to Stokes' formula being exactly valid). Any waveform u(t) for which u(t) = 0 will result in an average force F(t) on the particle

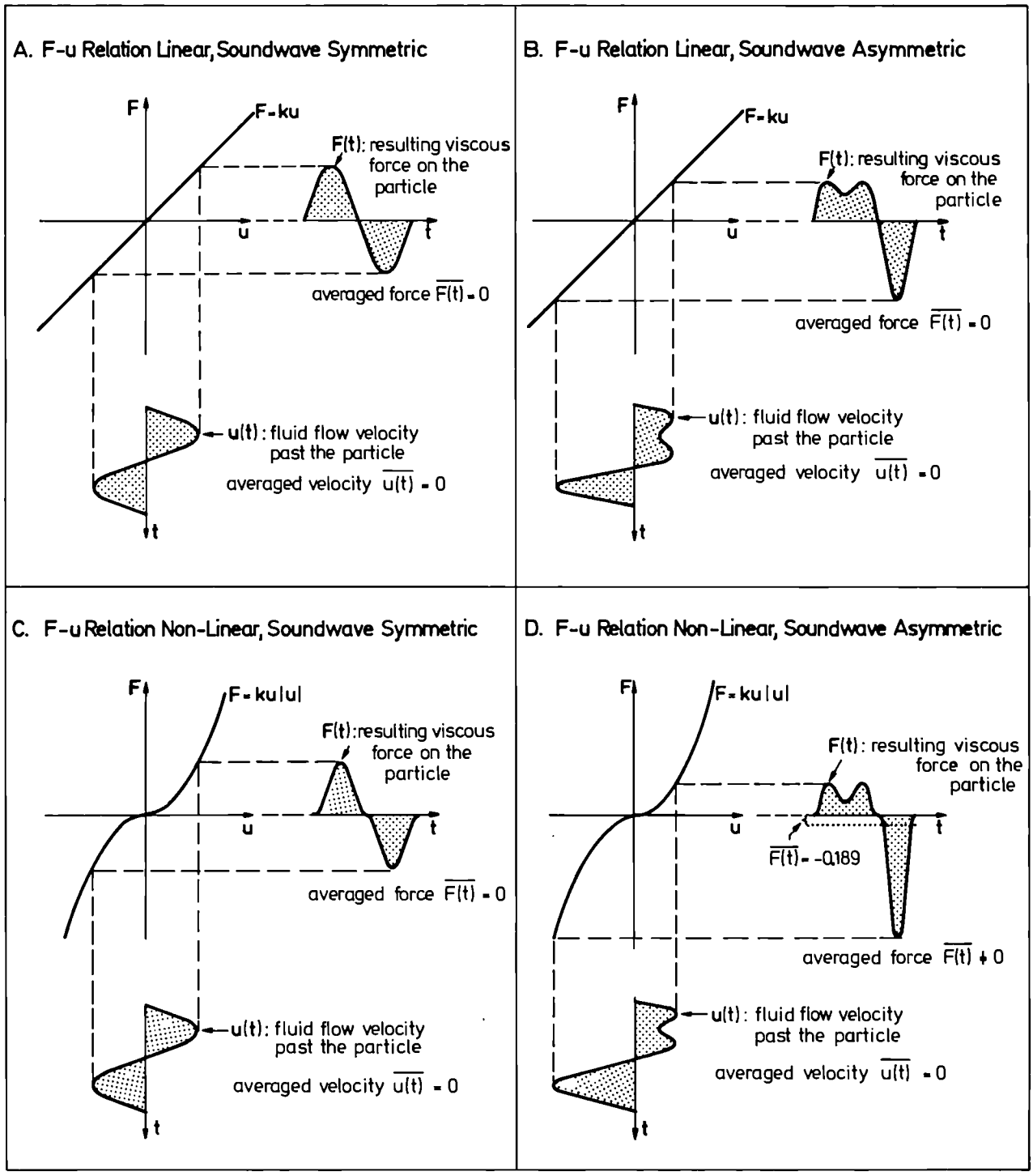

Fig. 6.9 Geometric representation of the averaged Oseen force induced by the action of a sound wave on a small particle. A net force results provided the force - velocity relationship is non-linear (as is the case at high intensities) and, in addition, the sound wave is symmetric.

which is zero. If, however, the force velocity relationship is not linear (as is the case with Oseen's formula) then a non-zero average force will result from any fluid velocity wave u(t) provided it is asymmetric (as shown in Fig. 6.9d).

This so called averaged Oseen force is obtained by averaging equation (2) over one cycle of the motion i.e.

$$F_{Oseen} = (9/4)\pi a^2 \rho u |u| \qquad (4)$$

The resulting steady force on the particle depends on the precise form of the fluid velocity wave u(t). For symmetric waves, the resultant force is symmetric and it's average value is zero (Fig.6.9c). For asymmetric waves, the resultant force is asymmetric with a non-zero average value (Fig.6.9d).

An asymmetric wave can be simply constructed by the addition of two symmetric waves. Consider a wave of the type

$$u(t) = u_0\{\sin(\omega t) + m.\sin(2\omega t + \emptyset)\} \qquad (5)$$

which is constructed from a pure tone by adding the second harmonic with an amplitude factor m and phase Ø. The case for which m = 0.5, Ø = π/2 is shown in Figs. 6.9b and 6.9d. Notice that u(t) = 0 and that the wave is asymmetric. Numerical integration leads to the result $u|u|/u_0^2 = -0.189$ and this together with equation (4) allows one to calculate the averaged Oseen force on the particle. The negative sign implies that the averaged force acts towards the sound source.

This net force on the particle causes it to drift in the fluid medium with a drift speed u_d given combining equations (1) and (4) i.e.

$$u_d = (3/8)(a/\eta)\,\rho u_0^2\{u|u|/u_0^2\} = (3/16)u_0 Re\{u|u|/u_0^2\} \qquad (6)$$

To see that the induced drift velocities can be of considerable magnitude consider the waveform given by equation (5) with m = 0.5, Ø = π/2. At a sound pressure level of 150 dB, a 20 μm diameter particle will have a drift speed of 11 $cm.s^{-1}$. Drift velocities for various particle diameters and sound pressure levels are given in Fig. 6.10.

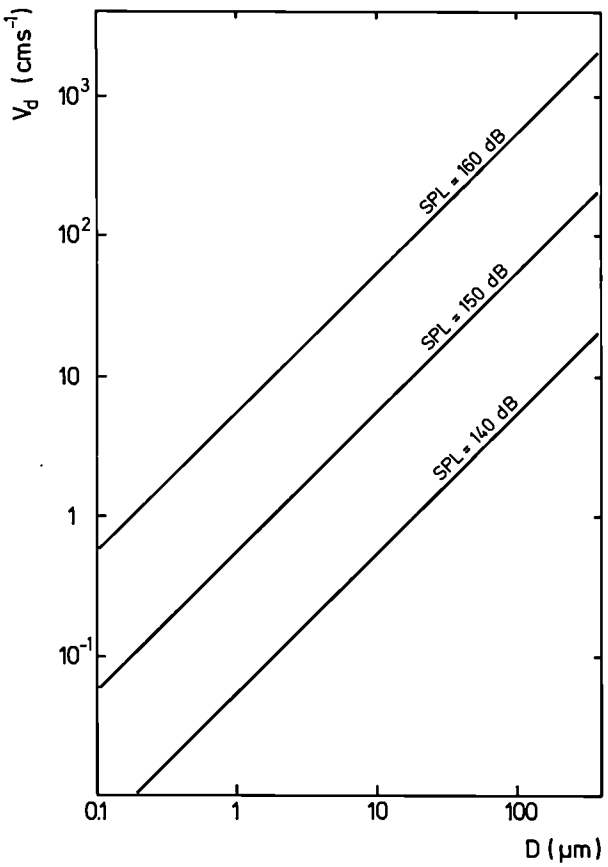

Fig. 6.10 Drift velocities for various particle diameters and sound pressure levels. Sound wave has the form $u(t) = u_0\{\sin(\omega t) + m.\sin(2\omega t + \emptyset)\}$ where $m = 0.5$, $\emptyset = +\pi/2$ have been used for the above evaluation.

It should also be noted that although equation (6) for the drift velocity does not contain the frequency explicitly, it is valid only in a particular frequency range. It should be clear that the frequency should be high enough such that the particle does not follow the oscillatory motion of the medium induced by the sound wave. It is also required that the frequency be low enough such that the displacement amplitude of the wave is greater than the diameter of the particle. If this were not the case different parts of the sphere would acted upon by forces in different directions which cancel each other.

Experimental Setup

The experimental setup used to investigate the averaged Oseen force on small particles is shown schematically in Fig. 6.11. From a master oscillator the dual wave synthesiser is used to produce two A.C. voltage signals with the required frequencies, amplitudes, and phase differences. These electrical signals are then applied to the acoustic resonators which produce progressive acoustic waves with desired amplitude and phase difference characteristics. The amplitudes and phase difference of the sound waves can be varied by varying the properties of the electrical signals.

Dual Waveform Synthesizer

A voltage controlled master-oscillator drives two synchronous binary counters (Fig. 6.12) whereby bit 1 of the first counter is the clock-pulse for the latter. This ensures that the count rates differ by a factor of exactly two. Each of these counters can address a memory in which data is stored for the generation of the two waveforms. This information is read from EPROMS which can be programmed with any signal form.

For the 20 kHz section this is a single sine wave stored as 128 samples and for the 40 kHz section the data is stored into 128 banks of 128 samples each. This defines the phase resolution to be $360°/128 \approx 3°$ between two subsequent samples or banks. For convenient selection of the phase angle, the setting of the thumb-wheel switches is converted from BCD into the required binary format by means of an EPROM look-up table. The data which is read from the memories are then directed to digital-analog convertors to

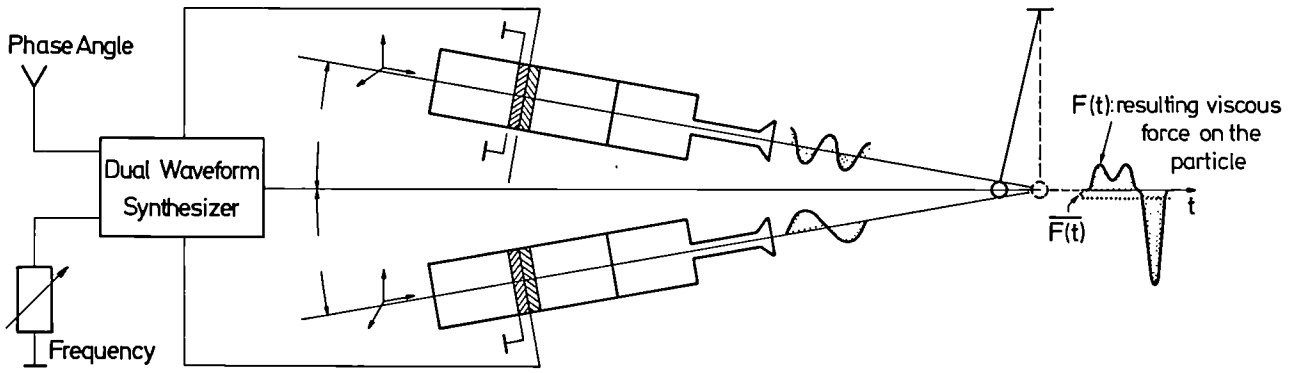

Fig. 6.11 Schematic experimental setup for the measurement of the acoustically induced drift velocities

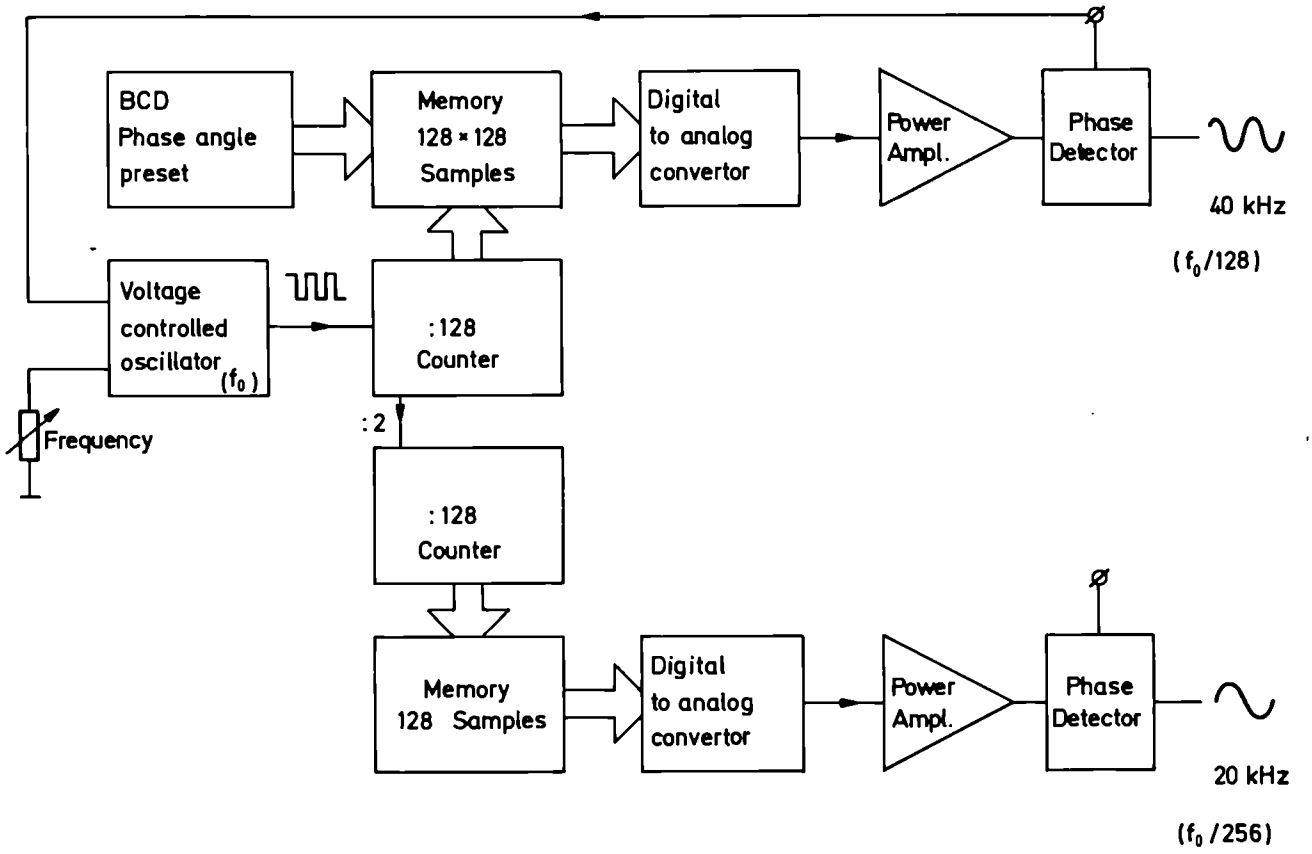

Fig. 6.12 Dual waveform synthesiser (simplified)

obtain the voltage signals. These signals are then applied to the power amplifiers.

The two resonators are driven through a matching / phase detector circuit whose output voltages are used for feedback to the master oscillator. This ensures a phase angle of 0° between current and voltage for that resonator where feedback is chosen. Obviously the other resonator has to run in slave (free) mode to keep the phase angle between the 20 kHz and the 40 kHz sound waves constant.

Acoustic Resonators

The design and construction of the resonators has been described in detail in TUAR 86. Resonant half-wave transducers were constructed to produce the acoustic power at the chosen frequencies e.g. 20 and 40 kHz. Stepped horns were coupled to the transducers to amplify the displacement amplitude of the transducers. The high power ratings required that the horns be machined from a special titanium alloy. Sound pressure levels of 155 and 145 dB could be produced at a distance of 10 cm from the 20 and 40 kHz resonators respectively.

References

[1] J. Magill, 'Verfahren und Vorrichtung zum Entfernen einer Aerosolwolke aus der Luft', Euratom Patent number 86900 registered in Luxembourg on 26.5.1987

[2] J. Magill and S. Pickering, 'Removal of radioactive and toxic aerosols and gases from the atmosphere by acoustic scavenging', poster presentation at the World Conference on Chemical Accidents, Istituto Superiore di Sanità, Rome 7-10 July 1987

[3] E.P. Mednikov, 'Acoustic Coagulation and Precipation of Aerosols', Consultants Bureau, New York 1965

[4] J. Magill, S. Pickering, 'Aerosol Coagulation and Trapping in a Standing Sound Wave', Poster presentation at the TECNOVA exhibition in Madrid, 14 - 19 Sept. 1987

[5] P.J. Westervelt, J. Acoust. Soc. Am. 23 (1951) 312-315

[6] P.J. Westervelt, "The interaction of a finite amplitude acoustic wave with small obstacles and orifices" Ph.D thesis, M.I.T. Physics Dept.,1951

[7] Prandtl and Tietjens, Applied Hydro and Aero Mechanics, 1st. Edition, Mcgraw Hill : New York 1934

Collaboration with External Organisations

Instituto de Acústica, CSIC, Madrid

7 Reactor Safety

Introduction

Up to now, the Institute's activity in the field of reactor safety consisted of several separate, historically grown relations to external projects, to which the Institute was asked to provide support from its expertise in a special field. These fields are: ultrasonic thermometry, modelling, and high temperature properties of nuclear fuels.

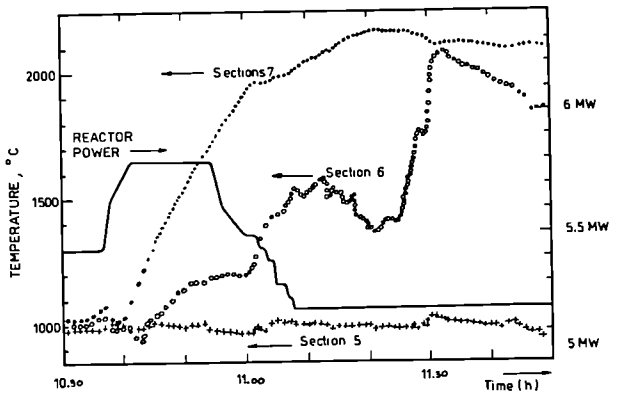

Fig. 7.1. Dry-out detected on 31.01.1987/10.40h in PAHR-Celia-1 by means of sections 6 and 7 of the ultrasonic thermometer. Also shown is the reactor power (scale at right). In spite of a power reduction at 10.56h, the indicated temperatures continued to rise to over 2000° C.

Ultrasonic Thermometry

PAHR In-pile

Within the frame of the PAHR project, the Institute provided three ultrasonic thermometers (UTs) and their data acquisition system, to be installed in the PAHR-Celia-1 simulated debris bed test rig, which was irradiated in the Melusine reactor in Grenoble on 23-31 January 1987. One of these UTs operated correctly throughout the experiment, whereas all installed high temperature thermocouples failed above 1200°C. The UT monitored a dramatic dry-out with a temperature rise of up to 1 K/s (Fig.7.1), and so provided an essential contribution.

SCARABEE-BF3

Since several years collaboration with CEA-CEN Cadarache exists for the SCARABEE programme. Presently the Institute prepares two UTs with ThO_2 sheaths for the experiment BF3. This experiment consists of a molten pool of UO_2 containing stainless steel, which should boil at a specified temperature of 3000°C. The two UTs, one with 6 measuring sections, the other with 4 sections, are planned to provide information of the temperature profile in the pool.

All structural pieces have been manufactured. The UTs were calibrated in November 1987. The ThO_2 sensor sheaths were delivered in December 1987, final assembly is in progress.

Liquid Level Detector for SCARABEE-BF3

At a request from CEA-CEN Cadarache, preliminary studies were made for an ultrasonic liquid level detector for Scarabee-BF3, capable of operation up to 3000°C in the presence of sodium vapour. Ultrasonic level detectors have been proposed in the literature, employing torsional waves. This limits their application to much lower temperatures than foreseen in BF3. First tests with a flexing wave sensor were not encouraging. The activity was stopped after cancellation of the request by the CEA.

Coupling of the TRANSURANUS Code with the European Accident Code EAC

Many changes introduced in the TRANSURANUS code were made in the context of the development of the European Accident Code EAC which is developed to analyse the initial phase of a low-probability unprotected whole-core accident in an LMFBR ("hypothetical core disruptive accident"). Three phenomena mainly control the accident sequence in such an accident, namely fuel behaviour, sodium thermo hydraulics and fuel motion. The main activities were

1. Incorporation of an interface to couple the TRANSURANUS code with the in-pin motion model URADYN.
2. Coupling of the TRANSURANUS code with the single-phase hydraulics and homogeneous boiling model CFEM developed at JRC Ispra.

The progress achieved is given in more detail in Ref. [1] and in the annual report describing the work performed on the EAC code [2].

References

[1] G.van Goethem, K.Lassmann: 9th International Conference on Structural Mechanics in Reactor Technology, Lausanne (1987), Transactions Vol.C, Invited Paper C4

[2] Annual Report "Reactor Safety, 1987", Ispra

8 Radioactive Waste Management

Radioactive Waste Management and the Fuel Cycle

Radiochemical Separations - Verification of the OXAL-MAW Process

The objective of this activity is to verify the OXAL process with waste solutions of intermediate activity level. The capabilities of this process, previously developed at JRC-Ispra on simulated highly active solutions, to produce an "alpha free" waste is to investigated on active waste with samples having volumes of a few litres; the characterisation of the resulting solidified product is included in the study.

Introduction

In the current programme period the activities have been centered around the following items: a) The development of a new denitration process based on photochemical destruction of the nitrates in the waste solution, b) the optimisation of the carrier used in the oxalic acid precipitation based on a parametric study involving 4 different carriers, 4 carrier-to-actinide ratios, 3 pH-values, 2 temperatures, and 3 different digestion times, and c) the setting up of a gamma-spectrometric measurement system in the low energy range for the simultaneous determination of plutonium and americium in waste solutions.

The experiments were carried out on simulated solutions of intermediate activity level waste (MAW) to which Pu and Am had been added as tracers, as well as on real active MAW solutions in a hot cell.

Results on OXAL have been given in previous reports, but for convenience the most important results are summarised here: The feasibility of photochemical denitration of MAW solutions has been demonstrated; in alkaline solutions the residual nitrate concentration was a few ppm and the reaction products were only N_2 and O_2. Ca or Ba have been shown to be the best choice as carrier for the actinides; the influence of pH on the yield in the precipitation is pronounced; the decontamination factors for Pu and Am were however very high, hence an alpha free waste can be achieved. The application of the low energy spectra of Pu and Am, provided a useful tool for the determination of these elements; such simultaneous, direct measurements showed adequate sensitivity and precision. They also allowed a considerable saving in man-power to be achieved, as the long counting times needed for low activities do not present an intense of labour load.

Tests on the OXAL Process with Simulated MAW Solutions

The tests on simulated MAW (TUAR **86**, 15) were supplemented by a series of precipitations using ^{238}Pu as tracer isotope. The aim was to check the previous results on decontamination factors for Pu, found with ^{239}Pu (including higher isotopes). The gamma ray intensities of ^{238}Pu are more favourable than those of ^{239}Pu in the low energy range considered. The latter nuclide required counting times as long as 4 hours for its determination under our particular circumstances. It is however quite feasible to carry out the simultaneous determination of Am and Pu by direct gamma spectroscopy in these samples which have a very high salt content (sodium nitrate) and Pu and Am concentrations in the order of 10 mg/l and 3 mg/l, respectively. The experiments with the simulated MAW solutions were verified by hot-cell tests on real solutions of intermediate activity level (see below).

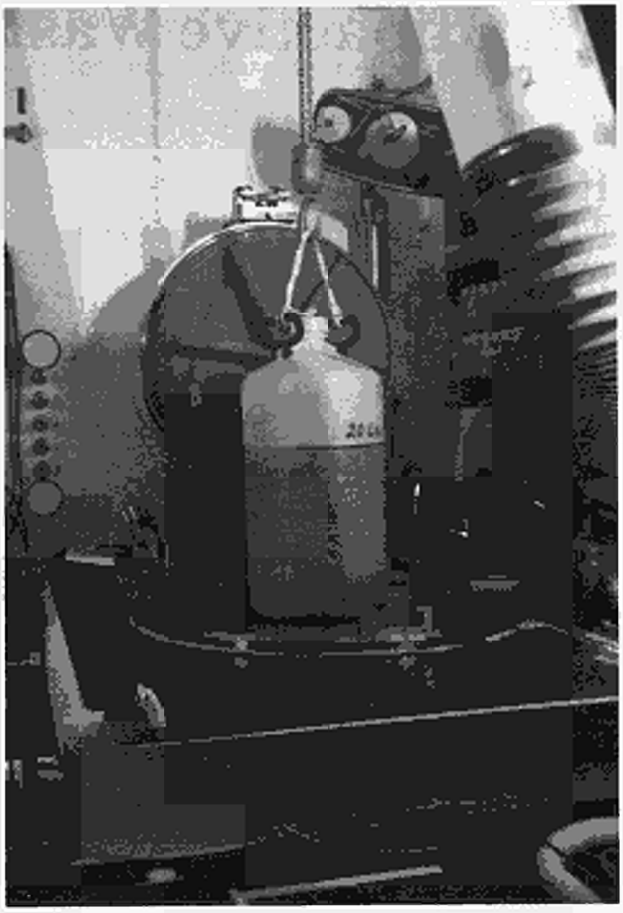

Fig. 8.1 A view of the bottle with 20 litre MAW solution under transfer into the new hot cell

Tests on OXAL Using Active MAW

About 20 litres of a waste solution of intermediate activity level, (MAW), were transferred into a hot cell from a 200 litre drum provided with special lead shielding. Fig. 8.1 shows of the bottle containing the MAW solution inside the newly commissioned hot cell. The MAW solution was taken in the WAK plant during a reprocessing campaign on fuel with a burn-up of 44 000 MWd/t and had been concentrated about 10 times in the HDB, KfK, prior to the transfer to the Institute. The main part of the solution originated from the reprocessing process itself (process waste).

The solution was filtered, brought to a pH of 2.0 and was subdivided in batches of 2 litres for oxalate precipitation. The verification and evaluation of the OXAL process on active solutions is to be carried out in 1988.

The results of the radiochemical analyses of the feed solution are given in Tab. 8.1 The main activities came from ^{137}Cs and ^{90}Sr, as expected.

The precipitate present in the feed was found to contain Ru and Zr.

Based on the results from the experiments on the simulated solutions various conditions were chosen for the oxalate precipitation where parameters such as pH, type of carrier (Ba, Ca, Ce) were varied; the use of mixed carriers (Ba and

Table 8.1 Analysis of the MAW feed solution employed for the active verification of the OXAL process in a hot cell.

Nuclide	Activity concentration Bq/l
Cs-137	6.5 E 8
Sr-90	5.5 E 8
Co-60	1.0 E 7
Ru-106	3.4 E 8
Cs-134	2.1 E 8
Ce-144	1.8 E 8
Sb-125	1.5 E 8
Zr-95	4.1 E 4
Total alpha	1.0 E 8
Pu-239	2.9 mg/l
Pu-240	1.2 mg/l
Am-241	0.16 mg/l

Ce) was also investigated. The pH was adjusted to the chosen value by NaOH, the solution was thus not denitrated. A saturated oxalic acid solution was used as precipitation agent.

After the precipitation the solutions were filtered and samples of the filtrate as well as of the redissolved precipitate were taken for analysis.The Pu and Am were analysed by direct gamma spectroscopy in the low energy range; the concentration of fissions products in the filtrate will also be measured, allowing the calculation of decontamination factors, e.g. for the lanthanides.

Characterisation of the Solidified Product

The effects of the removal of the actinides and lanthanides from MAW by oxalate precipitation will be investigated by selected tests on solidified specimens of the mother liquor from cementation. The work on cementation has been started and inactive specimens have been prepared under different conditions. The ratio water/cement was not varied in these tests, but was kept at 0.5, complying with the usual practice, e.g. in KfK. These specimens will be exposed to leaching and their compressive strength will be measured. Another parameter to be followed as a function of time is the porosity of the specimen. For the analyses of Ca, Si, and Al in the leachant the appropriate spectophotometric methods have been tested.

One particular problem to be dealt with in these tests is the presence of oxalate ions in the mother liquor after the oxalate precipitation, as these ions have a pronounced delaying effect on the hardening of the cement. Experiments to quantify these effects have been started; the destruction of the oxalate ions by photochemical means is under investigation.The results of these tests will be reported upon in the next report in the frame of the waste characterisation programme.

Other Activities

During this year additional studies on the suitability of leaching vessels, i.e. inserts to be used in active experiments, were carried out; furthermore certain quality control aspects of the leaching procedure for glass specimens were evaluated and reported upon.

Evaluation of Leaching Vessels

Various metals have been tested out for their suitability as container materials for leaching tests which are to be carried out on active glass specimens. The vessels were fabricated seamlessly from the following metals: Nickel, Hastelloy-C, Inconel (alloys with high Ni

content), and from titanium. These vessels were used as inner containers in the usual leaching

Demineralized water and Q-brine were used as leachants in these tests at temperatures of 150°C and 200°C. After 10 days of "blank" leaching, without glass, the leachants were analysed for metallic impurities by ICP. The results of the blank experiments at 200 C are shown in Tab. 8.2. The concentrations of all the elements are low, except for Ni alloys leached in Q-brine, where the Ni concentration reached 60 ppm. The concentrations of the alloying constituents in the leachant increase slightly as the temperature is increased (not shown in the table). A likely choice as container material for long term leaching would be titanium. Follow-up experiments on these vessels under active conditions in a hot cell are under way; here the additional influence of irradiation will be tested.

Quality Control Measures Applied to Leaching Procedures

Simple statistical tests, such as regression analysis and analysis of variance have been applied to data obtained from leaching experiments carried out under various conditions of temperature and time. The precision and accuracy of the overall leaching procedure were evaluated taking into account the short term within laboratory effects.

The data originated from determinations of the mass loss of leached glass specimens and from

Table 8.2 *Results of "blank" leaching experiments with metallic inserts at 200°C. The results are presented in the table as the element concentration in ppm in demineralized water / element concentration in ppm in Q-Brine.*
dl = below detection limit.
The elements Cu, Eu and Nd were also looked for, but were always below the detection limit.

Element in leachant	Nickel insert	Hastelloy insert	Inconel insert	Titanium insert
Al	dl / 0.02	dl / 0.06	dl / 0.03	dl / 0.05
B	0.1 / 0.4	0.04 / 0.5	0.2 / 0.7	0.07 / 0.6
Ca	0.6 / 0.6	1.0 / 0.9	1.6 / 4.2	1.3 / 0.8
Ce	dl / 0.08	dl / 0.1	dl / 0.2	dl / 0.07
Cr	0.05 / 0.1	dl / 0.1	dl / 0.3	dl / 0.06
Fe	dl / 0.05	dl / 0.02	dl / 0.25	dl / 0.1
Mg	dl / dl	0.05 / dl	0.4 / dl	1.5 / dl
Mo	dl / dl	dl / 7.2	dl / dl	dl / dl
Mn	dl / 0.9	0.1 / 0.8	0.05 / 2.2	0.04 / 0.6
Ni	1.3 / 31	0.24 / 24	0.35 / 60	dl / 2.5
Si	0.1 / 0.4	0.1 / 0.6	0.3 / 1.1	0.3 / 0.6
Sr	<0.01 / 0.03	0.01 / 0.03	<0.01 / 0.06	<0.01 / 0.03
Ti	dl / dl	dl / dl	dl / dl	dl / dl
Zn	0.02 / 0.1	<0.01 / 3.3	dl / 2.7	dl / 3.3
Zr	0.3 / 1.8	dl / 1.5	dl / 4.0	dl / 0.1

the measurements of the electrical conductivity and the pH of the leachant. The solution conductivity correlates highly with the normalized mass loss; hence it provides a consistency check on the measurements of this parameter. The relative precision of the overall leaching test method was found to be 5-12 %, including the effects assignable to inhomogeneity of the glass specimens.

Conditions for the use of the teflon inserts often used in leaching devices have also been investigated. A modified cleaning procedure has been proposed to ensure the absence of systematic errors during repeat utilisation of such inserts. The cleaning of the containers should include a heat treatment at 200°C after the appropriate wet cleaning. The teflon inserts should not be used in leaching at temperatures equal to or above 200°C for extended periods [1].

Reference

[1] H.Bokelund, K. Deelstra, Radioactive Waste Management and the Nuclear Fuel Cycle, accepted for publication.

Safety of Waste Disposal in Continental Geological Formations

Near Field Evolution

This activity is intended to investigate the processes which occur in the near field of vitrified high level waste and of conditioned alpha waste. It is split into four subtasks:

- corrosion of the canister
- vitrified waste in clay and sea sediments
- alpha-contaminated waste embedded in concrete, and
- vitrified, high-activity waste in salt systems.

The last task is carried out at JRC Karlsruhe and the progress achieved is reported in the following.

The extensive research activity on physical processes occurring in the near field in a salt formation and in the glass itself was continued with emphasis on radiation damage effects and fracture behaviour. Work reported in previous Progress Reports had dealt with the interaction of waste glasses with the actual salt of salt domes, with leaching in Q-brine and with synergistic effects due to the presence of container metals and their corrosion products. The study of alkali diffusion in the waste glass was concluded. In 1987, an activity was initiated to characterise highly active glasses in the hot cells (collaboration ENEA/COMSVITE/JRC Ispra).

Radiation Damage Studies

Cm-Containing Glass

The on-going work with French, German and US waste glasses doped with ^{244}Cm in order to simulate realistic radiation damage in an acceptably short time were continued. Damage levels corresponding to storage times of real waste glasses in excess of ~10^5 years have been produced.

The previous work has shown important damage effects in waste ceramics which, in fact, lose part of their attractiveness in the damaged state: they become amorphous (metamict), show significantly increased leach-rates and swelling of up to 10%, etc. The effects observed for glasses are much smaller. As a typical example, results for the US glass MCC 76-68 doped with ^{244}Cm are given in Fig. 8.2. Similar results were obtained with the French glass SON 681617 L1C2A2Z1 and the German glass GP 98/12.

Fig. 8.2 shows a pronounced decrease in hardness and in crack length for Vickers indentations with increasing radiation dose. In a previous report, the theoretically expected slope [1] of 2/3 in a plot of crack length, c, versus indentation load, N, was observed for both undamaged and damaged glasses. An example for all three glasses at a damage level of 3.3×10^{24} α-decays/m^3 was given. The upper part of Fig. 8.2 shows the corresponding increase in load to achieve a 50% probability for fracture (critical load, P_c) as function of dose. At the same time, no significant effect on weight loss during leaching (for the conditions used, i.e. 150 °C, 14d, H_2O) was found;

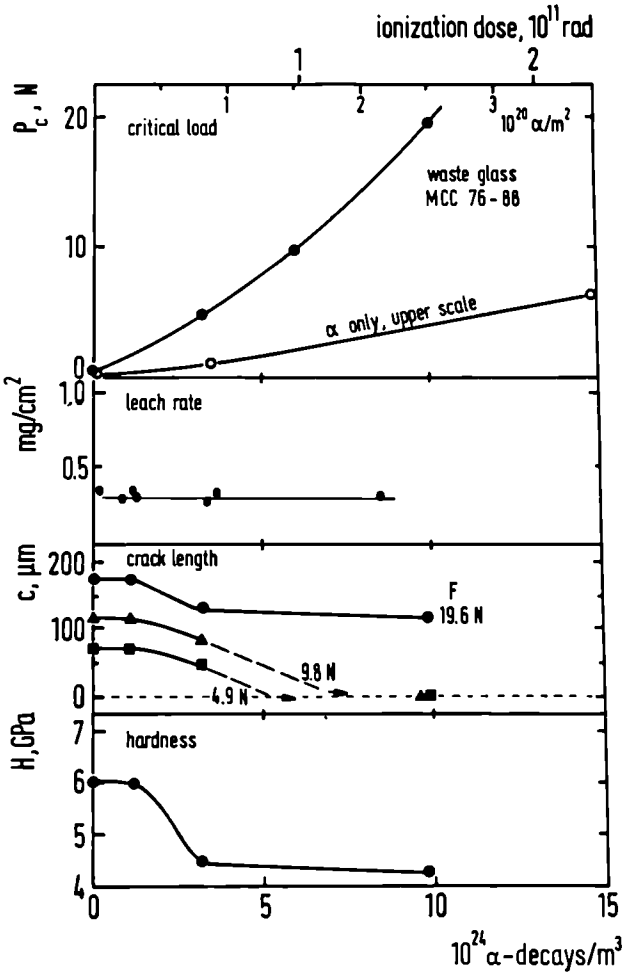

Fig. 8.2 Property changes in Cm-doped waste glasses versus damage level. The glass is MCC 76-68. Shown are increase in critical load for fracture (included are previous data with damage by α-particles alone, open circles (2)), the lack of a significant effect on leaching, the decrease in crack length at Vickers indentation leading to a disappearance of cracks at higher damage levels, and the decrease in hardness with damage dose.

the lack of a significant effect of damage on leaching was also supported by ICP-emission analysis of the solutions. The upper part of Fig. 8.2 showing the drastic increase in P_c of Cm-doped damaged waste glasses includes previous results [2] on a similar effect in the same glass bombarded with α-particles alone. In this case,

the recoil particles (e.g. a 100 keV ^{240}Pu daughter atom from the decay of ^{244}Cm) with their high energy, density cascades are absent. The α-bombardment damages a surface layer of ~25 μm thickness. The corresponding number of α-decays/m^3 (which, however, includes recoil atoms as well) has therefore been taken as being higher by a factor of 4.10^4. If this scaling is accepted, the contribution of α-particles to the observed increase in fracture toughness is a small fraction of that of the recoil atoms. A similar conclusion can also be drawn from previous results with 77 MeV α-particles from the Karlsruhe cyclotron [3]. The density changes of all glassses were <1% showing the absence of significant swelling (in contrast to the large swelling of the waste ceramics investigated so far).

Ion Implanted Glasses

The extensive work with glasses implanted at room temperature, reported in previous Progress Reports was continued with a study of the effect of temperature during damage production on properties of the nuclear waste glasses GP 98/12 and SON 681817 L1C2A2Z1. The chemically inert element Kr was implanted with energies between 50 and 200 keV in glasses held at high temperatures (100 to 250°C) during implantation. In a real waste glass, most damage occurs when the glass temperatures are in this range.

The fracture toughness K_{Ic} was measured as before by Vickers indentation using the equation

$$K_{Ic} = H\sqrt{a}\,(E/H)^{2/5}\,0.057\,(c/a)^{-3/2}.$$

This equation holds [1] when the average crack length, c, is significantly larger than a, the indentation half diagonal. H is the hardness, obtained from the indentation and E is the elasticity or Youngs modulus [4]. 5 indentations were made for each load (load range 5 to 20 N). The theoretically expected slope of 2/3 in a plot of c versus load P was again observed: The increase in K_{Ic} in the damaged glass compared with the undamaged glass reported in previous Progress Reports was still found at a bombardment temperature of 100°C, although not at 250°C.

Leaching was carried out in autoclaves using distilled water at 200 °C for 4h, with a ratio of water volume V to specimen surface area S of V/S=10 cm. Parallel measurements on unimplanted specimens were performed to deduce the contributions of the rear and of the sides of the glass specimens to the measured leach rates. Following leaching, Rutherford backscattering (RBS) analysis with 2 MeV He-ions was performed at the van-de-Graaff accelerator at KfK, Karlsruhe. Na profiles were measured with the nuclear reaction $^{23}Na(p, \alpha)^{20}Ne$ at the University of Firenze and H-profiles were measured using the nuclear reaction ^1H-(^{15}N, α)^{12}C at the University of Padova. For a description of the techniques see a recent review published within the reporting period [5]. A large set of specimens (2 glasses, SON and GP, 2 bombardment doses and 3 implantation temperatures each) were leached. Figs. 8.3 shows typical examples of the results. The analyses have not yet been completely finished. Fig. 8.3 shows significant enrichment of fission products and of Zr and Fe at the surfaces of leached SON glasses, and Fig. 8.4 shows

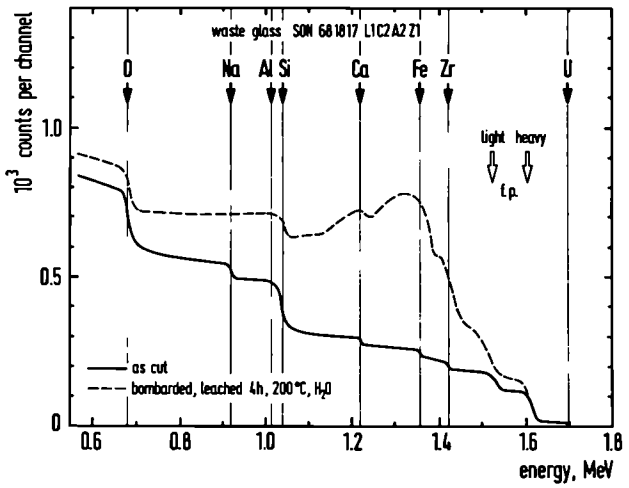

Fig. 8.3 RBS spectrum of the waste glass SON 681817 L1C2A2Z1 leached for 4h at 200 °C.

hydrogen uptake in GP 98/12 due to leaching. The results available so far show temperature effect during damage production on leaching as well. Radiation-enhanced Na-diffusion is also affected, as was shown for fracture toughness above. More details and a discussion in terms of damage recovery during damage formation will be given in the next Progress Report. The consequence of the present results for further

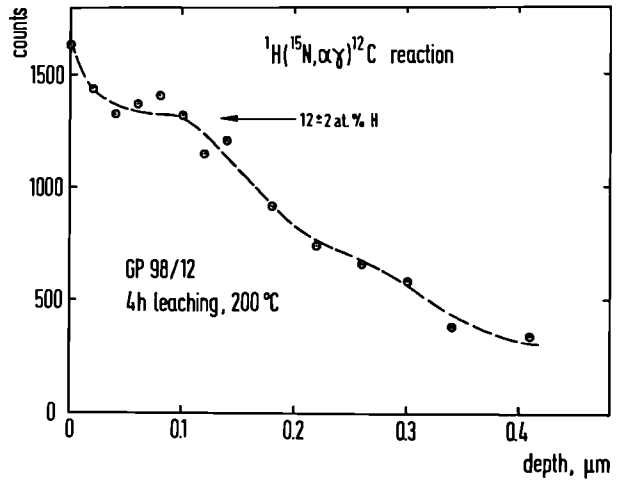

Fig. 8.4 Hydrogen profile at the surface of waste glass GP 98/12 leached for 4h at 200 °C.

damage work is to include temperature during damage production as an important parameter in future work.

Cm-Doped and Ion-Implanted Waste Ceramics

The extensive study on ^{244}Cm doped host phases of actinides, i.e. on zirconolite $CaZrTi_2O_7$, on $Ca_2Nd_8(SiO_4)_6O_2$ and on $Gd_2Ti_2O_7$ has been terminated and published [6].

In the reporting period, the radiation stability of the complex, tailor-made waste ceramic SYNROC B was studied. Gas release measurements had indicated transformation to the amorphous state during ion implantation [5]. Further ion implantation work using high energy (570 keV) Pb-ions of the Orsay accelerator showed that the anticipated metamictization is accompanied by a greatly enhanced leachability. Fig. 8.5 shows RBS spectra of the implanted SYNROC either leached in the as-bombarded state or pre-annealed at 400 and 800 °C for 15 min. before leaching (4d, H_2O, 150 °C). Good agreement between the spectrum calculated on basis of the components added in the fabrication step and the measured spectrum is found. The typical shoulders for all components (O, Al, Ca, Ti, Zr, Ba) are seen, indicated by arrows. The surface position of Pb.is also indicated. The Pb peak is buried to about 0.2 µm depth because of the high bombardment energy (570 keV, triply charged Pb-ions were used). Most of this implanted Pb-containing layer of about 0.2 µm thickness is dissolved in the damaged SYNROC (not annealed or annealed at

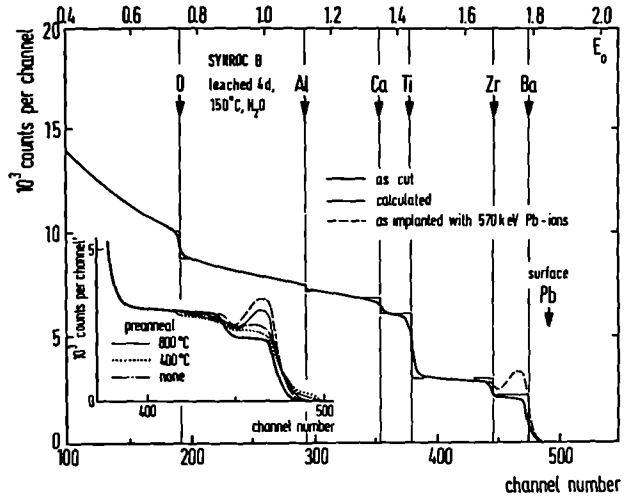

Fig. 8.5 RBS spectrum of Pb-implanted and leached SYNROC B. The implanted damaged layer is leached away in as-bombarded SYNROC and SYNROC preannealed at 400 °C whereas an anneal at 800 °C restores the original low leaching rates of the ceramic.

400 °C, which is not sufficient given the fact that recrystallization is known to occur in the temperature range of 500-700 °C). In contrast, annealing at 800 °C, expected to cause recrystallization, causes the bombarded SYNROC to show the normal low leach rates. Continued leaching for up to 1 month under the same conditions eroded away a layer of 0.05 µm thickness on the 800 °C sample as shown by the Pb-peak used as a depth marker. This gives a lower limit to the enhancement factor in leaching between damaged and undamaged SYNROC of 35; the real number is probably even larger since less than 4 d may have been necessary to leach the bombarded layer away. More experiments with shorter leaching times are planned.

Prolonged leaching caused the expected preferential loss of Ca and Ba from SYNROC. The was obvious in the RBS spectra, and was confirmed by ICP emission analysis of the leaching solutions.

A ^{244}Cm doped SYNROC-B was also prepared. Gradual shrinkage of X-ray lines with increasing dose indicated onset of amorphization. No microcrack formation has so far been seen at 1000x magnification. The specimen will be re-analyzed at higher increased dose levels.

Alkali Diffusion in the Waste Glass GP 98/12

In the TUAR 86, the reasons for this activity and extensive results on the diffusion of Rb using radioactive ^{83}Rb and ^{84}Rb from the Karlsruhe cyclotron as tracers were given. In brief, we wanted to improve our understanding of the leaching processes (the being basic step by hydrogen ions exchange of alkali), to explain the observed effects of alkali migration in thermal gradients (as they exist during storage) and during irradiation with external beams and also to provide data needed to decide whether the mixed-alkali effect and the recent picture of a modified random network for glasses are of importance for long-term storage.

In the reporting period, the Rb-tracer diffusion data given in TUAR 86 were confirmed with a Rutherford-backscattering (RBS) study of ion-implanted glasses. The German waste glass VG 98/12 was bombarded with Rb or Cs ions of 40 or 300 keV energy to doses of 5.10^{15} ions/cm^2. Following annealing treatments of different times at temperatures between 350 and 665 °C, RBS showed diffusion profiles (see Fig. 8.6) compatible with volume diffusion only at high

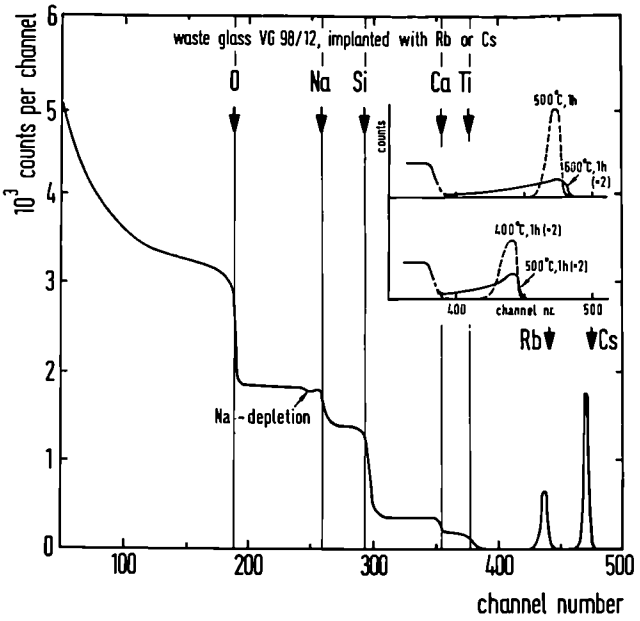

Fig. 8.6 RBS spectrum of the waste glass VG 98/12 implanted with Rb or Cs. The inset shows the high energy end of the spectra following different annealing treatments indicating diffusion of Rb and Cs with and without trapping of a fraction of the alkali ions.

temperatures, whereas composite diffusion profiles were obtained at lower temperatures. Radiation enhanced Na diffusion was observed during bombardment. In contrast, radiation damage retarded the thermally activated Rb and Cs diffusion: the implanted ions interacted with the damage configuration resulting from ion bombardment. Because of the complex structure of the multicomponent waste glass, the nature of the trapping defects cannot be specified yet. Damage annealing and/or dissociation of the alkalis from the damage needed annealing temperatures of ~500 °C for Rb and ~600 °C for the larger Cs-ions. Even following damage annealing, Rb and Cs diffusion was much slower than that of Na. The latter was measured with the boundary condition of a thin tracer layer. Fig. 8.7 shows the theoretically expected linear penetration plots typical for undisturbed volume diffusion, and Fig. 8.8 summarises all data in an Arrhenius diagram. The Arrhenius plot for Rb and Cs is curved.

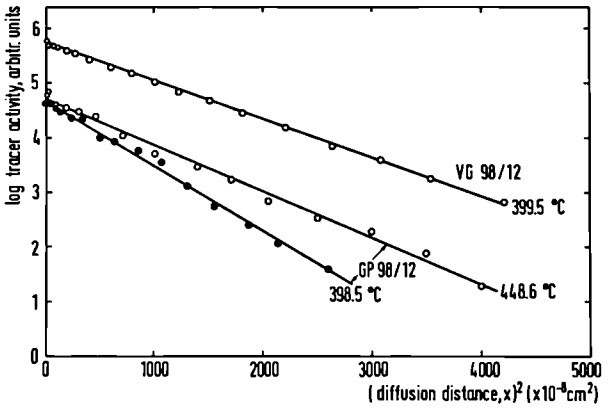

Fig. 8.7 Penetration profiles of the radioactive tracer ^{22}Na in the waste glasses GP 98/12 and VG 98/12 following diffusion anneals.

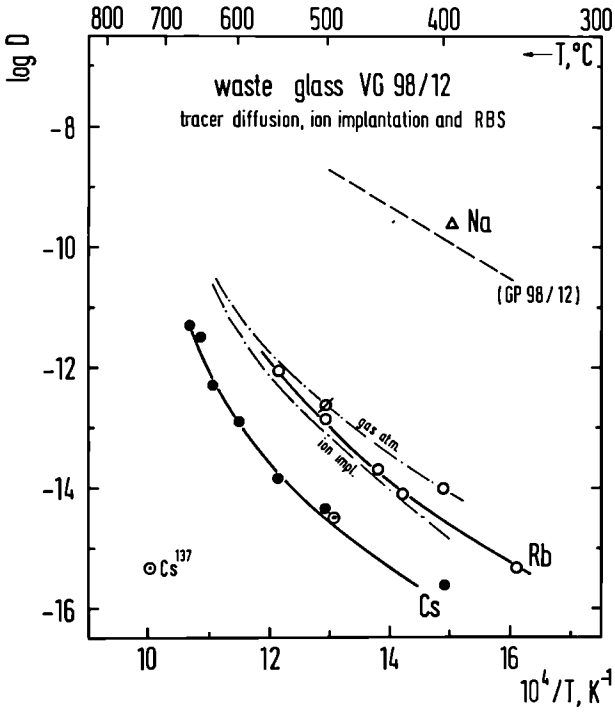

Fig. 8.8 Arrhenius diagram for alkali diffusion in the waste glass VG 98/12.

The data are of relevance for the storage of waste glasses: it is now possible to predict that thermodiffusion of the (radioactive) Rb and Cs will be a minor effect during long-time storage; that the pronounced decrease in the diffusion coefficient D in the series Na-Rb-Cs will overcompensate any possible changes in thermally activated ion diffusion in the complex waste glass due to the mixed-alkali effect during leaching, that thermodiffusion or biased radiation-enhanced Na diffusion cause local changes in the Na concentration of the glass; and that radiation-enhanced diffusion will exist during storage at temperatures below ~200 °C,but since there will be no biasing effect, it should not lead to any directional Na-migration but will rather contribute to maintain the glass at a homogeneous state.

This study has been terminated and the results were discussed at an international workshop on radiation effects in waste matrices organized by the Institute [7] and held in parallel with the 4th International Conference of Radiation Effects in Insulators. The proceedings containing all contributions are in print and will be available in April 88.

Fracture Toughness of Waste Glasses

Fracture toughness values K_{Ic}, have been obtained up to now with Hertz- or Vickers indentations (see previous Progress Reports and [1-4]). A so-called short-rod fractometer has now been installed to verify the results with more conventional fracture test. The short-rod fractometer uses chevron-notched specimens of ~6 mm diameter. The first results show good agreement with the previous data.

Vickers tests were also made in an attempt to investigate the effect of the presence noble-metal fission products and of the cooling rate of the glass. The rare metals (Pd, Rh, Ru) form small metallic inclusions in waste glasses and fast cooling leaves residual stresses in the glass. Both might affect the fracture behaviour. Glasses of the types GP 98/12, either with all, with 30% or with none of the otherwise present rare metals Ru, Rh and Pd (normally 0.2 at% in the waste glass loaded with 15 wt.% fission product oxides) were investigated. Different cooling times were also used (2h or 10h). Drop tests were performed at Battelle, Frankfurt in a pneumatic arrangement simulating accidental dropping of glass cylinders in mining shafts of some 100 m depth. Vickers indentations showed only a very small effect of the cooling rate, but a clear effect from the rare-metal inclusions and of the more complex structure of the fission product-containing waste glass GP 98/12 (see Tab. 8.3). This can be explained by the more distorted structure of GP 98/12 compared with that of the base glass VG 98/12, and due to toughening and crack branching of the rare metal inclusions. These results are compatible with those of the drop tests.

References

[1] Hj. Matzke "Indentation Fracture and Mechanical Properties of Ceramic Fuels and of Waste Ceramics and Glasses", Special Volume, Europ. Appl. Res. Reports **7** (1987)

Table. 8.3 Fracture Behaviour with Vickers Indentations in Waste Glasses Used for Drop Tests

Glass	Cooling Time h	Crack Length		Fracture Toughness K_{Ic}, $MPam^{1/2}$	Vickers Hardness H, GPa
		µm	relative		
VG 98/12.2	10	399.2	1.000	0.70	5.71
	2	396.8	0.993	0.71	5.59
GP 98/12.2 without rare metals	10	377.9	0.947	0.76	5.69
	2	371.7	0.931	0.78	5.70
GP 98/12.2 with rare metals	10	362.2	0.907	0.81	5.70
	3.5	362.8	0.909	0.81	5.61

Measurements performed in air (~ 21 °C, ~ 50% rel. humidity). The crack length given is the sum of the average of 20 cracks each at three loads (7.84 N, 12.54 N and 22.54 N)

[2] W.J. Weber and Hj. Matzke, Europ. Appl. Res. Reports 7 (1987)

[3] J.L. Routbort and Hj. Matzke, Mater. Sci. Eng. 58 (1983) 229

[4] Hj. Matzke, E. Toscano, J.L. Routbort and K. Reimann, J. Amer. Ceram. Soc. 69 (1986) C-139

[5] Hj. Matzke, Chapter 12 "Nuclear Waste Materials" in Book "Ion Beam Modification of Insulators", Eds. G. Arnold and P. Mazzoldi, Elsevier, Amsterdam (1987) p. 501

[6] Hj. Matzke, Cryst. Lattice Defects and Amorphous Mater. 17 (1987)21

[7] Hj. Matzke, ed., Proceedings Workshop on Radiation Effects in Waste Matrices, Nucl. Instrum. Methods in Phys. Research B (1988)

Characterisation of Highly Active Glasses

Taking into account the development of the programmes at JRC-Karlsruhe as well as the competence and the existing infrastructure for work with highly active material, and the benefits of a deeper collaboration with other JRC Establishments, it was decided to reconsider the future contribution to the "Waste" programme. The future availability of fully active glasses from the PETRA installation and the need for near-field model validation by tests on actual waste forms seem to well justify an effort in the "Characterisation of Nuclear Waste Forms".

Preliminary characterisation tests were started on three highly active borosilicate glasses (up to 287 Ci/kg, containing 15 to 33 $^{w}/_{o}$ fission products) provided from the ESTER experiment.

This activity was carried out in the framework of a collaboration between ENEA COMB-SVITE and JCR Ispra. The chemical composition of these materials is indicated in Tab. 8.4.

Table. 8.4 Chemical composition of ESTER glasses

	Crucible 4	Crucible 6	Crucible 8
SiO_2 (%)	36	50.9	43.4
B_2O_3	9	11.2	17
Al_2O_3	2	2.13	12.75
Na_2O	5	13	10.67
Li_2O	2	6.7	5
K_2O	3		
CaO	1		8.97
TiO_2	6	0.33	
CuO	3		
WO_x	33	15	15

In this work emphasis has been placed on the morphology, distribution and composition of the matrix and phases precipitated within it.

As the experimental results have not been entirely discussed with ENEA experts we will restrict ourselves to a brief description of the main experimental results giving more a picture of our experimental capabilities than a report on the characterisation of these borosilicate glasses.

- After checking the axial distribution of the mass and fission products of the glass crucibles by gamma scanning and radiography (Fig. 8.9) three transverse cross-sections through the crucible were cut and polished; from these, samples for microstructure examination were prepared. To this end quantitative microscopy, scanning electron microscopy, back-scatter imaging and EDAX analysis were employed.

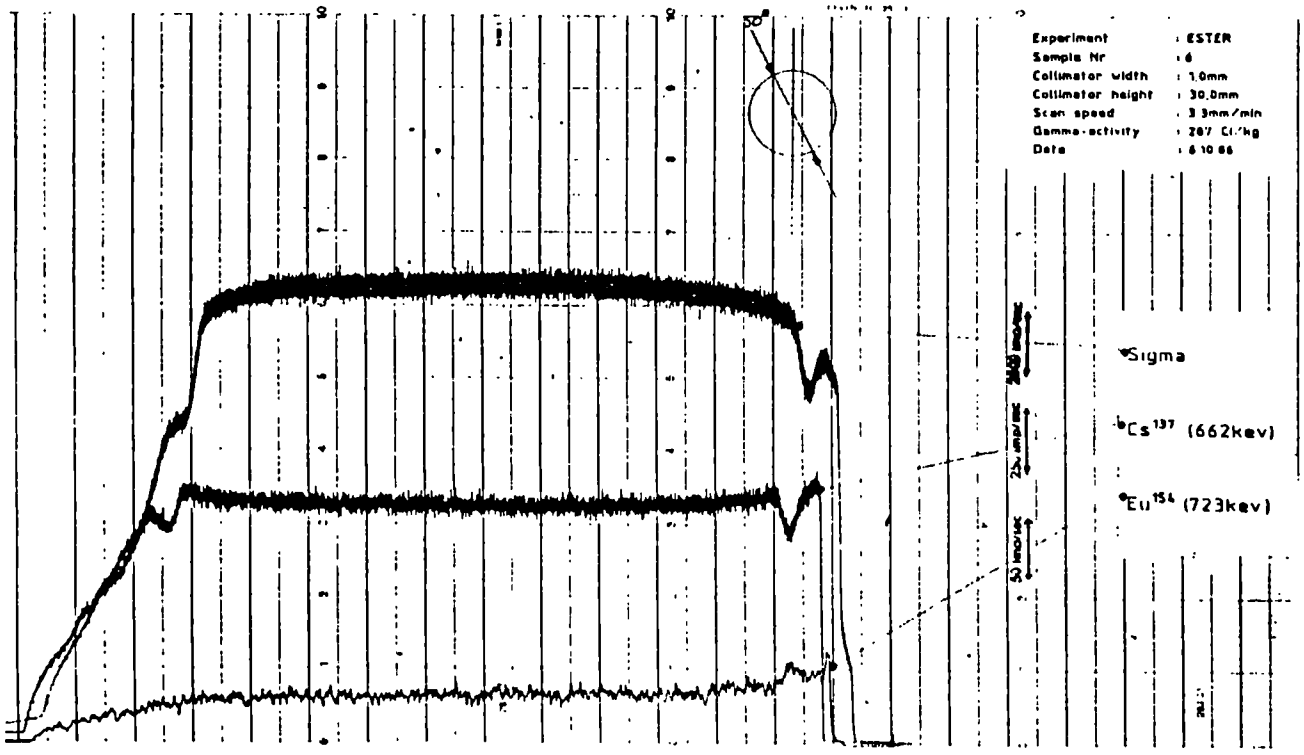

Fig. 8.9. Gamma scanning of crucible 6

- The more relevant analytical results can be summarised as follows:

  a - two of the glasses showed an unusual structure with precipitated secondary phases heterogeneously distributed within the matrix (Fig. 8.10); one of these

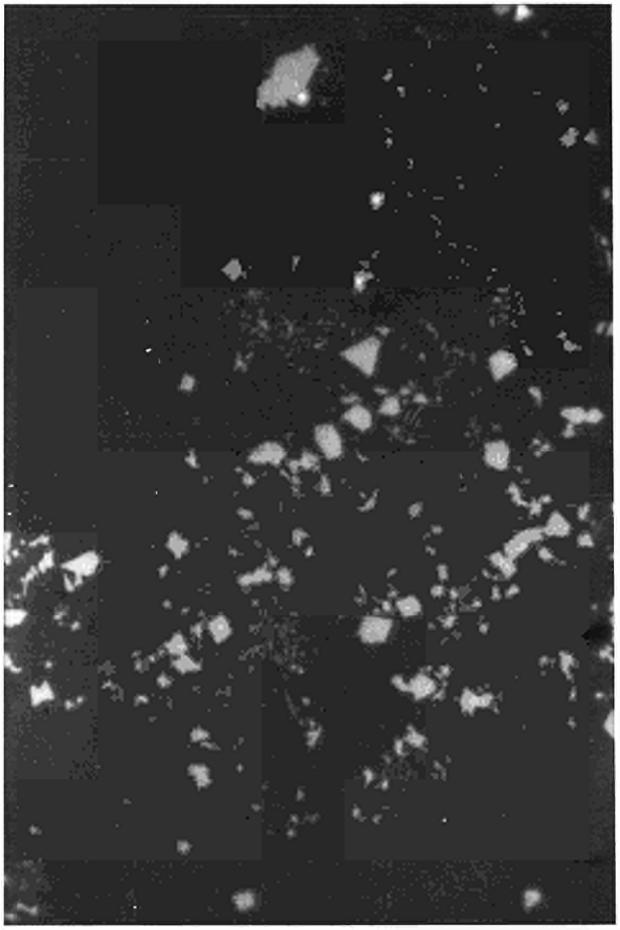

Fig. 8.10. Glass microstructure - crucible 6

  glasses (57 Ci/kg, 15 $^{w}/_{o}$ fission products), seems to be a two-glass system. (Fig. 8.11)

  b - elemental composition of the secondary phase, given by EDAX analysis, indicates the presence of four phases composed of following elements: Cr, Ni, Fe; U; U, Pu; and U, Pu, Mo compounds. (Fig. 8.12 and 8.13)

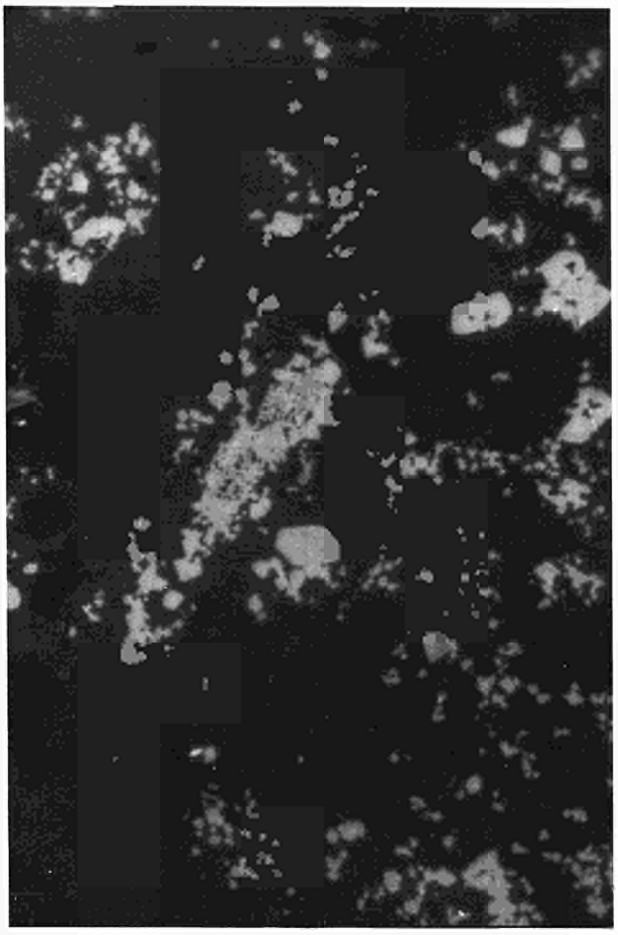

Fig. 8.11. Glass microstructure - crucible 8

  c - the glasses containing 33 $^{w}/_{o}$ fission products showed that a strong devitrification process had taken place (Fig. 8.14). In the matrix, hexagonal, tetragonal, spherical precipitates but also needles or plates were observed and analysed. Compounds of the type Fe, Ni, Cr (Co) and (Gd) - Ti, Fe, Gd, Nd - Ce - Mo, Cs, (Fe) and Ti, La, Nd, Gd were found. (Fig. 8.15)

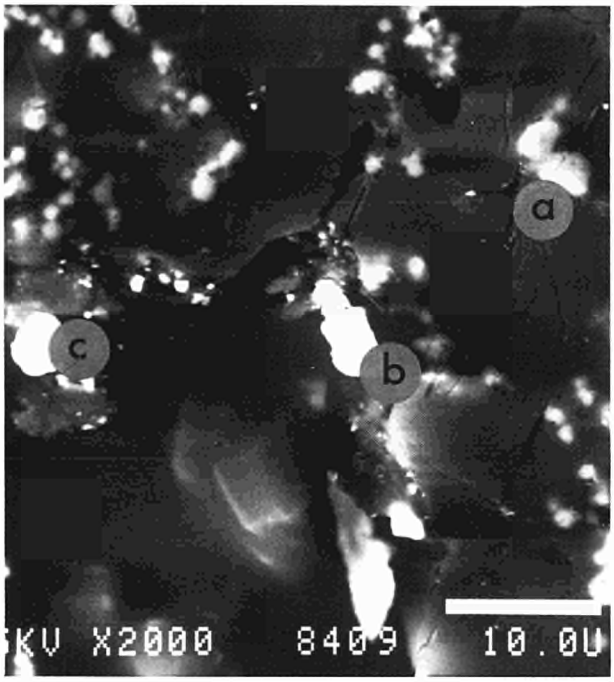

Fig. 8.12. EDAX analysis of glass crucible 8
a- Cr, Ni, Fe
b- U, Pu
c- U, Pu, Mo

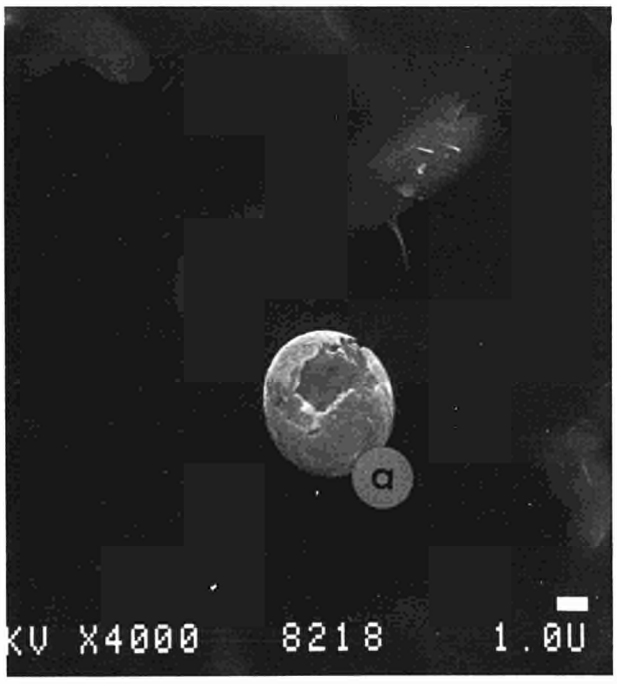

Fig. 8.13. EDAX analysis of glass crucible 4, spherical precipitate: Mo, Cs

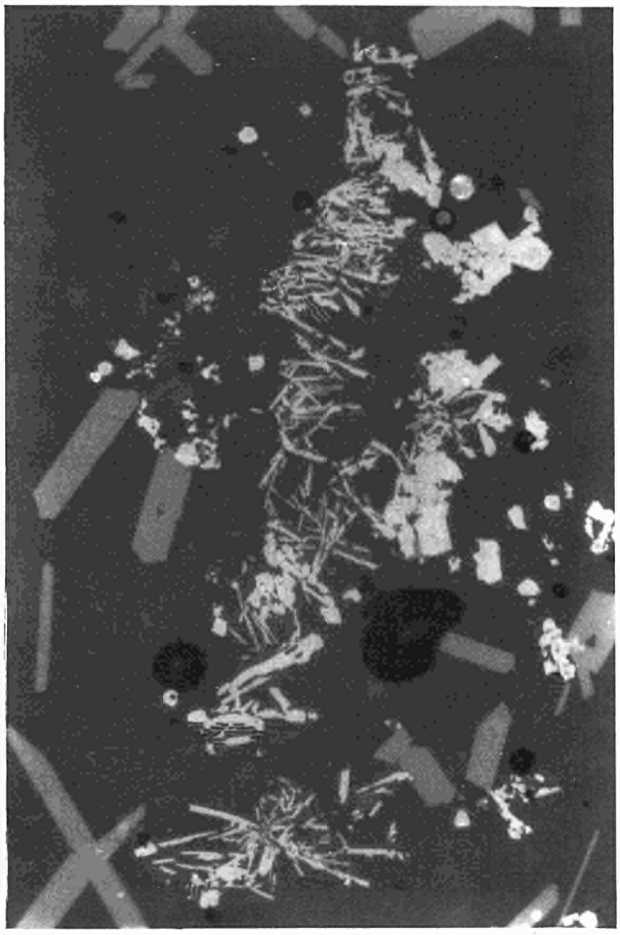

Fig. 8.14. Glass microstructure of crucible 4

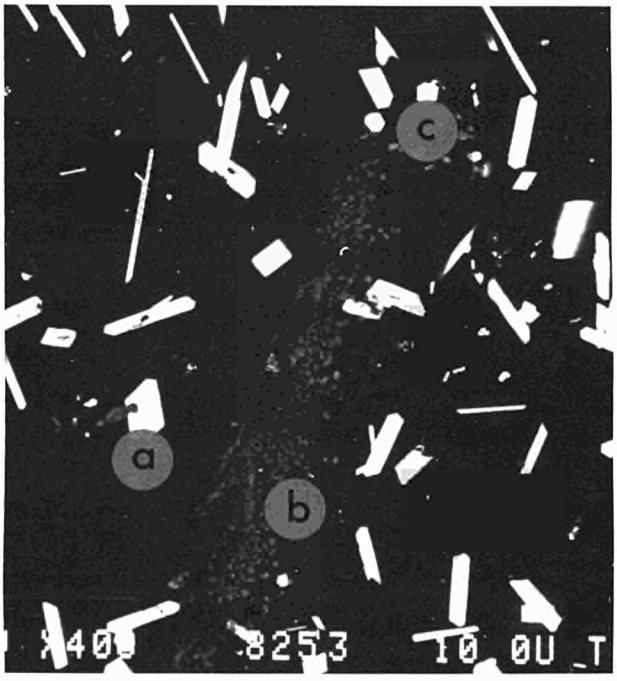

Fig. 8.15. EDAX analysis of glass/ crucible 4
a- Ti, La, Nd, Gd
b- Fe, Ni, Cr, Co
c- Ce

X-ray Absorption and Scattering Measurements.

An EXAFS experiment requires very precise measurement of the X-ray absorption coefficient as a function of energy. The energy interval investigated is usually of the order of 1 keV. An EXAFS spectrometer must then allow the wavelength of the incident photons to be rapidly changed and it must provide a beam with an energy band-width narrower than the lifetime broadening of the absorption edge. Energy resolutions of the order of $2\text{-}3\text{x}10^{-4}$ are usually requested for energies ranging from about 4 to 30 keV. Moreover, the total intensity at the sample position is of importance, and the whole available beam must be concentrated to a focus of a few mm^2. An additional requirement must be taken into account when high-level nuclear waste storage materials are studied: The gamma radiation coming from the sample must be shielded in order to reduce the background to acceptable levels.

For the instrument constructed at the Institut, Rowland circle geometry was chosen for monochromatization with Johansson-type curved crystals. To maintain the focussing geometry as the monochromating crystal is tuned at different Bragg angles during an energy scan, the Rowland circle centre must move along a circle of fixed radius around the focal spot, while the exit slit describes a lemniscate. The focal spot position and the direction of the primary beam are fixed. The required movements are obtained by means of a one-axis goniometer and three independent sliding carriages, one of which supports a two-axis diffractometer. The rotating stages have a resolution of 0.001 degrees. The sliding carriages have a resolution of 0.005 mm and lengths of 570 mm, 700 mm and 340 mm, respectively.

The sample is placed near the exit slit between two detectors which record the incident and the transmitted beam intensities. The exit slit, the detectors and the samples are mounted on a platform placed on the top of the diffractometer. An analyser crystal can be added after the sample position to allow measurements on highly active materials.

The X-ray source is an 18 kW rotating-anode generator mounted directly on the spectrometer table. It can be rotated around the focal spot and translated, in order to facilitate the alignment procedure and the definition of the take-off angle. Different anode materials are available (Cu, Ag, Cr, Fe, Ni, Mo), the choice depending on the energy region to be investigated. The focal-spot is $0.5\text{x}10$ mm^2 with a take-off angle of 6 degrees, leading to an effective source horizontal width of 0.05 mm. The tube voltage can be varied in steps of 1 kV between 5 and 60 kV, while the tube current can be varied in step of 2 mA between 10 and 300 mA. A low-voltage stage ($V < 20$ KV) has been added to work with low excitation voltages where the generation of harmonics must be avoided. Under these conditions, the maximum current is limited by space-charge effects, which can be reduced by increasing the electric field between anode and cathode.

The monochromator crystals are cut in the Johansson geometry in order to have optimal resolution with high intensity. Different crystals are used to cover different energy regions (Ge(111) for $4 < E < 7$ keV; Ge(311) for $7 < E < 11$ keV; Si (311) for $11 < E < 15$ keV). Energies

up to about 23 keV can be reached with the Si(933) reflection, while for higher energies Ge(333) or Ge(999) have to be used. It must be noted that the even Miller indices reflections of Si and Ge are forbidden, so that only the third harmonic contamination is present with the monochromators chosen. This will allow higher tube voltages to be used, so allowing greater intensities to be reached.

The detectors are ionisation chambers filled with Ar at atmospheric pressure. They show good linearity over a large dynamic range but do not allow energy discrimination. In order to be noise limited by statistics and not by current noise, current amplifiers with very low noise characteristics are used.

A PDP11 and an Olivetti M24 personal computer enable the instrument to be operated automatically; manual control is also possible. The program for the automatic data acquisition procedure has been written "user-friendly", in order to allow operators to be rapidly trained. The program is conversational, prompting for user input and is fool-proof with respect to the safety of the spectrometer and integrity of the data file in storage. All machine-dependent codes are isolated in low-level subroutines to perform primitive functions, while the main program is a simple command-cracker, branching to subroutines for the actual execution of commands.

The commissioning phase of the instrument will begin in 1988.

Collaboration with External Organisations

Battelle Institute Frankfurt

Ente Nazionale Energie Alternative (Cassaccia)

Kernforschungsanlage Jülich

Kernforschungszentrum Karlsruhe (Institut für Festkörperphysik, Institut für nukleare Entsorgung)

University of Padova

9 Safeguards and Fissile Material Management

Scope

This project aims at the development of improved methods for the destructive analysis of samples taken during nuclear material safeguards inspections. In the following we report on:

- A computer program to check the consistency of reprocessing input data,
- Results of a field demonstation of a so-called hybrid X-ray densitometer for measurement of U and Pu concentrations simultaneously in highly active solutions.
- Mass spectrometric analysis of sub-nano-curie samples of uranium and plutonium
- Analytical robot for on-site conditioning of reprocessing input samples
- Development of an expert system for specifying analysis details from input data

Progress and Achievements

Consistency Check of Reprocessing Input Data by Isotope Correlation Technique

In the frame of the EURATOM - IAEA Support Programme we have written software for the Safeguards Analytical Laboratory (SAL) of the IAEA to check the consistency of the reprocessing input analysis performed at this laboratory. The software takes account of the special situation there: only the data produced at SAL are available for this consistency check. (The earlier applications of the Isotope Correlation Technique (ICT) made use of historical data of the reactor fuel under consideraton.) For the application at SAL therefore we normalised all the isotopic concentrations to that of the final ^{238}U instead of to the initial fuel concentration, as done previously. The software was also rewritten to be run on a PDP-11 computer.

The program, described below, allows the form of the input analytical data to be selected from a menu. The data is checked for consistency by several predetermined isotope correlations and deviation from a regression analysis is determined. The results are given in the form of tables or plots.

Correlation program for analytical data

The program was written in FORTRAN IV on a PDP-11 computer running under TSX and coupled with the plot system INDIGO for graphical output on VDU or plotter.

The data are at present typed in by hand into a databank and consist of U and Pu concentrations and the weight % of uranium and plutonium isotopes. Program options are: addition of new data; correction of data already present; printout

of data; calculation of the chosen correlation and input of 'date of discharge' and/or 'date of measurement'. The last two data are needed to correct measured values of ^{241}Pu for decay.

The correlations are determined after inputing a) which degree of fit should be applied (normally only first and second degree fits are useful), b) selection of parameters (eg. ^{239}Pu vs. ^{240}Pu) and c) how severely the outlier tests should be applied.

Field Demonstration of an X-Ray Densitometer for Uranium and Plutonium Input Verification in Reprocessing

A prototype hybrid K-edge/XRF densitometer has been constructed at the Kernforschungszentrum Karlsruhe (KfK) and is being field-tested at the Institute. The instrument is receiving representative input solutions from the nearby Karlsruhe Reprocessing Plant (WAK) to evaluate its actual performance under realistic measurement conditions.

Apparatus

A schematic plan of the present instrument installation is shown in Fig. 9.1. The instrument is located outside a hot cell facility. It is connected to the interior of the hot cell through a leaktight stainless steel tube, which serves for sample transport.

The two X-ray methods incorporated into the instrument use a single X-ray tube as photon source. The tube, operated at a potential of 150 kV and at tube currents of between about 10 and

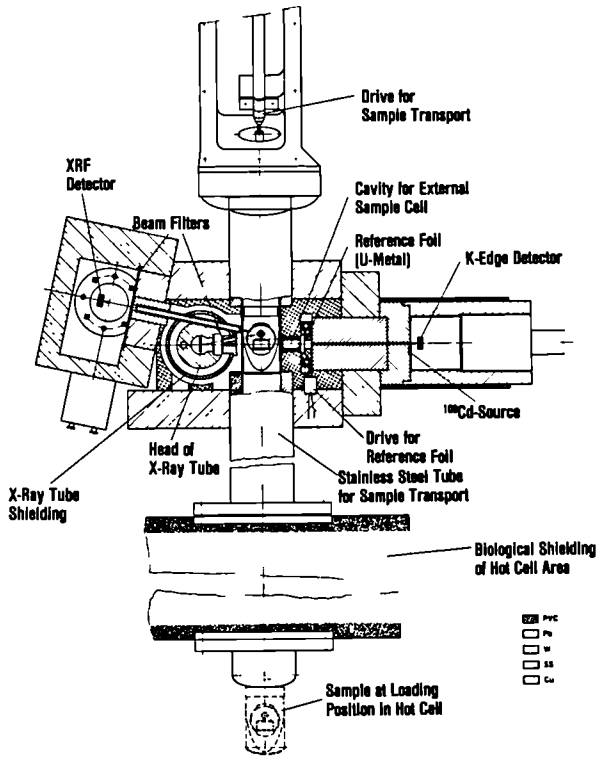

Fig. 9.1 Schematic plan of the hybrid K-edge/K-XRF instrument

15 mA, irradiates with two separate X-ray beams a dual sample contained in a 2 cm path length glass cell for K-edge densitometry and a 1 cm diameter polyethylene capsule for XRF. The straight-through X-ray beam for K-edge densitometry is highly collimated by a 12 cm long, 0.08 cm diameter tungsten collimator. The beam for the XRF cell is passed through a 14 cm long, 0.6 cm diameter tungsten collimator.

Both detectors are standard planar HPGe detectors. They are operated at total counting rates of between about 20 000 and 50 000 counts/s. The detector signals are digitized in two 400 MHz analogue-digital converters, and accmulated and analysed simultaneously on a computer-based data acquisition and analysis system. Typical measurement examples from both spectrometry modes are shown in Fig. 9.2. The uranium concentration is determined from

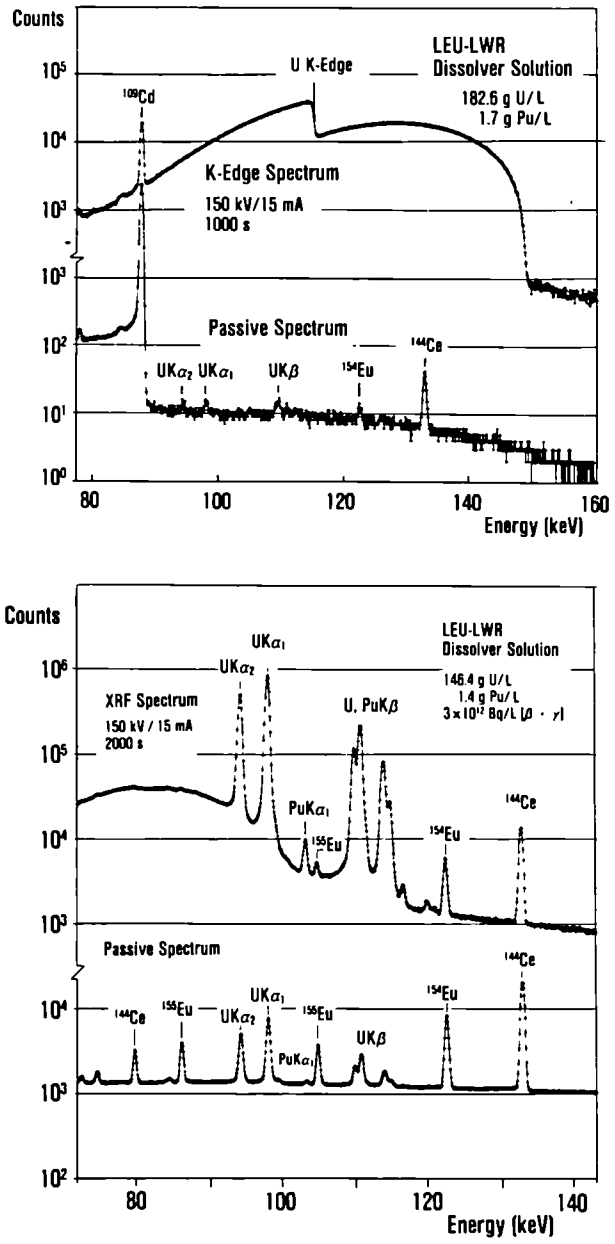

Fig. 9.2 Typical measurement examples from the K-edge densitometry mode (top) and from the K-XRF analysis mode (bottom)

the K-edge densitometry measurement, whereas the XRF analysis is employed for the U/Pu ratio determination. The plutonium concentration is derived from a combination of the two assay results.

Measurement Procedure

Only a few, fairly simple operator interactions are required for a measurement. Of the standard input sample, which normally contains 3 to 3.5 ml of the original dissolver solution, about 1.8 ml are pipetted into the glass cell for K-edge densitometry, and about 1 ml into the polyethylene vial for XRF. The actual sample volumes submitted for analysis are not critical and may vary by ±10%. The dual sample set is placed into a polyethylene capsule and transferred to the instrument outside the hot cell by means of a sample conveyor.

The parallel K-edge densitometry and XRF measurements run under a single job stream for automated data accumulation and evaluation. To run a measurement, the operator is prompted by the program for a few inputs (sample identification, counting time, number of repeat measurements, etc.). The standard measurement procedure includes 3 repeat runs of 1000 s counting time each, resulting in a total analysis time of about 1 hour. Evaluated uranium and plutonium concentration values with associated errors, together with some other pertinent experimental information, are directly printed out upon the completion of a measurement. Details on the instrument and its operation are documented in the operations manual [1].

Calibration

A careful initial calibration of the instrument was carried out in June 1985 [2]. Representatives from Euratom and the IAEA were present as observers during the preparation of the calibra-

tion samples and the calibration measurements. The reference solutions, jointly characterised by WAK, this Institute and the Safeguards Analytical Laboratory of the IAEA, included both pure uranium solutions, synthetic U/Pu mixtures without fission products, and actual dissolver solutions. Identical calibration constants have been evaluated from the measurements on the synthetic samples and the dissolver solutions, demonstrating the insensitivity of the two X-ray techniques to the presence of fission products. For this reason it appears sufficient to base future calibrations just on synthetic reference solutions, which can be analytically characterised with much better accuracy than dissolver-type solutions. In this way the calibration errors for the determination of uranium from K-edge densitometry and of the U/Pu ratio from XRF can be reduced to about 0.15%.

Field Test

The hybrid X-ray densitometer has been undergoing thorough field evaluation since mid-1985 with measurements on real reprocessing input solutions. The samples are received from WAK. The recent reprocessing campaigns at this plant included typical LWR fuels with burnup values in the range of 30 to 35 GW·d/t U, and cooling times of about 3 years. The dissolver solutions therefore exhibited fairly high total β/γ-activity levels of about $5 \cdot 10^{12}$ Bq/L. The U/Pu ratios typically varied between 100 and 120. The input samples are normally received at the Institute within a few days after sampling from the accountability tank at WAK.

No significant or unexpected difficulties have been experienced in the measurements of this kind of samples in the hybrid instrument. The measurement examples displayed in Fig. 9.2 show that the K-edge densitometry technique is insensitive in practice to the self-radiation. A somewhat larger susceptibility to the sample radioactivity is shown in the XRF analysis mode. However, gamma rays from fission products do not directly interfere with the X-rays of interest, and the intensity of the internally excited uranium and plutonium K X-rays is still about 2 orders of magnitude below that produced by the external X-ray beam from the tube.

The measured uranium and plutonium concentrations have been compared with results from parallel analyses performed by isotope-dilution mass spectrometry (IDMS). For the comparison the volume concentrations determined in the hybrid instrument were converted into weight concentrations. The density of the input solution measured by the operator at WAK was used for this conversion.

The results from measurements on 22 input batches are summarised in Tab. 9.1 . Separate samples taken from the accountability tank have been submitted for the NDA and IDMS analyses in this intercomparison. The samples for IDMS were diluted shortly after sampling. The undiluted NDA samples were measured on the hybrid instrument after an average delay of about 5 days. The following comments and observations apply to the data in Tab. 9.1:

1. Both the uranium and plutonium concentrations measured by the hybrid instrument are positively biased relative to the IDMS results. The observed average deviations of

Table 9.1 Flash evaporation results of NBS standards. Average of 10 measurements with 18 scans each

NBS-947	R 240/239	R 242/239
theor. value	0.241309	0.015595
exp. value (0.5 ng)	0.24124 ± 0.00012	0.015522 ± 0.00007
exp. value (1 ng)	0.24128 ± 0.00005	0.015568 ± 0.00003
NBS-946	**R 240/239**	**R 242/239**
theor. value	0.145012	0.006799
exp. value (1 ng)	0.144962 ± 0.00004	0.006759 ± 0.00007
NBS 948	**R 240/239**	**R 242/239**
theor. value	0.08632	3.605 E-4
exp. value (1 ng)	0.08636 ± 0.000027	3.872 E-4 ± 0.000016
NBS-010	**R 235/238**	
theor. value	0.01014	
exp. value (10 ng)	0.0101437 ± 0.0000107	

0.6% for uranium and 0.5% for plutonium are recognized as statistically significant by a 't-Test of Differences' [3]. Very good agreement was obtained for the measured U/Pu ratios.

2. The relative standard deviations of the differences between the NDA and IDMS measurement results appear to be well within the range of the expected combined uncertainties of both methods. The measurement precision of the hybrid instrument for the measured dissolver solutions is ≃ 0.15% for uranium, and ≃ 0.7% to 0.8% for plutonium.

3. The compared data have been subjected to an outlier test according to the criterion of Nalimov [3]. The number of results identified as outliers with a probability >99% is given in the table. In the two questionable cases the NDA and IDMS results differed by 0.8% for uranium and by 1.7% for the U/Pu ratio. The outliers have been excluded from the calculation of the average deviations and relative standard deviations.

The deviations observed between the two samples could partially be caused by undissolved matter in the input solution. The solutions were filtered (pore size: 1μ). This procedure however might have in turn induced errors from evaporation or by post dissolution of small particles not retained by filters. We therefore envisage to continue the field test in 1988 under better defined conditions.

Mass Spectrometric Analysis of Sub-Nanocurie Samples of Uranium and Plutonium

The tendency to increase the burnup of LWR fuel and to shorten its cooling time before reprocessing leads to higher specific radioactivity levels. Consequently the occupational radiation dose would grow if no counter measures were taken. Moreover the transport regulations for reprocessing input samples are becoming more stringent. Despite this adversely changing situation, the Safeguards laboratories have to verify a reprocessing input within 40 days.

One possibility of coping with these problems is to scale down the sample size to be handled on

site and in the Safeguards laboratory. Recently, new analytical equipment has been introduced on the market, e.g. robots and multidetector mass-spectrometers. A combination of these makes it possible to reduce the sample size and simultaneously the occupational radiation dose during mass-spectrometric isotope dilution analysis.

The advantage of multi-Faraday-cup detectors in thermal mass-spectrometry lies in their ability to scan simultaneously up to nine masses regardless of the stability of the ion current. Previously, in order to avoid instabilities when scanning the isotopes of an element, a sample had to be heated up carefully to produce a steady current. This technique required samples in the order of 0.1 to 10 µg.

Using a mass-spectrometer of type MAT 261 (Finnigan - MAT) equipped with a collector of nine Faraday cups we have developed a method where only one nanogram of Pu is analysed by the so-called flash evaporation method.

Under optimal conditions with this type of instrument, one ion can be detected per 500 atoms of a sample. Consequently, for a sample of one nanogram of uranium an ion current of 10^{-11}A can be observed over 90 seconds. The ionisation probability for plutonium is about ten times higher.

Experimental

The samples were prepared and measured according to the procedure described below. Fig. 9.3 illustrates the time dependence of the ion current for a 1 ng and 0.5 ng Pu NBS 947 sample.

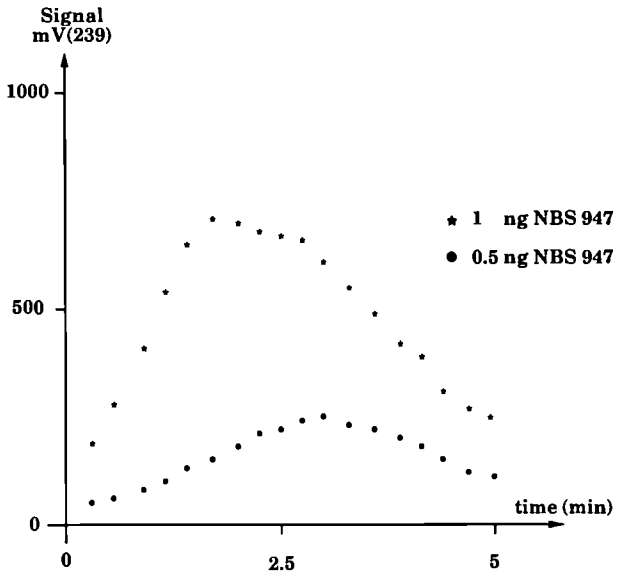

Fig. 9.3 Time-dependent signal for mass 239 of 1 ng and 0.5 ng Pu NBS 947 by flash-evaporation mass-spectrometry

During this time span, up to 18 scans of 8 masses (235, 238 to 244) are taken, each lasting for about 8 seconds. After every recording the current of the sample evaporation filament is raised by about 50 mA. Despite the noticeable instability of the signal the recorded data show the same reproducibility as obtained from a steady current thanks to the simultaneous recording of masses by the multidetector. The average internal reproducibility (1σ) of a measurement is 0.07 % where

$$\sigma = \sqrt{\frac{\Sigma_i (Ri-R)^2}{N_R - 1}}$$

as can be seen from the error bars of Fig. 9.4. The average deviation from the certified NBS value is 0.00002 and the standard deviation of the mean (2σm), expressed as usual as

$$\sigma_m = \sqrt{\frac{\Sigma (Rmi-Rm)^2}{n_m\ (n_m - 1)}}$$

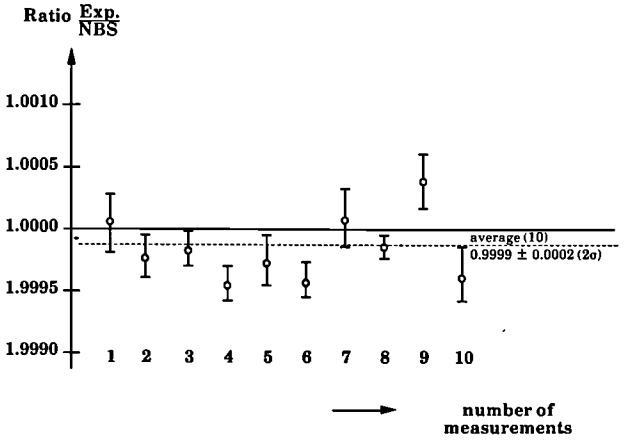

Fig. 9.4 Ratio of experimental to certified value for Pu 240/239 with the internal (1σ) reproducibility for 1 ng NBS-947 samples. The average of 10 analyses is given by the dotted line.

is 0.02 %.

This close agreement with the certified value is explained by the negligible integral isotope fractionation. Since all the sample is consumed during the measurement the isotopic fractionation - as seen from Fig. 9.5 is effectively zero.

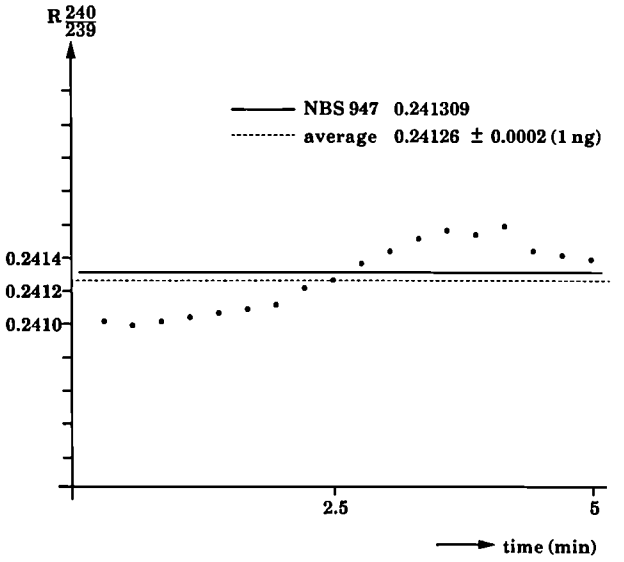

Fig. 9.5 Isotopic fractionation for Pu 240/239 of 1 ng NBS 947 during flash evaporation

Procedure

The analysis of ng-size samples requires some changes in our present procedure [4].
The Pu and U are still dissolved in 1 M HNO_3. However it is important to mount the sample in the middle of the rhenium filament and on a spot as small as possible.

When loaded in the MS-261 no preheating is done. The ionisation filament is heated up and the instrument is automatically focussed on the rhenium ion beam. In the next step the evaporation filament is heated up quickly until plutonium ions appear and from then by increments of 50 mA in intervals of about 15 seconds. During each interval a scan of all masses is taken (Fig. 9.6).

This step is repeated until the sample is consumed and the ion current decays. For a 1 ng size Pu sample about 18 scans are taken within 5 minutes. The whole operation is automatic from the insertion of the sample to the evaluation of the isotopic abundances including the statistical evaluation.

Most of the software is standard for this type of mass-spectrometer and had only to be adjusted to the measurement conditions. A new subroutine, COL 7 has been written - with the assistance of Finnigan MAT - to control the flash evaporation process and the data acquisition. This software is flexible enough to cope with changing sample conditions, for instance selecting the number of scans to be taken according to the ion current.

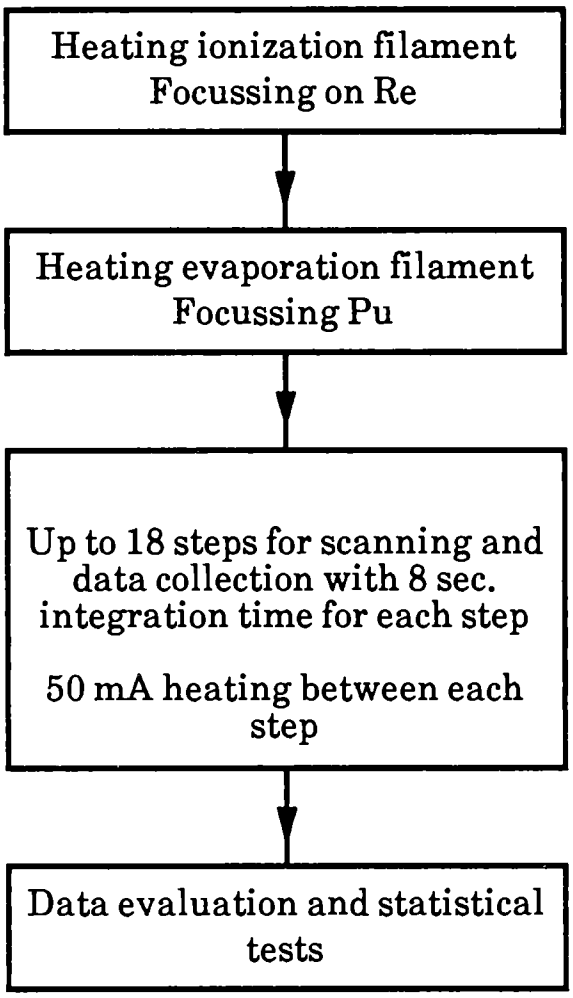

Fig. 9.6 Experimental procedure for the flash-evaporation technique

Results and Discussion

The results abtained for different NBS standards prove that the flash evaporation technique of nanogram-size samples yields, for the isotopes of Pu, an accuracy which easily meets the present requirements of nuclear material safeguards (Tab. 9.2).

The advantage of this technique lies in the sub-nanocurie amount of Pu (and U) needed for a measurement. According to the IAEA "Regulation of the Safe Transport of Radioactive Material" [5], material with a specific activity of 2 nCi/g should be exempted from transport regulation and regarded as non-radioactive. Since 1 ng of LWR grade Pu is less than 0.1 nCi, a mass-spectrometry holder loaded with this amount of Pu could be transported very quickly from a nuclear facility to the Safeguards laboratory.

The resin-bead-technique [6] is based on similar ideas. It requires larger Pu samples however and high skills in mounting the samples. The ng-size samples, as described in this paper, could be mounted by robots at the nuclear facilities.

Table 9.2 Comparison of NDA and IDMS results for 22 input batches

	Uranium	Plutonium	U/Pu ratio
Average deviation, NDA – IDMS (%)	+ 0.60	+ 0.50	- 0.04
Standard deviation of differences (%)	0.36	0.74	0.57
Outliers (Nalimov test, > 99%)	1	0	1

Analytical Robot for On-site Conditioning of Reprocessing Input Samples

In general, destructive analytical techniques - in the frame of Nuclear Materials Safeguards - are applied only in special Safeguards laboratories. There are two disadvantages with this scheme:

- The transport delay of nuclear material samples is of the order of 40 days. This is too long for the detection of an abrupt diversion.
- The conditioning of the samples prior to shipment has to be observed by an inspector - a rather costly operation.

Sample conditioning on-site, using laboratory robots, with the possibly subsequent and automatic measurement of the fissile material content would not only eliminate the transport delay but considerably reduce the time required for an inspector to observe the operations.

If a robot is to carry out all the steps needed to condition a sample, beginning with its introduction and ending with a loaded filament for subsequent mass spectrometry the following constraints have to be observed:

- the robot has to be adapted to the working conditions of a glove-box
- human interference has to be minimised

High reliability of the robot components and its peripheral devices is demanded for glove-box work. Therefore vulnerable parts, e.g. the electronics, should be separated from the instrument and installed outside the glove-box. Mechanical parts must be protected against corrosion.

For such an automated system to work unattended (e.g. overnight) appropriate measures must be taken in order to comply with the safety regulations. All disposable equipment (such as test-tubes, pipettes) and the reagents are loaded manually into the glove-box at the time when the sample is introduced. The disposal of the waste and remains of the sample as well as the prepared filaments for mass-spectrometry are removed manually at the end of the operation.

More details of the robot operation are to be found in [7] and in chapter 5 of this report.

Expert System for Preparation of Safeguards Sample Analyses

A variety of analyses can be carried out on Safeguards samples, such as isotopic ratios by mass spectrometry, concentrations of U or Pu by isotope dilution, titration or K-edge absorption. The number of analyses and the specific techniques to be used are dependent on external and internal factors. An analysis request from Luxembourg defines what analyses are to be done and internal data, such as availability of spikes define many of the details of the analyses. The concept which is presently under development is to hold the input data on a personal computer and employ a computer language flexible enough to translate the data into specifications for the subsequent analyses. In effect, the PC acts as a buffer between the incoming data and the laboratory. It will carry out three functions: holding Safeguards confidential data safely, transmitting results to and receiving requests from Luxembourg and

specifying the analyses details for the laboratory technicians.

The computer language used is TURBO PROLOG, a language suitable for 'expert systems' and flexible enough to handle the input data in all its forms.

The analysis requests are formulated in Luxembourg by means of a PROLOG program written previously in the Institute [8]. This program accepts and checks the formulated requests and transmits in a predefined format the data to the Institute via DATEX-P. Fig. 9.7 contains a flow diagram of the data-flow steps up to the application of the expert system.

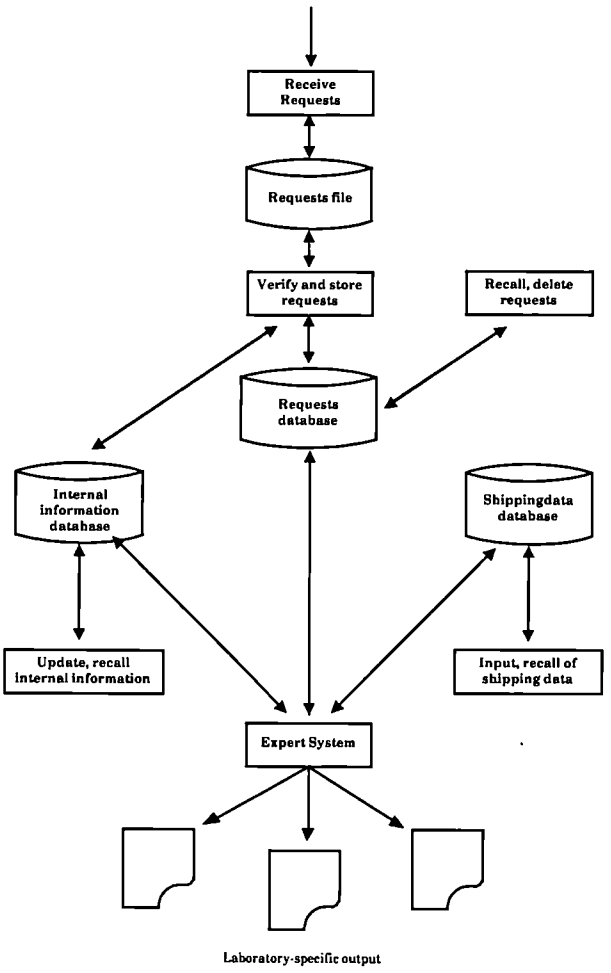

Fig. 9.7 . Flow diagram of data preparation for Safeguards analyses

After consistency checking of the requests and storage of the data contained there the next step entails determining the analysis methods and calculation of the complete analysis specifications for the measurement laboratory. This 'expert system' is under development and has the following tasks (Fig. 9.8) :

- determine the analysis to be carried out having regard to the nature, quantity, concentration and origin of the sample.

  This step requires the in-built knowledge of the analysis methods, details of spikes etc. as well as the input data as provided by Luxembourg and transport details. The ECSAM analysis codes and their implications, for example must be built into the system.

  transmit the necessary data to the laboratories where the analytical measurements are to be made. Each laboratory has different requirements depending on the work which is to be carried out there.

  The information will be partly in the form of printed sheets containing, for each laboratory the internal sample numbers and specifications of the analysis. Part of the information will also be transmitted directly to a PDP-11 computer which controls the laboratory robot. The robot is thus primed with the sample numbers (which are planned to be printed on each reagent glass to be read with a bar-bode reader) and the approximate weights of samples and spikes. The spike number (for each element, a variety of spikes having different concentrations are available) is also specified; this will also be checked by the bar-code reader.

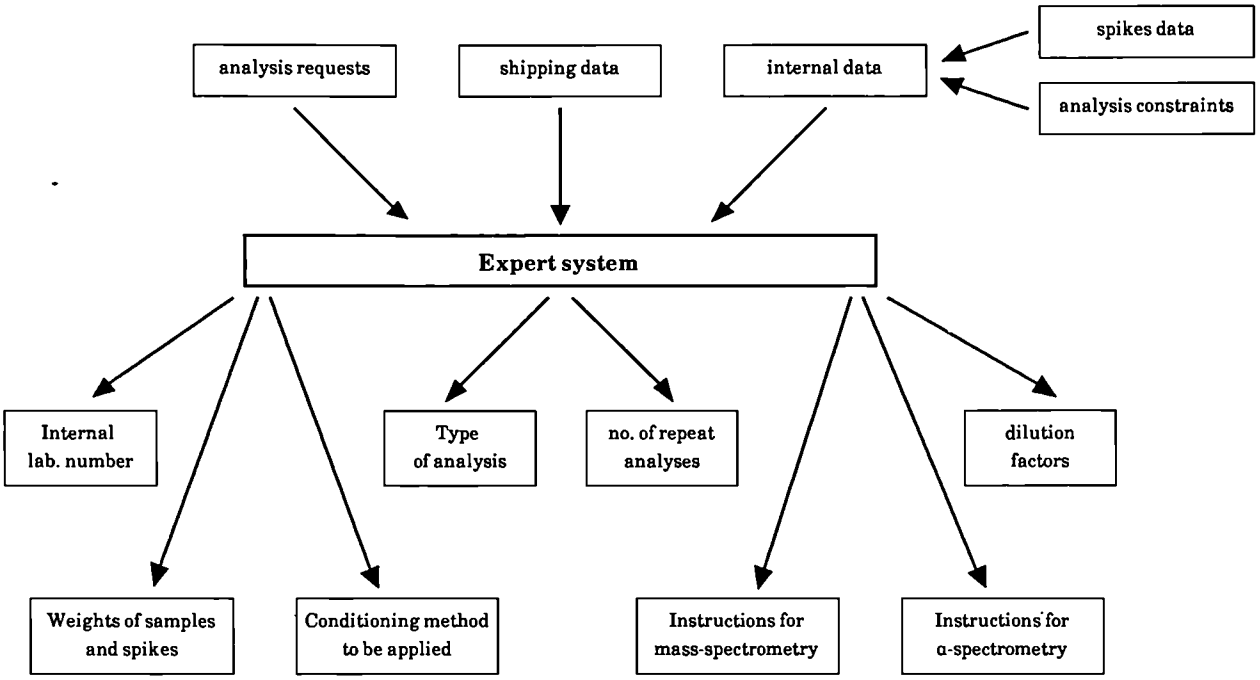

Fig. 9.8 Inputs and outputs of the expert system for the preparation of Safeguards analyses

At present, the transmission of data from Luxembourg and their incorporation in the data banks of the PC is in routine operation. Incorporation of transport data and internal data into the system is partially completed. A skeleton expert system is now being written holding a minimum of information which will then be extended as indicated by experience.

References

[1] H. Eberle, H. Ottmar, Operations Manual for the KfK Hybrid K-Edge/K-XRF Densitometer, rep. JOPAG/04.86-PRG-128, Kernforschungszentrum Karlsruhe (1986)

[2] H. Ottmar, H. Eberle, I. Michel-Piper, E. Kuhn, S. Johnson, "Calibration of X-Ray Densitometers for the Determination of Uranium and Plutonium in Reprocessing Input and Product Solutions", Rep. JOPAG/11.85-PRG-123, Kernforschungszentrum Karlsruhe (1985)

[3] R.E. Kaiser, J.A. Mühlbauer, "Elementare Tests zur Beurteilung von Meßdaten", B.I. Hochschultaschenbücher, Vol. 774, Bibliographisches Institut, Mannheim (1983)

[4] L. Koch, "Possible Verification Methods for the Input Measurements of Fast Reactor Fuel Reprocessing", Proceedings of the 5th Annual ESARDA Symposium

on Safeguards and Nuclear Material Management, Versailles, France (19-21 April 1983)

[5] IAEA Safety Series No 6: "Regulation for the Safe Transport of Radioactive Material" (1973), Revised edition as amended 1979 p.8, 134

[6] B. Clark, S. Deron, R. Fiedler, H. Mc Kown, H. Swietly, "Application of the Resin-Bead Technique to the Isotopic Analysis of Nanogram Size Samples at the Safeguards Analytical Laboratory of the IAEA", SAL-IR-12/77 (1977)

[7] M. De Rossi, H. Gerlach, L. Koch, M. Molinet, R. Wellum, "Application of a Laboratory Robot to Safeguards Analysis", Proceedings of the Meeting of the Working Group "Hot Cell and Remote Handling Technology", Ispra, Italy (23-24 September 1987)

[8] C. Schweyer, "E.S.P.A., Expertensystem für Probenanalysen", private communication (1987)

Collaboration with External Organisations

IAEA, Wien

IAK, KfK

10 Work for Third Parties

Fabrication of Plutonium Dioxide Sol-Gel Spheres

In collaboration with CBNM, Geel an installation was built and commissioned last year for the fabrication of PuO_2 spheres based on the Sol-Gel technique; the batch size of the unit is 200 grammes. In the beginning of 1987 the installation was tested with plutonium. During these test runs problems appeared with the mechanical stability of the unfired spheres; it was concluded that these problems were caused by the chemistry of the plutonium and neither by the equipment nor by known process parameters. The importance of the plutonium valency state is known, but varies with the process condition. The valency changes as a function of the concentrations of nitric acid and of metal, with temperature and due to selfirradiationThese influences are well-known for dilute solutions (< 0.1 M in Pu),whereas no data are available in our range of interest (about 1 M in Pu).For this reason an investigation on the plutonium chemistry in 1 M solutions was started, including polymerisation behaviour.

The availability of the Pu as Pu(IV) colloids is an important pre-condition for the formation of proper spheres in the precipitation procedure. However, after the concentration step most of the Pu is in the hexavalent stage. The reduction to Pu(IV) can be done by addition of H_2O_2 under carefully controlled conditions or by auto-reduction. Both possibilities were investigated using spectrophoto-metry; Fig. 10.1 shows the results for the latter case: The concentration of the plutonium present in the tetra- and hexavalent stage, respectively is plotted as a function of time. The fractions of the Pu(IV) and Pu(VI) were determined by measurements at the two wavelengths 950 nm and 1065 nm, respectively. These absorption bands have relatively low extinction coefficients [1], thus also allowing the measurements of high concentrations without dilution; furthermore, the two bands are relatively free from mutual interferences.

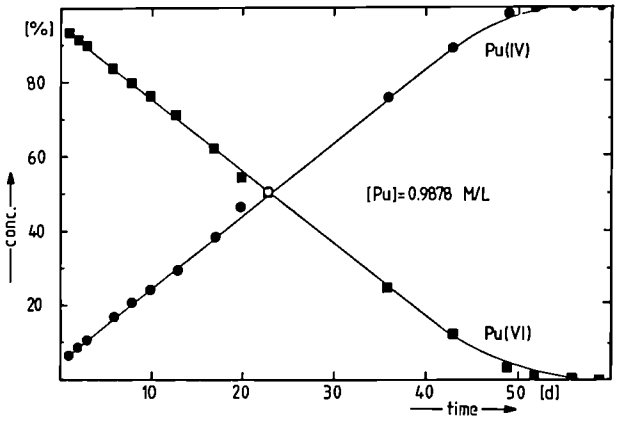

Fig. 10.1 Autoreduction of Pu(VI) to Pu(IV) in 0.7 M HNO_3, as followed in time by measurements with the Cary 17 Spectrometer. The concentration of plutonium is given in % and the time in days.

The course of the reaction Pu(VI)-Pu(IV), and thus the shape of the curves such as those in Fig. 10.1, depends upon the isotopic composition and, more strongly, on the concentration of the plutonium; however from the Figure it is seen that it takes about 2 months to bring the plutonium to the tetravalent stage, if one relies on auto-reduction.

Reference

[1] H. Schmieder, E. Kuhn, W. Ochsenfeld, KfK Report 1306 (1970).

Conditioning of Pu-Containing Materials for Transport and Reprocessing

Within the decommissioning of the SNEAK storage facility, larger quantities of Plutonium containing fuels, test samples and fabrication rests have been conditioned, homogenized and prepared for transport and reprocessing of fissile material. This work has been done on request of KFK and Alkem, partly in collaboration with Alkem and under supervision of the safeguards authorities DCS-Luxembourg and IAEA-Vienna.

The oxide and metallic materials were conditioned, homogenised and transported to Alkem in 1986. The mixed carbide fuels were transformed to oxides at the end of the year '86 begin '87 and transported in July '87 to Alkem.

Both helium and sodium bonded carbide fuel pins were conditioned. The fuel of the He-loaded pins was, after opening and weight control, directly oxidised under controlled atmosphere at 800 K/4h. The sodium loaded pins were opened at one side, heated to 400 K and the sodium drained into a steel vessel. The fuel pellets, cladding and structure material were cleaned from the rest of sodium by dissolution with alcohol. After drying and weight control the carbide pellets were oxidised as described before. The oxide powder contained less than 600 ppm carbon.

Preparation and Characterization of PuO_2-Standards for Non-Destructive Measurements in Perla (Ispra)

Within the frame of a contract for supply of fissile material standards between Alkem and Ispra, the TUI prepared on request and with the collaboration of Alkem 40 PuO_2 NDA-Standards from 10 g to 2.9 Kg PuO_2 per standard.

The homogenity, impurities, humidity and weight of the samples were specified by Ispra and Alkem. 3 types of PuO_2 powders were utilised

Table 10.1 Preparation and Characterisation of PUO_2 Standards

	Pu-239	Pu-fissile
lot A low burn-up (LB)	71 w/o	74.2 w/o
lot C medium burn-up (MB)	61 w/o	70.2 w/o
lot E high burn-up (HB)	58 w/o	67.9 w/o

The procedures for preparation and characterization of the standards (weighing procedures and controls, homogeneisation procedures, humidity and impurities controls, sampling for destructive analysis (DA) were specified. The weighing procedure ensured an overall uncertainity on Pu weight below 0.1 %. Preparation, homogeneisation, sampling and packaging were done under dry nitrogen atmosphere. Quality control and quality assurance as well as the documentation of the standard preparation and sampling were excecuted by Alkem collaborators in presence of JRC-Ispra representants and under supervision of DCS Luxembourg and IAEA Vienna. A part of the standards was measured directly after

preparation at TUI with an air calorimeter from IAEA. The plutonium isotopic composition and the Am 241 content were determined with a reference data for the Pu 241 decay correction.

All samples taken during preparation of the standards will be analysed by Alkem and in the laboratories of CEN-SCK Mol and IAEA Seibersdorf in order to characterize the PuO_2 material.

The originally forseen PVC bags as contamination barrier for handling and transport purpose could not be realized. The heat emission of the PuO_2 for the largest samples (2.5 kg Pu with 35 W) was so high, that the PVC foil reached temperatures > 375 K. This lead to a strong softening and partly destruction of this material.

The PVC-bags were substituted by polyurethan bag, which has better mechanical properties in the concerned temperature range. The welding problems connected with this new material have been solved in collaboration with industry.

The 40 PuO_2 standards were shipped to ALKEM on November 23, 1987.

In Tab 10.2 the Pu quantity and fissile material content for the 40 standards are reported.

Collaboration with External Organisations

Alkem

DCS-Luxembourg

JRC Ispra Establishment

KfK

IAEA-Vienna

Table 10.2 Perla-Standards: Pu and fissile material content

Standard No.	Burn-up	PuO_2 (g)	Pu tot (Faktor 0,87) (g)	Pu fiss (g)	Pu fiss in %
01	A	9,2041	8,0075	5,9446	74,237
02	A	9,1955	8,0000	5,9390	74,237
03	A	9,1837	7,9898	5,9314	74,237
04	A	9,1069	7,9230	5,8818	74,237
05	A	9,1545	7,9644	5,9125	74,237
06	E	9,1552	7,9650	5,4076	67,892
07	E	9,2362	8,0355	5,4555	67,892
08	E	9,0889	7,9073	5,3685	67,892
09	E	9,1750	7,9823	5,4193	67,892
10	E	9,1285	7,9418	5,3918	67,892
102	A	59,13	51,4431	38,1898	74,237
103	E	57,19	49,7553	33,7799	67,892
104	A	112,72	98,0664	72,8016	74,237
105	C	120,23	104,6001	73,4586	70,228
106	E	115,84	100,7808	68,4221	67,892
107	A	343,38	298,7406	221,7761	74,237
108	E	450,14	391,6218	265,8799	67,892
109	A	576,86	501,8682	372,5719	74,237
110	E	576,64	501,6768	340,5984	67,892
111	A	1148,96	999,5952	742,0695	74,237
112	C	1166,08	1014,4896	712,4558	70,228
113	E	1151,08	1001,4396	679,8974	67,892
114	A	1727,58	1502,9946	1115,7781	74,237
115	E	1659,83	1444,0521	980,3959	67,892
116	A	2301,40	2002,2180	1486,3866	74,237
117	E	2299,59	2000,6433	1358,2767	67,892
118	A	2874,46	2500,7802	1856,5042	74,237
119	C	2895,81	2519,3547	1769,2924	70,228
120	E	2829,49	2461,6563	1671,2677	67,892
1004	E	286,99	249,6813	169,5136	67,892
1005	E	575,06	500,3022	339,6652	67,892
1006	E	862,20	750,1140	509,2674	67,892
1007	E	1152,93	1003,0491	680,9901	67,892
1008	A	284,97	247,9239	184,0513	74,237
1009	A	577,08	502,0596	372,7140	74,237
1010	A	859,19	747,4953	554,9181	74,237
1011	A	1157,21	1006,7727	747,3978	74,237
1012	E	55,33	48,1371	32,6812	67,892
1013	E	11,54	97,0398	65,8823	67,892
1014	E	273,94	238,3278	161,8055	67,892
Gesamt		28754,4785	25016,3961	17.735,3411	

11 Radiation Protection

Introduction

The European Institute for Transuranium Elements at Karlsruhe is one of the four establishments making up the Joint Research Centre of the Commission of the European Communities. The Institute is in handling alpha-emitting radioactive substances, without shielding against beta, gamma or neutron radiation. In 30 hot laboratories, containing over 400 glove-boxes, and in 20 shielded cells considerable amounts of practically all available actinide elements are handled.

These actinide elements, ranging from actinium to californium are only handled inside glove-boxes or equivalent alpha-containment. m and uranium are handled in glove-boxes in order to avoid any measurable alpha-contamination in the laboratories. The emphasis of the radiation protection activities, carried out at the Institute, is on the risk of incorporation of potentially harmful quantities of #these actinides should these escape from their containment.

Factors Affecting Incorporation Control

The program for incorporation control at the European Institute for Transuranium Elements has to cope with the following factors :

- most glove boxes, many of which have seen more than 20 years of service, are internally contaminated with a mixture of actinides of generally unknown composition. Therefore, it is not sufficient to monitor a worker specifically for the nuclide which he is actually handling, but other nuclides, especially those with high specific activities, should also be taken into account.
- the amount of radioactivity, which must be measured in order to fulfil the requirement that 1/20 of the annual limit on intake (ALI) for radiation workers can be detected by the control programme, are very small indeed. This is especially true in the case of plutonium for which the limit of detection by lung counting is well above the ALI value. Moreover, after inhalation of poorly soluble plutonium compounds, the concentration of this element in urine is very low and decreasing with time. The concentration of inhaled poorly soluble plutonium in the feces initially is higher than in urine, however it decreases more rapidly with time. Consequently, a programme for individual monitoring of incorporation of plutonium, especially of insoluble plutonium compounds, requires that very frequent plutonium analyses in feces are made. The same problem occurs, to a certain degree, with the other actinide elements.

A solution to those problems may be found in a programme which consists of 2 components :

- under normal operating conditions : monitoring the concentration of non-natural alpha-emitters in the laboratory air.

- after a breach of containment : identification by alpha-spectrometry of the nuclide(s) involved and analysis of urine and feces of the persons concerned.

Monitoring of Air Contamination

In this paper we shall describe in some detail the programme of air contamination monitoring, which should guarantee that no worker inhales more than 1/20 of the ALI per year, without this being detected.

If we assume that a mixture of alpha-emitters not containing Cm-248 is handled, the ALI for radiation workers in the Federal Republic of Germany is 103 Bq. An activity concentration of 2,1 x 10^{-3} Bq/m^3 in a yearly inhalation volume of 2500 m^3 would lead to an intake of 1/20 of this ALI value. For an air monitoring programme based on this limiting concentration value to be reliable, it is essential that under normal operating conditions the concentration of alpha-emitters is well below 1/10 of this limiting value of 2,1 x 10^{-3} Bq/m^3 since it must be assumed that the alpha-concentration is not uniform in space. For this reason an effort was made to reduce as much as possible both the alpha-concentration under normal conditions and the detection limit of the monitoring equipment.

The air contamination is measured by drawing 25-30 m^3/h of laboratory air through 20 cm diameter glass fiber filters. The alpha-activity of the aerosol particles caught on these filters is measured with large-area proportional counters. Two types of procedures are used :

- in the laboratories and other frequently occupied working places, each filter stays in its sampling position during 1 week, during which time it is continually counted with proportional counters using the alpha-beta pseudocoincidence technique. This procedure serves for early detection of spills. After this seven days sampling period, the filter is collected and left for at least an 8 days waiting time to allow for the decay of radon and thoron daughter products.
- the other rooms, in which an alpha-contamination cannot be ruled out, are controlled on a discontinuous basis using filters which are collected each working day and counted 1-4 hours later in the radiation protection laboratory also using the alpha-beta-pseudocoincidence technique. After this immediate counting these "one-day" filters are also left for at least 8 days for decay of natural radioactivity.

After the decay of natural radioactivity the 40 "seven-days" filters and ca. 60 "one-day" filters are counted again using large-area proportional counters. These counters are equipped with personal computers, type Commodore CBM-8000 Series, for steering and data acquisition. From the various counters, the data are collected in a central storage and processing unit, from which they can be given out in various forms. Equipment and procedures used for counting are chosen with attention to obtain the lowest possible standard deviation in the count rates of fresh filters used as blanks. This standard deviation determines the detection limit.

The main factor influencing the detection limit for alpha-emitters is the variable radon daughter

activity in the counting room, although the air entering the room is passed through a HEPA-filter. The variations during the day in the blank count rate have an unfavourable influence on the detection limit. Therefore, measurements of blanks are made before and after each series of 6 filters. The gross count for each filter is corrected with a background correction which is a linear interpolation between the preceding and the following blanks. (Example : in the measuring series B_1, F_1, F_2, F_3, F_4, F_5, F_6, B_2, the background correction for F_2 is $5/7\ B_1 + 2/7\ B_2$) Using counting times of 20 minutes, detection limits of about 8×10^{-6} Bq/m^3 and 5×10^{-5} Bq/m^3 are obtained for "seven-days" and "one-day" filters respectively. The alpha-concentration values, which in this way are obtained each week, are combined for each of the ca. 100 monitoring stations to weekly, monthly and yearly averages. These averages are searched for values exceeding either 3 x detection limit, 10 x imit or 2,1 x 10^{-3} Bq/cm^3. The radiation protection personnel responsible for the rooms or laboratories showing such increased values mark these on control charts, which thus give an excellent view of the state of cleanliness of the area under their supervision. Depending on the level and persistance of the increased values, measures are taken ranging from an additional routine cleaning to temporary closing the laboratory for a thorough decontamination.

Inventory of Non-Fissile Radioactive Materials

At the European Institute for Transuranium Elements the need for a computerized bookkeeping system for non-fissile radioactive materials arose at a later stadium, an inventory for fissile materials had already been in operation for many years. It was decided not to integrate the new inventory into the existing one for fissile materials since they have several different characteristics :

- fissile materials are recorded only on a weight basis, other radioactive materials on a weight or activity basis.
- the inventory of fissile materials does not make provisions for radioactive decay since all relevant fissile nuclides, with the possible exception of Pu-241, are very long lived.
- the bookkeeping of fissile materials is closely connected with criticality control, therefore the recording of all movements must be immediate. With non-fissile materials a certain time-lag may be accepted.
- Also for reasons of criticality control, the inventory of fissile materials shows the location of the materials, whereas for non-fissile materials indication of the organisational unit responsible for the material may be more practical.

The characteristics of the bookkeeping procedure for fissile materials are :

- calculation and bookkeeping done by the laboratory personnel at each location without computer.
- central bookkeeping station (equipped with computer) checks bookings communicated by laboratory personnel and enters these into the computer-based central bookkeeping system.

The characteristics of the bookkeeping procedure for non-fissile radioactive materials are :

- laboratory personnel communicates movements of materials (quantities expressed in weight or activity units of choice) to the central bookkeeping system without any calculation or recording
- central bookkeeping station calculates by computer the new status of each group which is touched by a movement. A print-out of the new status is sent to these groups to be kept in their inventory files.

At the central bookkeeping station the inventory of non-fissile radioactive materials is calculated and kept on an Olivetti M24 personal computer, equipped with a Winchester Disk system. The programme has been written in PASCAL.

The size of the inventory is determined in the first place by the numbers of groups and nuclides. At present we have :

- 29 groups or organisational units divided over 2 areas
- 40 nuclides in form of unsealed material or sealed sources.

However, it is always possible to add new groups and nuclides to these lists.

In order to function properly in practice the system has a few limiting or complementary possibilities :

- a nuclide which has decayed to less than 1/100 of the exemption limit is cancelled.-The quantities are printed out as multiples of powers of 10, with at most 2 digits after the decimal point (e.g. 1,23 E 0 6)
- in the memory the quantities are stored with 11 digits.
- the system allows handling of mixtures of unknown composition and half lives, such as activation or fission products. These mixtures are treated each as a unique nuclide with infinite half life. They are measured only in activity units.

Changes in the account of a certain group may occur for the following reasons :

- transfer from or to another group (including waste disposal)
- correction of a previously estimated value
- decay (e.g. Cm-242, Cf-252)
- production, takes place when a non-fissile nuclide (e.g. Am-241) or mixture (e.g. fission products) is chemically separated from the fissile material in which it was formerly contained. (Generally, non-fissile impurities of fissile material are not included in the inventory).

The system handles about 200 entries per year.

The system is programmed to present the following information on request :

- the quantities of non-fissile radioactive nuclides present at a specified group, or in an area or in the whole institute. Unsealed and sealed material are listed separately. The quantity of each nuclide is presented either in grammes, in Becquerels or as a multiple of the exemption limit. This last unit of activity is useful, since in the institut's working licence the maximum permissible total amount of non-fissile radioactive substances is expressed as a multiple of the exemption limit without specification of individual nuclides. The quantities are automatically corrected for decay since the last print-out.
- the distribution of a certain nuclide within the institute.

the list of nuclides with half lives longer than 100 days, which every year is reported to the supervisory authorities

the answer to the question whether a certain quantity of radioactive material may be introduced into an area, without exceeding the limits defined in the working licence.

Publications 1987

Scientific - Technical Articles and Monographs

P.T. Elton, K. Lassmann
Calculational Methods for Diffusional Gas Release
Nucl. Eng. Des. 101 (1987) 259-265

J.W. Ward, W. Bartscher, J. Rebizant
A Re-Examination of the Neptunium-Hydrogen System
J. Less-Common Met. 130 (1987) 431-439

C. Ronchi, J. Sakellaridis
Boundary Loss-Term in the Diffusion of Radioactive Volatile Fission Products
Nucl. Sci. Eng. 95 (1987) 282-295

K. Lassmann, F. Hohlefeld
The Revised URGAP-Model to Describe the Gap Conductance Between Fuel and Cladding
Nucl. Eng. Des. 103 (1987) 215-221

J.C. Spirlet, J.R. Peterson, L.B. Asprey
Preparation and Purification of Actinide Metals
Advances in Inorganic Chemistry and Radiochemistry 31 (1987) 1

K. Lassmann
A Fast and Simple Iteration Scheme for the Temperature Calculation in a Fuel Rod
Nucl. Eng. Des. 103 (1987) 211-214

Hj. Matzke
Nuclear Waste Materials, Chapter 12 (book contribution) in: Ion Beam Modification of Insulators
Eds. G. Arnold and P. Mazzoldi
Elsevier Science Publishers (1987) 501-530

C. Ronchi
On Diffusion and Precipitation of Gas-in-Solid
J. Nucl. Mater. 148 (1987) 316-323

A. Boeuf, R. Caciuffo, M. Pages, J. Rebizant
F. Rustichelli, A. Tabuteau
Neutron Diffraction Study of the $U_{1-x}Np_xO_2$ Fluorites
Europhys. Lett. 3(2) (1987) 221-227

J. Rebizant, M.R. Spirlet, P.P. Barthelemy, J.F. Desreux
Structure of 13,13'-(1,4-Phenylen-ebis(methylene))bis-1,4,7,10-tetraoxa-13-azacyclopentadecane Dihydrochloride, a Bicyclic Macrocycle Containing Two (15)-NO_4 Subunits
Acta Crystallogr. C43 (1987) 909-912

M.R. Spirlet, J. Rebizant, J. Goffart
Structure of Triindenyluranium Bromide, $U(C_9H_7)_3Br$
Acta Crystallogr. C43 (1987) 354

C. Van den Bossche, M.R. Spirlet, J. Rebizant, J. Goffart
The structure of $((UO_2)_4\ O_2\ Cl_4\ (C_4H_8O)_2\ (H_2O)_4)$, a Tetranuclear Uranyl(VI) Complex
Acata Crystallogr. C43 (1987) 837-839

K. Richter, C. Sari
Phase Relationships in the Neptunium-Oxygen System
J. Nucl. Mater. 148 (1987) 266-271

M.R. Spirlet, J. Rebizant, B. Kanellakopulos, E. Dornberger
Structure of Barium Tetrakis (Oxalato) Uranium (IV)Octahydrate
Acta Cryst. C43 (1987) 19-21

M. Mogensen, C.T. Walker
On The Rate Determining Step in Fission Gas Release from High Burn-up Water Reactor Fuel During Power Transients
J. Nucl. Mater. 149 (1987) 121-131

P.J. Kelly, M.S.S. Brooks
Electronic Structure and Ground State Properties of the Actinide Dioxides
J. Chem. Soc. (Faraday Transactions II) 83 (1987) 1189

J. Rebizant, M.R. Spirlet, P.P. Barthelemy, J.F. Desreux
Solid State and Solution Structures of the Lanthanide Complexes with Cryptand (2.2.1):
J. Inclusion Phenom. 5 (1987) 505

U. Benedict
Structural Data of the Actinide Elements and of their Binary Compounds with Non-Metallic Elements
J. Less-Common Met. 128 (1987) 7-45

K. Richter, H. Blank
Fast Reactor Fuel Fabrication Processes and Development
Nuclear Europe 3-4 (1987)

M. Coquerelle, C. Ronchi, J. Sakellaridis, J. van de Laar
Analysis of the Fission Product Behaviour under Normal and Off-Normal Reactor Conditions
IAEA Report IGWTPT/27 (1987)

J. Rebizant, G. Van den Bossche, M.R. Spirlet, J. Goffart
Structure of Dibromodioxouranium(IV)-Tris(tetrahydrofuran)
Acta Crystallogr. C43 (1987) 1298-1300

G. Kalkowski, G. Kaindl, S. Bertram, G. Schmiester, J. Rebizant, J.C. Spirlet, O. Vogt
5f Localization in Light Actinide Compounds Studied by L3-Edge X-Ray Absorption
Solid State Commun. 64 (1987) 193

G. Kalkowski, G. Kaindl, G. Schmiester, J. Rebizant, J.C. Spirlet, O. Vogt
L3 X-Ray Absorption in Compounds of U, Np, and Pu
(book contribution)in: Theoretical and Experimental Aspects of Valence Fluctuations. Eds. L.C. Gupta and S.K. Malik
Plenum Corp. (1987)

U. Benedict
The Effect of High Pressures on Actinide Metals
Handbook on the Physics and Chemistry of the Actinides
Eds. A.J. Freeman, G.H. Lander
North Holland Publ. vol. 5 (1987) 227-269

R. Caciuffo, J.M. Fournier, W.F. Kuhs, G.H. Lander, J.C. Spirlet
A Search for Anharmonic Effects in NpO_2 at Low Temperature by Neutron Diffraction
Solid State Commun. 64 No. 1 (1987) 149-152

P. Burlet, J. Rossat-Mignod, G.H. Lander, J.C. Spirlet, J. Rebizant, O. Vogt
Neutron Diffraction Study of PuSb: The Critical Regime
Phys. Rev. B 36 No. 10 (1987) 5306-5310

M.R. Spirlet, J. Rebizant, C. Apostolidis, B. Kanellakopulos
Structure of Tris (n5-cyclopentadienyl), bis(propionitrile) lanthanum(III)
Acta Cryst. C43 (1987) 2322-2324

G.H. Lander, J. Rebizant, J.C. Spirlet, A. Delapalme, O. Vogt, K. Mattenberger
Neutron Scattering and Magnetization Studies of Plutonium Monochalcogenides
Physica B plus C 146B (1987) 341-350

T. Adachi, K. Kammerichs, L. Koch
Inherent Isotope Dilution Analysis of ^{237}Np in Spent Nuclear Fuels
J. Radioanal. Nucl. Chem. Letters 117(4) (1987) 233-241

Hj. Matzke
Indentation Techniques Applied to Nuclear Materials Introduction, Basic Needs
Eur. Appl. Res. Rep.-Nucl. Sci. Technol. Sect. 7 (1987) 999-1027

Hj. Matzke
Definition of Problems and of Important Parameters for Indentation Tests
Eur. Appl. Res. Rep.-Nucl. Sci. Technol. Sect. 7 (1987) 1091-1108

K. Lassmann
The OXIRED Model for Redistribution of Oxygen in Nonstoichiometric Uranium-Plutonium Oxides
J. Nucl. Mater. 150 (1987) 10-16

F. Dyment, Hj. Matzke, E. Toscano
Diffusion of ^{83}Rb and ^{84}Rb Tracers in Waste Glasses
J. Non-Cryst. Solids 93 (1987) 22-34

A.J. Freeman, G.H. Lander (Eds.)
Handbook on the Physics and Chemistry of the Actinides
North-Holland Volume 5 (1987)

S. Pickering
Particle Distributions in Simulated Agglomeration
J. Aerosol Sci. 18 (1987) 631

S. Pickering, S. Fourcaudot
The Penetration of Filters by Alpha-active Aerosols
J. Aerosol Sci. 18 (1987) 923

S. Pickering
Resuspension of Uranium-Plutonium Oxide Particles from burning Plexiglas
J. Aerosol Sci. 18 (1987) 927

P.A. Thiry, J.J. Pireaux, R. Gaudano, J.R. Naegele, J. Rebizant, J.C. Spirlet
Infrared Dieletric Response of UO_2 Single Crystal Surfaces Investigated by High Resolution Electron Energy Spectroscopy
J. Chem. Soc. (Faraday Transactions II) 83 (1987) 1229

N. Martensson, B. Johansson, J.R. Naegele
A Possible Interpretation of the Photo-electron Spectrum for Americium Metal
Phys. Rev. B 35 (1987) 1437

G. Van den Bossche, M.R. Spirlet, J. Rebizant, J. Goffart
Structure of Diammonium Tetrabromo Sioxouranate (VI) Dihydrate
Acta Crystallogr. C43 (1987) 383

Hj. Matzke (Ed.)
Indentation Fracture and Mechanical Properties of Ceramic Fuels and of Waste Ceramics and Glasses
Eur. Appl. Res. Rep.-Nucl. Sci. Technol. vol. 7 no. 7 (1987) 995-1242

E. Hovestreydt, E. Parthe, U. Benedict
ENDIX - A Computer Program to Simulate Energy Dispersive X-Ray and Synchrotron Powder diffraction Diagrams
J. Appl. Crystallogr.

Hj. Matzke, A.G. Solomah, E. Toscano, C.T. Walker
Neptunium Doping of the Crystalline Ceramic Waste Form SYNROC B
J. Am. Ceram. Soc.

H. Bokelund, K. Deelstra
Statistical Tests Applied as Quality Control Measures to Leaching of Nuclear Waste Glasses
Radioactive Waste Management

J. Staun Olsen, L. Gerward, U. Benedict, S. Dabos, O. Vogt
High-pressure Phaes of Uranium Mono-phosphide Studied by Synchrotron X-Ray Diffraction
Phys. Rev. B

M. Wulff, G.H. Lander, J. Rebizant, J.C. Spirlet, B. Lebech, C. Broholm, J. Brown
Magnetic Moments and Pu form factor in $PuFe_2$
Phys. Rev. B

M. Thomas, Hj. Matzke
Sodium diffusion in the nuclear waste glass GP 98/12
J. Am. Cer. Soc.

J. Magill, G.J. Hyland, M.H. Rand
New Ionic Contributions to the Vapour Pressure of Urania
J. Chem. Phys.

R. Osborn, A.D. Taylor, Z.A. Bowden, M.A. Hackett, W. Hayes, M.T. Hutchings, G. Amoretti, R. Caciuffo, A. Blaise, J.M. Fournier
High Resolution Neutron Spectroscopy of Crystal Field Excitations in Uranium Dioxide
Phys. Rev. Lett.

Contributions to Conferences

J.P. Itie, U. Benedict, S. Dabos, E. Dartyge
A. Fontaine, G. Tourillonen, J. Staun Olsen
High Pressure X-ray Absorption Spectroscopy on Uranium Compounds
2nd Int. Conf. on the Basic and Applied Chemistry of f-Transition (Lanthanides and Actinides)and Related Elements
06.04.-10.04.1987 Lisbon, Portugal
Proceedings Inorg. Chim. Acta Vol. 140 (1987) 193-195

C. Apostolidis, H. Bokelund, A. Moens, M. Ougier
Redox Behaviour of Neptunium in the Presence of U, Pu, and Am Applied in their Separation by TBP and Ion Exchange (HPLC)
2nd Int. Conf. on the Basic and Applied Chemistry of f-Transition (Lanthanides and Actinides)and Related Elements
06.06.-10.04.1987 Lisbon, Portugal
Proceedings Inorg. Chim. Acta Vol. 140 (1987) 253-255

J. Schultz, C.A. Colmenares, J. Naegele, J.C. Spirlet
Surface Studies of UFe_2 and Evalutation of its Catalytic Properties with a $2H_2$:CO Mixture
2nd Int. Conf. on the Basic and Applied Chemistry of f-Transition (Lanthanides and Actinides)and Related Elements
06.04.-10.04.1987 Lisbon, Portugal
Proceedings Inorg. Chim. Acta Vol. 140 (1987) 37-38

J. Naegele, L.E. Cox, J. Ward
Photoelectron Spectroscopy (UPS/XPS) Study of Np_2O_3 Formation on the Surface of Neptunium Metal
2nd Int. Conf. on the Basic and Applied Chemistry of f-Transition (Lanthanides and Actinides)and Related Elements
06.04.-10.04.1987 Lisbon, Portugal
Proceedings Inorg. Chim. Acta Vol. 139 (1987) 327-329

T. Gouder, J. Naegele, C.A. Colmenares, J.J. Verbist
UPS Study of the O_2, CO_2, CO and C_2H_4 Adsorption on Uranium
2nd Int. Conf. on the Basic and Applied Chemistry of f-Transition (Lanthanides and Actinides)and Related Elements
06.04.-10.04.1987 Lisbon, Portugal
Proceedings Inorg. Chim. Acta Vol. 140 (1987) 35-36

J. Rebizant, C. Apostolidis, M.R. Spirlet, B. Kanellakopulos
Crystal and Molecular Structure of a Novel Organoactinide Complex: $(U(C_5H_5)_3(NCCH_3)_2) + (Th(C_5H_5)Cl_4(NCCH_3))$
2nd Int. Conf. on the Basic and Applied Chemistry of f-Transition (Lanthanides and Actinides) and Related Elements
06.04.-10.04.1987 Lisbon, Portugal
Proceedings Inorg. Chim. Acta vol. 139 (1987) 209-210

M.R. Spirlet, J. Rebizant, C. Apostolidis, B. Kanellakopulos
Structural Investigations of the Isomorphous Propionitrile- tris (na5-cyclopentadienyl) Lanthanoid (III) (Ln = La,Pr,Yb) Complexes and of the Corresponding 1:2 Adducts
2nd Int. Conf. on the Basic and Applied Chemistry of f-Transition (Lanthanides and Actinides)and Related Elements
06.04.-10.04.1987 Lisbon, Portugal
Proceedings Inorg. Chim. Acta Vol. 139 (1987) 211-213

S. Kern, C.K. Loong, G. Goodman, G.H. Lander, B. Cort
Neutron Inelastic Experiments on Actinide Dioxides -Search for Crystal-Field Levels in NpO_2
32nd Conference on Magnetism and Magnetic Materials
09.11.-12.11.1987 Chicago, Illinois, USA
Proceedings J. Appl. Phys.

G.H. Lander, M. Wulff, J. Rebizant, J.C. Spirlet, P.J. Brown, O. Vogt
Studies of the Magnetization Densities in Pu Compounds: Determination of the Degree of 5f Localization
32nd Conference on Magnetism and Magnetic Materials
09.11.-12.11.1987 Chicago, Illinois, USA
Proceedings J. Appl. Phys.

K. Richter, U. Benedict, J.F. Gueugnon, H. Kutter, C. Sari, G. Mühling
Specification, Fabrication and Characterisation of (U,Pu)C Fuel
3rd Conference on Characterization and Quality Control of Nuclear Fuels
25.05.-27.05.1987 Karlsruhe
Proceedings J. Nucl. Mater. vol. 153 (1988) 205-210

H. Blank
Specification and Characterization of Dense Fuels for Liquid Metal Cooled Fast Breeder Reactors
3rd Conference on Characterization and Quality Control of Nuclear Fuels
25.05.-27.05.1987 Karlsruhe
Proceedings J. Nucl. Mater. vol. 153 (1988) 171-177

G.H. Lander, Argonne Nat. Lab.
Scientific Opportunities with Neutron Scattering
Introductory Lecture for NATA-ASI on "Chemical Crystallography with Pulsed Neutrons and Synchrotron X-Rays"
March, 1987 Alvor, Portugal
Chemical Crystallography eds. M.A.Carrondo,G.A.Jeffrey,

L. Koch, B. Brandalise, M. De Rossi, H. Gerlach, R. Molinet, M. Romkowski
Automatic Analysis for Input of Nuclear Fuel Reprocessing
4th Meeting on Nuclear Analytical Techniques
O4.O5.-O8.O5.1987 Dresden, DDR
Proceedings Isotopenpraxis

L. Koch
Potentials of Np and Am Recycling
Int. Symp. on the Back-End of the Nuclear Fuel Cycle -Strategies and Options
IAEA 11.05.-15.05.1987 Vienna
IAEA-SM-294/7P

J.-P. Glatz, H. Bokelund, S. Zierfuss
Dissolution of Different Types of Nuclear Fuels in Nitric Acid
Int. Conf. on Nuclear Fuel Reprocessing and Waste Management
24.08.-28.08.1987 Paris
Proceedings p 587

L. Koch
New Procedures to Verify the Input Analysis of Nuclear Fuel Reprocessing
Sicherheit der Nuklearen Entsorgung
15.3.-21.3.1987 Obertraun, Österreich
Bd. 4 Nukleare Entsorgung, VCH-Verlag, Weinheim

Ch. Apostolidis, B. Kanellakopulos, J.I. Kim, F. Klein, J. Müller, J.T. Vida
The Behaviour of Technetium and Neptunium in Natural Aquatic Systems
Int. Conf. on Chemistry and Migration Behaviour of Actinides and Fission Products in the Geosphere
14.9.-18.9.1987 Mnchen
Proceedings p 143

Ch. Apostolidis, P. Dressler, B. Kanellakopulos, J.I. Kim
Study of the Hydrolyzed and Colloidal Species of Tetravalent Plutonium in Aquatic Solutions
Int. Conf. on Chemistry and Migration Behaviour of Actinides and Fission Products in the Geosphere
14.9.-18.9.1987 München
Proceedings p 159

Hj. Matzke
Radiation Damage Effects in Nuclear Materials
Int. Workshop on Radiation Damage in Nuclear Waste Materials
REI-87
6.7.-10.7.1987 Lyon
Proceedings Nucl. Instrum. Methods

Hj. Matzke, E. Toscano, G. Linker
Alkali Diffusion and Radiation Effects in the Waste Glass VG 98/12
Int. Workshop on Radiation Damage in Nuclear Waste Materials
REI-87
6.7.-10.7.1987 Lyon
Proceedings Nucl. Instrum. Methods

B. Johansson, O. Eriksson, M.S.S. Brooks, H.L. Skriver
Theoretical Studies of Actinides Intermetallic Compounds
2nd Int. Conf. on the Basic and Applied Chemistry of f-Transition (Lanthanides and Actinides)and Related Elements
06.06.-10.04.1987 Lisbon, Portugal
Proceedings Inorg. Chim. Acta Vol. 140 (1987) 59-66

L. Koch
New Concept for Reprocessing Input Verification - Poster
3rd Int. Conf. on Facility Operations-Safeguards Interface
American Nuclear Society 29.11.-4.12.1987
San Diego, California, USA
Suppl. 1 to Transactions Vol. 55 Nov. 1987

G. Lederberger, R. Herbst, H.U. Zwicky, H. Kutter, P. Fischer
Characterization and Quality Control of Uranium-Plutonium Carbide for the AC-3/FFTF Experiment
3rd Conference on Characterization and Quality Control of Nuclear Fuels
25.05.-27.05.1987 Karlsruhe
Proceedings J. Nucl. Mater. vol. 153 (1988) 189-204

S. Franzini, P.P. Trincherini, S. Facchetti, J. Gordon
ICP-MS Activity at Ispra
3. Incontro italo ungherese di spettroscopia
JRC 8.6.-12.6.1987 Ispra
Proceedings

S. Dabos, U. Benedict, J.C. Spirlet, M. Pages
Structural Phase Transition in PuTe Under Pressure
17emes Journées des Actinides
26.03.-28.03.1987 Lausanne, Switzerland

M. Wulff, G.H. Lander, J. Rebizant, J.C. Spirlet, B. Lebech, C. Broholm, P.J. Brown
Magnetic Moments and Pu from Factor in $PuFe_2$
17emes Journées des Actinides
26.03.-28.03.1987 Lausanne, Switzerland

S.F. Kern, C.K. Loong, G. Goodman, G.H. Lander, B. Cort
Neutron Inelastic Experiments to Determine the Crystalfield Levels in NpO_2
17emes Journées des Actinides
26.03.-28.03.1987 Lausanne, Switzerland

M.S.S. Brooks, O. Eriksson, B. Johansson
Spin-orbit Effects in the Energy Bands of Actinide Transition Metal Intermetallics
17emes Journées des Actinides
26.03.-28.03.1987 Lausanne, Switzerland

J. Rebizant, J.C. Spirlet, E. Bednarczyk, T. McMenamin, K. Rijkeboer
Preparation and Structure of New Ternary Intermetallic Compounds
17emes Journées des Actinides
26.03.-28.03.1987 Lausanne, Switzerland

T. Gouder, C. Colmenares, J. Naegele, J.S. Spirlet, J. Verbist
Photoemission Study of the CO Adsorption on U, UNi_2 and UNi_5
17emes Journées des Actinides
26.03.-28.03.1987 Lausanne, Switzerland

J. Naegele, L.E. Cox, J. Ward
Photoemission Study of Surface Oxidation of Np-Metal
17emes Journées des Actinides
26.03.-28.03.1987 Lausanne, Switzerland

J.P. Sanchez, J. Rebizant, J.C. Spirlet, O. Vogt
Electronic and Magnetic Properties of NpSb and NpTe
Studies by ^{237}Np, ^{121}Sb and ^{125}Te Mössbauer Spectroscopies
17emes Journées des Actinides
26.03.-28.03.1987 Lausanne, Switzerland

O. Cromboom, H. Kutter, M. Ougier, Ch. Apostolidis, H. Bokelund
Determination of Traces of Thorium and Neptunium in Plutonium Nitrate Solutions
17emes Journées des Actinides
26.03.-28.03.1987 Lausanne, Switzerland

J. Goudiakas, J. Fuger
Thermochemical Studies of Alkaline Earth-Lanthanide and Actinide (IV) Complex Oxides
42nd Annual Calorimetry Conference
26.07.-31.07.1987 Boulder, Colorado, USA

G. Kaindl, G. Kalkowski, S. Bertram, G. Schmiester, J. Rebizant, J.C. Spirlet, O. Vogt
L3-Edge X-Ray Absorption Study of Light-Actinide Compounds
17emes Journées des Actinides
26.03.-28.03.1987 Lausanne, Switzerland

J. Fuger
Actinide Research at the European Institute for Transuranium Elements
2nd Int. Conf. on the Basic and Applied Chemistry of f-Transition (Lanthanides and Actinides)and Related Elements
06.04-10.04.1987 Lisbon, Portugal

U. Benedict
General Diagram of the Phase Relations of Actinide Metals Under Pressure
2nd Int. Conf. on the Basic and Applied Chemistry of f-Transition (Lanthanides and Actinides)and Related Elements
06.04.-10.04.1987 Lisbon, Portugal

J. Fuger
Thermodynamic Properties of the Transplutonium Elements: From Experimental to Extrapolated Values
194th National Meeting of the American Chemical Society
30.08.-04.09.1987 New Orleans, LA, USA

R.G. Haire, S. Dabos, U. Benedict, C. Dufour
The Effect of Pressure on Am-Cm Alloys
194th National Meeting of the American Chemical Society
30.08.-04.09.1987 New Orleans, LA, USA

M. Coquerelle, C. Ronchi
Analysis of the Various Modes of Fission Product Release from LWR Fuel
Jahrestagung Kerntechnik `87
02.06.-04.06.1987 Karlsruhe

S. Bertram, G. Schmiester, G. Kaindl, O. Vogt, J. Rebizant, J.C. Spirlet
L3 Röntgenabsorptionsexperimente an Uran-Verbindungen unter hohem Druck
Frühjahrstagung der Deutschen Physikalischen Gesellschaft
09.03.-14.03.1987 Münster

M.S.S. Brooks, O. Eriksson
Spin-Orbit Coupling and the Magnetism of UFe_2
7th General Conference of the Condensed Matter Division
of the European Physical Society
07.04-10.04.1987 Pisa, Italy

M. Romkowski, S. Franzini, L. Koch
Mass-Spectrometric Analysis of Sub-Nanocurie Samples of Uranium and Plutonium
9th Annual Meeting of the European Safeguards Research and Development Association (ESARDA)
12.05.-14.05.1987 London

M. de Rossi, H. Gerlach, L. Koch, M. Molinet R. Wellum
Application of a Laboratory Robot to Safeguards Analysis
9th Annual Meeting of the European Safeguards Research and Development Association (ESARDA)
12.05.-14.05.1987 London

J. Magill, G.J. Hyland, M.R. Rand
The Role of Molecular Ions in the High Temperature Vaporization of Urania
5th Int. Conf. on High Temperature and Energy Related Materials
25.05.-29.05.1987 Rome, Italy

J. Magill, R. Beukers, F. Capone, W. Heinz J.-P. Hiernaut, E. Kramer, M. Martellenghi, R. Selfslag, P. Werner
A New Technique for Containerless Processing of Materials at High Temperatures
5th Int. Conf. on High Temperature and Energy Related Materials
25.05.-29.05.1987 Rome, Italy

Hj. Matzke, G. Della Mea, R. Dal Maschio, J.C. Dran, A.A. Stefanini
Effect of Temperature During Damage Production on Properties of Nuclear Waste Glasses Using Ion Implantation
Int. Workshop on Radiation Damage in Nuclear Waste Materials
REI-87
6.7.-10.7.1987 Lyon

H. Blank, K. Lassmann
Modelling of Fuel Rod Behaviour and Recent Advances of the TRANSURANUS Code
89th Annual Meeting of the American Ceramic Society, Inc.
26.4.-30.4.1987 Pittsburgh, PA, USA

K. Richter, H. Blank
Fabrication Processes and Characterisation of LMFBR Carbide and Nitride Fuels and Fuel Pins
Technical Committee Meeting on Advanced Fuel for Fast Breeder Reactors
IAEA 3.11.-5.11.1987 Vienna

H. Blank, M. Campana, M. Coquerelle, K. Richter
Performance of He-bonded LMFBR Carbide and Nitride Fuels at the Beginning of Life and Consequences for their Subsequent Behaviour
Technical Committee Meeting on Advanced Fuel for Fast Breeder Reactors
IAEA 3.11.-5.11.1987 Vienna

L. Koch
New Concept for Reprocessing Input Verification
3rd Int. Conf. on Facility Operations-Safeguards Interface
American Nuclear Society 29.11.-4.12.1987 San Diego, California, USA

H. Bokelund
The Removal of Actinide Elements from Waste Solutions of Intermediate Activity Level by Their Precipitation with Oxalic Acid
Int. Symposium on the Management of Low and Intermediate Level Radioactive Wastes
IAEA 16.5.-20.5.1987 Stockholm, Sweden

C. Apostolidis, B. Kanellakopulos
Preparation of Single Crystals of Organo-metallic Compounds of the Lanthanides and Actinides
2nd Int. Conf. on the Basic and Applied Chemistry of f-Transition (Lanthanides and Actinides)and Related Elements
06.04.-10.04.1987 Lisbon, Portugal

J.C. Spirlet
Experimental Techniques of Single Growth of f-element Materials
2nd Int. Conf. on the Basic and Applied Chemistry of f-Transition (Lanthanides and Actinides)and Related Elements
06.04.-10.04.1987 Lisbon, Portugal

L. Koch
Sample Preparation using Laboratory Robots at the European Institute for Transuranium Elements
Advisory Group Meeting on Evaluation of the Quality of Safeguards Analytical Services
24.8.-28.8.1987 Ispra

K. Lassmann
Treatment of Axial Friction Forces in the TRANSURANUS Code
9th Int. Conf. on Structural Mechanics in Reactor Technology
6th Int.Seminar on Math./Mech.Modeling of Reactor Fuel Elem.
24.8.-25.8.1987 Kippel, Switzerland

E. Drosselmeyer, H. Mueller, S. Pickering, A. Seidel
Pulmonary Distribution of Different Aerosol Particles as a Function of Time after Inhalation by Rats
Proc. Conf. Design and Interpretation of Inhalation Studies
1987 Hannover

G.Neuer, H.E.Schmidt, B.Schulz
Ringversuche im Arbeitskreis Thermophysik der Deutschen Keramischen Gesellschaft
Jahrestagung der Deutschen Keramischen Gesellschaft, 21.-23.Sept. 1987, Berlin

Reports

C.T. Walker, R. Windbiel, W. Ziehl
EPMA Investigation of Xe and Cs Release from the KWU Segments
-April 1987 - K0287093

K. Lassmann
OFT Database: Experiment KWU-169
-February 1987 - K0287094

K. Lassmann
OFT Database: Experiment KWU-171
-February 1987 - K0287095

K. Lassmann
OFT Database: Experiment KWU-453
-February 1987 - K0287096

K. Lassmann
OFT Database: Experiment KWU-455
-February 1987 - K0287097

M. Gardani, C. Ronchi
Program MITRA Multicomponent Isotope TRAnsport User Guide
-June 1987 - K0287098

H. Blank
Basic Mechanisms Responsible for the Performance of He-bonded Nitride and Carbide Fuels
-June 1987 - K0287099

C. Ronchi, J. van de Laar
The Fuel Performance Code F U T U R E (Description of the Models and Introduction to the Program)
-July 1987 - K0287101

C.T. Walker, R. Windbiel, W. Ziehl
EPMA Results for the KWU MOX Segments PN 225 and PN 317
-August 1987 - K0287102

K. Lassmann
Berechnung von axialen Reibkräften in Brennstäben
-Oktober 1987 - K0287103

K. Lassmann
Transfer of the Revised URGAP-model to Describe the Gap Conductance between Fuel and Cladding
-September 1987 - K0287104

K. Lassmann
Transfer of the URGAS-model for Diffusional Gas Release
-September 1987 - K0287105

M. Campana, J.F. Gueugnon, K. Richter
Reacteur PHENIX Cahier de Specifications des aiguilles fiss. nitrure et carbure NIMPHE 2 fabriquées par l'Inst.des Trans.
-Novembre 1987 - K0287106

M. Campana, J.F. Gueugnon, K. Richter
Experience NIMPHE 1
Irradiation de 5 aiguilles nitrures mixtes dans Phenix
-Septembre 1987 - K0287107

C.T. Walker, R. Windbiel, W. Ziehl
Composition of an As-fabricated KWU MOX Fuel Pellet
-December 1987 - K0287108

H.-L. Müller, A. Seidel, E. Drosselmeyer, G. Hotz, H. Thiele, S. Pickering, I.L. Ray
Zum biologischen Verhalten von Uran-Plutonium-Mischoxid-Aerosolen: Inhalationsversuche mit Ratten und in vitro-Studien mit Alveolarmakrophagen
- EUR 10846 DE (1987)

E. Hovestreydt, E. Parthe, U. Benedict
ENDIX - a computer program to simulate energy dispersive X-ray and synchrotron powder diffraction diagrams
- EUR 10874 EN (1987)

Hj. Matzke
Indentation Fracture and Mechanical Properties of Fuels and of Waste Ceramics and Glasses
European Applied Research Reports 7 (1987)
- EUR 10957 EN (1987)

Glossary

ADC: Analog Digital Converter
AECL: Atomic Energy of Canada Limited
AERE: Atomic Energy Research Establishment Harwell (UK)
An: Actinide
ANL: Argonne National Laboratory
BNWL: Batelle North-West Laboratory
B.O.L.: Beginning of Life
BUMMEL: Irradiation experiment for bubble mobility measurement at HRR
CARLO: "Low in Oxygen" Carbide Irradiation (Petten)
CARRO: "Rich in Oxygen" Carbide Irradiation (Petten)
CBNM: Central Bureau for Nuclear Measurements, Geel (B)
CEA: Commissariat à l'Energie Atomique
CEN: Centre d'Etudes Nucléaires
CNEN: Comitato Nazionale Energia Nucleare
CNRS: Centre National de la Recherche Scientifique
Cp: C_5H_5
CRNL: Chalk River Nuclear Laboratory
DECPu: Département du Plutonium, CEN Cadarache, CEA
DEH: Direct Electrical Heating
DESY: Deutsches Elektronen-Synchrotron (Hamburg)
DKFZ: Deutsches Krebsforschungszentrum
DLA: Diffusion-Limited Aggregation
EAC: European Accident Code
ECSAM: European Commission Safeguards Analytical Measurement
EDAX: Energy Dispersive X-Ray Analysis
EDXRD: Energy Dispersive X-Ray diffraction
EEOS: Experimental Equation of State
EM: Electron Microscope
EMPA: Electron Micro Probe Analysis
ETH: Eidgenössische Technische Hochschule (Zürich)
EURATOM: EUropean community of ATOMic Energy
EXAFS: Extended X-ray Absorption Fine Structure
FACT: Sub-project "Formation of ACTinides in-pile"
FBR: Fast Breeder Reactor
FLAME: Fire Aerosol Monitoring Experiments
FR: Fast Reactor
FUTURE: Code for fuel transient calculations
GC-MS: Gas Chromatography - Mass Spectrometry
GSID: Gamma-Spectrometric Isotope Dilution
GSP: Geel-Supported Precipitation
HASYLAB: HAmburger SYnchrotronstrahlungs-LAbor (DESY)
HAW: Highly Active Waste
HCDA: Hypothetical Core Disruptive Accident
HEPA Filter: High Efficiency Particulate Air Filter
HFR: High Flux Reactor (Petten)
HPLC: High Performance Liquid Chromatography
HPXRD: High Pressure X-Ray Diffraction
IAEA: International Atomic Energy Agency
ICP: Inductively Coupled Plasma emission spectroscopy
ICRP: International Commission on Radiation Protection
ICT: Isotope Correlation Technique
IDMS: Isotope-Dilution Mass Spectrometry
ILL: Institute Laue-Langevin (Grenoble)
IMF: Institut für Material- und Festkörperforschung (KfK)
INR: Institut für Neutronenphysik und Reaktorforschung (KfK)
IR: Infra Red
IRCh: Institut für RadioChemie (KfK)

IUPAC: International Union of Pure and Applied Chemistry
IWGFR: International Working Group on Fast Reactors
JRC: Joint Research Centre
KfK: Kernforschungszentrum Karlsruhe (Germany)
KNK: Kompakte Natriumgekühlte Kernenergieanlage
KNK-MTE: Irradiation test at KNK
LANL: Los Alamos National Laboratory
LAT: Laser Autoclave Technique
LMTO: Linear Muffin Tin Orbitals
LLNL: Lawrence Livermore National Laboratory
LMFBR: Liquid Metal Fast Breeder Reactor
LWR: Light Water Reactor
M: U_xPu_{1-x}
MA: Minor Actinides (NP,Am,Cm)
MAW: Middle Active Waste
MC: Mixed (uranium, plutonium) Carbide (fuel)
MCN: Mixed Carbo-Nitride (fuel)
MITRA: Code to calculate the release of radionuclides
MN: Mixed Nitride fuel
MOX: Mixed OXide (fuel)
MSID: Mass-Spectrometric Isotope Dilution
MX: U,Pu-fuel containing a combination of the elements C,N,O
NAA: Neutron Activation Analysis
NDA: Non Destructive Assay
NILOC: Nitride Irradiation with Low Carbon Content
NIMPHE: Nitride Irradiation in PHEnix
O/M: Oxygen to Metal ratio
OFT: Oxide Fuel Transients
OPDEF: Sub-project "OPtimisation of DEnse Fuels"
ORIGEN: Code to calculate fission yields (Oak Ridge version)
ORNL: Oak Ridge National Laboratory
PAHR: Post Accident Heat Removal
PCI: Pellet Cladding Interaction
PHENIX: French prototype fast reactor
PIE: Post Irradiation Examination
PMMA: Polymethacrylate (Plexiglas)
POMPEI: Irradiation experiment to study the structure of nitride fuel at high burn-up in HFR
PPR: Programme Progress Report
PROFI: Irradiation experiment for the study of fission product release
PSB: Projekt Schneller Brüter (KfK)
PWR: Pressurised Water Reactor
QLLR: Quasi-Local Linear Regression
R&D: Research and Development
RBS: Rutherford BackScattering
REM: Replica Electron Microscopy
REPRO: Sub-project "REPROcessing of nuclear fuels"
RLMTO: Relativistic Linear Muffin Tin Orbitals
SAP: Sintest Al-powder
SEM: Scanning Electron Microscopy
SFD: Severe Fuel Damage
SHAPE: Sub-project "Safe Handling of Nuclear Materials
SIMFUEL: Thorium-based fuel with major non-volatile fission products (simulated)
SPAKOR: LWR stress-corrosion cracking model
STEM: Scanning Transmission Electron Microscopy
SUPERFACT: Minor Actinide Irradiation in Phenix
SWELAC: Irradiation experiment to study SWELling ACcomodation
TBP: Tri Butyl Phosphate
TD: Theoretical Density
TEM: Transmission Electron Microscopy
TIW: Tungsten electrode Inertgas Welding

TOP: Transient of Power
TRANSURANUS: Fuel Behaviour Code
TU: European institute for TransUranium elements
TUSR: TU Semiannual Report
UHV: Ultra-High Vaccum
UK: United Kingdom
UKAEA: United Kingdom Atomic Energy Authority
UPS: Ultraviolet light induced Photoelectron emission Spectroscopy
URADYN: In-Pin Motion Model
URANUS: Fuel pin code
UFRIC: Fuel Code to calculate friction forces
URGAP: TRANSURANUS subroutine for gap conductance calculations
URGAS: Fuel Code to calculate gas diffusion
VISIR/MITRA: Code for calculating build-up and release of shortlived isotopes
VOLEX: Irradiation experiment to study VOLume EXpansion in UO_2 at HFR
WAK: WiederAufarbeitungsanlage Karlsruhe
XAS: X-ray Absorption Spectroscopy
XPS: X-ray induced Photoelectron emission Spectroscopy
XRD: X-Ray Diffraction
XRF: X-Ray Fluorescence

List of Authors

Programme Manager : J. van Geel

1. Operation Limits of Nuclear Fuels

Project Manager : H. Blank

1.1 Optimisation of Dense Fuels
H. Blank, M. Campana, M. Coquerelle, J.F. Gueugnon,Hj. Matzke, K. Richter, C. Sari, C.T. Walker, S. Fritz*,
*visiting scientist

1.2 Properties of Reactor Materials at Very High Temperatures
C.Ronchi, J.-P. Hiernaut, H.A. Tasman, J. Magill, P. Werner,

2. Oxide Fuel Transients

Project Manager : H. Blank

M. Campana, M. Coquerelle, K. Lassmann, Hj. Matzke, I. Ray, C. Ronchi, , C.T. Walker, M. Gardani*, P. Bailey and S.E. Donnelly (Univ. Salford), A. Mazzone (LAMEL, Bologna)
*visiting scientist

3. Actinide Cycle Safety

Project Manager : H.E. Schmidt

3.1 Formation of Actinides In-Pile (FACT)
L. Koch, W. Bartscher, M. Coquerelle, J.F. Gueugnon, K. Mayer*, K. Richter, C. Sari, R. Wellum
*visiting scientist

3.2 Safe Handling of Nuclear Fuels (SHAPE)
H.E. Schmidt, K. Buijs, B. Chavane de Dalmassy, S. Pickering, V. Prodi*
*University of Bologna

3.3 Reprocessing of Advanced Fuels (REPRO)
H. Bokelund, C. Apostolides, J.-P. Glatz

4. Actinide Research

Project Manager : J. Fuger

G.H. Lander,W. Bartscher, U. Benedict, M.S.S. Brooks, Hj. Matzke, H.J. Naegele, J. Rebizant, J.-C. Spirlet,
S. Dabos*, T. Gouder*,F. Wastin*, K. Zikou*, M. Wulff**, H. Luo (Jilin Univ.), J.R. Peterson (University of Knoxville), M.R. Spirlet (Univ. of Liège), G. Stewart (Univ. of Florida)
* Ph.D. Student or grantee, ** Post Doctoral Appointee

5. Work for the Safeguard Directorate Luxembourg

Project Manager : L. Koch

S. Franzini, R. Wellum

6. Prospective Studies

Project Manager : J. van Geel

Acoustic Aerosol Scavenging
J. Magill, J.F. Babelot, S. Pickering

7. Reactor Safety

Project Manager: H. Blank

K. Lassmann, H.A. Tasman

8. Radioactive Waste Management

Project Manager : J. Fuger

H. Bokelund, M. Coquerelle, J.P. Glatz, Hj. Matzke

9. Safeguards and Fissile Materials Management

Project Manager : L. Koch

S. Franzini, D. Wojnowski, R. Wellum

10. Work upon Request

Project Manager : G. Samsel

C. Apostolidis, H. Bokelund, J.F. Gueugnon, K. Richter

11. Radiation Protection

Project Manager : K. Buijs

Previous Programme Progress Reports

TUSR/AR	Periods	COM	EUR
1	Jan - Jun 1966	1580	
2	Jul - Dec 1966	1522	
3	Jan - Jun 1967	1745	
4	Jul - Dec 1967	2007	
5	Jan - Jun 1968	2172	
6	Jul - Dec 1968	2300	
7	Jan - Jun 1969	2434	
8	Jul - Dec 1969	2576	
9	Jan - Jun 1970	2664	
10	Jul - Dec 1970	2750	
11	Jan - Jun 1971	2833	
12	Jul - Dec 1971	2874	
13	Jan - Jun 1972	2939	
14	Jul - Dec 1972	3014	
15	Jan - Jun 1973	3050	
16	Jul - Dec 1973	3115	
17	Jan - Jun 1974	3161	
18	Jul - Dec 1974	3204	
19	Jan - Jun 1975	3241	
20	Jul - Dec 1975	3289	
21	Jan - Jun 1976	3358	
22	Jul - Dec 1976	3384	
23	Jan - Jun 1977	3438	6475 E
24	Jul - Dec 1977	3484	7209 E
25	Jan - Jun 1978	3526	7459 E
26	Jul - Dec 1978	3582	7227 E
27	Jan - Jun 1979	3657	7483 E
28	Jul - Dec 1979	3714	7509 E
29	Jan - Jun 1980	3822	7857 E
30	Jul - Dec 1980	3846	8230 E
31	Jan - Jun 1981	3898	8447 E
32	Jul - Dec 1981	3927	8777 E
33	Jan - Jun 1982	3990	9581 E
34	Jul - Dec 1982	4048	10251 E
35	Jan - Jun 1983	4094	10266 E
36	Jul - Dec 1983	4117	10454 E
37	Jan - Jun 1984	4150	10470 E
38	Jul - Dec 1984	4165	11013 E
39	Jan - Jun 1985	4201	11835 E
40	Jul - Dec 1985	4265	11836 E
86	Jan - Dec 1986	4302	(01.01.89)
87	Jan - Dec 1987	--------	11783 E

Previous Programme Progress Reports were confidential for a period of two years. Since 1977 they are made freely accessible after that period as EUR-Reports. They can be ordered from the Office for Official Publications of the European Communities, 2 rue Mercier, L-2985 Luxemburg, Tel. 49 92 81, Telex PUBOF LU 1324 b

This report was compiled and edited by H.E. Schmidt, J. Richter, L. Ruczka and R. Wellum.

For further information concerning JRC programmes please contact the Directorate General Science, Research and Development of the Commission of the European Communities, 200 rue de la Loi, B-1049 Brussels, Belgium.